Dissertation

submitted to the

Combined Faculties of the Natural Sciences and Mathematics

of the Ruperto-Carola-University of Heidelberg, Germany,

for the degree of

Doctor of Natural Sciences

Put forward by

Adriana Pohl

born in Saarlouis, Germany

Oral examination: January 23, 2018

Structure of Planet-forming Disks: Multi-wavelength Polarization Diagnostics

Referees:

Prof. Dr. Thomas Henning

Dr. Leonardo Testi

Abstract

The study of dynamic processes that drive the evolution of planet-forming disks is fundamental to understand the origin and diversity of planetary systems. This requires observations at high spatial resolution and sensitivity, which nowadays typically reveal intriguing disk substructures including gaps, rings, spirals, and shadows. This thesis investigates the capability of polarization observations at multiple wavelengths to trace the earliest stages of planet formation. In-depth radiative transfer calculations are carried out in order to link numerical simulations of dust and gas evolution in disks with their observational indicators. This approach demonstrates that measuring polarization is a powerful tool to identify the shaping effects that possible embedded planets have on the density distribution of different dust grain sizes. On the observational part, this work presents several case studies of individual planet-forming disks that were observed with polarimetric imaging by the VLT/SPHERE instrument and subsequently modeled to quantify their structure. A particular focus is the characterization of spiral and ring/gap structures in the context of dust growth, planet-disk interactions, and dust dynamics near ice lines. Furthermore, a modeling study of marginally gravitationally unstable disks is presented to study the influence of the disk self-gravity on the shape and contrast of planet-induced spiral arms in scattered light images. Additionally, it is demonstrated that polarized emission of disks at millimeter wavelengths can be caused by self-scattered thermal dust emission. It is shown that the latter is a viable method to constrain grain properties and identify dust concentrations of different origin. New ALMA observations are presented that offer the first look at a dust trap in polarized scattered light in the sub-millimeter range.

Zusammenfassung

Die Untersuchung von dynamischen Prozessen, die die Entwicklung von planetenbildenden Scheiben maßgeblich beeinflussen, ist fundamental, um die Entstehung von Planetensystemen und deren Vielfalt zu verstehen. Dies erfordert Teleskop-Beobachtungen bei hoher räumlicher Auflösung und Empfindlichkeit, die heutzutage für gewöhnlich faszinierende Scheibensubstrukturen einschließlich Lücken, Ringe, Spiralen und Schatten zum Vorschein bringen. Diese Doktorarbeit erforscht das Leistungsvermögen von Polarisationsbeobachtungen bei unterschiedlichen Wellenlängen, um das Frühstadium der Planetenentstehung nachzuvollziehen. Zur Verknüpfung von numerischen Simulationen der Staub- und Gasentwicklung in Scheiben mit ihren beobachtbaren Indikatoren werden ausführliche Strahlungstransportrechnungen durchgeführt. Dieses Vorgehen demonstriert, dass das Messen von Polarisation ein leistungsfähiges Werkzeug zur Identifizierung der formgebenden Effekte ist, die etwaige eingebettete Planeten auf die Dichteverteilung von verschiedenen Staubkorngrößen haben. Seitens der Beobachtungen präsentiert diese Arbeit mehrere Fallstudien einzelner planetenbildender Scheiben, die mit Hilfe des polarimetrischen Bildgebungsmodus des VLT/SPHERE Instruments beobachtet und anschließend modelliert wurden, um ihre Struktur zu erfassen. Ein besonderer Schwerpunkt liegt dabei auf der Charakterisierung von Spiral- und Ring-/Lochstrukturen im Rahmen von Staubwachstum, Planet-Scheiben-Wechselwirkungen sowie Staubdynamik nahe Eislinien. Des Weiteren wird eine Modellierungsstudie von marginal gravitativ instabilen Scheiben vorgestellt, um die Auswirkung der Eigengravitation der Scheibe auf Form und Kontrast der durch Planeten verursachten Spiralarme in Streulichtbildern zu untersuchen. Darüber hinaus wird demonstriert, dass polarisierte Emission von Scheiben im Millimeterbereich durch Selbststreuung von thermischer Staubemission verursacht werden kann. Es wird aufgezeigt, dass Letzteres eine aussichtsreiche Methode ist, um Teilcheneigenschaften einzuschränken und Staubkonzentrationen unterschiedlichen Ursprungs zu identifizieren. Neue ALMA-Beobachtungen werden vorgestellt, die erstmals einen Blick auf eine Staubfalle in polarisiertem Streulicht im Submillimeterbereich bieten.

Contents

1 | Introduction

Besides the sun and our moon, only five of our eight solar system planets can be generally seen with the human eye without optical aids - Mercury, Venus, Mars, Jupiter, and Saturn - and apart from that about 3000 stars from any fixed viewpoint. Only little was known about our own solar system planets, their major moons, comets and asteroids, until space missions were sent out to study them. Close flybys and rover landings allowed for in situ measurements exploring the surface and mineralogical content of these bodies. As an example, the space probe Juno is currently orbiting Jupiter (see Fig. 1.1a) to measure its composition, gravity variations, and magnetic field. First scientific Juno results reported on the existence and mass of Jupiter's core as well as a strong magnetic field with significant spatial variations (Bolton et al., 2017; Connerney et al., 2017). Furthermore, the Rosetta space probe, which carried the lander Philae, lately performed a cornerstone mission between 2014 and 2016 by going into orbit of and landing on the Jupiter-family comet 67P/Churyumov-Gerasimenko. It revealed a remarkable array of surface features covered by dust and debris (Fig. 1.1, panels b and c). Its overall composition is dominated by water ice and dust clumps with a very high porosity of 70-80%. Gases were measured to escape from the surface, which play an important role in transporting dust across the surface. This way, dune-like ripples and boulders with 'wind-tails' are produced (e.g., Gulkis et al., 2015; Rotundi et al., 2015; Thomas et al., 2015, see Fig. 1.1c).

Unfortunately, such in situ measurements are not yet technically feasible for bodies located outside of our solar system. The question whether our solar system together with our life-harboring planet are an anomaly or an ordinary appearance in the milky way is still waiting to be answered. Remote sensing techniques are used to study extrasolar planets, or short exoplanets, which can shed light on this question and also give us valuable information about the formation of our own planet. Back in the 17th century, the breakthrough innovation of the first telescope and the continuous further instrument development were the starting point towards the modern time of astronomy. In fact, we see many more stars than planets in the nightly sky, because stars are self-luminous in the optical wavelength segment, whereas planets only reflect light making them so much fainter than the stars they orbit. Direct imaging of planets beyond the solar system has been challenging astronomers for a long time since the angular separations between planets and their host star are extremely small, making it hard to distinguish planetary and stellar signals. In

(a)

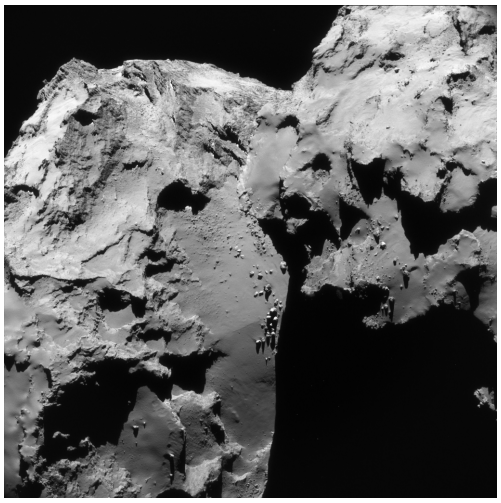

(b)

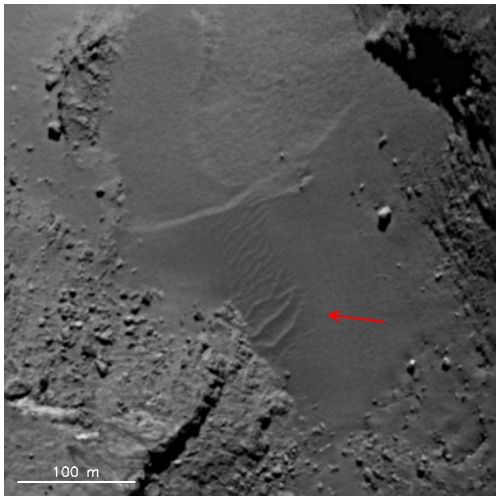

(c)

Figure 1.1: (a): Processed image of Jupiter captured by the JunoCam on board of NASA's Juno spacecraft on September 1, 2017. At that point it performed its eighth Jupiter flyby at a distance of ∼7600 km. Image credit: NASA/JPL-Caltech/SwRI/MSSS/Gerald Eichstädt. **(b):** Rosetta NavCam image (actual size of 2.7 km across) taken on June 17, 2016, when ESA's Rosetta was about 30.8 km from the center of the nucleus of Comet 67P/Churyumov-Gerasimenko. Image Credit: ESA/Rosetta/NAVCAM – CC BY-SA IGO 3.0. **(c):** 'Zoom-in' onto the surface with the Rosetta OSIRIS narrow-angle camera. The image was taken on September 2, 2014 and shows Aeolian ripples in the Hapi region on 67P. The surface of the comet is covered by dust, debris, and boulders up to meter sizes. Image credit: ESA/Rosetta/MPS for OSIRIS Team MPS/UPD/LAM/IAA/SSO/INTA/UPM/DASP/IDA.

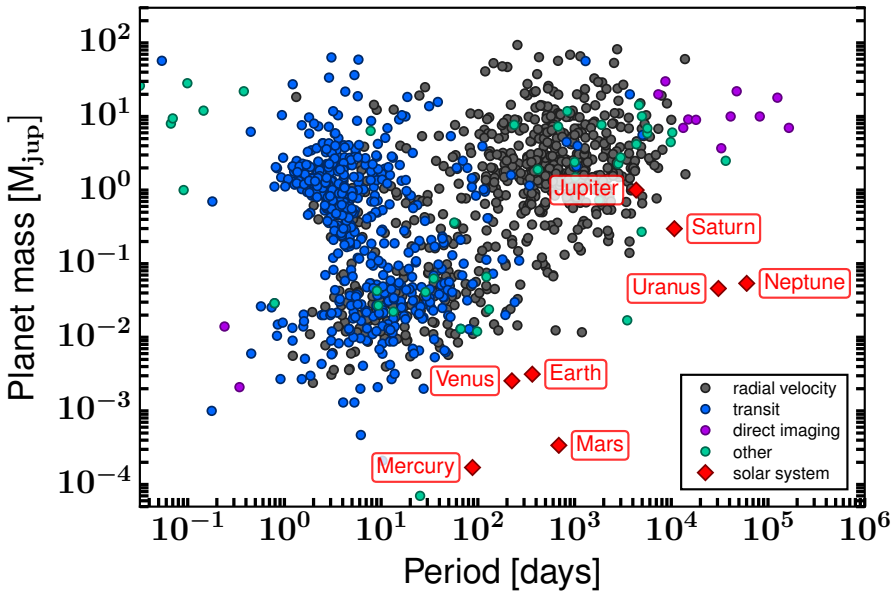

Figure 1.2: Distribution of the masses of confirmed exoplanets in dependence of their orbital period sorted by the detection method. Data are taken from the exoplanet.eu database[1]. For comparison, our eight solar system planets are shown with red diamonds.

fact, it was not until 1995 that the very first exoplanet was detected at all in the orbit around a main sequence star. Logically, this was not inferred by measuring the planet's light signal directly, but from observations of periodic variations in the star's radial velocity (Mayor & Queloz, 1995).

The large number of exoplanets discovered by now with various techniques indicates that planet formation around young stars is a very common and efficient process (see Fig. 1.2, 3671 confirmed planets and another 2422 candidates according to the exoplanet.eu[1] catalog on September 26, 2017). As more than 600 of those planets are in multiple systems, there seem to be more planets than stars in our milky way (Cassan et al., 2012). Accordingly, there might be billions of potentially habitable planets making it plausible that biological evolution could have started to create extraterrestrial life. Another striking argument for the frequent existence of life is how 'fast' on cosmological timescales the first life appeared on Earth. The observed exoplanetary systems display a variety of architectures, which mostly do not follow the configuration of our solar system. In order to understand the physical processes and constituents involved in forming planetary systems, their formation and evolution environment, that is the circumstellar material, needs to be studied. These so-called protoplanetary or planet-forming disks[2] are of particular interest for this thesis. They are introduced in Sect. 1.1 and further addressed in theoretical and observational contexts in Sects. 1.2 and 1.3.

[1] www.exoplanets.eu

[2] The terms 'protoplanetary' and 'planet-forming' are used interchangeably in this thesis.

1.1 Planet-forming disks around young stars

1.1.1 Star and disk formation

The circumstellar material in form of gas and dust that surrounds young low- and intermediate mass ($\lesssim 8\,M_\odot$) stars is thought to be the cradle of planets. These planet-forming disks are a natural outcome of the star formation process. Stars themselves form within giant molecular clouds, which contain dense, cool interstellar gas (mostly molecular hydrogen) and dust left over from the formation and evolution of the galaxy. Molecular clouds are hierarchically structured, where the smallest structures are high density ($\sim 10^4 - 10^6\,\mathrm{cm}^{-3}$) cores with a typical size of $\sim 0.1\,\mathrm{pc}$ and masses between $\sim 1\,M_\odot$ and $1000\,M_\odot$ (e.g., Lada, 2005; Draine, 2011). If such a core reaches a mass in excess of the critical Jeans mass, an imbalance occurs between the internal gravitational and gas pressure forces, and it will collapse. The dust in the cloud is still optically thin (cf. Sect. 2.1 for a definition of the optical depth), so that the energy gained by the collapse is effectively radiated away. The innermost material at the center eventually becomes dense enough to be optically thick to its own radiation allowing the formation of a protostar, referred to as Class 0 stage.

The initial cloud is not homogeneous and far from static, since the cores rotate and given the influence of magnetic fields and turbulence. Thus, any collapsing region will possess nonzero angular momentum, leading to the formation of a circumstellar disk, whose plane is perpendicular to the angular momentum. Apart from the protoplanetary context, this is also seen around black holes and other compact objects. More precisely, during the accretion phase of protostellar evolution, material is accreted onto the protostar from its infalling envelope. At the same time, the initial rotation of the core increases due to angular momentum conservation. This enhanced rotation prevents further infall directly onto the protostar and, instead, the infalling material will form a disk surrounding the protostar (Class I stage, $\sim 10^4 - 10^5\,\mathrm{yr}$ after the onset of the collapse). Disk material is transported inwards and accreted onto the star, while angular momentum is transported outwards. As the material moves inwards, it also loses energy which is radiated away by the disk. When the envelope of the star is completely dissipated due to accretion and molecular outflows, a star with a moderate accretion rate and its circumstellar disk remain, where heating from the star will be the main source of energy in the outer disk regions (Class II or classical T Tauri stars (CTTS), $\gtrsim 10^6\,\mathrm{yr}$). In the latest stage (Class III or weak-line T Tauri stars (WTTS), $\gg 10^7\,\mathrm{yr}$), the gaseous disk has been accreted onto the star and a pre-main-sequence (PMS) star remains surrounded by a tenuous, optically thin disk consisting of debris and possibly hosting a planetary system.

An observed PMS star representing the Class II objects can be either a low mass T Tauri star for $M_\star \lesssim 2\,M_\odot$, or their massive counterpart, a Herbig Ae/Be star ($2\,M_\odot \lesssim M_\star \lesssim 8\,M_\odot$, Herbig, 1960). While T Tauri objects are precursors of solar-type stars, Herbig Ae/Be stars have a higher luminosity and are thus more easily observable. Modeling studies for disks around both stellar types will be presented in this thesis (see Chapter 3 and the following).

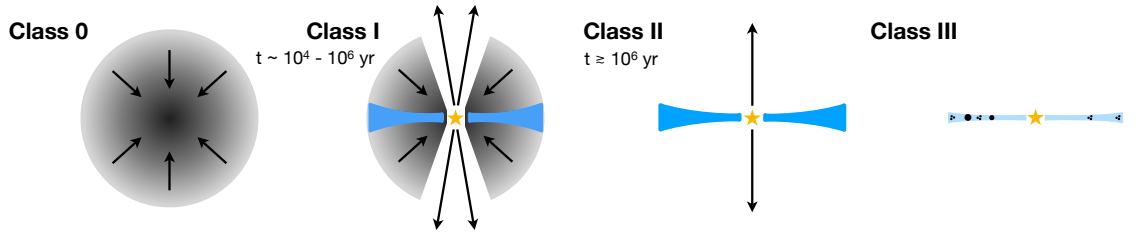

Figure 1.3: Evolutionary stages of a YSO, classified according to the Lada sequence. Shown are sketches of the geometry of the star-disk system. The four classes roughly correspond to: gravitational collapse and formation of a protostar (Class 0), accretion of the stellar envelope and disk formation (Class I), non-embedded planet-forming disk (Class II), and disk dissipation leading to a debris disk with a possible planetary system (Class III). Note that this illustration is not to scale.

From an observational point of view, with the availability of infrared data from the InfraRed Astronomical Satellite (IRAS) and the Infrared Space Observatory (ISO) (see Sect. 1.3.1 for more details), the transition from a core to a star-disk system can be described by the Lada sequence (Lada & Wilking, 1984; Lada, 1987; Adams et al., 1987). It classifies protostars based on the spectral energy distribution (SED), which measures the distribution of flux F_λ as a function of wavelength. Dust grains in the disk are heated by viscous heating and stellar irradiation. Therefore, the dust temperature depends on the distance from its central heating source, producing a range of temperatures throughout the disk. Thus, the disk emission in the SED is visible as a broad-band continuous excess above the stellar photosphere at infrared and millimeter (mm) wavelengths. Emission in the near-infrared (NIR) and mid-infrared (MIR) originates from warm dust close to the star, while emission at longer wavelengths traces colder material further away from the star. Disk emission is distinct from envelope emission since a spherical halo obscures a much larger fraction of the protostar emission. The reason lies in the different geometry. Without the presence of an envelope, sight lines that are not close to the disk plane yield a relatively unobstructed view to the star. The spectral index in the MIR to NIR, α_{IR}, which is defined as the slope of the SED, describes the energy flux received at a given wavelength range (Lada & Wilking, 1984; Lada, 1987),

$$\alpha_{\mathrm{IR}} = \frac{d \log \lambda F_\lambda}{d \log \lambda} \,. \tag{1.1}$$

As already terminologically introduced, the following four different evolutionary phases of young stellar objects (YSOs) are distinguished (cf. Fig. 1.3):
Class 0: Optical photons are absorbed by the optically thick envelope surrounding the protostar and re-emitted at longer wavelengths, so that the SED peaks in the far-infrared (FIR) or mm part of the spectrum (α_{IR} undefined).
Class I: The SED shows an approximately flat or rising spectrum between the NIR

and MIR with $\alpha_{\rm IR} \geq 0$.
Class II: The SED consists of the optically visible star (envelope is totally dissipated) together with circumstellar disk emission at infrared and mm wavelengths ($-1.6 \leq \alpha_{\rm IR} < 0$).
Class III: The SED is dominated by the stellar photosphere with $\alpha_{\rm IR} < -1.6$.

1.1.2 Physical disk structure

This section summarizes the basic physical structure of planet-forming disks, with particular attention paid to those properties used in the modeling effort of this thesis. Primarily, the density and temperature structures of both, dust and gas, dominate the physical evolution of the disk. The following brief summary follows the calculations from Armitage (2013).

Density

In a first approximation, a protoplanetary disk can be assumed to have an axisymmetric geometry and to be vertically isothermal, that means $\partial T/\partial z = 0$. A further simplification assumes that the disk self-gravity can be neglected, thus, the gravitational potential is dominated by the star. In cylindrical coordinates, this potential is given by

$$\Phi(r, z) = \frac{GM_\star}{\sqrt{z^2 + r^2}}\,, \tag{1.2}$$

where G is the gravitational constant, and $M_\star$ denotes the stellar mass. Under the further assumption of a thin disk ($z \ll r$), the gravitational acceleration in vertical direction yields

$$\frac{\partial \Phi}{\partial z} = -\frac{GM_\star}{\left(z^2 + r^2\right)^{3/2}}\, z \simeq -\frac{GM_\star}{r^3}\, z = -\Omega_{\rm K}^2(r)\, z\,, \tag{1.3}$$

with $\Omega_{\rm K} = \left(GM_\star/r^3\right)^{1/2}$ being the Keplerian angular frequency. Hence, the vertical hydrostatic equilibrium equation is given by the balance between the stellar gravitational force and the counteracting pressure force,

$$-\frac{1}{\rho_{\rm g}}\frac{\partial P_{\rm g}}{\partial z} = \Omega_{\rm K}^2\, z\,. \tag{1.4}$$

Assuming an ideal gas, the pressure is defined as $P_\mathrm{g} = \rho_\mathrm{g} c_\mathrm{s}$, with sound speed

$$c_\mathrm{s} = \sqrt{\frac{k_\mathrm{B} T}{\mu m_\mathrm{p}}}\,, \tag{1.5}$$

with Boltzmann constant k_B, midplane disk temperature T, molecular weight of the gas μ, and proton mass m_p. Equation 1.4 can be then written as

$$\begin{aligned} c_s^2(r)\,\frac{\partial \rho_g(r,z)}{\partial z} &= -\rho_g(r,z)\,\Omega_K^2(r)\,z \\ \Leftrightarrow \frac{\partial \ln\left(\rho_g(r,z)\right)}{\partial z} &= -\frac{\Omega_\mathrm{K}^2(r)}{c_s^2(r)}\,z\,. \end{aligned} \tag{1.6}$$

By integrating Eq. 1.6, the resulting gas density structure is that of a Gaussian profile,

$$\rho_\mathrm{g}(r,z) = \rho_{\mathrm{g},0}(r)\,\exp\left(-\frac{z^2}{2\,H^2(r)}\right)\,, \tag{1.7}$$

where the disk pressure scale height H is defined as the ratio of sound speed and Keplerian angular frequency

$$H(r) = \frac{c_\mathrm{s}(r)}{\Omega_\mathrm{K}(r)}\,. \tag{1.8}$$

The quantity $\rho_{\mathrm{g},0}(r)$ is by definition the midplane gas density and can be determined by means of the gas surface density $\Sigma_\mathrm{g}(r)$. The latter is the amount of material vertically integrated in a column perpendicular to the disk plane, at a certain distance from the star,

$$\Sigma_\mathrm{g}(r) = \int_{-\infty}^{\infty} \rho_\mathrm{g}(r,z)\,dz\,. \tag{1.9}$$

Combining Eqs. 1.7 and 1.9 eventually leads to

$$\begin{aligned} \int_{-\infty}^{\infty} \rho_\mathrm{g}(r,z)\,dz &= \int_{-\infty}^{\infty} \rho_{\mathrm{g},0}(r)\,\exp\left(-\frac{z^2}{2\,H^2(r)}\right)\,dz \\ \Rightarrow \rho_{\mathrm{g},0}(r) &= \frac{\Sigma_\mathrm{g}(r)}{\sqrt{2\,\pi}\,H(r)}\,. \end{aligned} \tag{1.10}$$

With this in hand, Eq. 1.7 can be rewritten as

$$\rho_{\mathrm{g}}(r,z) = \frac{\Sigma_{\mathrm{g}}(r)}{\sqrt{2\,\pi}\,H(r)}\,\exp\left(-\frac{z^2}{2\,H^2(r)}\right)\,. \tag{1.11}$$

Temperature

The disk temperature structure is set by the balance between cooling and heating processes since their corresponding timescales are much shorter than the overall disk and stellar evolution timescales. Depending on the location within the disk, either viscous heating (inner disk) due to accretion or heating due to irradiation (outer disk) by the star dominates, while the cooling mostly originates from dust grain emission.

The amount of viscous heating per unit disk area for a constant accretion rate, which is the amount of matter per second that moves radially through the disk, $\dot{M} \equiv -2\pi\Sigma r v_{\mathrm{r}} = \text{const.}$ with radial velocity $v_{\mathrm{r}} = -3v/(2r)$, can be estimated by

$$Q_{+}^{\mathrm{accr}} = \frac{3}{4\pi}\dot{M}\Omega_{\mathrm{K}}^2 \propto r^{-3/2}\,. \tag{1.12}$$

When the predominant heating source is stellar irradiation, the disk temperature structure is determined by the re-emission of this radiation and the shape of the disk characterized by the disk aspect ratio $h(r) := H(r)/r$. Parameterizing the sound speed as $c_{\mathrm{s}}(r) \propto r^{-\beta_{\mathrm{s}}}$ leads to a disk aspect ratio of $h(r) \propto r^{-\beta_{\mathrm{s}}+1/2}$. The disk has a constant aspect ratio for $\beta_{\mathrm{s}} = 1/2$, while it is flared for $\beta_{\mathrm{s}} < 1/2$, consequently meaning that the aspect ratio increases with radius. Kenyon & Hartmann (1987) found that flared disks give indeed the best observational match with T Tauri star disks, and that the temperature is well approximated by $T(r) \propto r^{-1/2}$. However, a more accurate approach takes the feedback of the scale height profile on the temperature structure into account, which is addressed in Chiang & Goldreich (1997). In this case, the temperature profile is slightly shallower, $T(r) \propto r^{-3/7}$.

Considering that most disks are supposed to be flaring, stellar light is intercepted by the disk surface under a shallow grazing angle φ_{inc} with respect to the tangent to the disk surface at a certain distance. The rate of this irradiation heating per unit disk area can be estimated by

$$Q_{+}^{\mathrm{irr}} = 2\sin(\varphi_{\mathrm{inc}})\left(\frac{L_\star}{4\pi r^2}\right) \simeq 2\,\varphi_{\mathrm{inc}}\left(\frac{L_\star}{4\pi r^2}\right)\,, \tag{1.13}$$

where $L_\star$ is the stellar luminosity. While Chiang & Goldreich (1997) estimate the

following general form for the grazing angle,

$$\varphi_{\rm inc} \approx \frac{0.4 R_\star}{r} + r \frac{d}{dr}\left(\frac{H}{r}\right) , \tag{1.14}$$

a value of $\varphi_{\rm inc} \sim 0.05$ seems a reasonable assumption for analytical models (e.g., Dullemond & Dominik, 2004b).

Assuming that the dust in the two disk surfaces radiates as a blackbody, the disk cooling rate can be estimated by

$$Q_- = 2\sigma_{\rm SB} T_{\rm eff}^4 , \tag{1.15}$$

with Stefan-Boltzmann constant $\sigma_{\rm SB}$. Combining Eqs. 1.12, 1.13 and 1.15, the effective disk temperature can be obtained,

$$T_{\rm eff} = \left(\frac{3}{8\pi\sigma_{\rm SB}} \dot{M} \Omega_{\rm K}^2 + \varphi_{\rm inc} \frac{L_\star}{4\pi\sigma_{\rm SB} r^2} \right)^{1/4} . \tag{1.16}$$

It has to be noted that unlike the assumptions so far, in reality disks deviate from the vertically isothermal idealization due to optical depth effects (see Eq. 2.2 for definition). The effective disk temperature is different from the actual temperature structure of the surface and the interior. Therefore, gas and especially dust opacities have to be included when modeling a disk. A more accurate temperature distribution can therefore only be reached by numerical radiative transfer calculations. These points are further addressed in Sect. 2.

Velocity

The radial component of the equation of motion in disks considers contributions from centrifugal force, gravity, and radial pressure gradient,

$$\frac{v_{\phi,\rm g}^2}{r} = \frac{G M_\star}{r^2} + \frac{1}{\rho}\frac{dP}{dr} , \tag{1.17}$$

where $v_{\phi,\rm gas}$ is the orbital speed of the gas. A pressure support parameter η, which parameterizes the difference between gas and Keplerian velocity, can be defined as

$$\eta = -\frac{r}{\rho_{\rm g} v_{\rm K}^2}\frac{dP}{dr} . \tag{1.18}$$

Hence, Eq. 1.17 simplifies to

$$v_{\phi,\mathrm{g}} = v_{\mathrm{K}} \left(1-\eta\right)^{1/2} \simeq v_{\mathrm{K}} \left(1-\eta/2\right) \ . \tag{1.19}$$

Since the pressure gradient is negative for a smooth disk, implying $\eta > 0$, the gas rotates with a sub-Keplerian velocity. This has a significant influence on the motion of dusty solids and particle trapping as described in Sects. 1.2.1 and 1.2.2.

1.1.3 Disk evolution on its global scale

Circumstellar disks are observed to slowly evolve and eventually disperse over a timescale of a few Myr (e.g., Alexander et al., 2014). Interestingly, this timescale is comparable to that predicted for planet formation by core accretion (Pollack et al., 1996, see Sect. 1.2.2). The evolution of the surface density of disks is primarily driven by accretion of matter through the disk and onto the central object, but it is still unclear whether disk viscosity or magnetically-launched winds drive this accretion and which role is assigned to photoevaporation (see e.g., recent review by Ercolano & Pascucci, 2017). It seems likely that multiple disk clearing mechanisms operate concurrently and/or consecutively in disks. Studies on the infrared two-color plane point at an inside-out disk clearing (Ercolano et al., 2011). The mass-loss throughout the disk's lifetime also influences ongoing planet formation, since the disk gets depleted of gas, which enhances the dust-to-gas ratio and the fractional abundances of heavy elements in the disk.

The basic evolution of the disk's surface density seems to be consistent with viscous theory (e.g., Lynden-Bell & Pringle, 1974; Hartmann et al., 1998), which predicts a rather slow disk dispersal. Active accretion of disk material onto the star, with average rates of $\dot{M}_{\mathrm{disk}} \sim 10^{-10} - 10^{-8}\,\mathrm{M}_{\odot}\,\mathrm{yr}^{-1}$ (e.g., Manara et al., 2012, 2016), requires the transport of mass inwards and therefore a transport of angular momentum outwards. According to Shakura & Sunyaev (1973), this transport can be attributed to a turbulent viscous stress in the following way.

Considering the Navier-Stokes equations for a viscous fluid, the evolution of the surface density under the influence of a global viscosity ν_{t} is given by (Lynden-Bell & Pringle, 1974)

$$\frac{\partial}{\partial t}\Sigma_{\mathrm{g}}(r,t) = \frac{3}{r}\frac{\partial}{\partial r}\left(r^{1/2}\frac{\partial}{\partial r}\left[\Sigma_{\mathrm{g}}(r,t)r^{1/2}\nu_{\mathrm{t}}\right]\right) \ . \tag{1.20}$$

Originally introduced for accretion disks around black holes, ν_{t} can be parameterized by estimating the typical length scale and velocity of the disk. For a protoplanetary disk, this is the disk pressure scale height H and the sound speed of the gas c_{s}, which

leads to

$$\nu_{\rm t} = \alpha\, c_{\rm s}\, H\,, \tag{1.21}$$

where α is a dimensionless proportionality coefficient. This so-called $\alpha-$prescription represents the efficiency of turbulent transport. It is used as a basic assumption for turbulence in disk models presented later on in this thesis. While the source of turbulence is actually still under debate, idealized theoretical models invoke magnetorotational instability (MRI) as a main candidate (Balbus & Hawley, 1991). Pure hydrodynamic mechanisms appear unable to provide a sufficient level of turbulent viscosity. MRI can, however, only work if the ionization fraction in the disk is large enough. A weak level of ionization introduces strong non-ideal magnetohydrodynamic (MHD) effects that suppress or damp MRI in many disk regions. In the conventional picture, where only ohmic resistivity is taken into account, there is a more or less laminar midplane called 'dead zone' and a better-ionized, active surface layer where MRI-driven accretion proceeds. However, the other two non-ideal MHD terms, Hall effect and ambipolar diffusion, also play a crucial role in determining the mechanism and efficiency of angular momentum transport as well as the level of turbulence in disks. Recently, non-ideal MHD simulations found that a large portion of the disk is actually stable to the MRI. Simulations including the Hall effect showed that this can produce a dominant azimuthal magnetic field and a large-scale Maxwell stress throughout the midplane without inducing a turbulent flow Lesur et al. (2014). It was also shown that the inclusion of ambipolar diffusion reduces the efficiency of MRI, suggesting magnetized winds as a promising alternative to drive angular momentum transport (e.g., Bai & Stone, 2013; Bai, 2013, 2016). MRI may still operate in the surface layer of the outer disk, which can lead to a certain level of viscous transport of angular momentum (e.g., Simon et al., 2013b,a).

In general, disk clearing is not a homogeneous process given that the disk dispersal timescale is about ten times faster than the global disk lifetime. Moreover, disk accretion can proceed 'in bursts' for FU Orionis objects, such that relatively long periods of low accretion rates are followed by sudden bursts of accretion that can rise the accretion rate up to a few $10^{-4}\,{\rm M_\odot yr^{-1}}$ (e.g., Audard et al., 2014). Surveys of nearby star-forming regions have shown that the infrared excess fraction for single stars is close to 100% in young clusters ($< 1\,$Myr). This fraction dramatically decreases with time, is around 10% for an age of $\sim$5 Myr and reaches zero at $\sim$10-20 Myr (e.g., Mamajek, 2009; Ribas et al., 2014). Hence, all these points indicate that there must be other non-viscous disk dispersal mechanisms at work as well (see e.g., detailed reviews by Hollenbach et al., 2000; Clarke, 2011; Ercolano & Pascucci, 2017).

Magnetically-launched disk winds present a plausible explanation for jets in young stars (Ferreira et al., 2006). As mentioned above, numerical simulations show that even a weak vertical magnetic field can launch such a wind, which extracts both mass and angular momentum from the disk (e.g., Bai & Stone, 2013). The second

considered mechanism for disk dispersal is photoevaporation (e.g., Clarke et al., 2001; Alexander et al., 2006a,b; Owen et al., 2011, 2012). High-energetic radiation (far-ultraviolet, extreme-ultraviolet, soft X-rays) is able to efficiently heat the disk's upper layers above the midplane temperature. If the thermal energy of the heated gas at a given location exceeds its gravitational binding energy, the gas escapes via a pressure-driven wind flow. The mass loss rate of the wind must become larger than the disk accretion rate in order to cause dispersal.

Transition disks

There is a significant number of disks that are thought to be in an intermediate phase between an optically thick, gas-rich disk (Class II) towards a cleared-out debris disk consisting of large dust, planetesimals, and planets (Class III). They are called 'transition' disks and their fraction is thought to be 5%-30% depending on the exact definition (e.g., Andrews et al., 2011; Ansdell et al., 2016; Pascucci et al., 2016). This implies that the evolutionary path through a transition disk phase is either rapid or uncommon. They provide a unique opportunity to directly study the processes that drive the evolution from a protoplanetary disk to a mature planetary system. Transition disks are usually identified by their at least partially evacuated inner dust hole, whose signature is seen as a reduced NIR to MIR emission in the SED (Strom et al., 1989). They are, however, a diverse class of objects and it remains unclear whether all circumstellar disks actually undergo a transition disk phase. While some transition disks host relatively small dust holes of a few astronomical units (au) in size and are weakly accreting gas onto the central star, others show large inner dust cavities and significant accretion (e.g., Manara et al., 2014).

Different mechanisms could play a role for the formation of transition disks, among others these are: photoevaporation driven by the central star, MHD turbulence, dust grain growth beyond sizes where emission at the observed wavelength is efficient, dynamical clearing by a substellar companion, and planet-disk interaction processes (see Sects. 1.2 and 1.3 for further information). However, photoevaporation alone can be dismissed as the origin for some of the transition disks that have a high accretion rate, but also a large disk mass and large cavity at the same time (Alexander & Armitage, 2007; Ercolano & Pascucci, 2017). Moreover, a totally different formation scenario could be at work connected to secondary disk formation (Dullemond et al., in prep.). Transition disks sometimes show a tiny inner disk close to the star instead of hosting a full cavity, whose plane is inclined with respect to the outer disk (Lazareff et al., 2017, see also Chapter 5).

In this scenario, the outer disk has originated from late-time infall of gas and dust from a passing low mass molecular cloud filament. Statistically speaking, the accreted material from these flybys should build up a second disk at arbitrary orientation compared to the inner dust disk. Independent of their formation mechanism, observations of transition disks at multiple wavelengths have been revealing a large variety of substructures, such as multiple rings and gaps, spiral arms, warps, dips, and shadows. Their possible origins and characteristics are further described in

Sect. 1.3.2.

1.2 Internal disk processes

The initial conditions for planet formation are determined by the protoplanetary disks, making it inevitable to understand their ingredients. The mechanisms involved in the evolution of planetary building blocks remain a mystery. Increasingly sophisticated evolution models together with new multi-wavelength spatially resolved dust and gas observations only slowly start to connect the different puzzle pieces. This section summarizes those physical processes happening in the disk that are most important for the studies in this thesis. Starting with the dynamics of dust particles and their spatial distribution, scenarios of dust trapping and efficient grain growth are presented (Sect. 1.2.1). The subsequent formation of planetesimals and planet cores is addressed in Sect. 1.2.2. Once planets have formed, planet-disk interaction processes can sculpt the disk density and temperature structure which is summarized in Sect. 1.2.3.

1.2.1 Dust evolution

During the evolution of solid particles from sub-micron-sized monomers to planetesimals, they pass through an extreme range in mass and size, spanning over more than forty and ten orders of magnitudes, respectively. The goal of state-of-the art dust evolution models, for example Brauer et al. (2008); Birnstiel et al. (2010); Gonzalez et al. (2017), is to trace the evolution of dust during the whole lifetime of a planet-forming disk, considering grain growth, fragmentation, radial drift, and turbulent mixing. Dust particles in protoplanetary disks are subject to gravitational and centrifugal forces, and also interact aerodynamically with the gas. The strength of the aerodynamic drag can be expressed in terms of the stopping time t_s. This is the typical timescale it takes for a dust particle to adapt its motion to that of the gas,

$$t_\mathrm{s} = \frac{mv}{F_\mathrm{D}}\,, \tag{1.22}$$

where m is the particle's mass, v its relative velocity with the gas and F_D the gas drag law. The drag force acting on a solid is defined as

$$F_\mathrm{D} = -\frac{1}{2} C_\mathrm{D} A \rho_\mathrm{g} \Delta v^2\,, \tag{1.23}$$

where A is the projected surface area of the particle, Δv denotes the relative velocity between gas and dust, and C_D is the value of the drag coefficient. In protoplanetary disks, there are two relevant drag regimes, called Epstein and Stokes regimes

(Epstein, 1924; Whipple, 1972; Weidenschilling, 1977). The mean free path of a gas molecule is defined as

$$\lambda_{\mathrm{mfp}} = \frac{m_{\mathrm{g}}}{\rho_{\mathrm{g}} \sigma_{\mathrm{g}}}\,, \tag{1.24}$$

where m_{g} is the gas molecule mass and σ_{g} is the collisional cross section. It can be used to distinguish between the two regimes. The Epstein regime applies to small grains, for which the drag can be considered as individual collisions with gas molecules. Assuming compact, spherical dust grains, this holds for radii $a < 9\lambda_{\mathrm{mfp}}/4$. Dust grains with $a > 9\lambda_{\mathrm{mfp}}/4$ are in the Stokes regime, where the regime with a Reynolds number smaller than one is mostly relevant for the conditions in disks. The Reynolds number Re of the gas is defined as the ratio of the inertial and the viscous forces,

$$\mathrm{Re} = \frac{2a\Delta v}{\nu}\,, \tag{1.25}$$

with the vertically integrated kinematic viscosity of the gas $\nu = 1/2\, v_{\mathrm{th}} \lambda_{\mathrm{mfp}}$ and the mean thermal velocity $v_{\mathrm{th}} = \sqrt{8/\pi}\, c_{\mathrm{s}}$.

Moreover, the interaction between dust and gas can be parameterized with the dimensionless Stokes number, which is the ratio of the stopping time and the turnover time of the largest eddies (e.g., Schräpler & Henning, 2004),

$$\mathrm{St} = \frac{t_{\mathrm{s}}}{\tau_{\mathrm{L}}} = t_{\mathrm{s}} \Omega_{\mathrm{K}}\,. \tag{1.26}$$

In the Epstein regime the Stokes number becomes (Birnstiel et al., 2010)

$$\mathrm{St} = \frac{\rho_{\mathrm{s}} a}{\Sigma_{\mathrm{g}}} \frac{\pi}{2}\,, \tag{1.27}$$

with ρ_{s} being the solid density of the particles.

For the calculation of the rates and outcomes of dust collisions, relative velocities between the particles have to be considered, which can be caused by Brownian motion, relative radial and azimuthal velocities, turbulent relative velocities, and differential settling (see e.g., Birnstiel et al., 2010). Mutual collisions can increase or decrease the mass of the colliding particles, or keep it unchanged depending on impact speed and mass ratio. The smallest grains experience hit-and-stick growth, meaning that they stick together due to the weak van der Waals interactions (for silicates) or dipole forces (for icy particles, cf. Chapter 8). This results in porous, fractal aggregates as tested by laboratory experiments (Ossenkopf, 1993; Wurm &

Blum, 1998). As the grains grow, their relative velocities rapidly increase in the presence of turbulence and drift. At higher impact velocities, the sticking process for compact grains does not work well anymore, rather leading to fragmentation (Weidling et al., 2009) and bouncing effects with possible mass transfer (e.g., Wurm et al., 2005; Teiser & Wurm, 2009; Güttler et al., 2010). The collision velocity at which this occurs has been experimentally estimated in the laboratory. For compact, mm-sized particles it is about 1 m/s (Blum & Münch, 1993) and for centimeter (cm)-sized particles in the order of 0.4 m/s (Schräpler et al., 2012).

Growth barriers

A number of barriers have been identified with numerical models and laboratory experiments, which inhibit the dust from growing to planetesimal sizes. These barriers are either related to collisional dust physics, such as fragmentation (Weidenschilling, 1980; Blum & Münch, 1993), bouncing (Güttler et al., 2010; Zsom et al., 2010), and charging effects (Okuzumi, 2009; Okuzumi et al., 2011a,b), or the radial drift timescale (Whipple, 1972; Weidenschilling, 1977). Broadly speaking, the growth of dust particles in the inner disk is fragmentation limited, while it is drift limited in the outer disk.

The radial drift barrier concerns the interplay between growth and radial drift timescales. As already described in Sect. 1.1.2, disks are partially pressure supported causing the gas to orbit the star at a velocity slightly less than Keplerian. Dust grains do, however, not feel this pressure and in the absence of gas would move on a Keplerian orbit. Because of the sub-Keplerian gas velocity, there exists a constant friction force ('headwind'), which causes the particles to lose angular momentum, and drift inwards. The equations of motion of a particle are (following Adachi et al., 1976; Takeuchi & Lin, 2002)

$$\frac{dv_{\mathrm{r,d}}}{dt} = \frac{v_{\phi,\mathrm{d}}^2}{r} - \frac{v_{\mathrm{K}}^2}{r} - \frac{1}{t_{\mathrm{s}}}\left(v_{\mathrm{r,d}} - v_{\mathrm{r,g}}\right) , \tag{1.28}$$

$$\frac{d}{dt}\left(r v_{\phi,\mathrm{d}}\right) = -\frac{r}{t_{\mathrm{s}}}\left(v_{\phi,\mathrm{d}} - v_{\phi,\mathrm{g}}\right) , \tag{1.29}$$

where v_{r} and v_{ϕ} are the r- and ϕ-components of the velocity, respectively. The stopping time as defined in Eq. 1.22 is given here by $t_{\mathrm{s}} = \rho_{\mathrm{s}} a / \left(\rho v_{\mathrm{th}}\right)$. Using Eq. 1.19 and neglecting higher order terms, Eq. 1.28 simplifies to

$$v_{\mathrm{r,d}} = \frac{v_{\mathrm{r,g}}}{1 + \mathrm{St}^2} - \frac{\eta v_{\mathrm{K}}}{\mathrm{St}^{-1} + \mathrm{St}} . \tag{1.30}$$

By assuming that $d(rv_{\phi,\mathrm{d}})/dt \simeq v_{\mathrm{r,d}}\, d(rv_{\mathrm{K}})/dr = v_{\mathrm{r,d}}v_{\mathrm{K}}/2$, Eq. 1.29 modifies to

$$v_{\phi,\mathrm{d}} - v_{\mathrm{K}} = -\frac{\eta v_{\mathrm{K}}}{2\left(1+\mathrm{St}^2\right)} - \frac{v_{\mathrm{r,g}}\mathrm{St}}{2\left(1+\mathrm{St}^2\right)}\,. \tag{1.31}$$

Equation 1.31 shows that particles with $\mathrm{St} \gg 1$ have $v_{\phi,\mathrm{d}} = v_{\mathrm{K}}$, while particles with $\mathrm{St} \ll 1$ have the sub-Keplerian motion as the gas (cf. Eq. 1.19). The second term on the right hand side of Eq. 1.30 becomes small for both $\mathrm{St} \ll 1$ and $\mathrm{St} \gg 1$. The first term on the right hand side of Eq. 1.30, the drag term, shows that small particles ($\mathrm{St} \ll 1$) are not affected by drift as they are fully coupled to the gas. Large solids ($\mathrm{St} \gg 1$), such as planetesimals and planets, are also not influenced by drift as they are fully decoupled from the gas and not affected by the drag. They still feel a headwind, but their momentum is so large that the gas drag does not lead to significant loss in orbital energy over the relevant time scales. Particles with $\mathrm{St} \simeq 1$ acquire the highest drift. This is highly problematic as the timescale involved can be very short, on the order of ∼100 yr, many orders of magnitudes below the ages of observed protoplanetary disk systems. This is one of the most serious challenges in planetesimal formation by dust coagulation as this scenario actually requires particles to gradually grow through $\mathrm{St} \sim 1$.

In the case of the fragmentation barrier, whenever a particle becomes to large and is subject to high-velocity collisions, it fragments. These small fragments can again grow to reach that barrier, which produces a continuous growth & fragmentation cycle as shown in numerical models (Birnstiel et al., 2010). Growth to $\mathrm{St} \simeq 1$ would require weak turbulence and/or a high fragmentation velocity. If the collision energy is too high for sticking, but too low for fragmentation, colliding particles just bounce and become more compact, which halts their growth and results in a pile-up of grains with a certain size.

The barrier that actually arises earliest in the evolution of the disk is the charging or Coulomb barrier. Disks are expected to be weakly ionized, such that dust particles charge up negatively by capturing electrons, which have higher thermal velocities than ions. Thus, the electrostatic repulsion between aggregates (negatively charged on average) becomes strong enough to prevent their collision already at micrometer sizes.

1.2.2 Planetesimal and planet formation

Several concepts have been proposed to overcome the growth barriers from Sect. 1.2.1 in order to form planetesimals and eventually planets. Among others, these are sweep-up growth (Windmark et al., 2012a,b; Drążkowska et al., 2013, 2014), porous grain growth (Okuzumi et al., 2012; Kataoka et al., 2013), ice condensation (Cuzzi & Zahnle, 2004; Ros & Johansen, 2013), streaming instability (Youdin & Goodman, 2005; Johansen et al., 2007, 2011; Drążkowska & Dullemond, 2014), secular gravitational instabilities (Youdin, 2011; Takeuchi & Ida, 2012), and long-lived particle

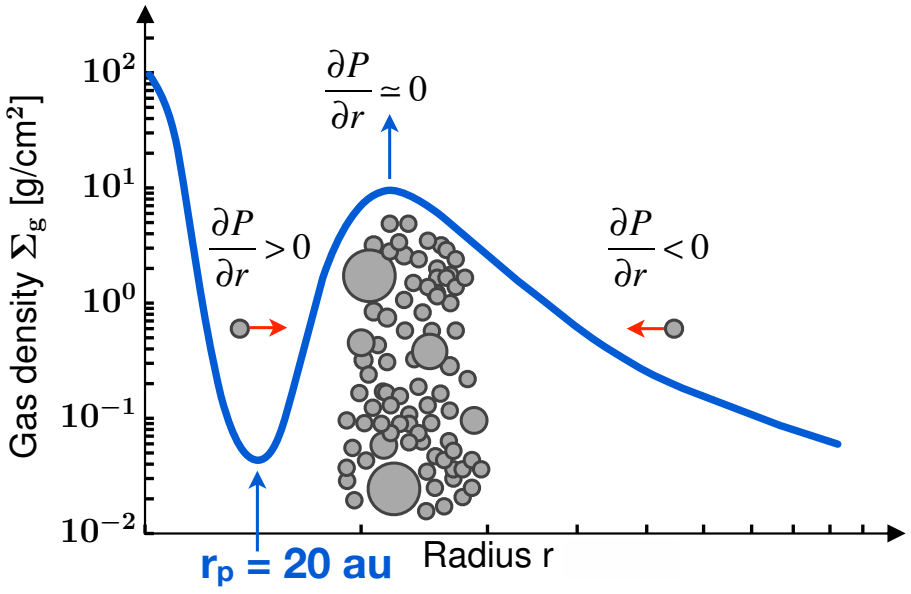

Figure 1.4: Sketch of the principle of a planet induced radial pressure bump. A planet is carving a gap at radius r_p and a pressure maximum is created at the outer edge of this planetary gap, where particle trapping and efficient growth can happen.

traps. The latter are most important for the models presented in this thesis, and will be further explored in the following.

Pressure bumps and dust trapping

As described in Sect. 1.2.1, dust particles drift towards the star in a smooth disk with $dP/dr < 0$. However, planet-forming disks could host pressure bumps, which locally modify the pressure gradient to create radial particle traps (Whipple, 1972; Klahr & Henning, 1997; Pinilla et al., 2012b; Zhu et al., 2012). At such locations, either planetesimal formation via efficient coagulation could happen, or these traps might favor the gravitational collapse into planetesimals (e.g., Safronov, 1972; Haghighipour & Boss, 2003). From an observational point of view, they seem to be required to explain the existence of mm-sized grains observed in the outer parts of disks (e.g., Ricci et al., 2010a; Pinilla et al., 2012b, see also Sect. 1.3 and Chapters 6, 7, 10). Figure 1.4 shows the basic principle of such a particle trap. Dust grains with larger Stokes number are driven towards a pressure maximum from both directions, but their drift stops at the maximum where $dP/dr = 0$. In regions where the pressure gradient is positive, $dP/dr > 0$, the gas moves with super-Keplerian velocity, and the particles thus experience a tailwind. It is important to note that particles with $\mathrm{St} \simeq 1$ move fastest into the trap to favor efficient concentration and growth, while small particles ($\mathrm{St} \ll 1$) are coupled to the gas, and will not be trapped as effectively.

It has been shown by hydrodynamic simulations that predominantly axisymmetric particle traps can exist at the outer edge of a gap created by a giant planet (e.g.,

Paardekooper & Mellema, 2006; Pinilla et al., 2012a; Zhu et al., 2012). Furthermore, MHD effects can generate ring shaped pressure bumps and subsequent dust accumulation. This happens either due to zonal flows (e.g., Johansen et al., 2009; Simon & Armitage, 2014), or at the edge of magnetically inactive dead zones (e.g., Kretke & Lin, 2007; Dzyurkevich et al., 2010; Pinilla et al., 2016; Ruge et al., 2016). In addition, anti-cyclonic vortices can host non-axisymmetric pressure maxima, and dust grains are accumulated near the centers of these vortices (e.g., Barge & Sommeria, 1995; Klahr & Bodenheimer, 2003, 2006; Varnière & Tagger, 2006; Lin, 2014).

Planetesimal evolution

Once the formation of kilometer-sized bodies, the planetesimals, is completed, gravity plays a driving role in successive growth. Gravitational focusing enhances the cross section for collisions, and since it increases with mass, more massive planetesimals have a higher chance of colliding. Thus, in this so-called 'runaway growth' scenario (e.g., Ida & Makino, 1993; Kokubo & Ida, 1996), a few massive bodies grow much faster than the other ones. The negative feedback from viscous stirring, which excites the eccentricities of the planetesimals in the feeding zones, brings runaway growth to a stall, and the so-called 'oligarchic growth' begins (e.g., Kokubo & Ida, 1998; Ormel et al., 2010). Protoplanets with equal mass grow oligarchically in separate feeding zones, while leftover planetesimals remain at their smaller size.

Once a rocky planet or solid core of a giant planet with a mass larger than about ten Earth masses has been formed, the core accretion model predicts the accretion of gas to eventually form a gas giant (Pollack et al., 1996). There is, however, a timescale problem since the core formation timescale must be shorter than the disk dissipation timescale. Thus, explaining gas giant planets which are repeatedly discovered far beyond 30 au remains difficult. In order to fasten the core formation process, the 'pebble accretion' model has been proposed (Ormel & Klahr, 2010; Lambrechts & Johansen, 2012). Planet-forming disks often appear bright at mm wavelengths, suggesting that a significant fraction of pebble-sized particles ($\sim$100 μm to cm) is present. Numerical models suggest that they might be effectively accreted onto a growing core on a suitable timescale shorter than 1 Myr. In general, there is still the issue that the local gas reservoir at the planet's orbit is limited, but planet-disk interactions (cf. Sect. 1.2.3) can lead to planet migration toward places with sufficient gas supply. Giant planets at the late stages of their formation are also capable to form a so-called circumplanetary disk around themselves, which can affect the gas accretion rate (e.g., Szulágyi et al., 2014, 2017).

Gravitational instability

A second hypothesis on how gas giants can form is the disk fragmentation via self-gravity (Boss, 1997). Gravitational instability occurs when regions in the gaseous protoplanetary disk become unstable to their own gravity and collapse. At a given radius the disk will be unstable if it either has a sufficiently high density and/or if it is

cool, i.e. small c_s. Mathematically, this is expressed by the so-called Toomre criterion (Toomre, 1964, cf. Eq. 3.1 for details of the criterion description). The formation timescale involved is supposed to be much shorter than that of the core accretion scenario. Thus, at distances beyond ∼50 au, where the disk temperature is lower and sufficient mass is available at least during the early disk evolution, gravitational instability may be a feasible mechanism to explain giant planets. The main question is whether protoplanets formed by gravitational instability can survive to evolve to gravitationally bound objects given tidal disruption and fast inward migration.

In summary, neither planet formation hypothesis provides a complete description of the observed planet distribution. However, there might be an observational bias in the types of planets and substellar companions that have been observed so far. The new generation of high contrast imaging instruments, such as the Spectro-Polarimetric High-contrast Exoplanet REsearch (SPHERE, Beuzit et al., 2008) on the Very Large Telescooe (VLT) and the Gemini Planet Imager (GPI, Macintosh et al., 2008) on the Gemini South Telescope, complements other detection techniques and opens the path to better characterize planet properties.

1.2.3 Planet-disk interactions

Planets embedded in the disk modify the disk structure in their orbital neighborhood and excite non-axisymmetric structures, such as spiral density waves (Goldreich & Tremaine, 1979). Depending on the planet mass and the local disk properties a planet may open a radial gap in the gas density structure through its gravitational influence on the disk (Lin & Papaloizou, 1979). In addition, the edges of this gap are prone to the formation of large-scale anticyclonic vortices (Lin & Papaloizou, 2010). The reader is referred to the recent reviews by Kley & Nelson (2012) and Baruteau et al. (2014) for a more detailed analysis, especially for the physical processes that determine the characteristics of planet migration. Observational signatures of planet-disk interactions are reviewed in Sect. 1.3.2 and are subject of Chapters 3 to 7.

Spiral density waves

A planet induces perturbations in the disk in form of spiral density waves, which propagate throughout the disk. Angular momentum and energy are transferred due to the torques that a planet exerts on the disk at 'Lindblad' resonances, at which the waves are launched, and corotation resonances, where angular momentum is deposited (Goldreich & Tremaine, 1979, 1980). The radially propagating density waves are sheared out by the Keplerian differential rotation. As a result, spiral waves form due to the constructive interference of density waves with different azimuthal wavenumbers m. Both an inner spiral arm inside the planet's position and an outer arm outside the planet's position are generated. The two-dimensional (2D) linear density wave theory can accurately describe the shape of the excited spirals for the case of planets less massive than Saturn as proven by two-dimensional hydrodynamic simulations (e.g., Zhu et al., 2015). In this theory, spiral waves are

basically sound waves, and their pitch angle ψ is directly connected to the disk's sound speed c_s and rotation profile Ω_K (Rafikov, 2002). Figure 1.5 illustrates that the pitch angle satisfies $\tan\psi = |dr/(rd\phi)|$. The wave has the same phase along the curve, so that $dr/d\phi = -m/k(r)$ with radial wave number $k(r)$. Using the dispersion relation for density waves far, i.e. several scale lengths, from their launching point, $m^2\left(\Omega_\mathrm{K}(r) - \Omega_\mathrm{K}(r_\mathrm{p})\right)^2 \approx c_\mathrm{s}^2 k^2(r)$ (Rafikov, 2002), the pitch angle in polar coordinates (r, ϕ) is then given by

$$\psi = \arctan\left(\frac{c_\mathrm{s}}{r\left|\Omega_\mathrm{K}(r) - \Omega_\mathrm{K}(r_\mathrm{p})\right|}\right), \tag{1.32}$$

where $\Omega_\mathrm{K}(r_\mathrm{p})$ is the orbital frequency at the planet's location $r = r_\mathrm{p}$. Since the pitch angle is independent of m, the constructive superposition of different modes leads eventually to a one-armed spiral wake supported by pressure (Ogilvie & Lubow, 2002). Assuming a power law sound speed profile and a power law rotation angular frequency profile for the disk, i.e. $c_\mathrm{s}(r) \propto r^{-\beta_\mathrm{s}}$ and $\Omega_\mathrm{K}(r) \propto r^{-\gamma}$, the shape of a spiral density wave is determined by

$$\begin{aligned}\phi(r) = \phi_0 - \frac{\mathrm{sgn}(\mathrm{r} - \mathrm{r_p})}{h_\mathrm{p}} \\ \times \left\{\left(\frac{r}{r_\mathrm{p}}\right)^{1+\beta_\mathrm{s}}\left[\frac{1}{1+\beta_\mathrm{s}} - \frac{1}{1-\gamma+\beta_\mathrm{s}}\left(\frac{r}{r_\mathrm{p}}\right)^{-\gamma}\right]\right. \\ \left. - \left(\frac{1}{1+\beta_\mathrm{s}} - \frac{1}{1-\gamma+\beta_\mathrm{s}}\right)\right\},\end{aligned} \tag{1.33}$$

where r_p equals the corotation radius and h_p is the disk aspect ratio at $r = r_\mathrm{p}$ (Rafikov, 2002; Muto et al., 2012). This formula is only valid far from the spiral's launching point, and not applicable in the immediate vicinity of the planet.

However, spiral waves excited by higher mass planets turn into shock waves, which propagate at speeds faster than the local sound speed. Thus, the linear density wave theory breaks down and has to be extended by the spiral shock theory (Goodman & Rafikov, 2001; Rafikov, 2002; Dong et al., 2011). Therefore, in order to accurately study spiral arms launched by Jupiter mass planets, non-isothermal hydrodynamic simulations have to be carried out (e.g., Zhu et al., 2015; Pohl et al., 2015). This will be further addressed in Chapter 3 of this thesis, along with possible effects of the disk self-gravity, which have been neglected in the discussion above.

Gas gap opening criteria

Once a planet reaches a sufficient mass, it may clear the material around its orbit to form a radial gap in the disk. The gravitational influence of the planet on the disk results in torques exerted on the disk inside of and beyond the planet's orbit.

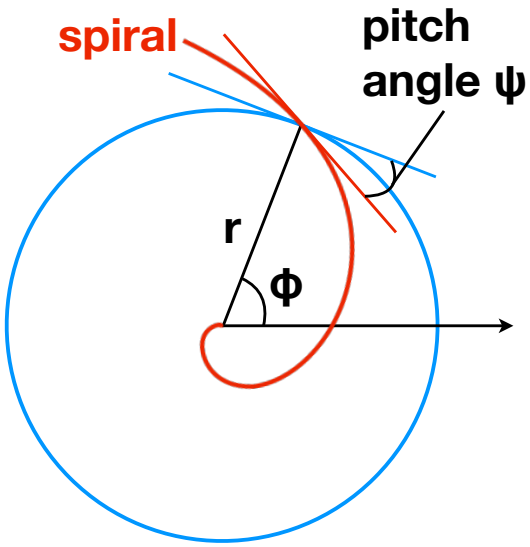

Figure 1.5: Illustration of a spiral's pitch angle definition in polar coordinates (r, ϕ).

As already mentioned, spiral density waves transport angular momentum through the disk. More precisely, the inner spiral wake takes angular momentum from the inner disk to the planet, whereas the outer spiral wave transfers angular momentum from the planet to the outer disk. As a consequence, the disk material appears to be pushed away from the planet location, which leads to a (partial) gap opening (e.g., Kley & Nelson, 2012). This process is counteracted by the viscous frictional torque responsible for disk spreading, which refills the void areas with mass. If the torque exerted by the planet on the disk is larger than the viscous torque in terms of their absolute values, a planetary gap is carved out (Lin & Papaloizou, 1979; Papaloizou & Lin, 1984; Lin & Papaloizou, 1986).

The rate of angular momentum transfer from the planet to a local fluid element of the disk, the tidal torque, can be approximated by (Papaloizou & Lin, 1984; Lin & Papaloizou, 1986)

$$T_{\mathrm{tid}}(\Delta) \simeq 0.23\, q^2\, \Sigma_{\mathrm{g}}(r_{\mathrm{p}})\, r_{\mathrm{p}}^4\, \Omega_{\mathrm{K}}^2(r_{\mathrm{p}}) \left(\frac{r_{\mathrm{p}}}{\Delta}\right)^3 , \tag{1.34}$$

where $\Delta = |r_{\mathrm{p}} - r|$ denotes the impact parameter between the fluid particle's unperturbed trajectory and the planet, and $q = M_{\mathrm{p}}/M_\star$ indicates the mass ratio of the planet to the central star. This approximation only applies as long as $\Delta \geq \Delta_{\mathrm{m}}$, here Δ_{m} is the maximum of the local disk scale height H and the radius of the planet's Hill sphere $r_{\mathrm{H}} = r_{\mathrm{p}}(q/3)^{1/3}$ (Goldreich & Tremaine, 1980).

The intrinsic viscous angular momentum transfer rate, the viscous torque, is given

by (Lynden-Bell & Pringle, 1974)

$$T_{\rm visc} = 3\pi\,\nu\,\Sigma_{\rm g}(r_{\rm p})\,r_{\rm p}^2\,\Omega_{\rm K}(r_{\rm p})\,. \tag{1.35}$$

Provided that the tidally excited waves are completely damped, and adopting $\Delta = H$ (gap width that is representative of the smallest radial scale), a first gap opening requirement for non-migrating planets is deduced by balancing Eqs. 1.34 and 1.35 (e.g., Bryden et al., 1999),

$$q \equiv \frac{M_{\rm p}}{M_\star} \gtrsim \frac{40\,\nu}{\Omega_{\rm K}(r_{\rm p})\,r_{\rm p}^2}\,. \tag{1.36}$$

With the ad hoc α-prescription introduced in Eq. 1.21, Eq. 1.36 modifies to

$$\frac{M_{\rm p}}{M_\star} \gtrsim 40\,\alpha\left(\frac{H}{r_{\rm p}}\right)^2\,. \tag{1.37}$$

In addition, while still assuming that the gravitational torque is entirely deposited in the disk, an independent criterion for gap opening in a gaseous disk with very small viscosity was proposed by Lin & Papaloizou (1993). It is based on the requirement that a strong shock forms within a scale height of the planet's location, leading to the so-called 'thermal' gap opening criterion (Ward, 1997; Bryden et al., 1999),

$$r_{\rm H} \gtrsim H\,, \text{or equivalently, } \frac{M_{\rm p}}{M_\star} \gtrsim \left(\frac{M_{\rm p}}{M_\star}\right)_{\rm th} \simeq 3\left(\frac{H}{r_{\rm p}}\right)^3\,. \tag{1.38}$$

This gives the threshold planet mass above which the density waves cause instantaneous shocks and deposit their angular momentum locally in the disk where they are excited (e.g., Kley & Nelson, 2012).

However, even if this shock condition is satisfied, a key problem is to determine which fraction of the tidal torque is locally deposited in the disk and which fraction is actually evacuated by pressure supported waves (Papaloizou & Lin, 1984; Goldreich & Nicholson, 1989; Rafikov, 2002; Crida et al., 2006). Crida et al. (2006) found that pressure effects in the disk tend to oppose the gravitational influence of the planet. Thus, the steady state of the disk is set by the equilibrium between the total gravitational torque, the viscous torque, and the pressure torque. The resulting gap criterion, defining a gap as a reduction to 10% of the unperturbed density at the planet's location, yields

$$\frac{3}{4}\frac{H}{r_{\rm H}} + 50\,\alpha\left(\frac{M_\star}{M_{\rm p}}\right)\left(\frac{H}{r_{\rm p}}\right)^2 \lesssim 1\,. \tag{1.39}$$

Numerical simulations have shown reasonable agreement for larger viscosity values and planet mass (e.g., Duffell & MacFadyen, 2013). However, Duffell & MacFadyen (2013) found that a low mass planet ($q \simeq 10^{-4}$) on a fixed orbit can open a gap even if the Hill radius is smaller than the disk scale height. Such gap opening by planets significantly below the thermal mass (cf. Eq. 1.38 for definition) has been confirmed by hydrodynamic as well as ideal MHD simulations (Zhu et al., 2013). Moreover, gap opening by low mass planets is even possible in low viscosity disk regions ($\alpha \lesssim 10^{-4}$), as it is expected for example for dead zones (Duffell & MacFadyen, 2013). It is noted that planet migration may affect the ability of the gap opening, such that the herein discussed critical planet masses might be underestimated (Malik et al., 2015). A sufficient criterion has to consider an additional gap-opening timescale since it is crucial to check whether the planet can carve out a gap quickly enough compared to the migration timescale.

Gas gap profile

The gap shape (depth and width) depends on the disk physics, such as viscosity and aspect ratio, and on the planet-to-star mass ratio. In a simple approach, the gap width created by a fixed and non-accreting planet should be set by the location where gravity and viscous torques balance each other (Varnière et al., 2004). Several numerical and (semi-)analytical studies have elaborated the structure profile of the gas surface density across the gap region (e.g., D'Angelo et al., 2002; Crida et al., 2006; Zhu et al., 2013; Fung et al., 2014; Duffell, 2015). Crida et al. (2006) derived an equilibrium solution for the gas surface density considering the viscous torque, gravitational torque, and the pressure torque,

$$\left(\frac{r_\mathrm{H}}{\Sigma_\mathrm{g}}\frac{d\Sigma_\mathrm{g}}{dr}\right) = \frac{T_\mathrm{g,Crida} - \frac{3}{4}\alpha c_\mathrm{s}^2(r_\mathrm{p})}{\left(\frac{H}{r}\right)^2 r\, r_\mathrm{p}\Omega_\mathrm{K}^2(r_\mathrm{p})a'' + \frac{3}{2}\alpha c_\mathrm{s}^2(r_\mathrm{p})\frac{r}{r_\mathrm{H}}}\,, \tag{1.40}$$

with a dimensionless function a'' described by

$$a''\left(\frac{\Delta}{r_\mathrm{H}}\right) = \frac{1}{8}\left|\frac{\Delta}{r_\mathrm{H}}\right|^{-1.2} + 200\left|\frac{\Delta}{r_\mathrm{H}}\right|^{-10}. \tag{1.41}$$

$T_\mathrm{g,Crida}$ is a modified gravitational torque measured from their numerical simulations,

$$T_\mathrm{g,Crida} = 0.35\, q^2\, r_\mathrm{p}^5\, \Omega_\mathrm{p}^2\, r \left(\frac{1}{\Delta}\right)^4 \mathrm{sgn}(\Delta)\,. \tag{1.42}$$

The semi-analytic approach by Crida et al. (2006), however, does not take into account the transfer of angular momentum from the planet to the disk by shock propagation. As a consequence, the gap profiles are not fully consistent with nu-

merical models as the gap depth is rather overestimated, while the gap width is underestimated.

Fung et al. (2014) numerically determine the surface density inside the gap and give an empirical formula for Jupiter-like planets, which can be used to correct for the depth of the gap,

$$\Sigma_{\mathrm{g,gap}} \propto q^{-2.2}\, \alpha^{1.4} \left(\frac{H}{r}\right)^{6.6} . \tag{1.43}$$

This model recovers the power-law dependence of the gap depth on q, α, and H/r as found in numerical studies (e.g., Duffell & MacFadyen, 2013).

The analytic prescription of Duffell (2015) considers the non-local deposition of the tidal torque by shock propagation (cf., Goodman & Rafikov, 2001; Rafikov, 2002). Assuming a Keplerian disk in steady sate, the gap profile is estimated by

$$\Sigma_{\mathrm{g}}(r) = \Sigma_{\mathrm{g},0}(r) \left(1 - \frac{f(r)K(q)/(3\pi)}{1 + f(r_{\mathrm{p}})K(q)/(3\pi)} \sqrt{r_{\mathrm{p}}/r}\right) , \tag{1.44}$$

where

$$K \equiv \left(\frac{M_{\mathrm{p}}}{M_\star}\right)^2 \alpha^{-1} \left(\frac{H_{\mathrm{p}}}{r_{\mathrm{p}}}\right)^{-5} , \tag{1.45}$$

and $\Sigma_{\mathrm{g},0}(r)$ is the 'unperturbed' surface density profile. The function $f(r)$ is related to the angular momentum flux due to the shocking of the planetary wake (cf. Eq. 13 in Duffell (2015); semi-analytical calculation originally by Goodman & Rafikov, 2001). This analytical model provides a good approximation in the 'partial gap' regime of relatively low mass planets, but fails to correctly predict the gap shape from 2D numerical simulations once the gap becomes very deep.

Dust gaps

So far, only the gap opening and shape for the gas density has been considered. There is also a tidal interaction between the planet and the dust component of a protoplanetary disk. There are physical mechanisms for a gap opening in the dust density by embedded planets (e.g., Paardekooper & Mellema, 2006; Dipierro et al., 2016; Rosotti et al., 2016; Dipierro & Laibe, 2017). It is important to note here that dust gaps do not necessarily indicate the presence of gas gaps. More precisely, this scenario involves only small perturbations in the gas that do not lead to a gas gap formation, but they induce strong enough changes in the dust distribution to result in a dust gap. Low mass planets, that do not disturb the gas, can carve gaps in the dust by tidal torques assisted by drag in the inner disk, and resisted by drag in the

outer disk (Dipierro et al., 2016). Higher mass planets can produce partial or total gas gaps which are deeper in the dust phase.

An order of magnitude estimate for the minimum mass required for a planet to open a dust gap is given by Dipierro & Laibe (2017),

$$\frac{M_\mathrm{p}}{M_\star} \sim \mathrm{St}^{-3/2} \left(\frac{H}{r_\mathrm{p}}\right)^3 . \tag{1.46}$$

It can be recognized that the critical mass is lower for large Stokes numbers and lower disk aspect ratios. In order to carve out a gap in the dust only, the condition $\mathrm{St} \gtrsim 1$ should be fulfilled, otherwise the critical mass required to open a gap in the gas as well is reached (cf. Eq. 1.38).

As described in Sect. 1.2.1, if planets are massive enough to open gaps in the gas disk, a pressure bump is created at the outer gap rim, which initiates the process of particle trapping. This is, however, not the case for lower mass planets that only open gaps in the dust. In this case, the local gas azimuthal velocity can be slightly affected without creating pressure maxima. As a consequence, the drift velocity of the particles is slowed down, which can create a traffic jam of particles that are slightly decoupled from the gas (Rosotti et al., 2016). A shallow gap can be carved out, and dust can still accumulate just beyond the orbit of a low mass planet.

1.3 Disk observations

While the previous Sects. 1.1 and 1.2 focused on the theoretical aspects of the formation and evolution of planet-forming disks, this section now tries to link this theory to observations. Disk observations are used to better understand and to constrain the earliest stages of planet formation. Moreover, they help to study how disks can be re-shaped by ongoing planet formation.

1.3.1 Spectral energy distribution

Before any kind of imaging, an often used indicator of the presence of a circumstellar disk, or at least of circumstellar material, has been the shape of the SED (cf. Sect. 1.1.1). Starting from the late 1970s ultraviolet and infrared data became available in the following twenty years through observations by several space telescopes, such as the International Ultraviolet Explorer (IUE, $0.12 - 0.32\,\mu$m), IRAS ($12 - 100\,\mu$m) and ISO ($2.5 - 240\,\mu$m). The latter two observed strong infrared flux around PMS stars, in excess of what can possibly be explained by a stellar photosphere, which provided the first evidence of circumstellar disks. The infrared excess is due to the reprocessing of the optical stellar light by the dust grains in the disk. Moreover, large surveys with the Spitzer Space Telescope (Spitzer) have mapped a large fraction of all the low mass star-forming regions within 500 pc from the sun (Evans et al., 2009), which allowed the first statistical studies of disk occurrence.

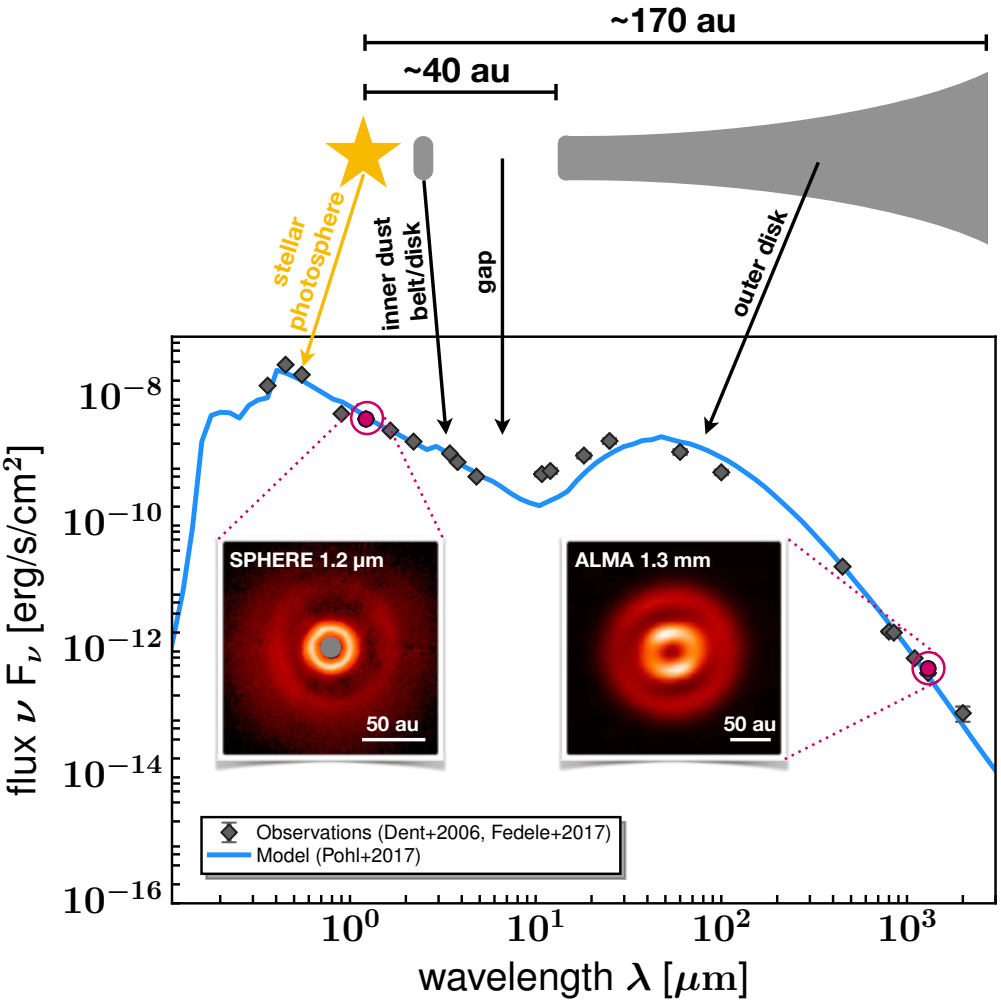

Figure 1.6: SED of the transition disk around the Herbig Ae star HD 169142 (cf. Chapter 7). The different components of the star-disk system are connected to their emitting wavelengths (sketch dimensions not to scale). The two inset images show the 1.2 μm scattered light image from SPHERE/VLT (Pohl et al., 2017) and the 1.3 mm dust continuum emission from ALMA (Fedele et al., 2017), respectively.

Planet-forming disks span a wide range in temperature from more than 1000 K in the inner disk to only a few tens of Kelvin in the outer disk, and are observable over a large wavelength range from the optical to the radio. Because of this, and the various dust species involved, disks can have quite complex spectra. A particular interesting class of disks to look at are transition disks, which host a dip in the MIR excess in their SED (Strom et al., 1989, , cf. Sect. 1.1.3). Many transition disks were discovered by observations with the Spitzer Infrared Spectrograph (IRS) working in the $\sim 5-38\,\mu$m range. Infrared color criteria (e.g., Merín et al., 2010; van der Marel et al., 2016) are a proper tool to select transition disk candidates from surveys.

As an example, Fig. 1.6 illustrates the SED of HD 169142, a Herbig Ae star surrounded by a transition disk. In general, the wavelength range can be split into four main regions, each of which is sensitive to a specific component of the disk. At optical to NIR wavelengths ($\lambda \lesssim 1\,\mu$m) the energy emission is dominated by the blackbody emission of the stellar photosphere. Hot dust grains close to the star cause a NIR excess above the photosphere, indicating the presence of an optically thick inner disk, an optically thin dust belt or a halo. A gap in the disk translates to a reduced level of this NIR excess and of the MIR flux. If the gap is an actually completely empty cavity, no NIR excess is detectable above the stellar photosphere. Espaillat et al. (2007) distinguished between objects with a gap and objects with a full inner disk hole as 'pre-transitional' disks and their successor, the classical transitional disks. However, since the clearing mechanisms are yet to be understood, putting these two classes into an evolutionary sequence remains questionable. The bulk of the dust in the outer disk emits from FIR to mm wavelengths.

The MIR spectrum often shows silicate and polycyclic aromatic hydrocarbon (PAH) features. Their presence or absence sets constraints on the dust shape and composition (cf. Sect. 2.4.3). In particular, the silicate feature at $10\,\mu$m can vary from strongly peaked to weak or flat, depending on the grain size. A strong silicate feature is seen in the presence of small grain sizes ($\sim 0.1\,\mu$m), which starts to weaken once the grains grow to sizes beyond micron (e.g., Kessler-Silacci et al., 2006; Natta et al., 2007).

Spitzer data points can be complemented by additional MIR and FIR photometry (e.g., Wide-Field Infrared Survey Explorer (WISE), Akari, Herschel-PACS), and (sub-)mm photometry (e.g., Atacama Pathfinder Experiment (APEX), James Clerk Maxwell Telescope (JCMT)).

1.3.2 Imaging disk substructures

Direct imaging is one of the most promising investigation tools for planet-forming disks. However, the difficulty lies in detecting and resolving these disks as they are often far away from Earth and thus faint and very small on sky. Therefore, high angular resolution imaging is required to retrieve any details. Given the telescope's diffraction criterion (angular resolution $\theta_{\rm lim} \simeq 1.22\lambda/D$, with dish/mirror diameter D), it is either favorable to go to shorter wavelengths or to use large telescopes, ideally it is a combination of both.

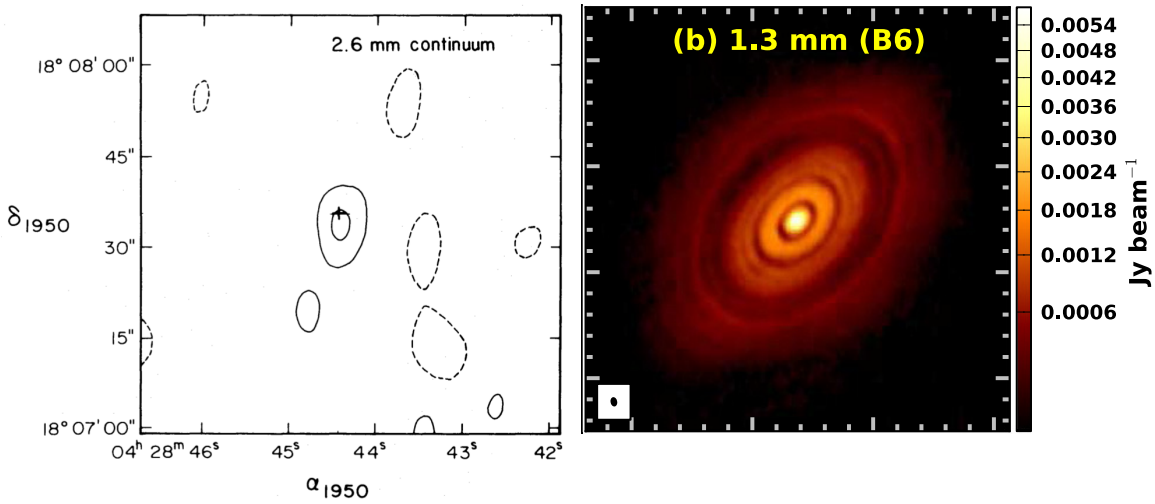

Figure 1.7: *Left:* Map of the 2.6 mm continuum emission of HL Tau observed by the Owens Valley Radio Observatory in 1984 with a beam size of $10.5'' \times 6.0''$ (Beckwith et al., 1986). *Right:* 1.3 mm continuum image of HL Tau observed by ALMA in 2014 with a beam size of $0\overset{''}{.}035 \times 0\overset{''}{.}022$ (ALMA Partnership et al., 2015).

Naturally, observing at optical and NIR wavelengths provides a good angular resolution. However, at these short wavelengths the stellar emission dominates over the disk signal, resulting in a contrast problem between a low brightness disk surface and a bright central source. Several observational techniques have been proposed to eliminate the stellar light, among them coronagraphs and polarimetric differential imaging (PDI, see next paragraph). Moreover, observations by ground based telescopes are challenged by the atmospheric conditions, which typically limit the seeing to be not better than ∼0.5 arcsec for the prime locations (e.g., Mauna Kea on the island of Hawaii or the Chajnantor plateau in the Atacama desert in Chile). Constantly developing techniques, such as active optics or adaptive optics (AO), where mirrors are tilted or deliberately distorted, can compensate for the atmospheric disturbances. New capability instruments such as SPHERE, GPI, and the High Contrast Instrument for the Subaru Next Generation Adaptive Optics (HiCIAO) contain high-performance AO and provide good inner working angle (IWA) and are thus a crucial tool to resolve disk structures.

In the mm and radio wavelength regimes, high angular resolutions are only achievable by interferometers, which combine at least two or more antennas to form an array. Long baselines and extended configurations are desired, since the effective angular resolution of two antennas separated by a distance B is $\theta_{\rm lim} \simeq \lambda/B$. State-of-the-art (sub-)mm antenna arrays are the Submillimeter Array (SMA, Hawaii, USA), the NOrthern Extended Millimeter Array (NOEMA), the Karl G. Jansky Very Large Array (VLA, New Mexico, USA), and predominantly the Atacama Large Millimeter Array (ALMA, Chile), which have been opening up new possibilities in the study of planet-forming disks. How important the technological progress has been for the observational research of planet-forming disks is illustrated in Fig. 1.7 for the case

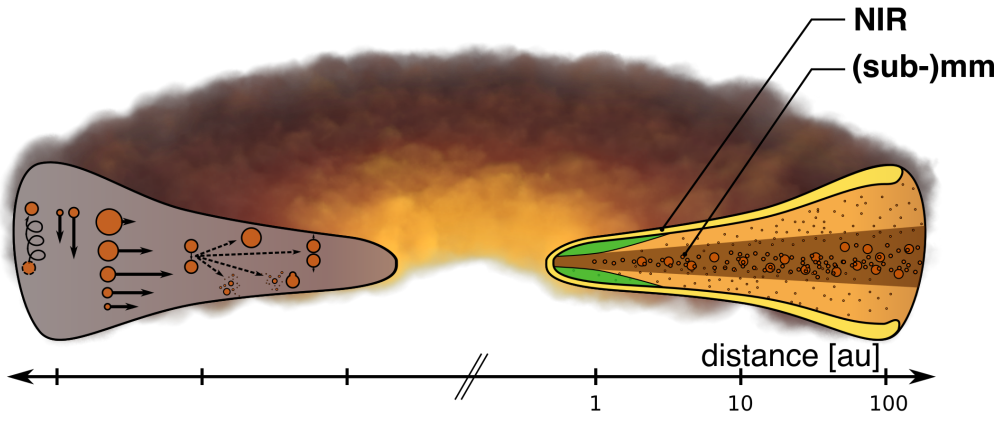

Figure 1.8: Sketch illustrating the structure of a planet-forming disk. Observations at different wavelength regimes trace specific disk regions. Adapted from Testi et al. (2014)/T. Birnstiel.

of HL Tau. While the left panel, the 2.6 mm continuum emission observed by the Owens Valley Radio Observatory in 1984 shows an unresolved continuum source spatially coincident with the star (Beckwith et al., 1986), the right panel shows a high resolution ALMA image at 1.3 mm for the same source, taken twenty years later and displaying lots of disk substructures (ALMA Partnership et al., 2015).

High angular resolution observations with the above mentioned instruments have been providing new insights in the nature of planet-forming disks by revealing various disk substructures. Covering multiple wavelengths is crucial for our understanding of disks because each wavelength regime is sensitive to a particular disk region (Fig. 1.8). Due to the high dust opacity at short wavelengths, optical and NIR scattered light observations trace the micron-sized dust grains that are located at the disk surface and that are well coupled to the gas. More precisely, the scattering surface of the disk that is measured for example with VLT/SPHERE, is the height above the midplane where the scattering optical depth reaches about unity. Contrarily, continuum (sub-)mm and radio observations trace large grains that settled down towards the disk midplane. Hence, multi-wavelength analyses enable to study the differences and similarities in the radial and azimuthal distribution between small, micron-sized dust particles and large, mm-sized grains. ALMA is also able to investigate the chemical composition of the disk, the disk gas distribution and its kinematics through spectral line emission.

Figure 1.9 shows multi-wavelength observations of the disk around the young solar analog TW Hya, which is a prominent target to characterize disk substructures as

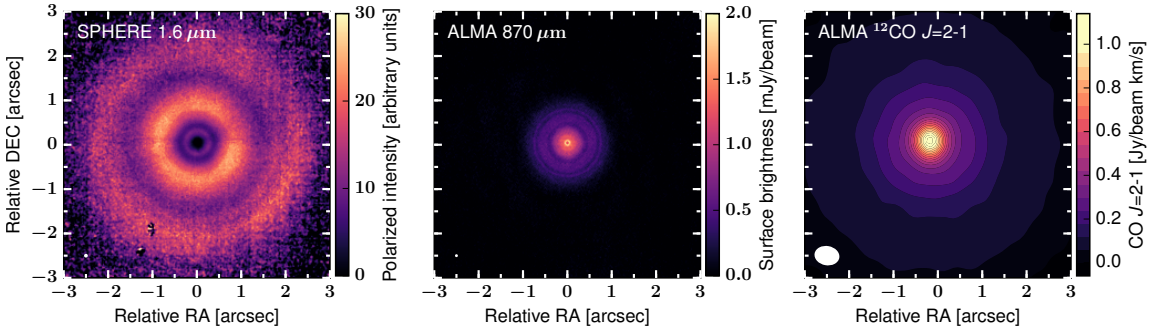

Figure 1.9: The TW Hya disk observed in polarized scattered light at 1.62 μm (scaled by r^2 to correct for the dilution factor of the stellar irradiation), in 870 μm continuum emission, and in CO $J = (2-1)$ emission at 1.3 mm. The data were originally published in van Boekel et al. (2017), Andrews et al. (2016), and Teague et al. (2016), respectively. The white ellipse in the bottom left corner of each panel corresponds to the beam size.

it is the closest gas-rich disk to Earth ($59.5^{+0.96}_{-0.93}$ pc, Gaia Collaboration et al., 2016). The left panel shows SPHERE polarized scattered light at H-band (1.62 μm) with a spatial resolution of ≈3 au. The middle panel corresponds to ALMA dust continuum emission at Band 7 (870 μm) with a linear resolution of ≈2 au, thus comparable to the NIR scattered light data. Both images reveal a highly structured radial intensity distribution with a series of concentric bright and dark rings, but they probe very different disk regions vertically (Andrews et al., 2016; van Boekel et al., 2017). In azimuthal direction, the disk is overall highly symmetric. The right panel shows the carbon monoxide (CO) $J = (2-1)$ zeroth moment map with, however, a much lower spatial resolution of ≈30 au. The disk radius in CO is in agreement with the spatial extension of the SPHERE data since micron-sized dust grains that dominate the light scattering are strongly coupled to the gas. On the contrary, the mm dust continuum emission is mostly limited within the central ∼60 au from the star.

The case of TW Hya and further multi-wavelength studies (see e.g., Chapter 7 for HD 169142) have demonstrated that smooth power-law distributions of gas densities and temperatures assumed in most classical disk models are only correct as a first order approximation. The presence of multiple rings and gaps seems quite a common feature for disks. They have been found in both young (HL Tau, ALMA Partnership et al., 2015; Carrasco-González et al., 2016, see Fig. 1.7) and older objects (TW Hya, Andrews et al., 2016; van Boekel et al., 2017, see Fig. 1.9). Furthermore, these structures are present in disks around stars of very different spectral types (see Fig. 1.10). Several theoretical interpretations of ring-like disk substructures have been proposed in the literature, which can be assigned to the following categories: fluid dynamics, magnetic origin, dust evolution effects, and planet-disk interaction (cf. Chapters 7 and 8 for more details).

Moreover, spiral arms were observed in scattered light (e.g., Muto et al., 2012; Grady et al., 2013; Avenhaus et al., 2014; Benisty et al., 2015; Stolker et al., 2016; Benisty et al., 2017, see Fig. 1.10), but also in the sub-mm in dust continuum (Pérez

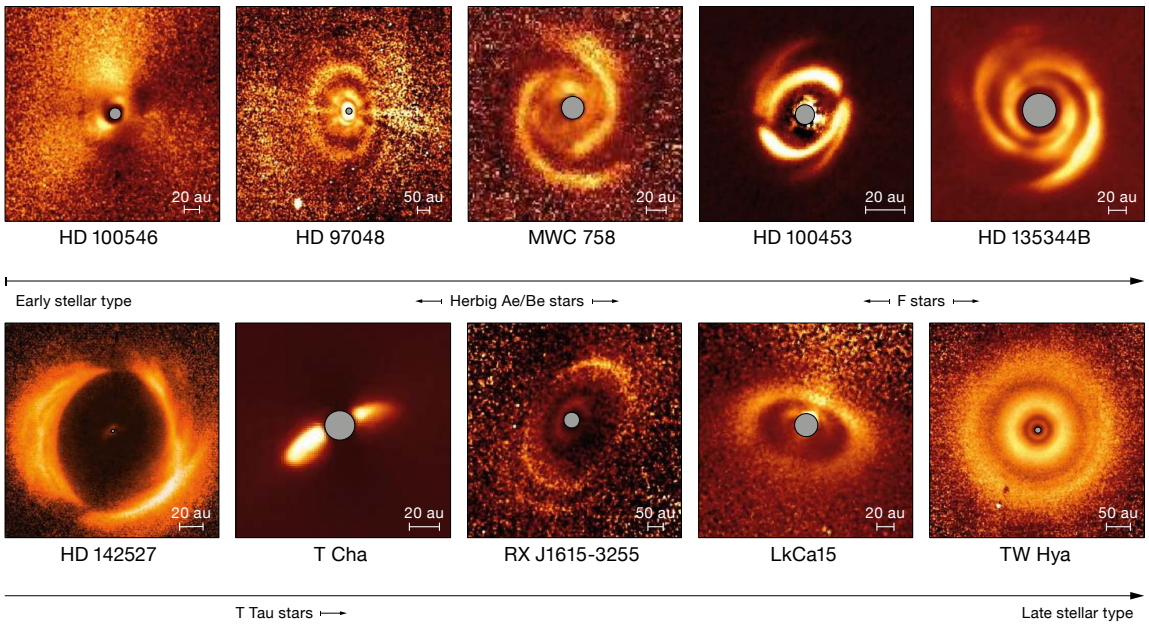

Figure 1.10: Gallery of images of planet-forming disks observed in PDI with SPHERE (from Garufi et al., 2017b). The data of these images were originally published in (from left to right, top to bottom) Garufi et al. (2016); Ginski et al. (2016); Benisty et al. (2015, 2017); Stolker et al. (2016); Avenhaus et al. (2017); Pohl et al. (2017); de Boer et al. (2016); Thalmann et al. (2016); van Boekel et al. (2017).

et al., 2016) and CO gas lines (Christiaens et al., 2014; Tang et al., 2017). Local dips were put in context with shadows by disk material close to the star (e.g., Marino et al., 2015; Stolker et al., 2016; Benisty et al., 2017) or were connected to spiral arm formation (Montesinos et al., 2016).

Polarimetric differential imaging (PDI)

As already mentioned in the previous paragraph, imaging circumstellar disks at the optical and NIR is challenged by the low contrast of the disk emission compared to the stellar flux. PDI is an observational technique that makes use of the fact that stellar light is mainly unpolarized, while scattered light from the disk surface is strongly polarized (see Sect. 2.2 for details on scattering). Observing a star-disk system in polarized light enables the efficient removal of the stellar signal such that only the disk will eventually show up in the image. In reality, the polarization pattern of the image is often affected by instrumental effects which can modify the polarization state of the disk signal (cf. Chapter 6).

The general technical realization is that the telescope beam is split into two perpendicular polarization directions using a Wollaston prism. Observations in four different polarization states (0°, 45°, 90°, 135°) are simultaneously taken, where the rotation of a half-wave plate (four times by 22.5°) allows to shift the orientation of the polarization. The full set of linear stokes paramaters (Q and U) is obtained,

from which the polarization signal $PI = \sqrt{Q^2 + U^2}$ can be calculated. Moreover, the radial and tangential polarization, also known as the azimuthal counterparts Q_ϕ and U_ϕ, can be derived (e.g., Schmid et al., 2006; Avenhaus et al., 2014),

$$Q_\phi = +Q\cos(2\phi) + U\sin(2\phi) \quad \text{and} \quad U_\phi = -Q\sin(2\phi) + U\cos(2\phi)\,, \tag{1.47}$$

with ϕ being the position angle of the location of interest (x, y) with respect to the star location. With this definition, positive signal in Q_ϕ corresponds to azimuthally polarized flux, and U_ϕ contains the signal with $\pm 45°$ offset with respect to the tangential direction.

Figure 1.10 shows that a variety of disk morphologies, especially spirals and rings, are now routinely detected in PDI images. Interpreting the images' signal is a challenging task because of the following reasons. The fraction of stellar light that scatters from the disk surface layer towards the observer depends on the disk geometry (orientation, vertical extend) as well as dust characteristics (grain size, shape, composition). Depending on these properties, dust grains scatter photons anisotropically, leading to a scattering angle distribution (phase function, cf. Sects. 2.4.3, 6, and 10). The polarized scattered light obtained in PDI mode is again only a fraction of the total scattered light, since the polarization efficiency (or polarizability) also depends on the scattering angle. Therefore, the polarized light detected in a PDI image depends on the combination of phase function and polarizability. Because of the degeneracy between this and disk geometry and illumination effects, an interpretation of scattered light images in the context of planet-forming disks is not a straightforward task.

1.3.3 Radio observations

Disk mass

In order to study the disk midplane, where the bulk of the dust and gas content resides, (sub-)mm observations play a key role. At these wavelengths the disk starts to become optically thin to its own thermal radiation (apart from the innermost disk region). Hence, the observed continuum emission F_ν can be directly related to the total mass (gas+dust) inside the disk (e.g., Beckwith et al., 1990),

$$F_\nu = M_{\rm disk}\frac{\kappa_\nu B_\nu(T)}{d^2}\,, \tag{1.48}$$

where d is the distance to the source, κ_ν corresponds to the dust opacity, and $B_\nu(T)$ is the Planck function at frequency ν at the average disk temperature. At mm wavelengths, the latter is close to the Rayleigh-Jeans regime with only a linear dependence on the temperature, $B_\nu \approx 2\nu^2 k_{\rm B} T/c^2$. Using this technique, several large mm wavelength surveys have been carried out (e.g., Beckwith et al., 1990; Andre

& Montmerle, 1994; Andrews & Williams, 2005, 2007; Mann & Williams, 2010). However, these first surveys were incomplete as the observational facilities involved lacked the sensitivity to detect faint molecular line emission. Moreover, the dust continuum emission was used as a proxy to determine the gas mass, assuming a certain dust opacity and gas-to-dust ratio, both strongly depend on the disk evolution. These uncertainties represent the primary sources of error in the disk mass estimate.

Now, by means of ALMA, the first near-complete surveys of planet-forming disks in both dust and gas in several star-forming regions have been carried out (Lupus: Ansdell et al. 2016, Chameleon I: Pascucci et al. 2016, Upper Scorpius: Barenfeld et al. 2016, σ Orionis: Ansdell et al. 2017). Using CO isotopologues to estimate the disk gas mass, these surveys reveal a severe depletion in gas relative to the dust compared to the canonical interstellar medium (ISM) value of 100. This either argues for a depletion in the total gas mass or rather likely in CO. Conversely, the three disk systems for which hydrogen deuteride (HD) was used as a gas mass tracer (TW Hya, DM Tau, GM Aur), show much larger gas masses with gas-to-dust ratios closer to 100 (Bergin et al., 2013; McClure et al., 2016, see also Chapter 9 of this thesis for more details).

Evidence for grain growth

In order to understand how planets form, we have to observationally investigate the dust evolution processes that are theoretically introduced in Sect. 1.2.1. Adopting a power law prescription for the dust opacity, $\kappa_\nu \propto \nu^\beta$, changes in the spectral index β can be directly linked to changes in dust properties (e.g., Pollack et al., 1994; Henning & Stognienko, 1996). In particular, β is sensitive to the maximum particle size $a_{\rm max}$ in the dust size distribution $n(a)$ (Draine, 2006). Thus, it can be interpreted in terms of grain growth such that small β values hint at dust grain sizes larger than 1 mm. Although β is not directly measurable, the mm spectral slope $\alpha_{\rm mm}$ with $F_\nu \sim \nu^{\alpha_{\rm mm}}$ can be used to derive β via $\beta \simeq \alpha_{\rm mm} - 2$ (applicable in the Rayleigh-Jeans limit, $h\nu \ll k_{\rm B}T$). By measuring disk-averaged low β values at mm wavelengths, large grains have been proven to be present in the outer disk (e.g., Beckwith & Sargent, 1991; Testi et al., 2001; Ricci et al., 2010a,b; Guilloteau et al., 2011). This, in turn, challenged theoretical studies of dust growth since local or global dust retention mechanisms must occur in disks (e.g., review by Testi et al., 2014, cf. also Sect. 1.2.1 of this thesis). The expectation of the radial stratification of dust properties was observationally confirmed by Pérez et al. (2012, 2015); Tazzari et al. (2016), although optical depth effects might influence the interpretation. There is evidence for a decrease in the maximum grain size with radius. A key goal in order to constrain dust properties as a function of radius is the simultaneously fitting of spatially resolved multi-wavelength mm and radio observations of disks (Trotta et al., 2013; Tazzari et al., 2016).

1.3.4 (Sub-)millimeter-wave polarization

Polarization observations are not only limited to short wavelengths, but also a very useful diagnostic tool at (sub-)mm wavelengths. In star-forming regions they were performed across many wavelengths and different size scales (e.g., Girart et al., 2006, 2009; Rao et al., 2009; Hull et al., 2014). Radio observations taken with SMA and the Combined Array for Research in Millimeter-wave Astronomy (CARMA) towards young circumstellar disks that are still embedded in their envelopes (Class 0-I) successfully detected (sub-)mm polarization (Rao et al., 2014; Segura-Cox et al., 2015). However, polarization observations of evolved circumstellar disks (Class II-III) with these instruments so far only gave non-detections (Hughes et al., 2009, 2013), which is likely explainable by a lack of spatial resolution. Thanks to the high resolution and sensitivity of ALMA the polarized emission at smaller scales, namely from planet-forming disks, has been meanwhile detected (cf. Sect. 10.5; HL Tau: Stephens et al. 2014, 2017; Kataoka et al. 2017 and HD 142527: Kataoka et al. 2016b).

The mm-wave polarization in molecular clouds and star-forming regions has been commonly interpreted in terms of grain alignment. Spinning aspherical dust grains are expected to align themselves with their long axes perpendicular to the magnetic field, thus the polarization vectors arising from thermal emission of these aligned grains become perpendicular to the magnetic field (e.g., Hildebrand, 1988; Cho & Lazarian, 2007; Lazarian, 2007). This line of thought has been used to infer the magnetic field morphology.

Three classes of grain alignment theories can be found in the literature: mechanical alignment (Gold, 1952b,a), paramagnetic relaxation alignment (e.g., Davis & Greenstein, 1951; Jones & Spitzer, 1967; Purcell, 1979), and radiative torque alignment (e.g., Dolginov & Mitrofanov, 1976; Draine & Weingartner, 1996, 1997; Weingartner & Draine, 2003; Lazarian, 2007; Hoang & Lazarian, 2009). The reader is referred to Andersson et al. (2015) for an extensive review on this topic. In the case of planet-forming disks, dust grains are assumed to be aligned by radiative torques, either along the magnetic field (e.g, Bertrang & Wolf, 2017) or in the direction determined by the radiation flux (Tazaki et al., 2017). Millimeter-sized grains at the disk midplane do not align with the magnetic field as the Larmor precession timescale for such large grains becomes longer than the gaseous damping timescale. Instead, the alignment axis is determined by the grain precession with respect to the radiative flux (Tazaki et al., 2017). However, grain alignment is not the only mechanism that can explain mm-wave polarization in disks since scattering of dust grains might also have a major contribution.

Polarization due to self-scattering

It is important to point out that in contrast to the classical scattering picture of stellar light in the optical and NIR, the radiation source for scattering in the mm regime is the thermal disk emission itself. Dust grains located in the disk midplane emit

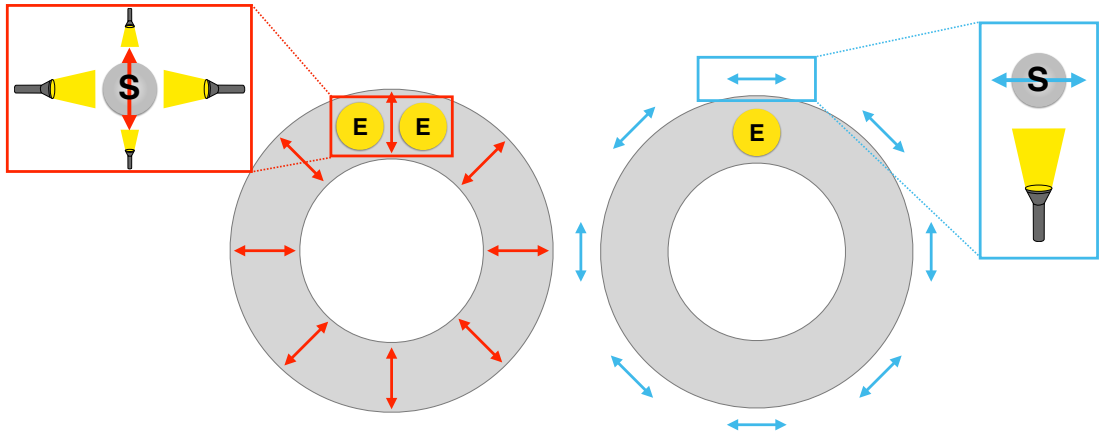

Figure 1.11: Graphical illustration of the working principle of self-scattering on the basis of a ring-like toy model. This situation can be easily transferred to a face-on disk. The flashlight beams indicate the direction and strength of the local anisotropic thermal dust emission. The red and blue arrows represent the polarization direction within (left) and outside (right) the ring after scattering the incident radiation. Yellow circles named 'E' stand for emitting grains, while those labeled with 'S' represent grains working as a scatterer. It is assumed here that the polarization degree shows a peak at a scattering angle of 90 deg.

thermal radiation that is then scattered by other dust grains called 'self-scattering'. If the thermal dust emission has an isotropic radiation field, the net polarization degree is zero for a face-on disk orientation. When the radiation field gets anisotropic, for example for lopsided disks, or when the disk is inclined with respect to the line of sight a considerable net polarization degree is expected (Kataoka et al., 2015, 2016a; Pohl et al., 2016; Yang et al., 2016). It is noted here that the self-scattering is sensitive to both a quadrupole anisotropy, and a flux gradient. Figure 1.11 illustrates the basic principle of the self-scattering by means of a face-on ring toy model. If the incident photons propagate in azimuth along the ring before the last scattering, the scattered radiation is polarized in radial direction (red arrows). Outside of the ring, the majority of the incident photons come from the ring region and propagate radially outwards. Thus, the scattered radiation is polarized in azimuthal direction (blue arrows). Such a flip in polarization is a typical feature of self-scattering.

The single-scattering albedo η is defined as the ratio of the scattering efficiency to total extinction efficiency (cf. Eq. 2.9). Dust grains that are comparable to or larger than the observing wavelength, $a \gtrsim \lambda/(2\pi)$, are expected to have a large albedo, so that their scattering efficiency is high enough to produce scattered emission. An efficient polarization is reached for $a \lesssim \lambda/(2\pi)$ because for grains much larger than the observing wavelength the scattering is strongly forward peaked and no polarization is expected as long as the disk is not highly inclined (cf. Fig. 2.4). Thus, a high polarization degree is achieved when the grain size is comparable to the wavelength. Figure 1.12 shows the opacity situation for amorphous silicate in the case of $\sim$150 μm grains. The reader is referred to Sect. 2.4.3 for the details on the opacity

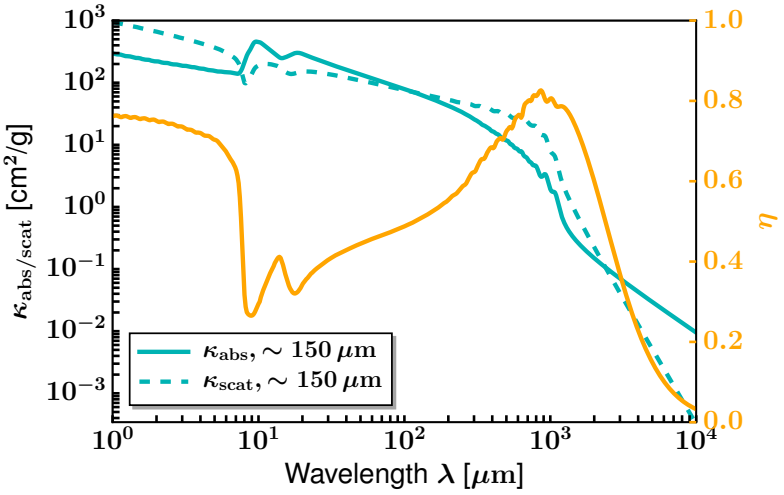

Figure 1.12: Opacities (cyan) and albedo (orange) as a function of wavelength for ∼150 μm grains.

calculation. The scattering opacity (dashed cyan line) is comparable or even larger than the absorption opacity (solid cyan line) for wavelengths between ∼100 μm and a few mm.

This scattering-induced polarization can be used to make constraints on the grain size in planet-forming disks. It provides an independent test for dust coagulation theories (Kataoka et al., 2015; Pohl et al., 2016, see Chapter 10). The detection of polarized emission due to dust scattering is the evidence for the existence of dust grains that are of comparable sizes to the observing wavelength. This method can be compared to measurements of the spectral index map (cf. Sect. 1.3.3) in optically thin disk regions in order to obtain grain size constraints at the disk midplane from both, scattering and absorption opacities. Multi-wavelength, high angular resolution polarization observations are needed in order to disentangle the signatures of grain alignment and dust scattering (see Sect. 10.5).

1.4 Outline of this thesis

The goal of this thesis is to use polarization diagnostics at different wavelengths in order to trace and scrutinize early stages of planet formation. In the light of recent groundbreaking observations of small-scale disk substructures and latest numerical studies that include complex physical processes, this thesis aims at bridging the gap between these theoretical and observational results of transition disks. By means of detailed radiative transfer modeling, observational predictions of different disk processes over a large range of wavelengths are performed. Moreover, a series of planet-forming disk case studies is addressed, where polarimetric SPHERE and ALMA data are presented, modeled, and interpreted in terms of dust evolution and planet-disk interactions.

Chapter 2: In this chapter, we dive into the basics of radiative transfer modeling. The code RADMC-3D is introduced, which is used to connect the physics of planet-forming disks to observations in the following chapters.

Chapter 3: *Is the detection of spiral arms in scattered light images of circumstellar disks an indirect signpost of planets and related to planet-disk interaction processes? What is the role of gravitational instability?* The focus of this chapter lies on studying marginally gravitational unstable disks and the influence of the disk self-gravity on the shape and contrast of spiral arms that are induced by planet-disk interactions. By combining non-isothermal 2D hydrodynamic simulations with 3D radiative transfer calculations, it is investigated how planet and disk properties influence the appearance of the gap and spiral structures in NIR scattered light. The focus is set on the number of spiral arms, their pitch angles, and the brightness contrast between the spiral features and the surrounding background disk to investigate the observability.

Chapter 4: *Are planet-induced spiral arms observable in scattered light of edge-on disks?* This chapter deals with interpreting and modeling new VLT/SPHERE polarimetric images of the nearly edge-on transition disk around the T Tauri star RY Lup. In-depth 3D hydrodynamic planet-disk interaction simulations are paired with radiative transfer modeling in order to estimate the likelihood that the disk features are caused by a planet.

Chapter 5: *Is the origin of shadows and spirals in disks connected to each other?* In this chapter, the structure of the planet-forming disk HD 100453, especially its shadows and spirals, is studied based on VLT/SPHERE optical polarimetric images. The hydrodynamic consequences of the change in stellar irradiation at the shadows' locations are discussed.

Chapter 6: *Is it possible to trace signs of disk evolution and to give grain size constraints for highly inclined transition disks? What is the role of companion candidates in transition disks?* These questions are analyzed with a set of VLT/SPHERE data at NIR wavelengths for the case study of the transition disk around T Cha. An emphasis is put on the disk geometry, grain properties, multiple scattering, and companion candidates.

Chapter 7: *What can ring and gap substructures in disks tell us about dust evolution and planet-disk interactions? Can multi-wavelength observations be used to calibrate the initial conditions for current dust evolution models?* The observational signatures of different dust density distributions, with and without self-consistent dust evolution, in a disk-perturbed by two giant planets, are investigated. These simulations are tuned for the transition disk around HD 169142 and compared with VLT/SPHERE polarimetric observations.

Chapter 8: *What effects do ice lines have on the dust evolution and observational diagnostics at different wavelengths?* Dust evolution simulations that consider changes of the fragmentation velocity threshold at the radial location of main volatiles, specifically H_2O, CO_2, and NH_3, are presented. Radiative transfer calculations are performed using the resulting dust density distributions in order to make observational predictions and to compare with current multi-wavelength observations of TW Hya.

Chapter 9: *Can scattered light information be used as an independent tracer of the disk bulk mass and to reconstruct the disk surface density? How sensitive is the opacity structure of the disk to the disk gas mass?* In this chapter, it is explained that knowledge of the vertical extent of the protoplanetary disk provides a unique constraint on the total mass of the disk.

Chapter 10: *What is the mechanism for producing polarized emission from planet-forming disks at (sub-)mm wavelengths? How strong is the effect of self-scattering from dust grains of sizes comparable to the wavelength? Can we evaluate particle trapping and grain growth with mm-wave polarimetric imaging?* The dust polarization at mm wavelengths in the dust trapping scenario proposed for transition disks, when a giant planet opens a gap in the disk, is studied. 2D hydrodynamic simulations of planet-disk interactions, 1D self-consistent dust growth models, and 3D radiative transfer calculations are used to predict the polarization degree at ALMA bands due to scattered thermal emission. The focus is laid on the characteristic polarization patterns and their dependence on disk inclination, dust size evolution, planet position, and observing wavelength. In addition, new ALMA Cycle 4 sub-mm observations of the transition disk around HD 100546 are presented, which show the polarized emission of this disk for the first time.

Chapter 11: This chapter summarizes the findings of this thesis. Future prospects of follow-up work are also outlined.

2 | Radiative transfer

Observations of protoplanetary disks are based on remote-sensing methods, but they nevertheless provide direct constraints on the disk structure. In order to correctly interpret observational data, that is translating the observables into physical properties of the disk, understanding of the propagation of photons through the medium between the luminosity source and the observer is essential. This requires detailed numerical modeling in the form of radiative transfer calculations, a well suited tool for linking observations to simulation. Results of this are demonstrated throughout this thesis.

The following brief summary (Sect. 2.1) of the basic radiative transfer problem is based on the book by Rybicki & Lightman (1979) and benefits from the lecture notes by Dullemond (2012). Dust scattering including the description of polarized light is addressed in Sect. 2.2, the reader is referred to the book by Bohren & Huffman (1983) for more details. Section 2.3 will discuss the numerical treatment of radiative transfer focusing on the three-dimensional (3D) Monte Carlo radiative transfer code RADMC-3D[3] (Dullemond et al., 2012), which has been used for the radiative transfer models presented in this thesis.

2.1 Radiative transfer equations

Radiative transfer describes the energy transfer in the form of electromagnetic waves. If a light ray propagates through and interacts with a surrounding medium, energy may be added to or subtracted from it by absorption/scattering and emission. For dust in the ISM, and in particular in circumstellar disks, all these processes play a role. As a first consequence, the specific intensity I_ν at a frequency ν will not remain constant as in vacuum, but vary along a specific ray. Mathematically, the change in intensity I_ν along a path with length s in direction $\vec{n}$ is described by the radiative transfer equation,

$$\frac{dI_\nu(\vec{n},s)}{ds} = -\alpha_\nu(s)\, I_\nu(\vec{n},s) + j_\nu(s)\,, \tag{2.1}$$

[3]The freely available code and documentation can be found on http://www.ita.uni-heidelberg.de/~dullemond/software/radmc-3d/.

where $\alpha_\nu(s)$ is the absorption coefficient, which is defined as the inverse of the mean free path of a photon, and $j_\nu(s)$ is the emissivity. The number of mean free path lengths a photon travels between two positions along a ray, i.e. how effectively a material is able to absorb photons, is called optical depth and is defined as

$$\tau_\nu(s_0, s_1) = \int_{s_0}^{s_1} \alpha_\nu(s)\, ds \tag{2.2}$$

$$= \int_{s_0}^{s_1} \kappa_\nu(s)\, \rho(s)\, ds\,, \tag{2.3}$$

where $\kappa_\nu(s)$ represents the mass-weighted opacity and $\rho(s)$ the mass density of the absorbing medium. If a medium has a high optical depth, that is $\tau \gg 1$ when integrated along a typical path through the medium, it is said to be optically thick. On the contrary, when $\tau \ll 1$, only a small fraction of the photons are absorbed and the medium is said to be optically thin.

The intensity observed at a position s_1 can be expressed via the integral of Eq. 2.1, which is the formal solution of the radiative transfer equation,

$$I_\nu(\vec{n}, s_1) = I_\nu(\vec{n}, s_0)\, e^{-\tau_\nu(s_0, s_1)} + \int_{s_0}^{s_1} j_\nu(s)\, e^{-\tau_\nu(s, s_1)}\, ds\,. \tag{2.4}$$

One can now define the source function S_ν as the ratio of the emission coefficient and the absorption coefficient, $S_\nu(s) = j_\nu(s)/\alpha_\nu(s)$, so that Eq. 2.1 can be rewritten as

$$\frac{dI_\nu(\vec{n}, s)}{ds} = \alpha_\nu(s)\left[-I_\nu(\vec{n}, s) + S_\nu(s)\right]\,, \tag{2.5}$$

or with respect to τ_ν as

$$\frac{dI_\nu(\vec{n}, s)}{d\tau_\nu} = -I_\nu(\vec{n}, s) + S_\nu(s)\,. \tag{2.6}$$

In the case of local thermodynamic equilibrium (LTE) and if scattering can be neglected, Kirchoff's law applies and the source function is simply equal to the Planck function, $S_\nu = B_\nu(T)$. However, in order to model the dust in circumstellar disks, scattering also has to be considered, which increases the complexity of the radiative transfer equation. It has to be solved along all rays with different direction vectors $\vec{n}$ passing through a given point $\vec{x}$ at once in order to account for ray coupling effects, as a photon can switch from one ray to another ray through a scattering event. The

total extinction coefficient now consists of two contributions and can be defined as

$$\alpha_\nu^{\text{tot}} = \alpha_\nu^{\text{abs}} + \alpha_\nu^{\text{scat}} \,, \tag{2.7}$$

where α_ν^{abs} and α_ν^{scat} are the inverse mean free paths of absorption and scattering, respectively. Note that the explicit s and $\vec{n}$ dependencies are dropped for notational convenience. Similarly, the emissivity is also composed of two parts such that $j_\nu = j_\nu^{\text{emis}} + j_\nu^{\text{scat}}$. Hence, the source function becomes

$$S_\nu = \frac{j_\nu^{\text{emis}} + j_\nu^{\text{scat}}}{\alpha_\nu^{\text{abs}} + \alpha_\nu^{\text{scat}}} \,. \tag{2.8}$$

By further defining the albedo as

$$\eta_\nu = \frac{\alpha_\nu^{\text{scat}}}{\alpha_\nu^{\text{abs}} + \alpha_\nu^{\text{scat}}} \tag{2.9}$$

and the photon destruction probability as

$$\epsilon_\nu = 1 - \eta_\nu = \frac{\alpha_\nu^{\text{abs}}}{\alpha_\nu^{\text{abs}} + \alpha_\nu^{\text{scat}}} \,, \tag{2.10}$$

and assuming LTE for the emission, Eq. 2.5 modifies to

$$\frac{dI_\nu}{ds} = \alpha_\nu \left[\epsilon_\nu \, B_\nu(T) + (1 - \epsilon_\nu) \, S_\nu^{\text{scat}} - I_\nu \right] \,, \tag{2.11}$$

with scattering source function S_ν^{scat}. In the simplest case of isotropic scattering the emission coefficient is independent of direction. This means that the outgoing direction of the scattered photon has no dependence on its initial direction before the scattering event, and the scattered radiation is emitted equally into isotropic solid angles. Then, for isotropic scattering the scattering source function is given by the mean intensity J_ν,

$$S_\nu^{\text{scat,iso}} = J_\nu = \frac{1}{4\pi} \oint I_\nu \, d\Omega \,, \tag{2.12}$$

where $d\Omega$ denotes the solid angle. For the more general case of anisotropic scattering, the scattering source function includes a scattering phase function $\phi(\vec{n}, \vec{n}')$, that is the probability distribution that a ray $I_\nu(\vec{n})$, traveling in direction $\vec{n}$, is scattered into direction $\vec{n}'$. The scattering phase function holds $\phi(\vec{n}, \vec{n}') = \phi(\vec{n}', \vec{n}) \geq 0$ and is

normalized, so that $S_\nu^{\rm scat}$ becomes

$$S_\nu^{\rm scat} = \frac{1}{4\pi} \oint I_\nu(\vec{n})\, \phi(\vec{n}, \vec{n}')\, d\Omega\,. \tag{2.13}$$

A commonly used approximation for ϕ is the Henyey-Greenstein phase function. Introducing the angle of scattering θ such that $\mu = \cos\theta = \vec{n} \cdot \vec{n}'$, it is defined as

$$\phi_{\nu,g}(\mu) = \frac{1 - g_\nu^2}{(1 + g_\nu^2 - 2g_\nu\mu)^{3/2}}\,, \tag{2.14}$$

where g_ν denotes the scattering anisotropy factor,

$$g_\nu = \frac{1}{4\pi} \oint \phi(\mu)\, \mu\, d\mu\,. \tag{2.15}$$

In general, the scattering phase function can have an arbitrarily complex form, especially for polarized scattering off dust particles, which is the focus of the disk modeling in this thesis.

2.2 Polarized scattering off dust particles

2.2.1 Scattering and absorption cross sections

One of the primary objectives when treating a radiative transfer problem is to calculate the absorption and scattering cross sections at a given wavelength for dust grains of a specific shape and material. A typical dust grain is made out of dielectric material, so it reacts to the oscillating electromagnetic field of the radiation. The properties of the material are defined by the complex index of refraction $m(\lambda) = n(\lambda) - ik(\lambda)$, where the real part $n(\lambda)$ can be interpreted as scattering and the imaginary part $k(\lambda)$ as absorption, respectively. These refractive indices for different materials are measured with laboratory experiments for a sampled set of wavelengths (see Sect. 2.4.3 for more details on dust species in disks).

Besides chemical composition, the size of a grain is an important factor in determining the dust opacity. The radius of a spherical grain a is related to the wavelength λ via the so-called size parameter x,

$$x = \frac{2\pi a}{\lambda}\,, \tag{2.16}$$

where three different regimes are distinguished. For $x \ll 1$ in the Rayleigh regime the scattering opacity goes as $\sim \lambda^{-4}$, while the absorption opacity is proportional

to λ^{-1}. For $x \gg 1$, the geometric optics regime, the light can be considered as propagating along rays. The total opacity in this case is determined by

$$\kappa_\nu^{\mathrm{geo}} = \frac{\pi a^2}{m}\,, \tag{2.17}$$

with $\kappa_\nu^{\mathrm{scat}} = \eta_\nu\, \kappa_\nu^{\mathrm{geo}}$ and $\kappa_\nu^{\mathrm{abs}} = (1-\eta_\nu)\, \kappa_\nu^{\mathrm{geo}}$. For a given refractive index the scattering and absorption cross section of a compact spherical dust grain can be estimated with 'Mie theory', a series approximation of analytical solutions to the Maxwell equations for light interacting with the electric field (Mie, 1908). As a consequence, for $x \gg 1$ the theory of Mie scattering becomes difficult to apply, since more terms in the series expansion are required. One also has to keep in mind that more realistic grains might deviate from homogeneous spheres, for example a distribution of hollow spheres (e.g., Min et al., 2005) or aggregate structures made out of monomers (e.g., Min et al., 2006).

2.2.2 Stokes formalism and Mueller matrix

For a profound study of scattering a further description for polarized light is needed. The polarization state of light relative to a particular reference frame is characterized by a four component column vector, the Stokes vectors $S = (I,\, Q,\, U,\, V)^T$, where I is the intensity. Q and U are linear polarization states in directions parallel to (0°/90°) and ±45° from the reference direction, respectively. V defines circular polarization (right- or left-handed). The four Stokes components have to fulfill $I^2 \geq Q^2 + U^2 + V^2 \geq 0$. If $Q = U = V = 0$, the light is unpolarized, while for perfectly coherent light $Q^2 + U^2 + V^2 = I^2$. The effect of a scattering event on the polarization state of the incoming light can be mathematically described by a matrix multiplication of the incident Stokes parameters,

$$\begin{pmatrix} I_s \\ Q_s \\ U_s \\ V_s \end{pmatrix} = \frac{1}{k^2 d^2} \begin{pmatrix} S_{11} & S_{12} & S_{13} & S_{14} \\ S_{21} & S_{22} & S_{23} & S_{24} \\ S_{31} & S_{32} & S_{33} & S_{34} \\ S_{41} & S_{42} & S_{43} & S_{44} \end{pmatrix} \begin{pmatrix} I_i \\ Q_i \\ U_i \\ V_i \end{pmatrix}\,, \tag{2.18}$$

where $k = 2\pi/\lambda$ denotes the wave number and d is the distance from the observer. The 4 x 4 scattering matrix on the RHS of Eq. 2.18 is the so-called Mueller matrix (Mueller, 1948) for scattering on a single particle. The values S_{ij} depend on the direction into which the radiation is scattered and on the direction of the incoming flux. It is noted here that later on in this thesis a different normalization is used to be consistent with the convention of RADMC-3D, such that

$$Z_{ij} = \frac{1}{k^2\, m_{\mathrm{grain}}} S_{ij}\,, \tag{2.19}$$

where $m_{\rm grain}$ is the mass of one dust particle.

If the incident light is unpolarized, as it is the case for stellar irradiation, the Stokes parameters of the scattered light are $I_s = (kd)^{-2}\, S_{11}\, I_i$, $Q_s = (kd)^{-2}\, S_{21}\, I_i$, $U_s = (kd)^{-2}\, S_{31}\, I_s$, and $V_s = (kd)^{-2}\, S_{41}\, I_i$. The scattered light is, in general, partially polarized with degree of polarization,

$$P = \sqrt{\frac{S_{21}^2 + S_{31}^2 + S_{41}^2}{S_{11}^2}}\,. \tag{2.20}$$

For spherical particles (cf. Mie theory in Sect.2.2.1), the total angle-integrated scattering cross section is independent of the polarization state of the incoming photon and the scattering matrix simplifies to

$$\begin{pmatrix} S_{11} & S_{12} & 0 & 0 \\ S_{12} & S_{11} & 0 & 0 \\ 0 & 0 & S_{33} & S_{34} \\ 0 & 0 & -S_{34} & S_{33} \end{pmatrix}\,. \tag{2.21}$$

For the case of unpolarized incident light the Stokes parameters of the scattered light become $I_s = (kr)^{-2}\, S_{11} I_i$, $Q_s = (kr)^{-2}\, S_{12} I_i$, and $U_s = V_s = 0$. In the context of protoplanetary disks we therefore only expect a polarized signal in Stokes U_s for multiple scattering, i.e. scattering of already polarized light, as shown in the example case of the highly-inclined disk around T Chamaeleontis (T Cha, see Chapter 6). As already noted in Sect. 2.1, the radiative transfer equation including scattering (Eq. 2.11) cannot just be solved by Eq. 2.4, since the source function is a priori not known. It depends on the solution I_ν for all rays passing through a given point. In Sect. 2.3 it is shown how this radiative transfer problem is approached numerically, and in particular specified how the multiple scattering problem is solved.

2.3 Dust continuum radiative transfer with RADMC-3D

Nowadays, with the invention of high resolution and high contrast instruments, images of protoplanetary disks reveal complex non-axisymmetric substructures (such as gaps, spirals, and warps; cf. Sect. 1.3), requiring models that include multi-dimensional geometries and anisotropic scattering processes. Detailed radiative transfer modelling is required to derive a realistic temperature distribution and structural properties of the disk self-consistently. An increasing number of dust continuum radiative transfer simulation packages have been developed and applied to circumstellar disks (e.g., HOCHUNK3D: Whitney et al. 2013, MC3D: Wolf et al.

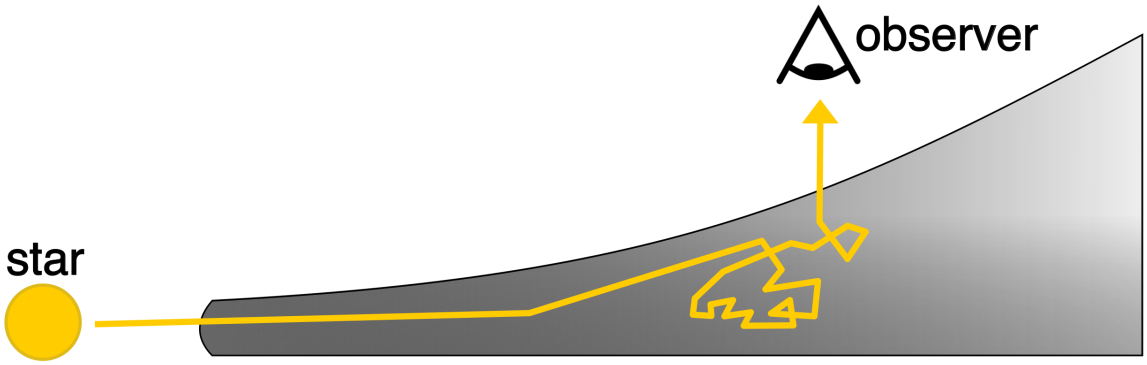

Figure 2.1: Sketch illustrating the Monte Carlo journey of a single photon package that undergoes multiple scattering events within the disk. It is emitted by the central star and changes its direction after each scattering and in addition its frequency after each absorption & re-emission event. It eventually escapes the disk region in direction of the observer.

1999, MCFOST: Pinte et al. 2006, MCMAX(3D): Min et al. 2009, and RADMC-3D: Dullemond et al. 2012). The numerical method of choice for all of these codes is a probabilistic one, the so-called 'Monte Carlo' method, which is suitable to directly simulate (multiple) scattering processes. The following paragraphs will briefly introduce this method with a particular emphasis on the numerical realization in RADMC-3D.

2.3.1 Monte Carlo method

The Monte Carlo method is an alternative option to 'Discrete Ordinate' and 'Moment' methods for solving the radiative transfer equation numerically. Instead of explicitly solving it, the Monte Carlo technique is based on a statistical approach. Packets of energy, henceforth called photon packages[4], are released successively from a luminosity source and their paths between absorption & re-emission and scattering events in a prescribed medium are traced. Random number sampling is used to determine the location of the next interaction event and the propagation direction of a photon after each scattering event. In case of absorption events new photons are generated through thermal emission. The journey of each photon ends when it eventually escapes the model grid (cf. Fig. 2.1), when it is extincted by a certain order of magnitude, or by getting re-emitted at a wavelength at which the medium is optically thin. In the 3D radiative transfer code RADMC-3D the Monte Carlo method by Bjorkman & Wood (2001) extended with the cell volume method (Lucy, 1999) and the modified random walk method (Min et al., 2009; Robitaille, 2010) is used.

[4]Each single package actually represents many photons at once assuming that all these photons follow the same path. As a notational convention the word 'photon(s)' is equally used throughout the thesis.

2.3.2 Computing the dust temperature

A typical dust continuum radiative transfer calculation for a protoplanetary disk starts with a thermal Monte Carlo simulation that computes the dust temperature distribution self-consistently. As already described, a photon package with some initial frequency travels through the disk grid from one interaction event with a dust grain to the next. This can be either a real scattering, i.e. a change of moving direction while keeping the same frequency, or an absorption event. Each absorption involves a luminosity injection into the current cell, which heats the medium and therefore raises the local cell temperature. When a photon package gets absorbed by the dust, it is immediately re-emitted at another wavelength following the frequency redistribution approach from Bjorkman & Wood, and it is assigned a randomly chosen new direction. Once the travel of all photons has been simulated, the total luminosity of a cell and its final dust temperature can be determined. This is an equilibrium dust temperature, which is a good approximation as long as the heating and cooling timescales in the disk are short compared to time-dependent dynamical processes. One also has to keep in mind that there is a stochastic error on the temperature values, since not all possible photon paths are covered with a finite number of photon packages. This error can be, however, minimized by considering a high enough number of photons.

2.3.3 Making synthetic images and spectra

As a second step, with the thermal source function S_ν^{therm} in hand, i.e. the dust temperature distribution computed by the thermal Monte Carlo run, a spectrum or an image at given wavelengths for a specific disk inclination and position angle (PA) can be calculated with the ray-tracing capability of RADMC-3D. For computational reasons, RADMC-3D calculates the scattering source function S_ν^{therm} just prior to the ray-tracing by means of an additional Monte Carlo run, without permanently storing it. Dust scattering can be treated as either isotropic or anisotropic, including polarized scattering off randomly oriented particles. The latter means that a photon package gets polarized when it undergoes a scattering event, which demands a treatment of the full Stokes vector as introduced in Sect. 2.2.2.

2.4 Radiative transfer modeling of a protoplanetary disk

In the following, the three main input quantities for modeling a protoplanetary disk with RADMC-3D are addressed. The particularities for each of the models presented in this thesis are described in the individual chapters.

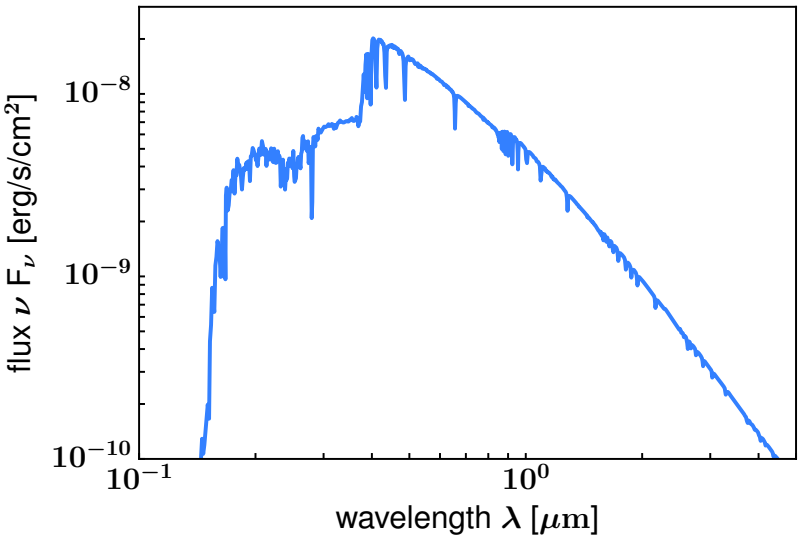

Figure 2.2: Stellar atmosphere model for a Herbig A5 star with solar metallicity, an effective temperature of 8500 K, a stellar radius of 1.5 $M_\odot$, and log gravity of 2.0. To obtain the observed flux, a distance to Earth of 140 pc is assumed. Based on data from Castelli & Kurucz (2004).

2.4.1 Disk structure

The typical setup of a dust continuum radiative transfer model of a protoplanetary disks starts with defining its initial geometry. It is described as a set of grid points, preferably in spherical coordinates (r, θ, ϕ), dividing the computational domain into $N_r \times N_\theta \times N_\phi$ grid cells. Furthermore, the dust density distribution for this grid structure is needed, such that the disk hosts an overall dust mass. For a parametric setup, the disk structure is further specified by the dust surface density $\Sigma_\mathrm{d}(r)$ as defined in Eq. 1.9. Assuming vertical hydrostatic equilibrium as an approximation (cf. derivation in Sect. 1.1.2), the volume density has the Gaussian structure from Eq. 1.11. Alternatively, the density output calculated from multi-dimensional hydrodynamical disk simulations can be directly used to define the density structure (see Chapters 3, 4). For each dust species, that has for example a specific grain size and/or composition, an individual dust density distribution is defined. Vertical settling can be taken into account by assigning individual dust scale heights to each grain size bin (cf. Chapters 7 - 10 for the details).

2.4.2 Luminosity source

As explained in Sect. 2.3 the radiation fields from luminosity sources are subdivided into a number of chromatic photon packages. In the case of a protoplanetary disk stellar light is injected into the model by placing one or more individual stars. Parameters such as radius, mass, position and surface temperature of the star are specified. Statistically, each star emits the same number of photon packages, but a

brighter star emits more energetic photon packages. For computational reasons, the stars are treated as point sources. This is valid for the extended disks around Herbig Ae/Be and T Tauri stars modeled in this thesis, because their spatial scales are much larger than the size of the star. The star is either simply assumed to be a blackbody of temperature $T_{\rm eff}$, or a more realistic stellar spectrum is used (Fig. 2.2). The latter can be for example taken from the Castelli-Kurucz atlas (Castelli & Kurucz, 2004)[5].

2.4.3 Dust opacity calculation

RADMC-3D requires dust opacities as a basic model input, where composition and size distributions can be arbitrarily chosen. For the radiatitive transfer models presented in this thesis, the BHMIE code of Bohren & Huffman modified by Bruce T. Draine[6] is used for the opacity calculation, and embedded into a `Python` script for conversion into RADMC-3D compatible form. More precisely, in addition to the mass-weighted absorption opacity $\kappa_{\rm abs}$, the whole scattering matrix with elements Z_{ij} (cf. Eqs. 2.19, 2.21) is precalculated for every wavelength of interest for a discrete sampling of scattering angles θ. Then, the mass-weighted scattering opacity and anisotropy factor can be determined as

$$\kappa_{\rm scat} = \oint Z_{11}\, d\Omega = 2\pi \int_{-1}^{1} Z_{11}(\mu)\, d\mu, \quad \text{and} \tag{2.22}$$

$$g = \frac{2\pi}{\kappa_{\rm scat}} \int_{-1}^{1} Z_{11}(\mu)\, d\mu\,. \tag{2.23}$$

Observations of protoplanetary disks show evidence for grains from sub-micron size to mm size, so that a broad range of sizes has to be covered (Sect. 1.3). Thus, often a single grain size distribution is used, where the number density follows a power law, $n(a) \propto a^{-q}$, with a default index of $q = 3.5$ (Mathis, Rumpl and Nordsieck (MRN) distribution, Mathis et al., 1977). Alternatively, several monodisperse grain sizes are considered, which, however, demand a specific numerical treatment. Mie scattering can produce quite strong oscillations in the opacity as a function of wavelength and scattering angle. Thus, even for an actual monodisperse grain size, a narrow distribution is considered by smearing out the single size with a Gaussian. Furthermore, for very small wavelengths compared to the grain size the scattering phase function is strongly forward-peaked (see Fig. 2.4) and shows wiggles at low scattering angles. Therefore, a fine sampling of the scattering angle grid is needed. The usual number of angle sampling points N_θ used between 0 and 90 deg is 901,

[5] More stellar spectral atlases can be found at `http://www.stsci.edu/hst/observatory/crds/astronomical_catalogs.html`.

[6] Download from `https://www.astro.princeton.edu/~draine/scattering.html`.

with a refinement factor ξ such that

$$\theta(i) = 90 \frac{\exp\left(\frac{\xi(i-1)}{N_\theta}\right) - 1}{\exp(\xi) - 1} \,. \tag{2.24}$$

In modeling cases, where forward scattering is not of interest at all, it can be neglected. This means that the forward peaking of the phase function has some upper limit. This is done by setting a minimum scattering angle, below which the scattering is replaced by the value computed for that particular threshold angle.

It is known that amorphous silicates, carbonaceous species, and ices are the most common solids in space (e.g., Semenov et al., 2003b). These three groups themselves represent entire families of minerals. While the simplest silicate is quartz (SiO_2), more complex ones combine Si and O with metals such as Al, Fe, Mg. Carbon can also exist in different forms, for instance graphite or PAHs. Dust grains in a protoplanetary disks likely have a composition mixed of these minerals, since in the formation process small particles of different homogeneous materials stuck together and coagulated to form dust aggregates (see Sect. 1.2.1). Furthermore, freeze-out of gas species (e.g., H_2O, CO, CO_2, NH_3) onto the dust grains can create icy mantles (cf. Chapter 8). In this thesis, the focus is laid on a mixture of pyroxene ($Mg,FeSiO_3$), simple amorphous pure carbon and water ice (H_2O). The optical constants of these materials are obtained from the Jena database[7] based on the original papers by Jaeger et al. (1994) and Dorschner et al. (1995), Preibisch et al. (1993), and Warren & Brandt (2008). Further optical constants for silicates ('astrosilicate') and carbonaceous material are taken from Draine (2003) and Zubko et al. (1996), respectively. The optical constants are calculated for mixed-composition particles using the Bruggeman mixing theory, rather than treating each species individually in the radiative transfer calculations. The dust temperatures are computed under the assumption that particles of different size with this composition are thermally decoupled, that is that they have independent radiative equilibrium temperatures.

Figure 2.3 shows the dependence of the absorption (solid lines) and scattering (dashed lines) opacity on intrinsic dust properties, such as composition and grain size. In general, the opacities are rather flat in the geometrical optics regime, and drop off quickly in the Rayleigh regime. Since the opacity in the geometrical optics regime scales with the surface to mass ratio as a^{-1} (cf. Eq. 2.17), it is dominated by the smallest grains in the optical and NIR. For amorphous silicates (left panel), the absorption opacities (red solid lines) are dominated by a major dip between $\sim$1 μm and $\sim$10 μm and two peaks at $\sim$10 μm and $\sim$20 μm, which arise due to the Si-O bond. The ratio of amorphous silicates over other species influences the strength

[7] Database of Optical Constants for Cosmic Dust created by the Laboratory Astrophysics Group of the AIU Jena.

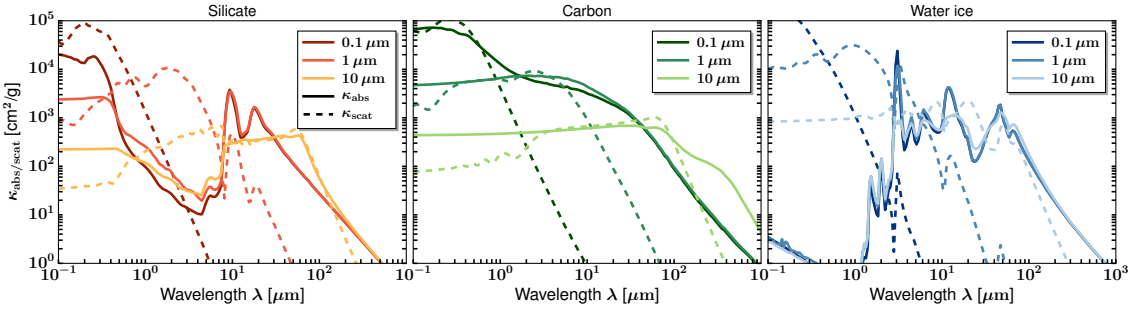

Figure 2.3: Dust opacities computed with Mie theory for compact, spherical particles of three different species (*left*: Mg(0.7)Fe(0.3)SiO(3) from Dorschner et al. 1995, *middle*: carbon from Zubko et al. 1996, *right*: water ice from Warren & Brandt 2008). The solid and dashed lines denote the absorption and scattering coefficients, respectively. Different grain sizes (0.1 μm, 1 μm, 10 μm) are shown in different colors.

of these silicate features visible in a SED (cf. Sect. 1.3.1). For the larger grain size of 10 μm there is a nearly flat behavior longward of the dip in the NIR. The larger the grain size, the smaller the opacity in the optical and NIR wavelength regime becomes. The scattering opacity is highest in the NIR, and then it drops below the absorption opacity for longer wavelengths. For carbon (middle panel), there are no particular dust features. It is, however, seen that carbon grains generally have much stronger opacities in the optical and NIR. The scattering opacity peaks at around $\lambda \simeq 2\pi a$ for all grain sizes and quickly decreases toward longer wavelengths. For water ice (right panel), one can conclude that the absorption opacity curves show several peaks and dips between $\sim$1 μm and $\sim$100 μm, whose strengths depends on the grain size. The overall behavior of the scattering opacity is similar to that of carbon.

Figure 2.4 shows the phase function (left panel) and the polarization efficiency (right panel) at a wavelength of 1.6 μm (H-band) for three different regimes of the size parameter $x = 2\pi a/\lambda$. They are numerically calculated with Mie theory for compact, spherical grains consisting of a mixture of amorphous silicates and carbonaceous material (Jaeger et al., 1994; Dorschner et al., 1995; Zubko et al., 1996). As introduced in Sect. 2.2, scattering occurs in the Rayleigh limit ($2\pi a \ll \lambda$) and in the limit of geometric optics ($2\pi a \gg \lambda$). Particles smaller than the wavelength scatter light almost isotropically (cyan curve in left panel). Particles comparable to or larger than the wavelength scatter light anisotropically, where the strength of the forward peak depends on the relative particle size (orange curve in left panel). Forward scattering by dust grains in an inclined disk leads to a brightness asymmetry between the near and far sides (see Chapter 6). As already mentioned in Sect. 1.3.2 the effect of the single scattering polarization (scattering angle dependent polarization efficiency) has to be taken into account. In the Rayleigh limit, the polarization efficiency is bell-shaped with 100% polarization at a scattering angle of 90 deg (cyan curve in right panel). Besides the grain size, the polarization is also sensitive to the

grain composition and structure (e.g., Min et al., 2016; Tazaki et al., 2016).

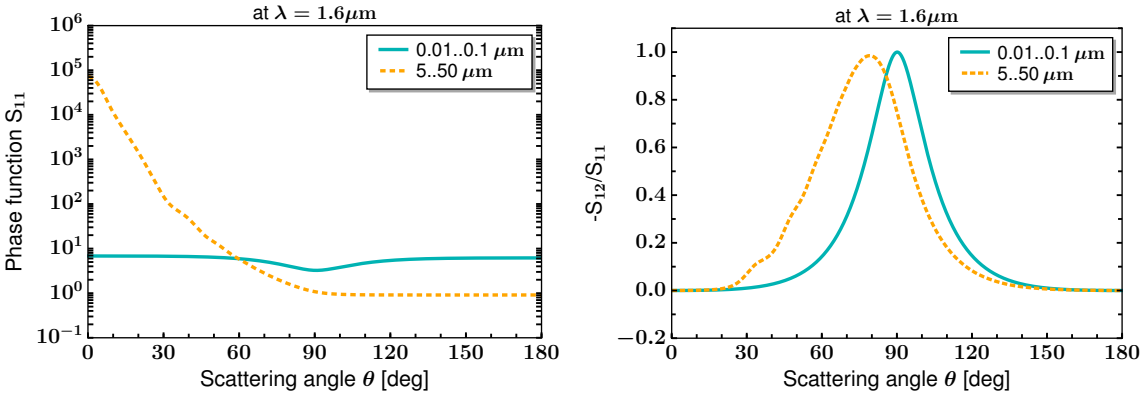

Figure 2.4: Phase function S_{11} and degree of polarization $-S_{12}/S_{11}$ of different grain size distributions at $\lambda = 1.6\,\mu$m for a dust mixture of 70% amorphous silicates and 30% carbonaceous material.

3 | Spiral arms in scattered light images of marginally gravitationally unstable protoplanetary disks

The content of this chapter is based on Pohl et al. (2015) published in *2015, Monthly Notices of the Royal Astronomical Society (MNRAS), 453, 1768.*

3.1 Motivation

In disk-related astrophysics, self-gravity and gravitational instability play a significant role on various scales, from Saturn's rings to spiral galaxies. In the context of circumstellar disks, the disk is supposed to be massive enough in the earliest stages of disk formation, so that the effect of its own self-gravity is non negligible. As a result, the disk can become gravitationally unstable and its structure is affected by the propagation of density waves leading to spiral arm formation. Gravitational instability provides efficient angular momentum transport in relatively massive disks. Furthermore, depending on the disk's cooling efficiency, a gravitationally unstable disk might fragment to produce overdensities of gas (cf. Sect. 1.2.2). An interesting question to address is how the disk's self gravity can influence the appearance of spiral arms created by planet-disk interactions, which have been introduced in Sect. 1.2.3.

3.1.1 Observational insights

Young forming protoplanets may leave observational signatures in their parental disk in the form of distinct gaps, vortices, warps, or spiral arms. This is thought to happen during the final stages of protoplanetary disk evolution. As seen in Sects. 1.1 and 1.3, there is a peculiar group called transition disks, whose SED and sub-mm observations suggest that the inner disk is strongly depleted of dust. Spiral arms have thus far been mainly observed in this kind of disks, suggesting that the gap

formation mechanism is related to spiral arm formation. This needs, however, to be treated carefully since there might be an observational selection effect. Observations in the NIR and (sub-)mm regime of transition disks show a variety of asymmetric features. Since disks are optically thick in the optical and NIR, high angular resolution scattered light images trace small hot dust particles in the upper disk layer. In these images the presence of spirals are intriguing, for example, MWC 758 (Grady et al., 2013; Benisty et al., 2015), HD 100453 (Wagner et al., 2015a; Benisty et al., 2017), HD 135344B/SAO 206462 (Muto et al., 2012; Garufi et al., 2013; Stolker et al., 2016), HD 142527 (Avenhaus et al., 2014, 2017). On the other hand, spiral arms have been observed in very few cases in gas spectral lines (Christiaens et al., 2014; Tang et al., 2017). Recently, the first spiral structure dust continuum sub-mm emission was detected by ALMA in the disk around Elias 2-27 (Pérez et al., 2016). Furthermore, the birth of a triple protostar system formed via fragmentation of a gravitationally unstable disk in the system L1448 IRS3B was suggested by Tobin et al. (2016). The spirals observed in nearly all of these disks share a number of common features. They have two symmetric arms that are shifted in azimuth by approximately 180 deg and have large pitch angles (angle between the spiral arm and the tangent circle, see Fig. 1.5) of about 10-25 deg. In most cases, there is a gap just inwards of the spirals whose origin might be related to yet unseen planetary companions.

The origin of the observed spirals is still debated. For instance, with a simple analytical description based on the spiral density wave theory, the morphology of spirals triggered by a hypothetical planet has been studied by Muto et al. (2012), Grady et al. (2013), and Benisty et al. (2015). The best spiral fitting model requires a high disk aspect ratio $h = H/r$ to account for the large pitch angles implying a very warm disk. However, as explained in Sect. 1.2.3, linear theory breaks down for more massive companions that produce a different spiral morphology. Thus, fitting a spiral's shape with linear density waves might lead to uncertainties in the local disk properties inferred. Juhász et al. (2015) focused on the contrast of spirals compared to their surrounding background disk. They modeled the spiral waves launched by planets by means of locally isothermal hydrodynamic simulations as well as analytic descriptions. Based on contrast arguments these authors suggested that the spiral arms observed are the results of pressure scale height perturbations rather than of pure surface density perturbations.

One of the most exciting explanation of the observed spirals is that they are launched by one or more substellar companion(s). They could be located inside the cavity/gap of a transition disk (e.g., Juhász et al., 2015; Dong et al., 2015c, this work) or outside (e.g., Dong et al., 2015b, see also Chapter 4). Dong et al. (2015c) also studied the observational signatures in transition disks by combining 2D two fluid hydrodynamic calculations with 3D radiative transfer simulations, but rather focused on the observational signatures of gaps opened by one or several planets. They stated that density waves and streamers inside the planetary gap, produced by planet-disk interactions, can be visible in NIR images. Besides processes involving planets, it

has been examined whether other mechanisms can lead to spiral features, such as non-ideal MHD effects (e.g., Flock et al., 2015; Lyra et al., 2015) or gravitational instability (e.g., Lodato & Rice, 2004, 2005; Rice et al., 2004; Dong et al., 2015a). Structures induced by the onset of gravitational instabilities tend to produce spirals with higher than $m = 2$ azimuthal wave number (e.g., Cossins et al., 2009; Forgan et al., 2011). Planets drive, depending on the planet-to-star mass ratio, a $m = 1$ or sometimes even a $m = 2$ mode, but the secondary spiral is substantially weaker. Our idea is to combine both spiral formation scenarios in order to see if this strengthens their amplitude and to produce various spiral morphologies.

3.1.2 Instability condition

In general, the precondition for a disk to become unstable is that the amount of gravitational potential energy overcomes pressure and rotational kinetic support. The axisymmetric stability of a thin disk is determined by the so-called Toomre parameter $\mathcal{Q}$ (Toomre, 1964). The local Toomre criterion for a disk to be unstable is defined as

$$\mathcal{Q} = \frac{c_\mathrm{s}\kappa}{\pi G \Sigma_\mathrm{g}} \lesssim 1\,, \tag{3.1}$$

where c_s is the sound speed, Σ_g is the gas surface density and κ corresponds to the epicyclic frequency, which is equal to the angular velocity $\Omega_\mathrm{K} = (GM_\star/r^3)^{1/2}$ in the case of a Keplerian disk. Using Eq. 1.8, i.e. the fact that $H = c_\mathrm{s}/\Omega_\mathrm{K}$, and estimating the disk mass as $M_\mathrm{disk} \simeq \pi r^2 \Sigma_\mathrm{g}$ the following global instability criterion can be written,

$$\frac{M_\mathrm{disk}}{M_\star} \gtrsim \frac{H}{r}\,. \tag{3.2}$$

Increasing the disk mass and/or decreasing the disk temperature leads to a lower $\mathcal{Q}$. Hence, the disk mass has to be a significant fraction of the stellar mass for the disk to be gravitationally unstable.

3.1.3 Disk mass estimates

Current observational methods to estimate the disk mass still have systematic uncertainties (see Chapter 9). The total disk mass is dominated by the gas, which mostly consists of H_2. Since its emission is hard to detect, there are only three objects (TW Hya, DM Tau, GM Aur) for which hydrogen was directly observed in the form of HD (Bergin et al., 2013; McClure et al., 2016). Two prominent proxies, dust continuum emission and CO and its isotopologues, are usually used to estimate disk gas masses. The first method is based on observations of the mm continuum emission

from dust grains (e.g., Beckwith et al., 1990; Andrews & Williams, 2005), assuming a certain dust opacity and gas-to-dust ratio. The generally assumed value of 100 for the gas-to-dust ratio may not be accurate for all disks, since it strongly depends on the disk evolution (e.g., Brauer et al., 2007; Birnstiel et al., 2010). Also, from observations it is known that mm-sized dust grains and the gas do not necessarily have the same spatial distribution in disks (e.g., de Gregorio-Monsalvo et al., 2013; Walsh et al., 2014). Furthermore, in this calculation dust opacity values at the observed frequency are assumed, which may have quite uncertain values in protoplanetary disks due to the various grain sizes, compositions, internal structures and the presence of ice mantles (e.g., Pollack et al., 1994; Henning & Stognienko, 1996; Semenov et al., 2003a; Demyk et al., 2013). The second method infers the gas mass independently of the dust content using molecular line observations. Due to its high abundance and line strength CO and its isotopologues are the most frequently used tracers of gas in protoplanetary disks (e.g., Dutrey et al., 1996; Williams & Best, 2014; Ansdell et al., 2016; Miotello et al., 2016). Uncertainties concern the H_2-CO abundance and the topologist ratios because of photo-dissociation and freeze-out processes. Miotello et al. (2014) showed that the disk mass may be underestimated by up to two orders of magnitude if only a single CO isotopologue line is observed and isotope selective effects are not properly taken into account. As mentioned above, the only direct measurements of hydrogen in disks actually suggests that the disks might be more massive than previously thought. However, it has to be proven whether this result is statistically robust. The different disk masses inferred by means of HD and CO detections suggest a gas phase carbon depletion. Overall, current disk mass estimations from gas and dust observations only give a very rough approximation and disks around Class II stars might be sufficiently massive to be gravitationally unstable, as it is expected for Class 0 and I objects.

3.1.4 Outline

All disk processes including planet-disk interactions and gravitational instability strongly depend on the cooling efficiency, and therefore, the disk temperature. The latter again has an important effect on the shape and contrast of non-axisymmetric disk features. However, many of the numerical simulations so far are limited due to the assumption of a locally isothermal disk. In this work, a 2D hydrodynamical code which includes an energy equation accounting for disk viscous heating and cooling is used to simulate planet-disk interactions. Gravitational instability is known to produce multi-armed spirals in disks, while planet-disk interactions mostly result in one- or two-armed spirals. In this work, we study the role of heating and cooling, and gravitational instability on the shape and contrast of spiral arms induced by planet-disk interactions. It is investigated what kind of structures the interplay between gravitational instability and planet-disk interactions can reproduce. This combination has not been investigated so far. The question asked here is whether the presence of a planet in a marginally gravitationally stable disk can tip it over the

limit. The information about the hydrodynamical disk structure is a prerequisite for our radiative transfer modeling in order to link simulation results to observations. The focus is on presenting synthetic scattered light images and on investigating whether they resemble the observations. This work is divided into four parts. In Sect. 3.2 the modifications to the hydrodynamical code and the basic models are introduced. The radiative transfer setup is described in Sect. 3.3. Subsequently, the simulation results are presented in Sect. 3.4. The associated discussion and the conclusions are summarized in Sect. 3.5.

3.2 Hydrodynamical setup

The 2D hydrodynamical grid-based code used for simulating the planet-disk interactions is based on the FARGO-ADSG version (Baruteau & Masset, 2008a,b). This modified version of the original FARGO code (Masset, 2000) implements an energy equation and the disk self-gravity. The full treatment of disk heating and cooling is important, since in addition to surface density perturbations, temperature perturbations occur as a consequence of shocks along the spirals.

3.2.1 Surface density description

The gas disk is characterized by an initial gas surface density profile $\Sigma_{\rm g}(r)$, a temperature profile $T(r)$ and a pressure profile $P(r)$. The density profile is taken to be a power law combined with an exponential cut-off at long radii, specifically,

$$\Sigma_{\rm g}(r) = \Sigma_{\rm g,0} \left(\frac{r}{r_{\rm c}}\right)^{-\delta} \exp\left[-\left(\frac{r}{r_{\rm c}}\right)^{2-\delta}\right], \tag{3.3}$$

where $r_{\rm c}$ corresponds to a characteristic scaling radius, which is set to $= 75\,\mathrm{au}$ in accordance with results from high angular resolution disk imaging in the sub-mm regime (Andrews et al., 2010, 2011). In our simulations this is equal to 0.3 times the outer boundary of the disk. $\Sigma_{\rm g,0}$ describes the density normalization factor. The surface density index δ is taken to be 1 in our simulations. With this surface density profile it is ensured that most of the disk mass ($> 60\,\%$) is located between $r_{\rm in}$ and $r_{\rm c}$, so that artificial reflections from the outer grid boundary can be minimized.

The initial temperature structure is a power law, leading for our case of a non-flaring (H/r = const.) disk to

$$T(r) = \frac{\mu m_{\rm p}}{\mathcal{R}_{\rm g}} G M_{\star} h_0^2\, r^{-1}, \tag{3.4}$$

with mean molecular weight μ, proton mass $m_{\rm p}$, universal gas constant $\mathcal{R}_{\rm g}$, grav-

itational constant G, and where the parameter h_0 defines the initial disk aspect ratio.

Such a conical disk defines the boundary between a flaring disk, i.e. H/r is a monotonic increasing function of radius r, and a self-shadowed disk, i.e. H/r becomes smaller with larger radii (Dullemond & Dominik, 2004a). Considering that we intend to analyze scattered light images, in the case of our non-flaring, constant opening angle geometry, any pressure scale height perturbation with a sufficient amplitude can cast a shadow over the remaining outer disk rather easily. In this case of grazing incidence an object can cast the largest shadow. Furthermore, the background brightness is as dark as possible for grazing infall. Therefore, high contrast spiral structures are most easily made in non-flaring disks. Furthermore, Juhász et al. (2015) showed that modeling a flaring disk affects the brightness of the disk in the outer regions, but does not improve the visibility of the spirals. From observations there is also evidence for very low flaring index in MWC 758, one of the sources where spirals were detected.

3.2.2 Heating and cooling terms

The development of gravitational instability leads to a self-regulation process due to the competition between heating from the instability and cooling. After a local temperature increase due to a weak shock induced by the spiral density waves, the disk cools back down to a predefined background temperature on a certain timescale. It takes at least a dynamical timescale ($t_{\rm dyn} \sim \Omega^{-1}$) for the disk to hydrodynamically react to any increased temperature. The form of the energy equation implemented in FARGO is

$$\frac{\partial e}{\partial t} + \nabla \cdot (e\,\vec{v}) = -P\nabla \cdot \vec{v} + Q_+ - Q_- \,, \tag{3.5}$$

where e denotes the thermal energy per unit area, $\vec{v}$ is the flow velocity, P is the vertically integrated pressure, and Q_+/Q_- corresponds to the vertically integrated heating/cooling term. The disk heating is assumed to be due to the disk viscosity. The cooling source term is assumed to be

$$Q_- = \frac{e}{t_{\rm cool}} \tag{3.6}$$

with a cooling timescale of (cf. Gammie, 2001)

$$t_{\rm cool} = \beta_{\rm cool}\,\Omega^{-1} \,, \tag{3.7}$$

where the $\beta_{\rm cool}$-factor is taken to be a constant. The powerlaw background temperature profile to which the disk cools down after each viscous heating event is set

by the initial locally isothermal temperature (cf. Eq. 3.4). It is assumed to be due to a balance between viscous heating and irradiation heating on the one hand, and radiative cooling on the other hand. With our choice of the background temperature we expect that local heating by shocks becomes relevant. This shock heating may increase the scale height of the disk, which causes local bumps on the disk surface (radial $\tau = 1$ surface with τ being the optical depth). This is different for a *flaring* irradiated disk ($T(r) \propto r^{-1/2}$) around a Herbig star, where the heating of the disk is dominated by the star apart from the very inner disk. It should be pointed out that in a flaring disk model a different background temperature profile is probably needed.

The question is how fast the disk is able to cool down after a shock. If the cooling is very efficient, i.e. $t_{\rm cool} \ll \Omega^{-1}$, no shock effects will occur and the disk can be assumed to be locally isothermal. For a rough estimation of $t_{\rm cool}$ in our models, i.e. $\beta_{\rm cool}$, the following calculation is done. The cooling rate of an accretion disk strongly depends on the optical depth τ, but since we are in the range $\tau \gg 1$, it is determined by (cf. Eq. 1.15)

$$Q_{-}(r) = 2\sigma T_{\rm eff}^4(r) = 2\sigma_{\rm SB}\frac{1}{\tau}T_{\rm mid}^4(r)\,, \tag{3.8}$$

where $\mathrm{T_{mid}}$ corresponds to the midplane temperature. The optical depth can be calculated by

$$\tau \simeq \frac{1}{2}\Sigma_{\rm d}\kappa_{\rm d}\,, \tag{3.9}$$

whereas a dust-to-gas ratio of 0.01 is assumed and for the dust opacity $\kappa_{\rm d}$ the Planck mean value is taken. Furthermore, the vertically integrated thermal energy is determined by

$$E = \frac{1}{\gamma - 1}\Sigma_{\rm g}\frac{k_{\rm B}T}{\mu m_{\rm p}}\,, \tag{3.10}$$

with Boltzmann constant $k_{\rm B}$, proton mass $m_{\rm p}$, adiabatic index $\gamma = 7/5$, and mean molecular weight $\mu = 2.3$. Using Eq. 3.6 and dividing $t_{\rm cool}$ by the orbital timescale $t_{\rm orb} = 2\,\pi\,\Omega^{-1}$ yields the $\beta_{\rm cool}$-factor. Using typical values for the gas density ($\Sigma_{\rm g}(50\,\mathrm{au}) \simeq 50\,\mathrm{g\,cm^{-2}}$) and temperature ($T_{\rm mid}(50\,\mathrm{au}) \simeq 12\,\mathrm{K}$), and setting $\kappa_{\rm d}(T_{\rm mid}) \simeq 10\,\mathrm{cm^2 g^{-1}}$ gives $\beta_{\rm cool} \simeq 5$.

There is a critical cooling timescale, $t_{\rm cool,c}$, and a corresponding critical value of $\beta_{\rm cool}$, $\beta_{\rm cool,c}$, below which the disk can fragment and form gravitationally bound clumps, rather than reaching a steady, gravitoturbulent state. In numerical experiments Gammie (2001) showed that disk fragmentation can happen for a typical

timescale of $t_{\mathrm{cool,c}} \lesssim 3\,\Omega^{-1}$. Using 3D smoothed particle hydrodynamic (SPH) simulations Rice et al. (2003a) generally confirmed this cooling time for fragmentation, even though the $\beta_{\mathrm{cool,c}}$ value is up to a factor of two higher for more massive disks. However, Paardekooper (2012) showed that disk fragmentation is a stochastic process and observed it for cooling times up to $20\,\Omega^{-1}$. In principle, fragmentation is even possible up to $\beta_{\mathrm{cool}} = 50$, but it becomes very rare for such high values. A detailed study on the convergence of the critical cooling timescale with resolution for SPH and grid-based hydrodynamics simulations was done by Meru & Bate (2012). They showed that reducing the dissipation from the numerical viscosity leads to larger values of $\beta_{\mathrm{cool,c}}$ at a given resolution. Furthermore, Baehr & Klahr (2015) altered the cooling timescale such that it is dependent on local surface density fluctuations, to make it more appropriately physical. They also found a strong resolution dependence, where for lower resolution simulations the disk is more stable to gravitational stresses.

In the following we decided to use β_{cool}-values of 1 and 10, for which none of our disk models is found to fragment for the selected resolution. This allows the disk to settle down into a quasi-steady, self-gravitating state. We note here that, following the argument from Meru & Bate (2012), repeating our simulations with a higher resolution could minimize the artificial viscosity and, therefore, possibly fragment the disk into bound objects.

3.2.3 Parameter choice

The basic model consists of a viscous, non-flaring disk with an embedded giant planet. An overview of all the parameters can be found in Table 3.1. For the complete series of models, the disk is tapered as described in Sect. 3.2.1. FARGO uses dimensionless units, therefore, the fixed orbital radius of the embedded planet of $r_{\mathrm{p}} = 1$ is used as the length scale. The disk is divided into 1280 azimuthal and 720 radial grid zones, ranging from 0.2 to 10.0. This corresponds to a physical disk extension from 5 au to 250 au, assuming that the planet's orbital radius is 25 au. The high resolution for the hydrodynamical part serves to avoid strong numerical diffusion effects. The outer boundary of the computational grid is therefore far enough away from the regions around the gap on which we focus our study. Thus, together with the choice of a tapered gas surface density, artificial boundary condition effects are minimized. The inner boundary conditions are open, allowing for mass outflow at the inner edge. The disk is considered to be non-flaring with a constant aspect ratio of $h = 0.05$. Furthermore, for the disk viscosity the α-type viscosity (Eq. 1.21) is used with $\alpha = [10^{-3}, 10^{-2}]$. The planet's potential itself is softened over a length that scales with the disk thickness with a factor of $\epsilon = 0.6$. The timescale over which the planet mass is switched on for the potential evaluation at the beginning of each simulation is set to 100 planetary orbits. The results of all hydrodynamic simulations are described in Sect. 3.4.1.

3.3 Radiative transfer setup

The output of the hydrodynamic simulations previously presented in Sect. 3.2, i.e. the gas surface density distribution $\Sigma_{\rm g}(r,\phi)$ and the temperature distribution $T(r,\phi)$, are taken for further processing in the context of 3D radiative transfer modeling. The radiative transfer code RADMC-3D (Dullemond et al., 2012) is used to calculate synthetic scattered light images in the NIR. For these calculations the same aspect ratio, flaring index, and radial and azimuthal grid extensions as in the hydrodynamic simulations are adopted. In order to avoid low photon statistics, the outputs from the hydrodynamic simulations are interpolated to a grid with a lower resolution ($N_r \times N_\phi = 384 \times 512$ grid cells) for the radiative transfer calculations. This does not affect the shape of any of the structures obtained in the FARGO simulations. In addition, $N_\theta = 128$ cells for the polar direction are taken. Assuming the vertical density profile to be Gaussian and adopting the canonical dust-to-gas ratio for the ISM of 0.01, the dust volume density is given by

$$\rho(R,\phi,z) = 0.01\,\frac{\Sigma_{\rm g}(R,\phi)}{\sqrt{2\,\pi}\,H(R,\phi)}\,\exp\left(-\frac{z^2}{2\,H^2(R,\phi)}\right)\,, \tag{3.11}$$

where the cylindrical coordinates R and z can be converted into spherical formulas via $R = r\,\sin(\theta)$ and $z = r\,\cos(\theta)$, where θ is the polar angle. The temperature output after a specific orbital evolution from the hydrodynamic simulations is used to determine the pressure scale height $H(R,\phi)$,

$$H(R,\phi) = \frac{c_s}{\Omega} = \sqrt{\frac{k_B}{\mu\,m_{\rm p}\,G\,M_\star}\,T(R,\phi)\,R^3} \propto \sqrt{T}\,. \tag{3.12}$$

The radiative transfer calculations start with computing the dust temperature structure by means of a thermal Monte Carlo simulation using 10^7 photon packages. We want to calculate an equilibrium dust temperature considering the star as the source of luminosity. This temperature is the result of a balance between radiative absorption and re-emission, i.e. a dust grain acquires as much energy as it radiates. This implies that the gas temperature from the hydrodynamic simulations is assumed to only influence the disk scale height (cf. Eq. 3.12), but is not explicitly related to the dust temperature itself. Hence, a self-enhancement effect, such that the further irradiation of a disk bump actually influences the scale height at those positions, is not included in our study. The main inputs for the radiative transfer modeling are the dust density structure from Eq. 3.11, dust opacities, and the radiation source. The latter is assumed to have typical stellar parameters of a Herbig Ae star ($T_{\rm eff} = 9500\,{\rm K}$, $M_\star = 2.0\,{\rm M}_\odot$, $R_\star = 2.5\,{\rm R}_\odot$). For simplicity, a black body radiation field is assumed. The dust in our models consists of silicate grains with a fixed grain radius of $0.1\,\mu$m. The optical constants are obtained from the Jena

Table 3.1: Overview of the hydrodynamical models and parameters studied.

#	$M_{\rm disk}[M_\star]$	α	$M_{\rm p}/M_\star$	$\beta_{\rm cool}$	r_c $[r_{\rm p}]$	SG
1	0.15	10^{-3}	10^{-3}	10	3.0	no
2	0.15	10^{-3}	10^{-3}	10	3.0	yes
3	0.15	10^{-3}	10^{-3}	1	3.0	yes
4	0.15	10^{-2}	10^{-3}	10	3.0	yes
5	0.15	10^{-3}	10^{-2}	10	3.0	yes
6	0.2	10^{-3}	10^{-3}	10	3.0	no
7	0.2	10^{-3}	10^{-3}	10	3.0	yes
8	0.2	10^{-3}	10^{-2}	10	3.0	yes
9	0.2	10^{-3}	10^{-3}	10	4.8	yes

Notes. When specified the parameters are given in dimensionless FARGO units, i.e. with respect to the planet's position and stellar mass. SG stands for self-gravity. For all simulations $N_r \times N_\phi = 720 \times 1280$ grid cells, a radial range from $r_{\rm in} = 0.2\,r_{\rm p}$ to $r_{\rm out} = 10.0\,r_{\rm p}$, and open boundary conditions at the inner edge are used. Model *1* is taken as the reference model considering a non self-gravitating disk.

database based on the work by Jaeger et al. (1994) and Dorschner et al. (1995). Scattering is considered to be anisotropic with a full treatment of polarization. The scattering phase function depends on the scattering angle and on the polarization state of the input radiation, i.e. the parameters of the full Stokes vector [I,Q,U,V] (cf. Sects. 2.1, 2.2). Linearized polarized intensity images can be calculated with $\mathrm{PI} = \sqrt{\mathrm{Q}^2 + \mathrm{U}^2}$. The dust opacity tables are produced with the BHMIE code of Bohren & Huffman (1984) for calculating scattering and absorption by spheres. The images are calculated at 1.65 μm using 10^8 photon packages.

The signal-to-noise ratio of the theoretical images obtained from RADMC-3D is limited only by photon statistics. In order to simulate synthetic observations from these models that are comparable to observational data, the images have to be convolved with the telescope's point spread function (PSF). The diffraction limited PSF for a perfect optical system based on circular elements would be an Airy pattern, whose central peak can be approximated by a 2D Gauss function. As size of the PSF a full width at half maximum (FWHM) of 0.″04 is chosen, which is representative for H-band observations with the SPHERE instrument at the VLT.

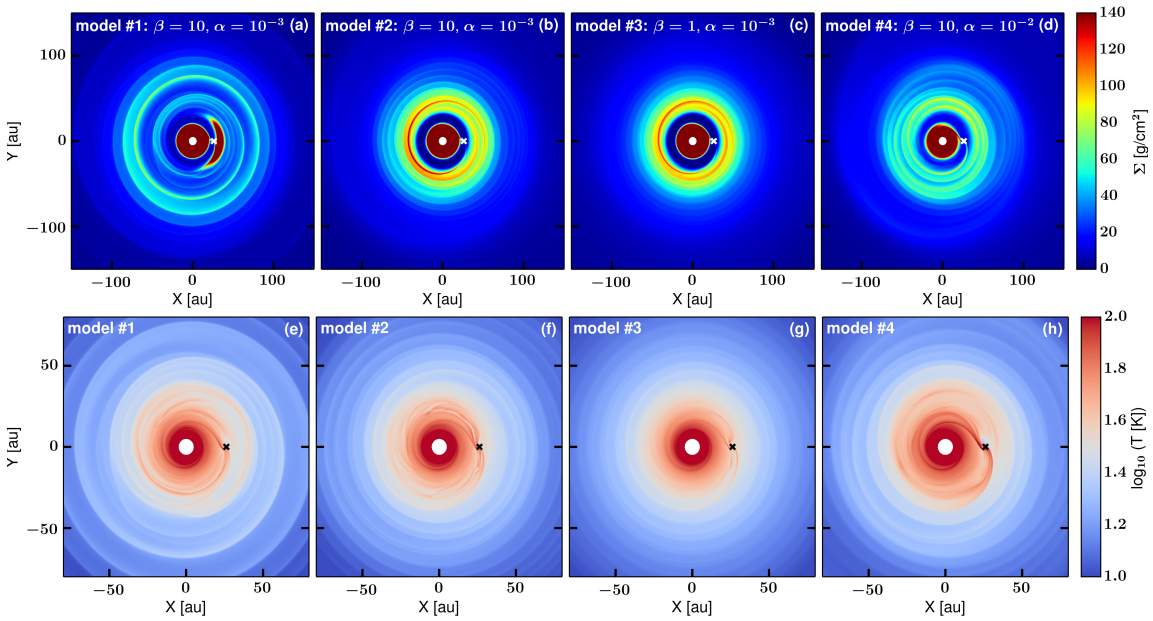

Figure 3.1: Surface density (top row) and temperature (bottom row) maps for a planet-to-star mass ratio of 10^{-3} after 1000 planetary orbits for different cooling factors $\beta_{\rm cool}$ and viscosity values α. The disk mass corresponds to 0.15 $M_\star$. Note the difference in the x-axis scaling. Panels (a) and (e) show the only model for which self-gravity is turned off. The planet's position is marked with the white and black cross, respectively.

3.4 Results

3.4.1 Hydrodynamic simulations

The numerical hydrodynamic simulations include a treatment of heating and cooling, providing a more realistic picture of the disk gas density and temperature distribution in self-gravitating disks. Hence, it is possible to study the effect of surface density and pressure scale height perturbations on the spiral morphology and contrast in scattered light images.

Energy equation vs. locally isothermal structure

For our reference model *1* the simulation considers a non self-gravitating disk with a mass of 0.15 $M_\star$, a planet-to-star mass ratio of 10^{-3} and an α-viscosity of 10^{-3}. The $\beta_{\rm cool}$-cooling factor is set to 10. In Fig. 3.1a a snapshot of the gas surface density after 1000 planetary orbits is shown. The embedded planet starts to clear out a gap in less than 100 orbits. The disk viscosity is sufficiently low and the planet-to-star mass ratio is high enough, for the angular momentum flux carried by the density waves to overcome the inflow due to viscous accretion in the disk, leading to the gap opening near the planet's position. The planet is not able to produce a full cavity as seen in observations of some transition disks. This might be, however, linked to

the possibility that dust located in the very inner disk close to the star could not be detected, for instance due to grain growth.

Furthermore, distinct spiral density waves are induced by the planet. The dominant feature of this model is a vortex at the outer edge of the gap that moves with the local Keplerian speed and survives until the end of the simulation. The existence of this vortex is in accordance with Ataiee et al. (2013), who showed that vortices can be long-lived for moderate disk viscosity values and massive planets (cf. also Zhu & Stone, 2014; Fu et al., 2014). The vortex influences the surface density perturbations induced by the planet close to its position.

Assuming a locally isothermal equation of state corresponds to an infinitely short cooling timescale. This means that the temperature always remains constant after a density increase since compressive work is immediately radiated away. Therefore, the decisive advantage of the energy equation simulations over locally isothermal models is that the information of the temperature distribution is tracked. In Fig. 3.1*e–h* it can be seen that the spirals themselves are hotter than the background disk. The temperature of the spiral depends on the cooling timescale. If the cooling timescale is long, the disk material is unable to cool down to its pre-shock equilibrium temperature before the next heating event occurs with the passing of the next shock wave. This leads to an overall higher temperature and disk scale height, also outside of the spiral itself. Another interesting finding is that in all temperature plots, best recognizable in Fig. 3.1*g*, the spiral close to the planet's position seems to split up in two parts. Outwards of the inner spiral and inwards of the outer spiral wake an additional high temperature arm is seen. Those structures are located within the planetary horseshoe orbit leading to a rather circular shape. They are caused by shock fronts going through the U-turn of the horseshoe orbit.

We can check whether a planet can generate a strong enough perturbation in the temperature to meet the criteria for spiral detection obtained from analytical modeling by Juhász et al. (2015). They found that a relative change of at least 0.2 in pressure scale height ($\delta H/H$) is required for the spirals to create detectable observational signatures. Calculating this relative change for our simulation with $\beta_{\mathrm{cool}} = 10$ gives 0.2 at the $\phi = 270°$ axis. This value increases to a maximum of 0.6 near the planet at a zero azimuth angle. Hence, we expect to see the spirals in scattered light (cf. Sect. 3.4.2).

Effect of self-gravity

In Fig. 3.1 the gas surface density (*a–d*) and temperature (*e–h*) maps of four different models for a disk mass of $0.15\,M_\star$ are displayed. The leftmost panel represents the reference model with a planet-to-star mass ratio of 10^{-3} after 1000 planetary orbits and a cooling time of $10\,\Omega^{-1}$. The other panels additionally include self-gravity and only differ in the β_{cool}-factor and α-viscosity value. Models *2* and *3* (Figs. 3.1*b,c*) are quite different from the reference model without self-gravity. The vortex present in the latter case is smeared out very quickly due to self-gravity effects and no inter-

action between the vortex and density waves can occur. Additionally, the gap around the planet's orbit is much more distinct. In contrast to very low mass planets driving a single one-armed spiral (Ogilvie & Lubow, 2002), two arms that spiral outward of the planet's position with a mutual azimuthal shift are present. Note that this $m = 2$ mode is not a result of self-gravity, but caused by the massive planet itself. The primary spiral arm launched at the planet's position is much stronger than the one azimuthally shifted which has a quite low density contrast. Furthermore, it is noticeable that the self-gravity models show more twisted spirals with lower pitch angles. This can be explained by the fact that the disk self-gravity modifies the positions of the Lindblad resonances, between which density waves can propagate. It shifts the location of the effective resonances closer to the planet (Pierens & Huré, 2005).

To study the disk stability we show the azimuthally averaged Toomre parameter $\mathcal{Q}$ as a function of radial distance in Fig. 3.4. The middle panel only includes the Toomre profiles for models with a disk mass of $0.15\,M_\star$. We compare the models with an embedded planet to the case of a self-gravitating disk without a planet (solid black vs. dotted red line). It can be seen that initially $\mathcal{Q}$ is always larger than 1 for all models, thus the disk by itself would not become gravitationally unstable. Adding a sufficiently massive planet considerably reduces $\mathcal{Q}$ and puts the disk just at the limit of being gravitationally unstable between 50 and 100 au from the star (blue dotted line). The explanation for this behaviour is the following. When a planet is present in the disk it will carve a gap around its orbit decreasing the surface density in the gap. Since most of the material from the gap is pushed away due to angular momentum exchange between the planet and the disk the surface density of the disk will increase outside of the gap edge. Hence, a sharp density jump is created. Since $\mathcal{Q}$ is proportional to Σ^{-1}, it is strongly increased near the planet's position within the gap, but can be reduced just behind the gap edge, where overdensities grow. Thus, if $\mathcal{Q}$ is low enough at the outer edge of the gap the local increase of surface density due to gap formation might tip the balance and lower $\mathcal{Q}$ below unity. The strong increase of $\mathcal{Q}$ from ~ 100 au on is caused by the exponential mass tapering and the disk mass loss (Fig. 3.4, left panel). The issue for a disk mass of $0.15\,M_\star$ is, however, that $\mathcal{Q}$ is not low enough at larger radii in order to let self-gravity affect the disk dynamics in form of additional gravitational instability structures. How a larger disk mass or an increased critical taper radius affect these results is discussed in Sect. 3.4.1.

Effect of cooling timescale

According to Eq. 3.7, for constant $\beta_{\rm cool}$, $t_{\rm cool}$ is proportional to $\mathrm{r}^{3/2}$, so that the cooling is faster in the inner disk. This means that the temperature profile returns back to the locally isothermal background values faster in these inner parts, but in any case not faster than the local dynamical timescale. In general, we expect to see stronger temperature changes for longer cooling times, i.e. larger $\beta_{\rm cool}$-values. The

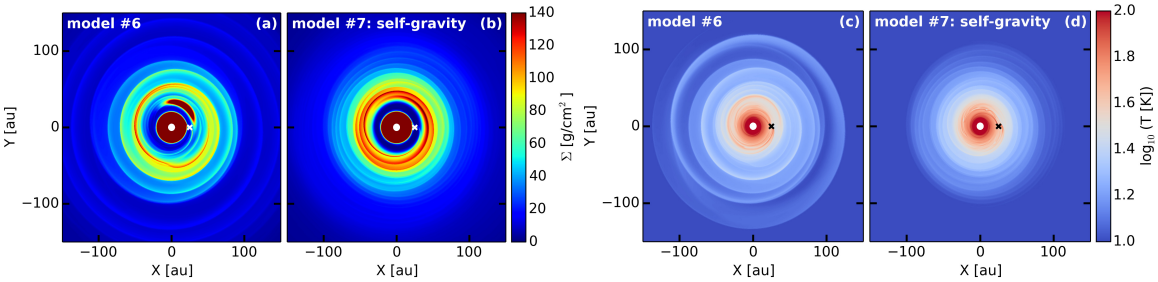

Figure 3.2: Surface density map for a planet-to-star mass ratio of 10^{-3} after 1000 planetary orbits for a model without (*a*) and with self-gravity (*b*). Panels (c) and (d) show the corresponding temperature distributions. The disk mass corresponds to $0.2\,M_\star$, $\beta_{\rm cool}$ is taken to be 10.

effect of the cooling timescale can be seen by comparing models *2* ($\beta_{\rm cool} = 10$) and *3* ($\beta_{\rm cool} = 1$). A very fast cooling ($\beta_{\rm cool} \leq 1$) is very close to the locally isothermal case. In Fig. 3.1*c,d* the final surface density and temperature show lower values in absolute strength and contrast along the spirals compared to model *2* (*b,f*). This slight drop in temperature also decreases the pitch angle, leading to more tightly wound spirals which are smeared out at larger radii. A larger $\beta_{\rm cool}$ value implies less effective cooling, which makes the whole disk, i.e. also the spirals, hotter. The higher the temperature, the faster the waves spread in the disk, since the sound speed is proportional to the square root of the temperature. Hence, more mass flows through the inner disk boundary for $\beta_{\rm cool} = 10$ (see Fig. 3.4, left panel).

Effect of viscosity

Another important parameter to explore is the viscosity, for which the gap profile dependence is already known (e.g., Crida et al., 2006). If the viscosity decreases the gap becomes gradually deeper. However, the dependence of the gap characteristic on viscosity is less sensitive in numerical simulations compared to theoretical calculations. In simulations there is no simple balance between viscous, pressure and gravitational torque, since parts of the latter are transported away by density waves (Papaloizou & Lin, 1984; Rafikov, 2002). Nevertheless, by comparing our model *2* ($\alpha = 10^{-3}$) with *4* ($\alpha = 10^{-2}$) in Fig. 3.1, one can see that as viscosity increases the gap is filled with more gas. Since the primary spiral is launched at the planet's position within the gap this also influences the spiral contrast, which is consequently reduced. Furthermore, a higher α-viscosity smears out the spiral structure and reduces the absolute surface density at the spiral position. Therefore, we use moderate values of viscosity for the rest of our models ($\alpha = 10^{-3}$).

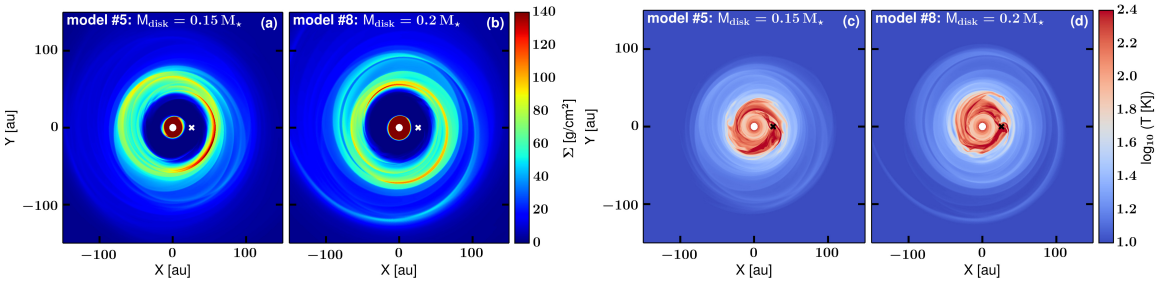

Figure 3.3: Surface density maps (a,b) for a planet-to-star mass ratio of 10^{-2} after 1000 planetary orbits. The disk mass corresponds to $0.15\,M_\star$ (a) and $0.2\,M_\star$ (b), respectively. The temperature plots are shown in panels (c,d).

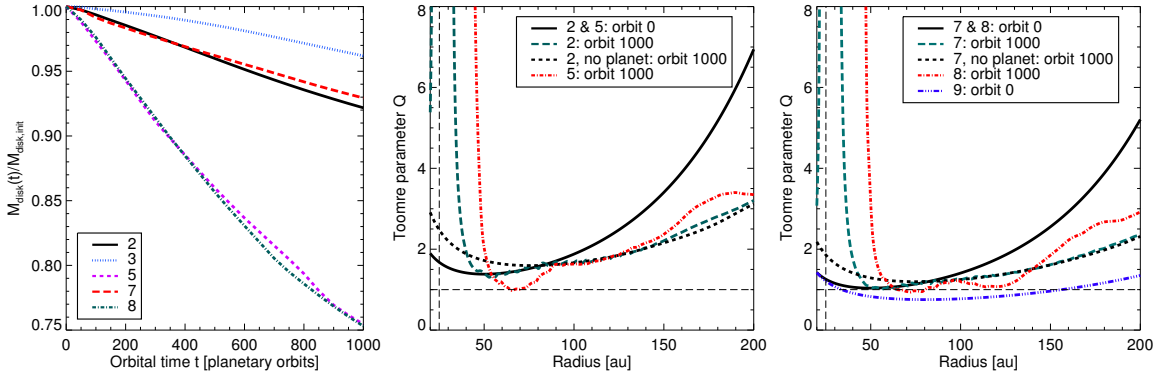

Figure 3.4: Disk mass evolution for models with different disk and embedded planet masses (left). Azimuthally averaged Toomre parameter $\mathcal{Q}$ as a function of radius (middle and right panels). For radii smaller than 20 au $\mathcal{Q}$ has very large values, which are not relevant for our study and therefore not plotted here. The disk mass in the middle panel corresponds to $0.15\,M_\star$, for the right panel to $0.2\,M_\star$. The vertical dashed line represents the position of the planet. The horizontal dashed line at $\mathcal{Q} = 1$ shows the critical Toomre value below which the disk is unstable to axisymmetric perturbations. A shearing disk becomes unstable to non-axisymmetric perturbations even at slightly larger values around $\mathcal{Q} \sim 1.5 - 2$.

Effects of disk and planet mass

For the simulations *6* and *7* presented in Fig. 3.2 the disk mass is increased to $0.2\,M_\star$, but the planet-to-star mass ratio of 10^{-3} is kept. The same trends as previously described for the lower disk mass in Sect. 3.4.1 can be seen. Self-gravity (model *7*) destroys the vortex and enhances the strength of the two-armed $m = 2$ spiral considerably. This is consistent with results from Lin & Papaloizou (2011), who showed that for sufficiently large disk mass and therefore sufficiently strong self-gravity the vortex modes are suppressed. Instead, new global spiral modes develop. Self-gravity effects become even more dominant for higher disk masses. The Toomre parameter profile for this model is plotted in the right panel of Fig. 3.4 (solid and dashed black lines). The disk is marginally gravitationally unstable from the begin-

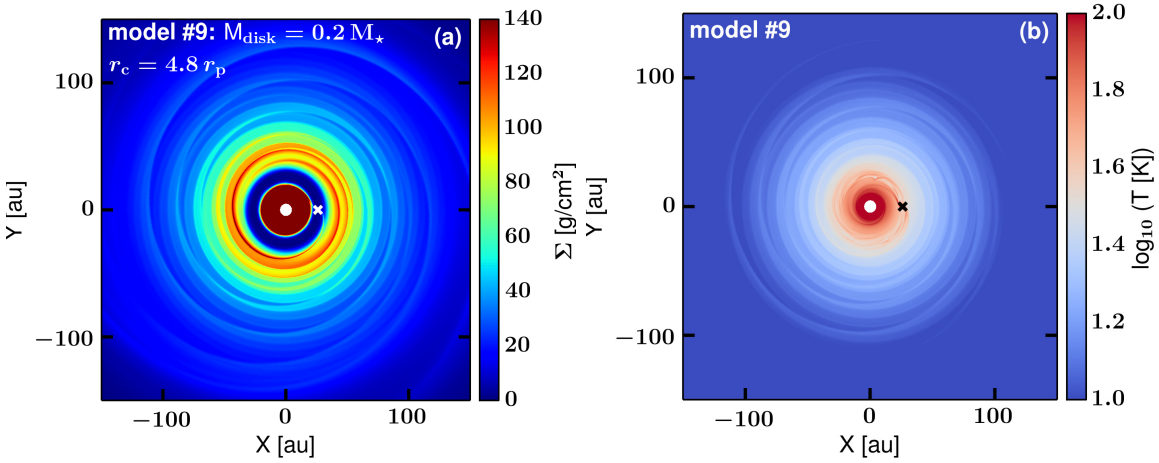

Figure 3.5: Surface density map (a) for a planet-to-star mass ratio of 10^{-3} after 1000 planetary orbits for the model with a critical taper radius of $4.8\,r_{\rm p}$. The disk mass corresponds to $0.2\,M_\star$. The temperature structure is shown in panel (b).

ning of the simulation between the planet's position at 25 au and $\sim$60 au. This is, however, not sufficient to induce gravitational instability, since the outer disk parts remain stable. Even the perturber with a planet-to-star mass ratio of 10^{-3} is not capable to reduce $\mathcal{Q}$ to a value ≤ 1 further out from 60 au (dashed green line). The general effect of increasing the planet-to-star mass ratio is illustrated by comparing Fig. 3.3 to Figs. 3.1 and 3.2. For both disk masses the higher planet mass forces the gap to become eccentric and a distinct two-armed spiral is not seen anymore. For a $10^{-2}\,M_\star$ planet mass $\mathcal{Q}$ is below or close to 1 even for the outer disk region between 100 and 150 au (red dashed line in Fig. 3.4). The consequence can be recognized in Fig. 3.3*b*. The massive planet is able to initiate gravitational instability, visible as a quite open spiral arm in the outer disk. Particular attention has to be paid to the temperature structure. The massive planet produces significant shock heating within the inner 50 au of the disk. These temperature changes cause perturbations in the vertical structure of the disk and following Eq. 3.12 this strongly influences the characteristics of our NIR scattered light images (cf. Sect. 3.4.2).

Apart from changing the planet mass the other possibility to trigger gravitational instability in the outer disk is to change the distribution of mass as a function of radius by increasing the mass in the outer disk for a given disk mass. This is done in our simulation with $0.2\,M_\star$ by shifting the critical mass taper radius outwards to $4.8\,{\rm r_p}$ (=120 au). The corresponding surface density and temperature plots are illustrated in Fig. 3.5*a,b*. A more open, global spiral pattern is seen. These large scale spirals reflect the onset of gravitational instability, but close to the planet they overlap with the planetary density waves. This instability is supported by the Toomre parameter profile in Fig. 3.4, right panel (blue dash-dotted line). The disk is initially gravitationally unstable in most locations.

When the disk is at the limit of being gravitationally unstable only a slight increase in disk mass changes the non-axisymmetric structures considerably. This effect can be seen in Fig. 3.3. For a disk mass of 0.2 $M_\star$ (Fig. 3.3*b*) a spiral arm in the outer disk induced by gravitational instability is present. Its pitch angle is significantly higher than for the planetary induced spirals from models with a lower disk mass (Fig. 3.3*a*).

3.4.2 Synthetic radiative transfer images

We aim to investigate the characteristics of the main observational features in transition disks, i.e. gaps and spiral structures, for which full 3D radiative transfer simulations are required. We are interested in the number of spiral arms, their pitch angle, and the brightness contrast between the spiral features and the surrounding background disk to investigate the observability of spirals. It is expected that the shock heating along the spiral may increase the scale height of the disk locally. This causes bumps on the disk surface, which are irradiated by the star, and thus produce a significant brightness contrast. Based on the model setup described in Sect. 3.3 scattered light images in polarized intensity at 1.65 μm are calculated. The disk is nearly face-on with an inclination angle of 10°. The wavelength at which the following images are made is chosen such that the images are directly comparable to H-band observations made with VLT/SPHERE, Gemini South/GPI, and Subaru/HiCIAO. For a realistic comparison to observations the radiative transfer images are first convolved with a 0.″04 Gaussian beam, assuming the source to be at 140 pc. Then, each pixel intensity value is multiplied with r^2, where r is its distance from the star, in order to compensate for the falloff of the stellar irradiation. This way the outer disk structures become much better visible. A coronagraph is mimicked by masking the inner 0.″1 of the disk (14 au at 140 pc distance). The images are normalized to the highest disk surface brightness while using a dynamic range of 1000 for plotting the images in logarithmic scale.

Images from models without self-gravity

The planetary $m = 1$ spiral is clearly visible in the scattered light image at infinite resolution based on the reference model *1* without self-gravity (see Fig. 3.6*a*). The brightness contrast between the spiral and the contiguous disk ranges from 12 to 30. The large vortex present in the hydrodynamic simulations is seen in the scattered light as well. This has, however, to be interpreted with caution, since it is related to the 2D character of our hydrodynamic simulations. Vortices can extend through the whole disk from the midplane to the atmosphere (cf. Zhu & Stone, 2014), but can be only accurately simulated with 3D hydrodynamical models. If the vertical elongation of the vortex is small, it is expected to appear less extended in scattered light, which traces the disk surface layer. After convolving this theoretical image with the Gaussian 0.″04 PSF the vortex as well as the planet-induced spirals are significantly smeared out, but still clearly visible. As can be seen in Fig. 3.8*a*, the

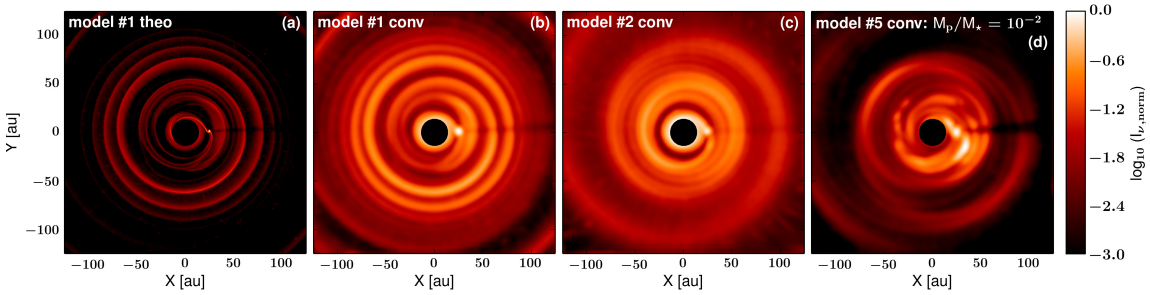

Figure 3.6: Simulated NIR scattered light images in H-band polarized intensity ($\lambda = 1.65\,\mu$m). All models consider a disk mass of $0.15\,M_\star$. (a) corresponds to the reference model *1* without self-gravity and shows the image at original resolution as calculated with the radiative transfer code RADMC-3D. All other images (b–d) are convolved with a Gaussian beam using a FWHM of 0.″04 (at 140 pc distance), which is representative for observations with VLT/SPHERE in the H-band. The central 0.″1 of the image were masked to mimic the effect of a coronagraph similar to real observations.

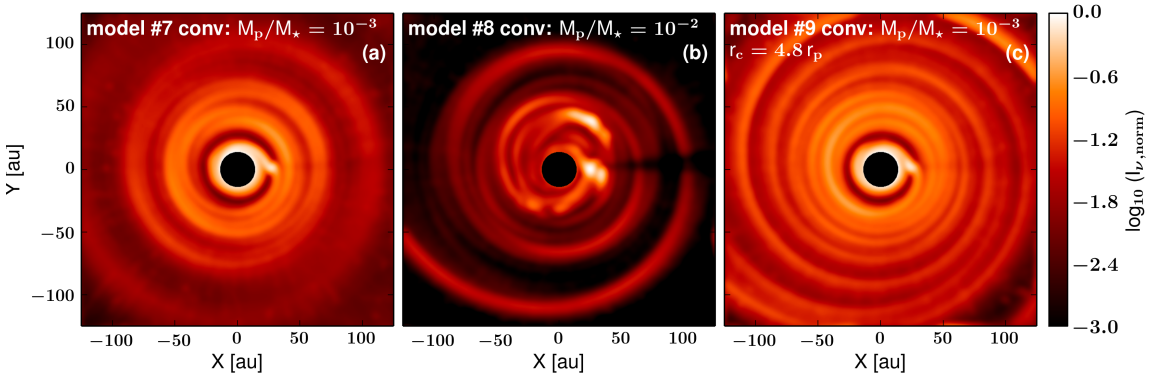

Figure 3.7: Simulated NIR scattered light images in H-band polarized intensity ($\lambda = 1.65\,\mu$m). All images are based on a $0.2\,M_\star$ disk. They are convolved with a Gaussian PSF with FWHM of 0.″04 (at 140 pc distance). For panel (c) the critical taper radius is set to $4.8\,r_p$. The central black region (0.″1) mimics the effect of a coronagraph similar to real observations.

contrast of the spirals with the surrounding disk is reduced by a factor of about three, giving contrast values between 3 and 10 (magenta line) for a resolution of 0.″04. We note that the contrast is expected to be further reduced in observations due to instrument related and additional noise effects.

Images from models including self-gravity

In all simulations shown in Figs. 3.6*c,d* and 3.7*a–c* self-gravitating disks are considered. First, we study the effect of self-gravity by comparing the results of models *1* and *2*. As already explained in Sect. 3.4.1, the inclusion of self-gravity destroys the vortex immediately. This leads to a more distinct primary spiral launched close to the planet's position (see Fig. 3.6*c*). Furthermore, the radial brightness cross-

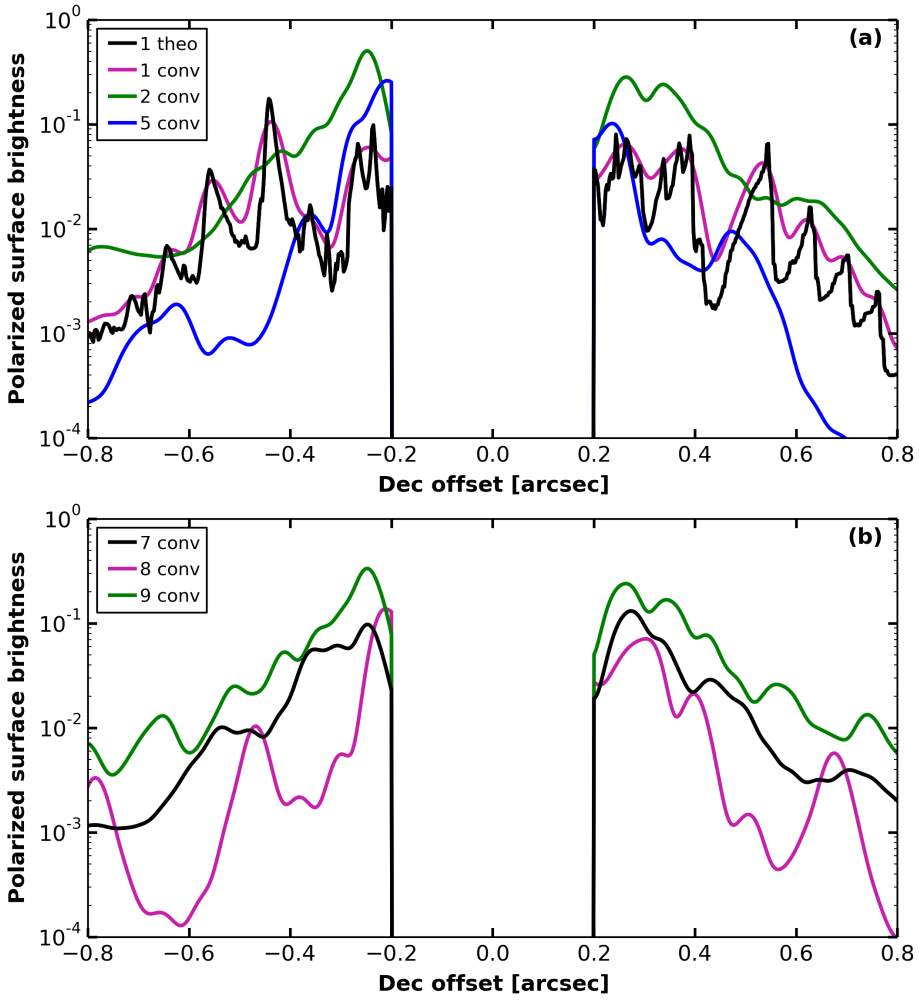

Figure 3.8: Radial profiles of the normalized polarized surface brightness belonging to the calculated images in Figs. 3.6 and 3.7, respectively. Since the focus is on measuring the contrast of the outer spirals, the profiles are only plotted beyond an inner circle with a radius of 0.″2.

sections in Fig. 3.8*a* illustrate that the clear wiggle structure from the models without self-gravity (magenta line) is smeared out (green line). Self-gravity forces the spiral close to the planet to be more tightly wound. This in turn reduces the total number of individual spiral windings seen in the scattered light, since they cannot be distinguished anymore. The contrast of the spiral with the surrounding disk varies between 1.5 to 10 for a resolution of 0.″04.

The effect of increasing the planet-to-star mass ratio is displayed in Figs. 3.6*d* and 3.7*b*. The absolute brightness near the planet is increased, leading to several bright spots. Moreover, the gap is not fully detectable anymore in the scattered light. The irregular structure close to the planet's position is caused by the perturbation in temperature (cf. Fig. 3.3*c,d*). Thus, this heating strongly increases the disk scale

height within the gap. This elevated region is now irradiated by the star hiding the gap in the scattered light image. At the same time structures characteristic of gravitational instability are visible. They occur as quite open spirals reaching also outer disk parts. The spiral contrast in the outer disk is extremely high with values of up to 40. A second possibility to create gravitational instability structures is a model with a disk that is gravitationally unstable from the beginning, i.e. no massive planet has to work as a trigger. The resulting scattered light image in Fig. 3.7*c* shows a quite symmetric spiral for the whole disk. The planet-induced spiral is only visible close to the planetary orbit and the outer disk is dominated by the spirals triggered by gravitational instability. For this model the polarized surface brightness in Fig. 3.8*b* has a clear wiggle structure (green line) with a brightness contrast of approximately three. This contrast is similar to the images from models without self-gravity, but a factor of ∼10 smaller than for a self-gravitating disk model with a massive planet ($10^{-2}\,M_\star$). This shows that the brightness contrast between the spirals and the contiguous disk is strongly influenced by the planet-to-star mass ratio in combination with the disk mass distribution. As soon as gravitational instability spirals triggered by a planet develop, the contrast increases tremendously, the spiral shape is strongly influenced and its pitch angle slightly increases.

Another feature to mention, which is present in all images, is the shadow of the planet along PA $= -90$ deg. This is just an artefact of our simulation methods, since we do 2D hydrodynamic, but 3D radiative transfer simulations. This means that a surface density enhancement, e.g. a circumplanetary ring, will increase the total density at all disk heights in the radiative transfer models. It is unlikely that even a circumplanetary disk around a massive planet with several tens of M_{jup} can cast a shadow over the whole outer disk in its full vertical extent. The shadow is expected to be seen in the midplane, but the disk atmosphere should remain nearly unaffected.

3.5 Discussion and summary

We present hydrodynamic simulations of planet-disk interactions considering viscous heating, cooling, and additionally self-gravity effects. Subsequently, the density and temperature structure resulting from these simulations are used for the follow-up radiative transfer modeling, in order to predict synthetic scattered light images from a protoplanetary disk around a typical Herbig Ae star. The focus is set on analysing the morphology and detectability of the main observational features of transition disks in scattered light observations, distinct gaps, and non-axisymmetric spiral arms. The conclusions of this work are as follows:

1. A clear $m = 2$ spiral structure, and in some cases even higher azimuthal wave number modes, can be excited by a single planet in a self-gravitating disk. The shape of the planet-induced spirals depends on the planet mass and disk parameters, such as the viscosity, and heating/cooling timescales.

2. When self-gravity of the disk is taken into account the planet-induced spirals are found to have a smaller pitch angle, making them more tightly wound. For sufficiently large disk mass, and therefore sufficiently strong self-gravity, the vortex modes are suppressed, and the strength of the spiral is enhanced considerably.

3. All our calculated polarized intensity images show a planetary gap and spiral arms with a variety of morphologies depending on planet mass, disk mass distribution, and the influence of the disk's self-gravity. Convolving the images with a circular Gaussian PSF with a FWHM of 0.″04 (typical for current 8-10m class telescopes) lowers the contrast by a factor of ~ 3, but the spiral features are still visible.

4. The scale height along the spiral increases due to the temperature changes, forming local bumps on the disk surface, and thus creating a signal in the reflected light. Therefore, the contrast in the images also depends on the cooling timescale via the $\beta_{\rm cool}$-factor. In a disk where the cooling is very efficient (i.e $\beta_{\rm cool} \lesssim 1$), which approximates the case of a locally isothermal disk, any temperature increase is immediately suppressed. The remaining density perturbation alone is not capable of producing a sufficiently strong spiral contrast in scattered light to be observable with current state-of-the-art telescopes (cf. Juhász et al., 2015).

5. Our result of a non-self-gravitating disk with an embedded planet shows that the combination of planet-induced density and scale height perturbation along the spiral due to shock heating is sufficient to achieve the contrast between the spiral and the contiguous disk necessary to be detectable in observations. The contrast values estimated for a resolution of 0.″04 are in a range from 3 to 10, which is consistent with the brightness contrast of spirals seen in recent observations.

6. There are two models in our series for which the Toomre parameter profiles allow the creation of spirals due to gravitational instability. However, their initiation mechanism is different in both cases. For model *9* the disk itself is massive enough, and the mass distribution allows it to be gravitationally unstable from the beginning of the simulation. Spirals are visible in the whole disk, a difference is, however, seen in the pitch angle between the spirals close to the planet and in the outer disk. The spiral is more tightly wound near the planet's position as it is driven by the planet, while the spirals in the outer disk are created by gravitational instability showing a larger pitch angle. A long-scale spiral with quite regular windings is visible in the corresponding scattered light image with a contrast of about three for a resolution of 0.″04.

7. The second possibility is a disk that is initially at the edge of being gravitationally unstable. As soon as a sufficiently massive planet is included, gravitational

instability can be triggered by this planet (model *8*). A spiral arm with a huge brightness contrast of ~ 40 and with a higher pitch angle than the spirals driven by a planet in a gravitationally stable disk is generated. The strong temperature perturbations near the high mass planet partly hide the low-density gap and dominate the irregular structures in this disk region.

To summarize, perturbations in the vertical structure of the disk, i.e. scale height perturbations caused by temperature variations due to planet-induced accretion heating or local heating by gravitational instability, are able to create the necessary spiral-background contrast seen in scattered light observations. The presence of a sufficiently massive planet embedded in a marginally gravitationally stable disk can lead to a variety of spiral morphologies depending on the planet and disk mass. It is possible to create a tightly-wound spiral close to the planet and a more open spiral arm in the outer disk. With our model setup there is either one dominant primary spiral in the outer disk when the planet is working as a trigger for gravitational instability, or higher mode spirals with similar contrasts are seen when the disk is already initially unstable. A second planet would be required in order to create two primary spirals of a $m = 1$ mode each or a $m = 2$ structure with nearly the same contrast. However, for this scenario the two planets would need to have just the right mass ratios and be located exactly at the right radial locations and azimuthal angles in the disk to cause symmetric spirals, making this scenario rather unlikely. Recently, Dong et al. (2015a) combined 3D smoothed-particle hydrodynamics and Monte Carlo radiative transfer calculations to study the morphology of spiral density waves solely induced by gravitational instability. They also conclude that high contrast, open spiral arms with azimuthal wavenumbers m between 2 and 8 induced by gravitational instability can be visible in NIR images for disk-to-star-mass ratios of $\gtrsim$0.25. However, the explanation of the origin of symmetric, double-armed spirals in transition disks remains challenging for scenarios of pure gravitational instability, outer spiral arms induced by a planet, or the combination of the latter two.

Other mechanisms apart from self-gravity may play a role for non-axisymmetric structure formation as well. We note that a caveat of our approach is that we do not perform fully consistent radiation hydrodynamics simulations, for example including the consistent release of accretion energy from the planet via radiation, since this is quite computational expensive for a parameter study. Long-term simulations in three dimensions that include these effects are needed to investigate the differences with our current results and for the direct comparison with observations. This will be addressed in future work (see Chapter 4). Additionally, we are aware that the cooling law from Gammie (2001), used also in most of the previous work about self-gravitating disks, is a simplified description. It has to be elaborated in order to calculate the disk temperature structure more precisely, which influences the local scale height changes, and thus also the brightness contrast in scattered light.

Recently, 3D global hydrodynamic simulations (isothermal and adiabatic, assuming a non self-gravitating disk) combined with radiative transfer calculations after a short-time of evolution (10–20 local orbits) have shown that inner spirals caused

by massive planets ($6\,M_{jup}$ at $\sim 100\,au$) can be visible at scattered light with similar pitch angle, extension and symmetry as observational results (Dong et al., 2015b, 2016b). However, at longer times of evolution when the disk reaches a quasi-steady state it is expected that such a planet opens a visible gap in the outer disk (100–200 au) contrary to observational results at NIR and (sub-)mm. The scenario of inner spiral arms and their observational signposts at different viewing angles for a target case study is further addressed in Chapter 4.

4 | The case of RY Lup: spiral arm modeling in a nearly edge-on transition disk

The content of this chapter is based on Langlois, Pohl, & The SPHERE consortium (2017) submitted to Astronomy & Astrophysics (A&A) and currently under revision. The observational data presented are part of the SPHERE guaranteed time observations (GTO) program and based on observations collected at the European Organisation for Astronomical Research in the Southern Hemisphere under ESO programs 097.C-0523(A) and 097.C-0865(A).

Details of authorship: The data reduction and other observational details will be published in Langlois, Pohl, & The SPHERE consortium (2017). I performed the radiative transfer modeling, wrote the text of this chapter, and made all the figures listed below. The hydrodynamic simulations have been performed in close collaboration with Hubert Klahr, who provided his TRAMP code.

4.1 Motivation

As mentioned in Sect. 1.2.3, stunning images of the scattering surfaces of transition disks have been taken in PDI mode at the optical and NIR. Among other non-axisymmetric features detected in these images, spiral structures are of particular interest because of their possible connection to planets-disk interactions (cf. Chapter 3). While they have been so far only detected in disks around the more luminous Herbig Ae/Be stars, there are now also hints for a spiral structure in T Tauri stars.

4.1.1 The target: RY Lup

One of these highly topical targets is the system RY Lup, a T Tauri G-type star surrounded by a circumstellar disk, which has been identified from its SED (Manset et al., 2009). The mass of RY Lup is estimated to $1.4\,M_\odot$, with an age of 12 Myr (Manset et al., 2009). Its distance was recently revised to (151 ± 51) pc from Gaia measurements (Gaia Collaboration et al., 2016). Ansdell et al. (2016) present high

resolution 890 μm observations and CO $J = 3 - 2$ line emission of RY Lup as part of the large ALMA Lupus survey. The mm dust continuum shows a clearly resolved dust ring with a cavity diameter of 0.″8 (∼120 au), which classifies it as a transition disk. The sub-mm continuum flux is used as a proxy for the dust mass, constraining it to 0.2 M_{jup}. CO isotopologue emission (^{13}CO and C^{18}O $J = 3 - 2$) gives a gas mass estimate of 2.5 M_{jup}. Considering the uncertainties in these measurements, the gas-to-dust ratio lies in the range between 5 to 50, significantly below the canonical ISM value. As already discussed, a lot of error sources can be induced in these calculations and especially the gas mass estimate is questionable and may be underestimated due to the assumption of an ISM-like abundance. Manset et al. (2009) explained photometric and polarimetric variabilities of RY Lup by an almost edge on circumstellar disk that is warped close to the star. This makes the system a very interesting target for polarimetric imaging, since this technique is a powerful tool to constrain the properties of the dust grains. Edge-on disks are particularly suitable to detect dust settling.

4.1.2 SPHERE observations

As part of the SPHERE disk GTO RY Lup has been detected in scattered light for the first time. High contrast polarimetric images were obtained with The Infra-Red Dual-beam Imager and Spectrograph (IRDIS, Dohlen et al., 2008) in Dual-band Polarimetric Imaging (DPI, Langlois et al., 2010) at BBH filter (1.625 μm) using the apodized pupil Lyot coronagraph (N-ALC-YJH-S). The disk appears as a dominant double-arch structure in southeast (SE) to northwest (NW) direction covering a spatial extension of ∼1.0″ (Fig. 4.1). This has been also recently reported for other high contrast transition disk imaging with SPHERE (e.g., Garufi et al., 2017a; Janson et al., 2016; Pohl et al., 2017, cf. Chapter 6). The disk appearance supports a high disk inclination with respect to the line of sight (> 70 deg), with a PA of ∼107 deg. A spiral-like feature branching off the arc structure is seen in the SE, and an additional faint spiral piece is visible on the opposite disk side. A possible explanation for these features is the gravitational interaction of the disk with a planetary companion located within or in the surrounding of the system. Detailed numerical hydrodynamic simulations in the context of planet-disk interaction combined with radiative transfer calculations are performed to study the disk morphology and this hypothesis.

4.2 Physical disk modeling

Our physical disk modeling aims to reproduce the polarized intensity, the orientation of the polarization vectors, and the two faint spiral arms observed on the SE and SW sides in the SPHERE polarimetric images. This requires the loss of disk symmetry, which could be explainable by planet-disk perturbation dynamics. Thus, it is tested whether the spiral pattern triggered by a Jupiter-like planet could eventually result in the scattered light features that are detected around RY Lup, assuming that its

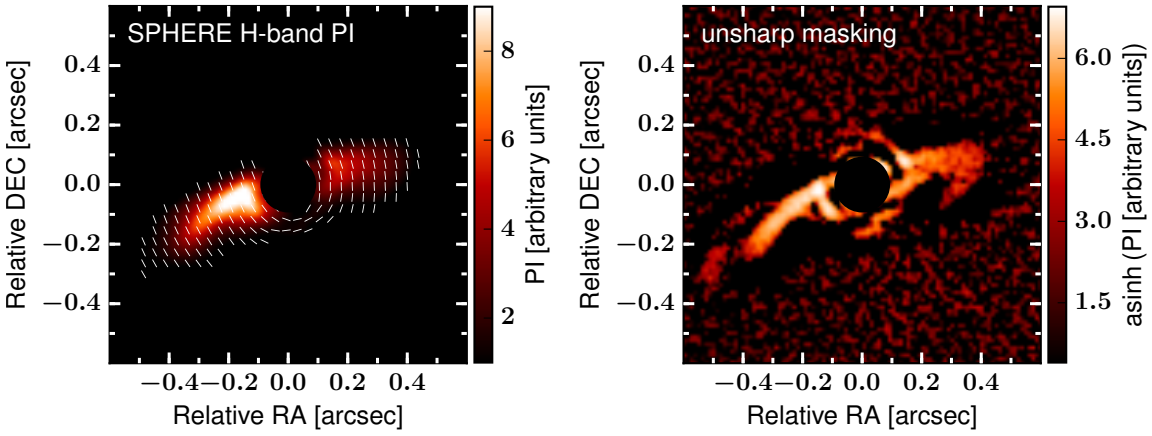

Figure 4.1: *Left:* SPHERE/IRDIS polarized intensity image showing the close environment of RY Lup. The white stripes represent the angle of linear polarization (fixed length, not scaled with the degree of polarization). The color scale units are arbitrary. *Right:* unsharp masking of the polarized intensity image in order to enhance the disk structure. The intensity scale follows the inverse hyperbolic sine for visualization reasons. North is up, east is left.

disk is seen close to edge-on. For this purpose, 3D global numerical hydrodynamic simulations are carried out to study the morphology of spiral arms excited by an outer planetary perturber. Using detailed 3D follow-up radiative transfer models synthetic scattered light images are produced for a highly inclined disk configuration at NIR wavelength. This modeling approach is motivated by recent work on spiral arms in the context of scattered light by Dong et al. (2015b, 2016a); Juhász et al. (2015); Pohl et al. (2015).

4.2.1 Hydrodynamical planet-disk simulations

The hydrodynamical code TRAMP (Three-dimensional RAdiation-hydrodynamical Modelling Project, Klahr et al. 1999) is used in its extended version (Klahr & Kley 2006), which applies a flux-limited diffusion approximation for the radiation. A giant planet embedded in a fully viscous disk is considered, where the consistent release of accretion energy from the planet via radiation is included. The disk model considers a spherical polar coordinate system (r, θ, ϕ), where the disk midplane coincides with the $\theta = 0$ plane. The number of grid cells in the radial (r), polar (θ), and azimuthal (ϕ) directions are 64, 31, and 89, respectively. The computational disk grid has a radial extent from $\sim$18 au to 235 au. The complete set of vertical disk structure equations is solved self-consistently, including both viscous dissipation and heating by irradiation from the central star (cf. D'Alessio et al. 1998). This results in detailed profiles of the density and temperature structure with vertical height and disk radius. Thus, it allows to determine the 3D temperature structure of the disk at each step of the planet-disk interaction processes. More precisely, the initial 3D data set, before adding the planet, is determined from a set of 1D vertical structure models

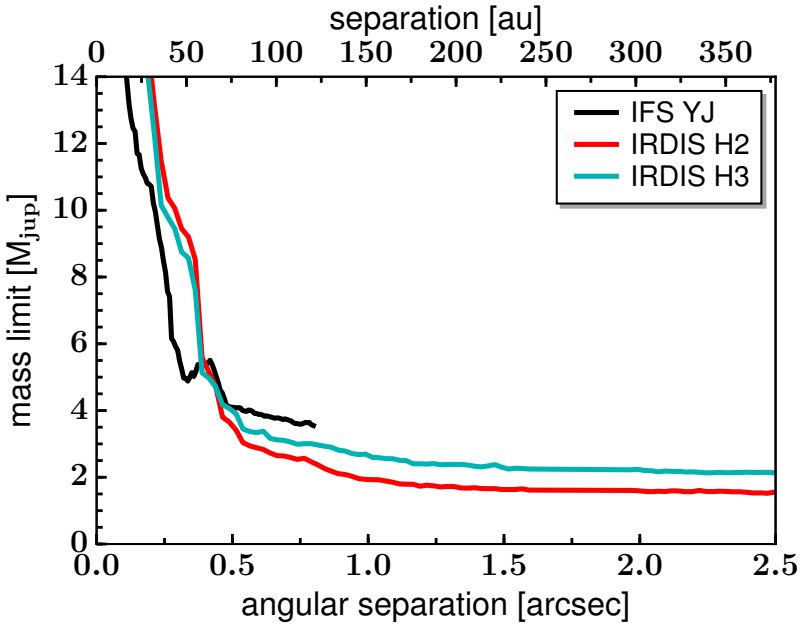

Figure 4.2: Companion mass limits derived for IFS (black curve) and for IRDIS *H2* and *H3* bands (red and cyan curves, respectively). The details of the derivation and reduction methods used can be found in Langlois et al. (2017).

for a given accretion rate (that will result in the desired total disk mass). Thus, the dynamical viscous evolution in the 3D radiation hydrodynamic simulation of the disk will not alter significantly the initial global gas distribution, but any development of structure in the 3D simulations is the result of the torques exerted by the planet. It is made sure that the 1D and 3D models use the same parameters including the dust opacities and α-viscosity. A central stellar mass of $M_\star = 1.4\,\mathrm{M}_\odot$, a radius of $R_\star = 1.72\,\mathrm{R}_\odot$, and an effective temperature of $T_\mathrm{eff} = 5669\,\mathrm{K}$ are assumed. These parameters are consistent with properties of RY Lup derived by a piecewise linear interpolation of the values from Manset et al. (2009) assuming an object's distance of 151 pc (Gaia Collaboration et al., 2016). Furthermore, the input parameters for the viscosity parameter and the mass accretion rate are chosen to be $\alpha = 10^{-3}$ and $M_\mathrm{accr,0} = 3.3 \times 10^{-10}\,\mathrm{M}_\odot\,\mathrm{yr}^{-1}$, respectively. The latter is rather low compared to typical values for T Tauri disks, but a natural outcome of the disk bulk mass considered. The accretion rate is calculated such that the disk gas mass corresponds to $M_\mathrm{disk} = 2.5 \times 10^{-3}\,\mathrm{M}_\odot$, distributed between an inner disk radius of $r_\mathrm{in} = 18\,\mathrm{au}$ and an outer disk radius of $r_\mathrm{out} = 123\,\mathrm{au}$, as measured by Ansdell et al. (2016).

The position of a possible planetary perturber is uncertain, but spiral arms exterior of a planet are unlikely to explain the observations as they are too tightly wound given typical disk scale height values (Juhász et al., 2015; Pohl et al., 2015). However, a location further out in the disk is compatible with the outer disk radius in the ^{13}CO ALMA emission map. Furthermore, the mm dust continuum suggests a truncation at ∼120 au and a depletion of large dust beyond (Ansdell et al., 2016). Following

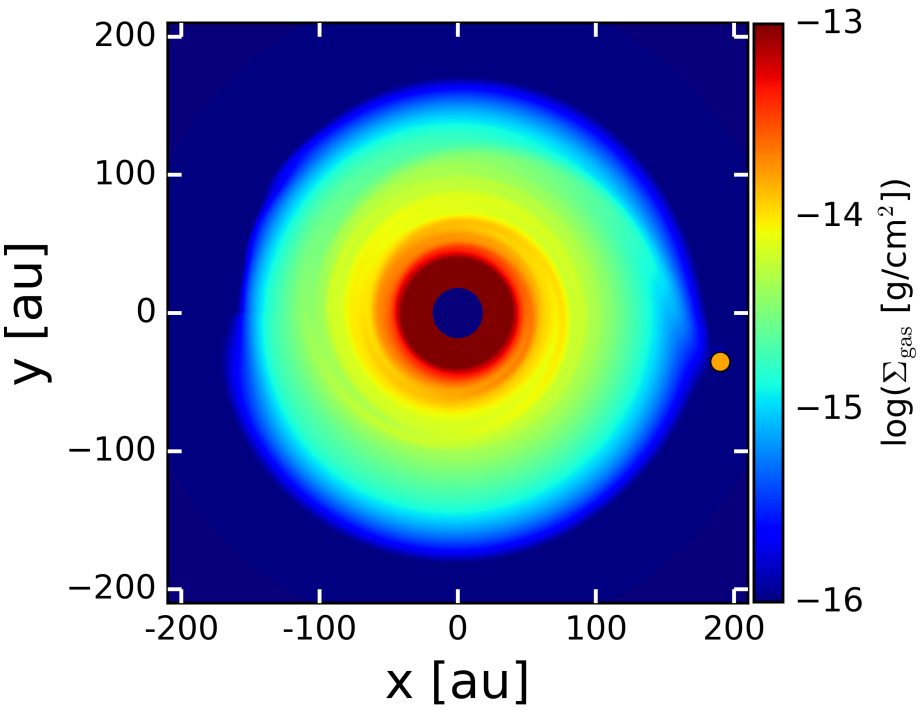

Figure 4.3: Simulated 2D vertically integrated density map for a planet-induced spiral wave considering a planet-to-star mass ratio of 1.4×10^{-3}. The orange dot highlights the position of the planet.

the approach by recent spiral arm models (Dong et al., 2015c), the planet can be roughly located at a distance three times the location of the inner arms. Thus, a planet located at 190 au is considered, that is outside of the disk radius in both scattered light and thermal emission. Given that the planet carves out a wide gap in the disk, this location is a justified assumption. We assume a fixed circular orbit, although spiral density waves may be also excited by a companion on an eccentric orbit. The mass of the embedded giant planet is considered to be $M_{\rm p}/M_{\star} = 1.4 \times 10^{-3}$ ($\sim$2 $M_{\rm jup}$). This mass is restricted by the mass detection limits for planetary companions obtained from our SPHERE contrast curves. Figure 4.2 shows that the upper mass limit at an angular distance of $\sim$1.1″ is $\sim$2 $M_{\rm jup}$. It is worth noting that the mass limit is model dependent and slightly higher if a warm start model is assumed ($\sim$5 $M_{\rm jup}$) (Marley et al., 2007; Spiegel & Burrows, 2012). It is also worth mentioning that a planet might be at a location behind the disk or might be geometrically close to the central star, where it could remain undetected. Hence, it is geometrically likely to have a projected separation less than $\sim$1.1″, at which a higher planet mass would be possible according to Fig. 4.2. However, our choice of a lower planet mass is thus conservative, which is reasonable given the uncertainties in the age of the system and in the atmospheric/evolutionary models used to estimate the mass detection limits. The planet-disk features, especially the contrast between spirals and the background disk, would be even stronger for higher planet masses

(cf. Dong et al., 2015c; Pohl et al., 2015). The simulation is run for 90 orbits at 190 au ($\sim$1.8$\times$10^5 yr), which is sufficiently long for the inner spiral arms to reach a quasi steady state, although this evolutionary time scale would be not enough to carve out a full gap around its orbit. This is, however, reasonable for our modeling purpose since the planet is located outside the disk and we are mainly interested in the observational appearance of the spiral arms.

A map of the surface density $\Sigma_{\rm gas}$ after an evolutionary time of 90 orbits at 190 au is shown in Fig. 4.3. While the planet always excites inner and outer waves, we concentrate here on the $m = 2$ spiral arm configuration inward of the planet's position at 190 au. The primary arm originates from the planet location, the secondary is shifted by $\sim$180° in the azimuthal direction. The density contrast of the secondary spiral wave with respect to the background disk is weaker compared to the primary one.

4.2.2 Radiative transfer models

The resulting 3D disk density presented in Sect. 4.2.1 and the simulated temperature structure are subsequently fed into the Monte Carlo radiative transfer code RADMC-3D developed by Dullemond et al. (2012). To convert the gas density to the dust density used in the radiative transfer calculations, a gas-to-dust ratio of 50 is adopted, which is lower than the canonical ISM value as suggested by the ALMA Lupus survey of Ansdell et al. (2016). For the dust opacity calculation a species mixture of silicates (60%), carbonaceous (30%) and icy (10%) material is considered, where the optical constants are taken from Draine (2003); Zubko et al. (1996); Warren & Brandt (2008). Two different grain size populations are assumed, small (0.01–1 μm) and large (1 μm–1 mm) grains, where each size distribution is a smooth power law with exponent -3.5. The mass ratio between the two populations is determined such that the number density follows $n(a) \propto a^{-3.5}$. Thus, the large fraction of mass is in the big grains ($\sim$95% of total dust mass), but the small grains dominate the opacity at NIR wavelengths. It is assumed that the gas and the small dust is well mixed, thus, their dust scale height is equal to the pressure scale height. We are aware that this choice will not reproduce the scattering colors of the disk, but our model approach focuses on the morphology of the image.

The stellar parameters for the radiation source as well as the radial disk extension are taken to be the same as in the hydrodynamical calculations. For the polar and azimuth a finer grid sampling is used with $\mathrm{N}_\phi = 192$ and $\mathrm{N}_\theta = 64$, and interpolate the density and temperature array values accordingly. All scattering MC simulations are run with 5×10^8 photon packages. Multiple scattering effects are considered and images for all four Stokes components are produced, from which the total intensity and linearly polarized intensity images are calculated at H-band (1.625 μm). The polarization of RADMC-3D was investigated by Kataoka et al. (2015), who performed a benchmark test against the numerical models presented in Pinte et al. (2009). The disk orientation is set by the inclination angle (0° is face-on) and the PA (from north to east). The theoretical radiative transfer images are convolved by the instrument

PSF with a FWHM of 0.″04, such that it mimicks the angular resolution of the data.

4.3 Results

4.3.1 Synthetic scattered light images

The convolved H-band polarized intensity image for our planet-disk interaction model in the RY Lup system is shown in Fig. 4.4. The disk is inclined by 75 deg with respect to the line of sight and rotated by a PA of 107 deg relative to the disk major axis. We note that we ran a grid of models for inclinations between 70 and 80 deg in steps of 1 deg, where the data is best represented by an inclination of 75 deg. This is consistent with the measurement from total intensity given the uncertainties. For such a highly inclined system, the symmetric two spiral arms produced by the external planetary perturber and known from face-on disk configurations can have a completely different morphology in scattered light (cf. Dong et al., 2016a). The spiral arms ($m = 2$ mode) rather appear as two arms located along the major axis at the top (illuminated) side of the disk (cf. sketch in Fig. 4.5). There is also a substructure branching off the SE spiral, possibly a second winding of the $m = 2$ spiral density wave, but in the convolved synthetic image it is not as pronounced as in the observed PDI image. Both spiral arms have an almost equal brightness contrast in the scattered light image. This result is consistent with a parametric study by Dong et al. (2016a) on how spirals driven by companions can appear in scattered light at arbitrary viewing angles.

4.3.2 Polarimetric comparison

Our disk model leads to a qualitatively good match with the IRDIS polarimetric image from Fig. 4.1. The bright double-arch structure in the SE-NW direction extending to 0.53″ in radius to the NW is well reproduced and corresponds to scattered light from the top side of the disk. The model also confirms that the disk must have a high inclination with respect to the line of sight. In addition to these bright components the two fainter spiral-like features on the SE direction, which break off, are also reproduced. Due to the multiple disk and planet parameters to adjust in these models and due to the high inclination of the disk, there is no perfect match of the brightness ratios between the east and west sides, and the bright and fainter features of the disk. In fact, for such a highly inclined system, the symmetric two spiral arms generated by the external planetary perturber have very different morphology in scattered light with the viewing angle.

Figure 4.4 shows our polarized intensity model for RY Lup overlaid with linear polarization vectors. Note that all vectors have the same length as the main interest lies in the polarization orientation. As also detected in the IRDIS polarimetric image (Fig. 4.1) it is noticeable that the polarization signal along the minor axis deviates from the azimuthal direction. Since the polarization angle is indeed more

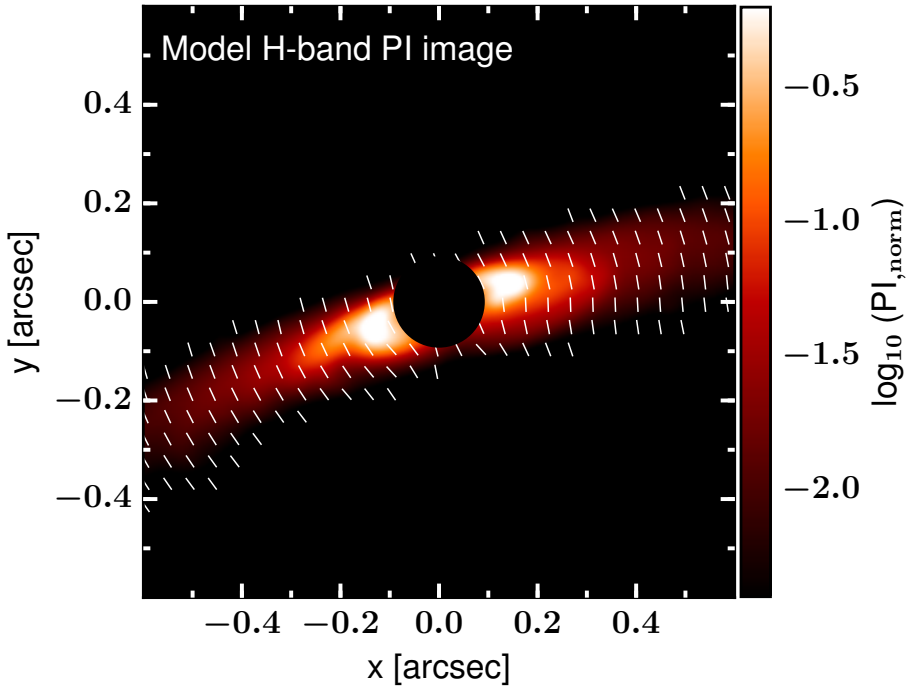

Figure 4.4: Convolved polarized intensity H-band image considering a planet-induced spiral model with $M_\mathrm{p}/M_\star = 1.4 \times 10^{-3}$. The image is produced at an inclination of 75 deg, and a PA of 107 deg. The inner 0.″18 are masked, represented by the black circular area, to mimic the coronagraph region. The white stripes represent the angle of linear polarization (fixed length, not scaled with the degree of polarization).

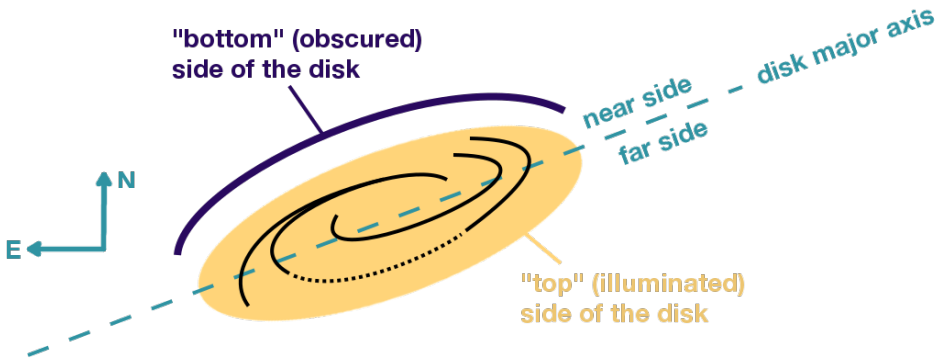

Figure 4.5: Sketch of the disk model suggested by the observations and the modeling. North is up, east is toward the left. The major axis of the disk is indicated by the dashed line and divides the disk into a near and far side. The top (illuminated) and bottom (obscured) halves are separated by the disk midplane.

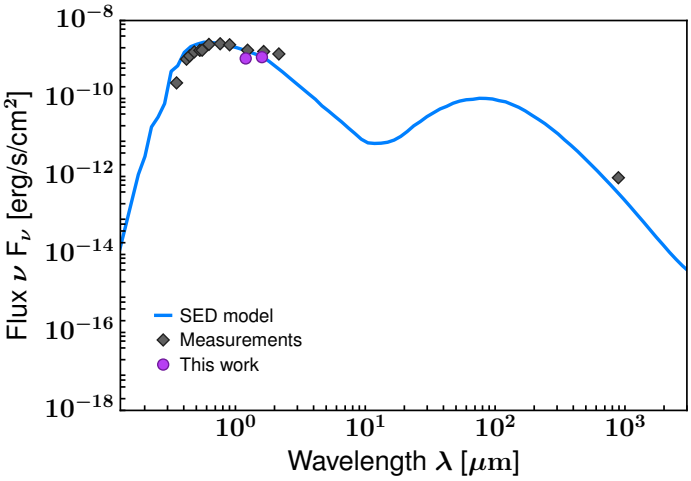

Figure 4.6: Synthetic SED from the radiative transfer model compared with direct measurements obtained with SPHERE IRDIS and IFS in violet (this work), Very Large Telescope Interferometer (VLTI)/PIONIER (Anthonioz 2015) and ALMA (Ansdell et al., 2016) in gray.

complicated than expected for single scattering, the U_ϕ signal must be physical and connected to multiple scattering, which is as well included in our radiative transfer calculations.

4.3.3 Spectral energy distribution

The SED model based on our hydrodynamic simulation compared to the observed photometry is shown in Fig. 4.6. The stellar spectrum is taken from the Castelli-Kurucz atlas (Castelli & Kurucz, 2004), choosing the model for a stellar type of G8V ($T_{\rm eff} = 5500\,{\rm K}$), and a surface gravity of $\log g = 4.5$. The flux measurements from VLT Interferometer (VLTI)/PIONIER and SPHERE/IRDIS/IFS hint at a strong NIR excess expected for a disk around a young star. Although our model lies within the measurement uncertainties of the SPHERE data points, there is a clear trend that it underestimates the fluxes between ∼5 and ∼50 μm. This can be explained by the fact that our model only considers the dust disk from our hydrodynamic simulations with a radial grid starting at $R_{\rm in} = 18\,{\rm au}$. The inner disk region is hidden behind the coronagraph for our SPHERE data, so there is no strong constraint on the geometry and orientation of an inner dust belt or halo. This makes the modeling of the inner disk regions very degenerate, and thus, in our model there is no dusty material close to the star. In general, the inner radius regulates the maximum temperature of the dust grains at the inner rim. For larger $R_{\rm in}$ the luminosity excess shifts from the NIR to the MIR (see e.g., Woitke et al., 2016). Exploring a larger grid of dust and disk structure parameters is beyond the scope of this work as we did not attempt to do a detailed fit of the SED. In general, it can be concluded here that there must be a significant amount of dusty material within ten au from the central star, but its

spatial distribution remains to be investigated in future observational and modeling studies.

The photometric point in the mm regime is well reproduced with our simulated flux. Due to the absence of additional photometric points in the (sub-)mm, the mm slope fit cannot be evaluated. For example, the dust size distribution power-law index (in our case a typical value of 3.5 is chosen for both populations) changes, in particular, the mm and cm slopes. Although our current model indicates a good disk mass estimate, this situation might change when additional dust is included into the inner disk regions in order to fit the NIR/MIR fluxes. The underestimation of this emission could result in a slight error in dust temperature and request a higher disk mass. This is certainly compatible with the disk mass estimate from Ansdell et al. (2016) as this value only gives a lower limit.

4.4 Summary

The scattered light from the nearly edge on protoplanetary disk around RY Lup is resolved and modeled in terms of planet-disk interactions for the first time. It has been shown that the observed disk morphology can be interpreted as spiral arms originating from a planetary companion. As seen in the previous Chapter 3, a planet scenario where it is simultaneously accounted for the inner gap/cavity and spirals is not likely. Thus, the planetary perturber is here placed outside of the disk, exterior to the spiral arms, where no scattered light is detected anymore. This hypothesis on the origin of the spiral-like features in RY Lup remains to be tested. However, given the high inclination of the disk, it is unlikely that the planet's thermal radiation is directly detectable. The planet-disk interaction scenario is in agreement with the ALMA dust continuum image, which shows a truncation at 120 au. Although the modeling effort does not fully resemble the observational scales, it helps to understand the disk structure and in particular, the distribution of small grains. Having the SPHERE data set as the only high resolution observations in hand, it is not possible to pin down a unique explanation for the spiral arms, especially due to the high disk inclination with respect to the line of sight.

5 | Shadows and spirals in the protoplanetary disk HD 100453

The content of this chapter is based on Benisty, Stolker, Pohl, de Boer, Lesur, Dominik, Dullemond, Langlois, Min, Wagner, Henning, Juhasz, Pinilla, Facchini, Apai, van Boekel, Garufi, Ginski, Ménard, Pinte, Quanz, Zurlo, Boccaletti, Bonnefoy, Beuzit, Chauvin, Cudel, Desidera, Feldt, Fontanive, Gratton, Kasper, Lagrange, LeCoroller, Mouillet, Mesa, Sissa, Vigan, Antichi, Buey, Fusco, Gisler, Llored, Magnard, Moeller-Nilsson, Pragt, Roelfsema, Sauvage, & Wildi (2017) published in *2017, A&A, 597, A42*. The observational data presented are part of the SPHERE GTO program and based on observations collected at the European Organisation for Astronomical Research in the Southern Hemisphere under ESO program 096.C-0248(B).

Details of authorship: Myriam Benisty is the main author of the paper Benisty et al. (2017), Jos de Boer produced the final DPI reduction products, and Tomas Stolker is responsible for the final radiative transfer model. The general idea for the semi-analytical model was suggested by Cornelis Dullemond, and extended during several discussions with him. I set up the model for HD 100453, and wrote the corresponding text below.

5.1 Motivation

5.1.1 The target: HD 100453

As described in Chapters 3 and 4 spiral structures have recently been observed in a significant number of disks (about half a dozen), mostly in scattered light by imaging the distribution of small grains at NIR wavelengths, and typically in the late stage of their evolution. Of particular interest for this chapter is HD 100453 A (hereafter HD 100453), a Herbig A9Ve star with a mass of $1.7\,M_{\odot}$ and an estimated age of 10 ± 2 Myr (Collins et al., 2009). It is located in the Lower Centaurus Association (Kouwenhoven et al., 2005), at a distance of $\sim103\pm3$ pc (Gaia Collaboration et al., 2016). VLT/NACO observations identified an early-M dwarf companion, HD 100453 B, (Chen et al., 2006), whose properties were further constrained by Collins et al. (2009). It is an M4.0 - M4.5V star with no detectable NIR excess, has

a mass of $0.20\pm0.04\,M_\odot$, and is located at $1.045''\pm0.025''$ (i.e., $\sim$108 au) at a PA of $126\pm1°$. HD 100453 was classified as a Group I (flared) disk by Meeus et al. (2001). It is rather compact compared to other Herbig Ae disks. Furthermore, the star is not actively accreting, with an upper mass accretion rate limit of $1.4 \times 10^{-9}\,M_\odot$/yr and $4.9 \times 10^{-9}\,M_\odot$/yr, respectively (Collins et al., 2009; Fairlamb et al., 2015). Collins et al. (2009) reported a non-detection of CO $J = 3 - 2$ with the JCMT, which indicates that the gas in the outer disk is likely optically thin. Assuming a [CO]/[H2] abundance of 10^{-4} and a depletion factor of 10^3, they find a cold molecular gas mass smaller than $\sim3.2\times10^{-4}\,M_\odot$.

5.1.2 Observations

HD 100453 was imaged by the Hubble Space Telescope (HST), but in this data no scattered light is detected beyond 0.″5 indicating the compactness of the disk (Collins et al., 2009). Recent SPHERE/VLT observations in differential imaging mode marginally detect a gap or cavity inside 0.″18, resolve a ring of emission from 0.″18 to 0.″25, and reveal a two-armed spiral structure in a disk extending to 0.″37 from the star (Wagner et al., 2015a).

In Benisty et al. (2017) we present the first polarized differential images of HD 100453 in the optical (R'- and I'-bands, 0.6 μm and 0.8 μm) and in the NIR (J-band, 1.2 μm) obtained with the VLT/SPHERE instruments ZIMPOL (Zurich IMaging POLarimeter, Thalmann et al., 2008; Schmid et al., 2012) and IRDIS, respectively. The data have an IWA of $\sim$0.″09, and the AO quality reaches a diffraction-limited regime such that the angular resolution is $\sim$0.″02. The polarized intensity Q_ϕ images reveal a number of disk features (Fig. 5.1, left panel). Polarized scattered light is detected up to 0.″42. An inner gap, an inclined ($\sim$38 deg) ring with azimuthal brightness variations and two shadows, and two symmetric spiral arms are detected. Interestingly, the shadows are located in the proximity of the spirals' launching points, which are close to the disk semi-major axis. GPI polarized intensity images of HD 100453 in Y-, J-, and $K1$ bands reveal similar disk features (Long et al., 2017b).

Figure 5.2 shows an azimuthal cut of the I' Q_ϕ image, after averaging across the rim width (0.″17-0.″20). The error bars are estimated as the standard deviation in each bin in the U_ϕ image. A maximum ratio of (radially averaged) polarized surface brightness of $\sim$5 between the shadows and the brightest regions of the rim is measured.

Shadows in transition disks are commonly interpreted as signs of a misaligned inner disk (e.g., Marino et al., 2015; Stolker et al., 2016). However, these disks often have the form of tiny dust belts close to the star, and thus, are not detectable with current high contrast imaging facilities. The properties of the shadows (location, width, contrast) as well as NIR interferometry give hints for the inner disk geometry (Min et al., 2017; Lazareff et al., 2017). A radiative transfer model is performed for HD 100453 (see Sect. 4 of Benisty et al. (2017) for the details), that reproduces the

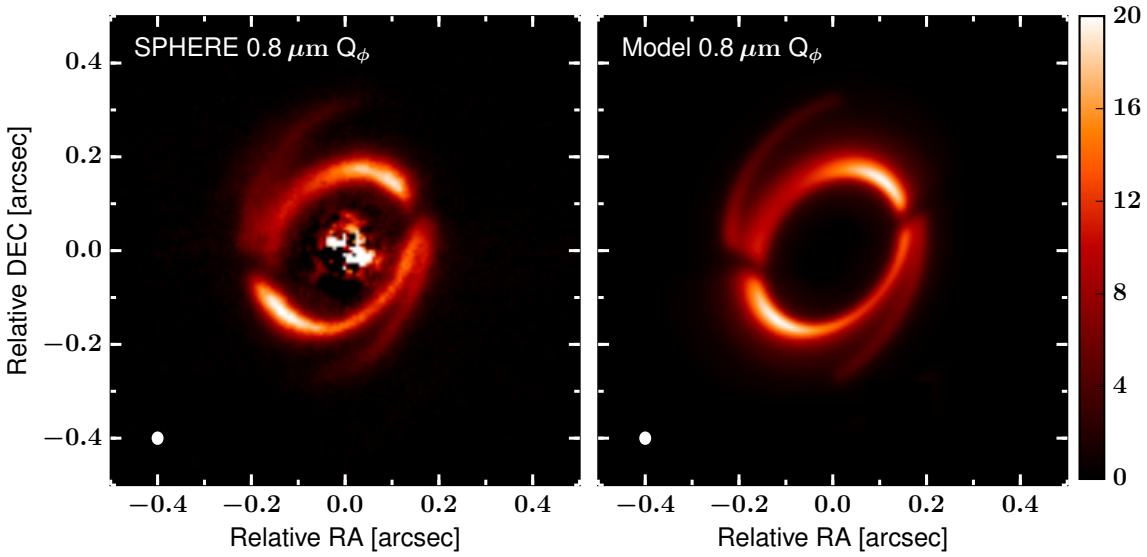

Figure 5.1: *Left:* SPHERE/ZIMPOL I' Q_ϕ polarized intensity image. The inner bright region corresponds to saturated pixels inside the IWA. North is pointing up, east is pointing left. *Right:* Synthetic I' Q_ϕ image from the best radiative transfer model. The dynamical color range of both images is the same, but the units are arbitrary.

main characteristics of the rim, the shadows, and the spirals seen in the scattered light image. The right panel of Fig. 5.1 shows the synthetic I' Q_ϕ image resulting from this radiative transfer calculation. The shadows are generated by an inner disk that is misaligned by 72 deg with respect to the outer disk. Their shape depends on the aspect ratio of the inner disk, and on the width and edge shape of the outer disk rim. In principle, the strong azimuthal brightness variations observed along the rim can be reproduced by the scattering phase function, but could be amplified by hydrodynamical consequences of the pressure loss in the two shadow blobs. This scenario will be described in the following.

5.2 1D model of shadow-induced scale height variations

5.2.1 Idea and methods

As discussed in Sect. 5.1.2, an inner disk that is considerably tilted with respect to the outer disk region casts two point-symmetric shadows onto the outer disk. Furthermore, there is an asymmetry in the brightness along the ring on each side of the dark shadow, where the brighter part is on the other side of where the spiral is seen. To investigate these azimuthal brightness variations and the origin of the spiral arms in HD 100453 we develop a one-dimensional (1D) semi-analytical model along a circular ring and calculate the hydrodynamical consequences of the periodic

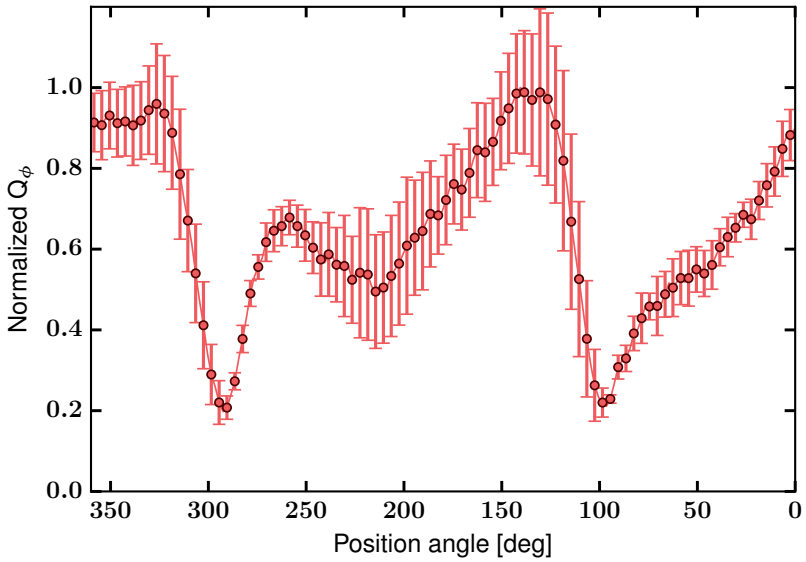

Figure 5.2: Normalized azimuthal cut of the SPHERE/ZIMPOL I' Q_ϕ image, after averaging radially between 170 and 200 mas.

pressure loss at the shadows' locations. It is examined whether this causes sufficient modulation of the disk scale height, which in turns can trigger spiral waves similar to the ones in the scattered light image of HD 100453.

At a given radius while orbiting the star, the gas periodically goes from an illuminated region, with large irradiation, to one with negligible irradiation heating (the shadow). Assuming that the cooling and heating timescales are shorter than the dynamical (orbital) timescale, the gas temperature and pressure are lower in these shadowed regions. As the pressure support of the gas fails, the gas falls towards the midplane, reducing the scale height. Upon exiting the shadow, the gas is heated again, causing the column to expand vertically. We apply Newton's second law of motion to H, the pressure scale height. Taking the vertical hydrostatic balance equation in the disk as a starting point, but assuming the scale height H to be a time dependent dynamic quantity, we follow the evolution of a Gaussian gas parcel along an azimuthal ring obeying

$$\frac{\mathrm{d}^2 H(t)}{\mathrm{d}t^2} = -\underbrace{\Omega_\mathrm{K}^2 H(t)}_{1} + \underbrace{\frac{c_\mathrm{s}(t)^2}{H(t)}}_{2} - \underbrace{\Gamma \frac{\mathrm{d}H(t)}{\mathrm{d}t}}_{3}, \tag{5.1}$$

where Γ describes a damping factor. This represents a second order equation similar to that of a driven damped oscillator, which has to be integrated several periods in order to achieve a periodic solution. The right hand side of Eq. 5.1 can be divided into three terms:

Term (1):
This is an externally applied driving force which periodically changes the sound speed along the ring assuming instant heating and cooling. This way the friction force (3) can be balanced and the scale height variation can be maintained. The external force determines the steady state solution from Eq. 1.8 ($\hat{=}$ particular solution to the inhomogeneous differential equation of a driven oscillator).

Term (2):
This is a restoring force that is dependent on the gas parcel's scale height and the angular Keplerian velocity leading to the following behavior of the scale height. Within the shadow there is no gas pressure support, so that the gas falls (in free fall) towards the midplane, which reduces the scale height. When the gas exits the shadow region again, it is instantaneously heated allowing the scale height to increase again.

Term (3):
This is a damping term linearly dependent on $\mathrm{d}H(t)/\mathrm{d}t$ accounting for the loss of energy, where a damping coefficient Γ is used to characterize the strength of the damping force. The damping factor Γ determines the time for the solution to reach a steady state, where Γ is assumed to be in the order of the dynamical time scale $1/\Omega_{\mathrm{K}}$.

The parcel of gas periodically enters and exits the shadowed regions, where the sound speed drops considerably. Hence, the latter is a time dependent function, where time can be converted into the azimuthal position ϕ along the ring via

$$\phi = \Omega_{\mathrm{K}} t\,. \tag{5.2}$$

For simplicity, instant cooling and heating are assumed, so we take the sound speed to be a step function

$$c_{\mathrm{s}}(\phi) = \begin{cases} c_{\mathrm{s,max}} & \text{for} \quad |\cos(\phi)| \geq w \\ c_{\mathrm{s,min}} & \text{for} \quad |\cos(\phi)| < w \end{cases}, \tag{5.3}$$

where w determines the width of the shadow. We choose $c_{\mathrm{s,min}}/c_{\mathrm{s,max}}$=0.6, as computed from the temperature in the shadows in our best radiative transfer model. We also compute the extreme value of $c_{\mathrm{s,min}}/c_{\mathrm{s,max}}$=0.

The left panel of Fig. 5.3 illustrates the assumed sound speed profile from Eq. 5.3 (dashed lines) and the modeled disk scale height (solid lines) for a single orbital period (i.e., two periods in the oscillation because of the two shadows). Note that the disk scale height is plotted against the azimuthal angle ϕ, which increases in the clockwise direction to match the observed locations of the bright regions along the rim.

Just before entering the shadow, that means moving from high to low pressure,

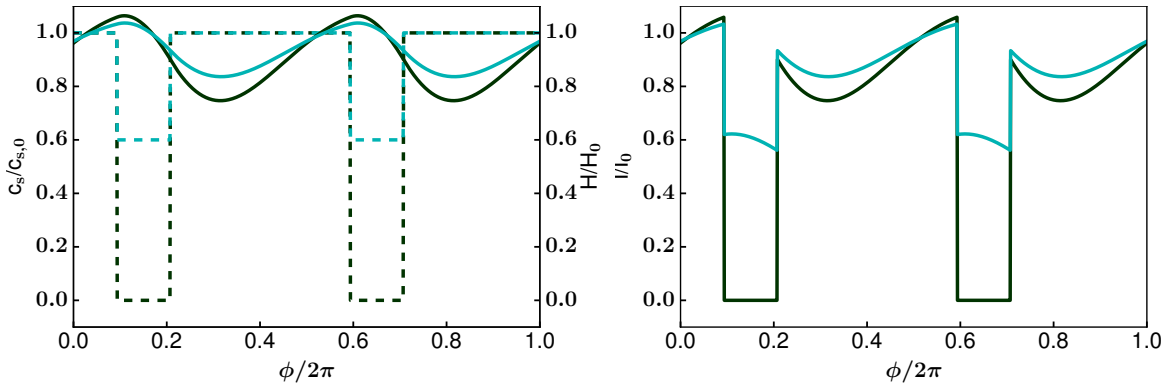

Figure 5.3: *Left:* Isothermal sound speed profile (dashed) and scale height of the disk as a function of azimuthal angle along the ring (solid). *Right:* The resulting scattered light brightness as a function of azimuth at the inner rim of the outer disk. All quantities are normalized, the comoving time increases toward the right.

the disk scale height reaches a peak height and increases above the initial value due to the inertia of the material. Within the shadowed region the gas experiences an acceleration leading to the downward curvature of the solution. As it exists the shadow and re-emerges, the sudden deceleration allows the scale height to eventually increase again.

5.2.2 Estimation of scattered light brightness

A variation in scale height changes the amount of stellar radiation intercepted by the disk and, at these locations, the rim scatters more stellar light and appears brighter. The width of this brightened region is related to the sound speed variation inside and outside of the shadows, and to the damping parameter. This leads to an asymmetric brightness distribution along the rim, the amplitude of which is determined by the pressure difference between shadowed and illuminated regions. To approximately estimate the effect on the scattered light brightness, it is assumed that the brightness varies proportionally to the scale height. We multiply the scale height by the incoming radiation of the star, neglecting the effects of inclination and scattering angle (Fig. 5.3, right panel). The idea is to consider a transition disk, which is the case for HD 100453, where the inner rim of the outer disk is directly illuminated in its full vertical extent. It is perfectly fair to only concentrate on the inner rim of the outer disk, since regions even further out in the disk only receive grazing radiation, so the far reaches of the shadow can be ignored. We find a maximum amplitude of ∼20% brightness variation along the rim. In the extreme case of $c_{\mathrm{s,min}}/c_{\mathrm{s,max}}$=0, the maximum amplitude reaches ∼30%, still significantly less than the factor observed.

The radiative transfer model (cf. Fig. 5.1, right panel) also produces an azimuthally asymmetric brightness distribution. This is due to the polarization efficiency being maximal along the semi-major axis. This effect likely dominates, and can be amplified by the scale height variations along the rim, in particular on the far side of

the (inclined) disk, for which the rim front is directly seen. However, these scenarios cannot be disentangled because, by chance, the shadows are located close to the major axis.

Comparing our model results to the scattered light observations of HD 100453 demands the disk to rotate clockwise, which seems at first sight in contradiction with the usual spiral arm winding direction being trailing. Considering the shadow, i.e. the triggering source of the asymmetry, to be fixed in space this is, however, a feasible possibility. This will be discussed in detail in Sect. 5.2.3.

5.2.3 Origin of spiral arms

Various mechanisms have been suggested for the origin of the spiral patterns observed in disks, where the most prominent scenarios involve planet-disk interactions (e.g., Ogilvie & Lubow, 2002; Zhu et al., 2015), gravitational instabilities (e.g., Lodato & Rice, 2004), non-ideal MHD (e.g., Lyra et al., 2015), and shadows (Montesinos et al., 2016). The low disk gas mass and the old age of the HD 100453 system suggest that gravitational instabilities are unlikely to occur. The striking symmetry of the two spiral arms seen in HD 100453 could be induced by two (yet-undetected) planets located inside the cavity. However, this scenario is rather unlikely for two reasons. First, the planets should be located at symmetrical locations inside the cavity, which is an unstable configuration. Second, the $m = 2$ mode is seen in a significant number of other disk as well.

A likely scenario for HD 100453 is that the tidal interaction between the disk and the outer M dwarf companion is responsible for the observed double-spiral-arm pattern (Dong et al., 2016b). Located at a projected separation of $\sim$108 au from the primary, this companion truncates the disk in scattered light, and excites two spiral arms in the circumprimary disk with a near $m = 2$ rotational symmetry.

Alternatively, the idea of connecting the presence of shadows with the excitation of spiral arms in protoplanetary disks has been proposed by Montesinos et al. (2016). Hence, the two shadows on opposite sides of the bright rim in HD 100453 cause a brief pressure loss and each of the related pressure peaks drives a wave. It is, however, noted that the stellar and disk parameters considered in the hydrodynamic simulations by Montesinos et al. (2016) are very far from the ones measured for HD 100453. In particular, self-gravity might play an important role in triggering and maintaining the spirals, but the Toomre parameter values for HD 100453 are much higher than the minimum ones in their simulations. Dedicated hydrodynamic simulations are needed to determine the conditions in which shadow-induced spirals could appear in HD 100453.

If spirals can be induced by steady shadows, the cooling timescale is required to be much shorter than the dynamical timescale (instantaneous), otherwise the gas does not have time to adjust and the pressure gradient is not significant enough to trigger spirals. On the other hand, if the inner disk (that is assumed to be responsible for the shadows) precesses, the shadows are not fixed anymore. At the radius that co-rotates with the shadows, the shadowed gas is maintained in a cold region and

the disk undergoes the strongest heating/cooling which might lead to spiral density waves, even with non-instantaneous cooling. For this to apply to HD 100453, the precession timescale must equal the orbital timescale at the radius where the spirals originate. We note that at the rim location (∼22 au), the orbital period is ∼80 years, already relatively fast compared to precession timescales (Papaloizou & Terquem, 1995).

Interestingly, the spirals generated by fixed or moving shadows are different. As in the case of a perturbing planet that co-rotates with the disk, if the shadows move at the precession rate of the inner disk, the spirals are trailing, and the rotational direction of the disk is counterclockwise. In contrast, if the spirals are induced by fixed shadows, the outer spirals are leading, and the rotational direction of the disk is clockwise.

5.2.4 Future prospects

The origin of misaligned inner disks is still an open question. A massive planetary or substellar companion that would carve a dust cavity inside the disk ring, and on an inclined orbit with respect to the outer disk, could be a possible explanation. In the case of the HD 142527 system, a companion was indeed detected inside the cavity (Biller et al., 2012; Close et al., 2014) and found to be on an eccentric orbit (Lacour et al., 2016). A massive inner companion inside the cavity could also explain the low gas-to-dust ratio and the very low mass accretion rate that are estimated for this object. It would halt material from flowing closer in towards the star, which would lead to an inner disk resembling a debris disk belt inside 1 au. However, depending on the amount of gas in the outer disk, it is not clear how long the misalignment can be sustained. Depending on the location and mass of the companion, the linear theory predicts that it can last ∼1 Myr at most (Foucart & Lai, 2013).

ALMA observations of this disk will undoubtedly shed light on the question whether there is an additional, yet undetected, massive companion inside the cavity. It will be able to estimate the amount of gas and dust across the disk, and to measure the kinematics of the gas. This may constrain the presence of a companion therein, and will help to constrain the spirals' generation mechanism by indicating whether the spirals are leading or trailing.

6 | New constraints on the disk characteristics and companion candidates around T Cha with VLT/SPHERE

The content of this chapter is based on Pohl et al. (2017) published in *2017, A&A, 605, A34*. The observational data presented are part of the SPHERE GTO program and based on observations made with European Southern Observatory (ESO) telescopes at the Paranal Observatory in Chile, under program IDs 095.C-0298(B), 096.C-0248(B) and 096.C-0248(C).

Details of authorship: The text was written by me, with contributions from Elena Sissa and Maud Langlois for Sects. 6.2.3 and 6.4.2. Figures 6.12 and 6.13 make use of SPHERE consortium plotting tools. The data reduction of the SPHERE data was performed with consortium or private pipelines from Christian Ginski, Maud Langlois, Dino Mesa, André Müller, Rob van Holstein, and Arthur Vigan. Elena Sissa provided the analysis of the contrast and mass detection limits.

6.1 Motivation

As pointed out in previous sections, protoplanetary disks are optically thick in the optical and NIR, so that scattered light imaging probes (sub-)micron-sized dust grains in the disk surface layer. The detection of (non-)axisymmetric disk features is fundamental in improving our current understanding of disk evolution and planet formation. Transition disks with large gas and dust gaps (see e.g., MIR surveys by Brown et al. 2007; Merín et al. 2010; van der Marel et al. 2016 and mm observations by Isella et al. 2010a, 2010b; Andrews et al. 2011; van der Marel et al. 2015) are particularly interesting targets, since they host possible planet-forming hotspots and may show signposts of planet-disk interaction processes. In recent observational studies, giant gaps and cavities have been directly imaged in scattered light observations of transition disk systems (e.g., Thalmann et al., 2010, 2015; Hashimoto et al., 2012; Avenhaus et al., 2014; Follette et al., 2015; Ohta et al., 2016; Stolker et al.,

2016; Benisty et al., 2017).

6.1.1 The target: T Chamaeleontis

T Chamaeleontis (T Cha) is a ∼2–12 Myr old (Brown et al., 2007; Torres et al., 2008; Murphy et al., 2013) T Tauri star (spectral type G8, Alcala et al., 1993) at an estimated distance of 107 ± 3 pc (first GAIA data release, Gaia Collaboration et al., 2016) surrounded by a transition disk. Several recent studies covering a wide wavelength range dealt with constraining the disk geometry around T Cha. Brown et al. (2007) studied its SED, which features a significant deficit of MIR emission. With radiative transfer based SED fitting they modeled this deficit by introducing a gap between 0.2 and 15 au, dividing the disk into two spatially separated parts. Hence, it became a prime candidate for investigating signatures of ongoing planet formation. Olofsson et al. (2011) presented spatially resolved, interferometric observations at high angular resolution in the NIR from the AMBER instrument at the VLTI to study the inner disk's structure. The inner disk is found to be extremely narrow and located close to the star with an extension from 0.13 to 0.17 au. Olofsson et al. (2013) presented a radiative transfer model accounting for several further interferometric and photometric observations, including VLTI/PIONIER, VLTI/MIDI and NACO/Sparse Aperture Masking (SAM) data, which further constrains the inner disk to extend from 0.07 to 0.11 au. Further SED modeling of T Cha by Cieza et al. (2011) suggests that there is a high degeneracy especially for the outer disk geometry, since a very compact outer disk provides an equally good fit to the Herschel data as a much larger, but tenuous disk with a very steep surface density profile. ALMA observations of the 850 μm dust continuum as well as of several emission lines presented by Huélamo et al. (2015) spatially resolved the outer disk around T Cha and helped to break the degeneracy of previous outer disk models. They report a compact dusty disk, where the continuum intensity profile displays two emission bumps separated by 40 au, indicating an inner gap size of 20 au and an outer disk radius of ∼80 au. In contrast, the gaseous disk is larger by almost a factor of three, giving a radius of ∼230 au based on the detection of CO(3–2) molecular emission. Huélamo et al. (2015) derived a disk inclination of $67° \pm 5°$ and a PA of $113° \pm 6°$ by fitting a Gaussian to the CO(3–2) integrated emission map.

All previous observations clearly confirm that there must be a significant gap in the disk's dust density distribution, while its origin is still debated. In general, radial gap structures can be created by a number of processes, including grain growth (e.g., Dullemond & Dominik, 2005), MRI effects at the outer edge of a dead-zone (e.g., Flock et al., 2015), a close (sub)stellar companion or the dynamical interaction of a planet formed within the disk (e.g., Rice et al., 2003b). For the latter, the disk density modification results from the torques exerted on the disk by the planet and by the disk itself (see Sect. 1.2.3). Studies of observational signatures of planet-disk interaction processes based on numerical simulations suggest that gaps detected in scattered light may be opened by planets (e.g., Pinilla et al., 2015b; Dong et al.,

2015c, 2016a; Juhász et al., 2015; Pohl et al., 2015). Using NACO/SAM Huélamo et al. (2011) detected a companion candidate at a projected distance of 6.7 au from the primary, which is well within the previously described disk gap. However, an analysis of several L' and K_s data sets covering a period of three years ruled out this companion hypothesis (Olofsson et al., 2013; Cheetham et al., 2015). The absence of relative motion for the companion candidate favors a stationary structure consistent with scattered light from a highly inclined disk. Sallum et al. (2015) checked if the closure phase signal from their VLT/NACO and Magellan/MagAO/Clio2 data shows any variation in time, which is not expected for the disk scattering model. While NACO L' data from 2011 and 2013 support the hypothesis of constant scattered light from the disk, the best fits for two other NACO data sets are inconsistent, requiring temporal variability in the amount of scattered light. Apart from this variability argument, Sallum et al. (2015) showed by means of Monte Carlo simulations that noise fluctuations could also cause the changing structure in the NACO and MagAO reconstructed images.

6.1.2 Outline

In this work we present the first scattered light observations of T Cha obtained with the SPHERE instrument at the VLT. The target is now one of the few T Tauri stars that have been spatially resolved in high detail in scattered light. We used the PDI technique complemented with total intensity images obtained with the angular differential imaging (ADI) technique. The observations provide the first spatially resolved high contrast images of T Cha in the optical and NIR. Our focus is set on analyzing the scattered light properties of the disk. Physical modeling of the disk is performed via radiative transfer calculations, which helps us to further constrain the disk's geometry and grain size distribution. Images in the full Stokes vector are calculated in order to consistently reproduce the observed total and polarized intensity. Furthermore, the total intensity images are used for a detailed search for substellar companion candidates and, in case of non-detection, to place constraints on the mass of putative companions using the detection limits. This work is laid out as follows. In Sect. 6.2 we describe our observations and the data reduction procedures; their results are shown in Sect. 6.3. Section 6.4 presents our results of the radiative transfer disk modeling and the search for substellar companions. A detailed discussion in Sect. 6.5 follows. In Sect. 6.6 the main conclusions of this work are summarized.

6.2 SPHERE observations and data reduction

Observations of T Cha were performed during the nights of 30 May 2015, 19 February 2016, and 31 March 2016 with several sub-systems of the high contrast imager SPHERE equipped with an extreme AO system (SAXO, Fusco et al., 2006, 2014) and mounted on the VLT at Cerro Paranal, Chile. All observations were part of

Table 6.1: Overview of observational data sets.

Date	Instrument	Mode	Filter	DIT [s] × NDIT	PC	t_{tot} [min]	Seeing [″]	H-band Strehl [%]
2015 May 30	IRDIS	IRDIFS	*DB_H2H3*	64 × 96	–	102	0.5–0.85	27±13
2015 May 30	IFS	IRDIFS	*YJ*	64 × 96	–	102	0.5–0.85	27±13
2016 February 19	IRDIS	DPI	*H*	32 × 1	30	64	0.9–1.0	76±4
2016 March 31	ZIMPOL	P2	*VBB*	40 × 2	18	96	0.8–1.1	87±3

Notes. Both filters of ZIMPOL were set to the Very Broad Band (*VBB*) filter covering a wide wavelength regime from *R*- to *I*-band. The following coronagraphs were used: N_ALC_YJH_SDIT for IRDIS/IFS and V_CLC_S_WF for ZIMPOL. DIT stands for the detector integration time and NDIT corresponds to the number of frames in the sequence. PC indicates the number of polarimetric cycles. The Strehl is calculated for the *H*-band. This leads to a Strehl of ∼43% for the ZIMPOL data at 0.65 μm.

the SPHERE consortium guaranteed time program under IDs 095.C-0298(B) and 096.C-0248(B/C). IRDIS and ZIMPOL were used in DPI mode and in field stabilized (P2) mode, respectively. In addition, data were taken simultaneously with IRDIS in dual-band imaging (DBI, Vigan et al., 2010) mode and the Integral Field Spectrograph (IFS, Claudi et al., 2008). In this IRDIFS mode, IRDIS is operated in the filter pair *H2H3* (1.593 μm and 1.667 μm) and IFS in *YJ* (0.95 – 1.35 μm) mode. Table 6.1 summarizes the observations and instrumental setups for each instrument. The Strehl ratio estimation (provided by SPARTA files) is based on an extrapolation of the phase variance deduced from the reconstruction of SAXO open-loop data using a deformable mirror, tip-tilt voltages, and wavefront sensor closed-loop data (Fusco et al., 2004). The observing conditions and the different data reduction methods for each data set taken by the various sub-systems are described in detail in Sects. 6.2.1 – 6.2.3.

6.2.1 IRDIS-DPI (*H*-band)

The IRDIS-DPI observations of T Cha were carried out on 19 February 2016 with the *BB_H* filter ($\lambda_c = 1.625\,\mu$m) using an apodized pupil Lyot coronagraph with a mask diameter of ∼185 mas (Soummer, 2005; Boccaletti et al., 2008). Dark and flat field calibration were obtained during the following day. Thirty polarimetric cycles were taken, consisting of one data cube for each of the four half wave plate (HWP) positions (0°, 45°, 22.5° and 67.5°). Dedicated coronagraphic images were taken at the beginning and at the end of the science sequence to determine accurately the position of the star behind the coronagraph. For this calibration a periodic amplitude is applied to the deformable mirror, which produces four equidistant, crosswise satellite spots of the stellar PSF outside of the coronagraph. The data were reduced following the prescriptions of Avenhaus et al. (2014) and Ginski et al. (2016), who consider the radial Stokes formalism. The first step consists of standard calibration routines, including dark-frame subtraction, flat-fielding and bad-pixel correction. These images are split into two individual frames representing the left and right sides (parallel and perpendicular polarized beams, respectively), and the precise position of the central star is measured using the star center calibration frames on both image sides separately. Then, the right side of the image is shifted and subtracted from the left side. To obtain clean Stokes Q and U images, that is, to correct for instrumental polarization downstream of the HWP's position in the optical path, Q^+ and Q^- (0° and 45°), and U^+ and U^- (22.5° and 67.5°) are subtracted, respectively. However, there might be still an instrumental polarization left upstream of the HWP in the final Q and U images, which is assumed to be proportional to the total intensity image as shown in Canovas et al. (2011). To obtain this residual instrumental signal, the azimuthal Stokes components are computed (see Eq. 1.47).

As shown by Canovas et al. (2015), the signal in the U_ϕ frame should be small for a centrally illuminated symmetrical disk. We thus determined the scaling factor for our second instrumental polarization correction such that the (absolute) signal in an

annulus around the central star in the U_ϕ frame is minimized. We then subtract the scaled Stokes I frame from the Q and U frame and use these final corrected frames to create the Q_ϕ and U_ϕ images displayed in Fig. 6.1.

To cross-check the IRDIS-DPI results, and especially to test the reliability of the U_ϕ minimization technique in the context of an inclined disk, we additionally perform an alternative reduction procedure. This includes a proper polarimetric calibration using a Mueller matrix model, whose details will be presented in van Holstein et al. (in prep.) and de Boer et al. (in prep.). A short explanation of the method and the corresponding results for T Cha can be found in Sect. 6.3.1 and Fig. 6.2.

6.2.2 ZIMPOL P2 (*VBB* filter)

T Cha was observed during the night of 31 March 2016 with the SlowPolarimetry detector mode of ZIMPOL using the *VBB* filter. The *VBB* filter covers a wide wavelength range from R- to I-band (0.55–0.87 μm). These observations were also obtained with an apodized Lyot coronagraph (mask diameter of ∼185 mas).

The ZIMPOL data were reduced following mostly the same strategy as described for the IRDIS data in the previous section. The main difference between the two data sets is the different structure of the ZIMPOL data. In ZIMPOL the two perpendicular polarization directions for each HWP position are recorded quasi-simultaneously on the same detector pixels. For a more detailed description of the instrument and the specialized data reduction steps involved we refer to Thalmann et al. (2008) and Schmid et al. (2012). We process both ZIMPOL detector images independently and only combine the images after the final data reduction to increase the signal-to-noise ratio (SNR). We first bias subtract and flat field the individual frames. We then extract the two perpendicular polarization directions from the interlaced rows in each frame, resulting in two 1024×512 pixel images per original frame. Then, it is corrected for charge-shifting artifacts by always combining two consecutive frames of the observation sequence. To create quadratic images each image is binned by a factor of two along the x-axis. Finally, the two perpendicular polarization directions are subtracted from each other to get Q^+, Q^-, U^+ and U^- frames (depending on the HWP position). These are then combined to create the final Q and U frames identical to the IRDIS reduction. In a last step, we again calculate the azimuthal Stokes components Q_ϕ and U_ϕ and employ the instrumental polarization correction from Canovas et al. (2011). The resulting images (after combination of both ZIMPOL images) are also displayed in Fig. 6.1.

6.2.3 IRDIS-DBI (*H2H3*-bands) and IFS (*YJ*-band)

T Cha IRDIFS observations where obtained during the night of 30 May 2015 as part of the SpHere INfrared survey for Exoplanets (SHINE) using the SHINE standard setup: pupil-stabilized images with IFS operating in YJ mode (39 channels between 0.95 and 1.35 μm) and IRDIS working in DBI mode using the *H2H3* filter

pair ($\lambda_{H2} = 1.593\,\mu$m; $\lambda_{H3} = 1.667\,\mu$m). This observing strategy allows for performing ADI (Marois et al., 2006) in order to reach high contrast. The spectral resolution of IFS YJ data amounts to R$\sim$50. The observations lasted about 6100 seconds with a field rotation of $\sim$28°. Since the target is located far to the south, obtaining a good rotation is challenging. The unstable weather conditions (Differential Image Motion Monitor (DIMM) seeing varied from 0.″5 to 0.″85 and clouds passed by) caused flux variations of up to one order of magnitude during the sequence.

The basic steps of the first IRDIS data reduction (#1) consist of flat-field and bad-pixel correction, cosmic ray detection and correction, and sky subtraction. Because of the variable atmospheric conditions during the observations, a very strict frame selection is applied at the end of the basic reduction and eventually only 42 out of 96 frames were used. This corresponds to selecting frames with Strehl ratio larger than $\sim$25%. The modeling and subtraction of the speckles follows the MPIA-PCA pipeline from André Müller. This is based on a principal component analysis (PCA) after Absil et al. (2013), which uses the Karhunen-Loéve Image Projection (KLIP) algorithm from Soummer et al. (2012). The following reduction steps are applied: (1) Gaussian smoothing with half of the estimated FWHM; (2) normalization of the images based on the measured peak flux of the PSF images; (3) PCA and subtraction of the modeled noise; and (4) derotation and averaging of the images. Each frame is divided into annuli of the size of the estimated FWHM. The noise of a single frame and annulus is modeled by PCA using a fixed value of five modes, which is found to be the best value after several attempts. In addition, only frames for modeling the noise of the individual frame were selected where a minimum protection angle can be guaranteed. This means that with this adaptive approach the effect of self subtraction for an extended source is minimized and the SNR maximized.

To cross-check the IRDIS-DBI results, a parallel reduction (#2 and #3) is performed using the SPHERE Data Reduction and Handling pipeline (DRH, Pavlov et al., 2008) implemented at the SPHERE Data Center. This includes dark and sky subtraction, bad-pixel removal, flat-field correction, anamorphism correction, and wavelength calibration. After these first steps the data were sorted according to their quality. Because of the difficult observing conditions, a stringent frame selection was used (using 77 frames out of 96). This roughly corresponds to selecting frames with Strehl ratio greater than 15% and leads to an average H-band Strehl of $\sim$33%. The location of the star is identified with the four symmetrical satellite spots generated from a waffle pattern on the deformable mirror. Then, to remove the stellar halo and to achieve high contrast, the data were processed with the SpeCal pipeline developed for the SHINE survey (Galicher et al., in prep.); this implements a variety of ADI-based algorithms: Classical Angular Differential Imaging (cADI, Marois et al., 2006), Template Locally Optimized Combination of Images (TLOCI, Marois et al., 2006) and PCA (Soummer et al., 2012; Amara & Quanz, 2012). In the following we discuss the results based on the TLOCI and PCA images for the morphology and photometric analyses. Separate reductions were performed for the extraction of the disk. In particular, for the SpeCal PCA reduction a small number

of PCA modes is used in order to enable optimal retrieval of the disk. The reduced numbers of modes, between two and four, are determined by maximizing the SNR inside a region delimited by the disk location. For the contrast curves, TLOCI images were considered because they provide the best compromise of contrast, stellar rejection, and throughput correction for the point source detection.

The data reduction for the IFS is performed using tools available at the SPHERE Data Center at IPAG following the procedure described in Mesa et al. (2015) and in Zurlo et al. (2014). Using the SPHERE DRH software we apply the appropriate calibrations (dark, flat, spectral positions, wavelength calibration and instrument flat) to create a calibrated datacube composed of 39 images of different wavelengths for each frame obtained during the observations. Similar to the procedure used for IRDIS, in order to take into account the variable weather conditions, a frame selection is applied resulting in 76 frames out of the original 96. A frame is considered as 'bad' if the AO loop opens or the star exits the coronagraph region, causing an excess of light in the central part of the image. For each frame two central areas with 20 and 160 pixels per side are defined, for which the flux ratio is determined. Frames are rejected by an automated sorting if this ratio exceeds 130% of the median value. The position of the star behind the coronagraph is estimated from images with four satellite spots, symmetric with respect to the central star taken just before and after the standard coronagraphic observations. Exploiting these images we are then able to define the re-scaling factor for images at different wavelengths to maintain the speckle pattern as stable as possible. Moreover, we are able to combine those images using the PCA algorithm from Soummer et al. (2012) to implement both ADI and spectral differential imaging (SDI, Racine et al., 1999) in order to remove the speckle noise.

6.3 Results

The disk of T Cha is detected in all data sets presented in this study. The analysis of the disk geometry primarily focuses on the IRDIS-DPI and IRDIS-ADI images (Sect. 6.4.1). Furthermore, the ADI images are used to search for point-source signals focusing on non-polarized companions, because this data set reaches a higher contrast (Sects. 6.4.2 and 6.4.3).

6.3.1 Polarized intensity images

Figure 6.1 shows the reduced Q_ϕ and U_ϕ images of the IRDIS-DPI H-band and ZIMPOL *VBB* observations of T Cha described in Sects. 6.2.1 and 6.2.2. The dark central region corresponds to the area masked by the coronagraph. The disk around T Cha is clearly detected in the IRDIS Q_ϕ image, which gives by far the best quality view of the outer disk structure and its rim in scattered light. Our SPHERE observations support a high disk inclination with respect to the line of sight, in agreement

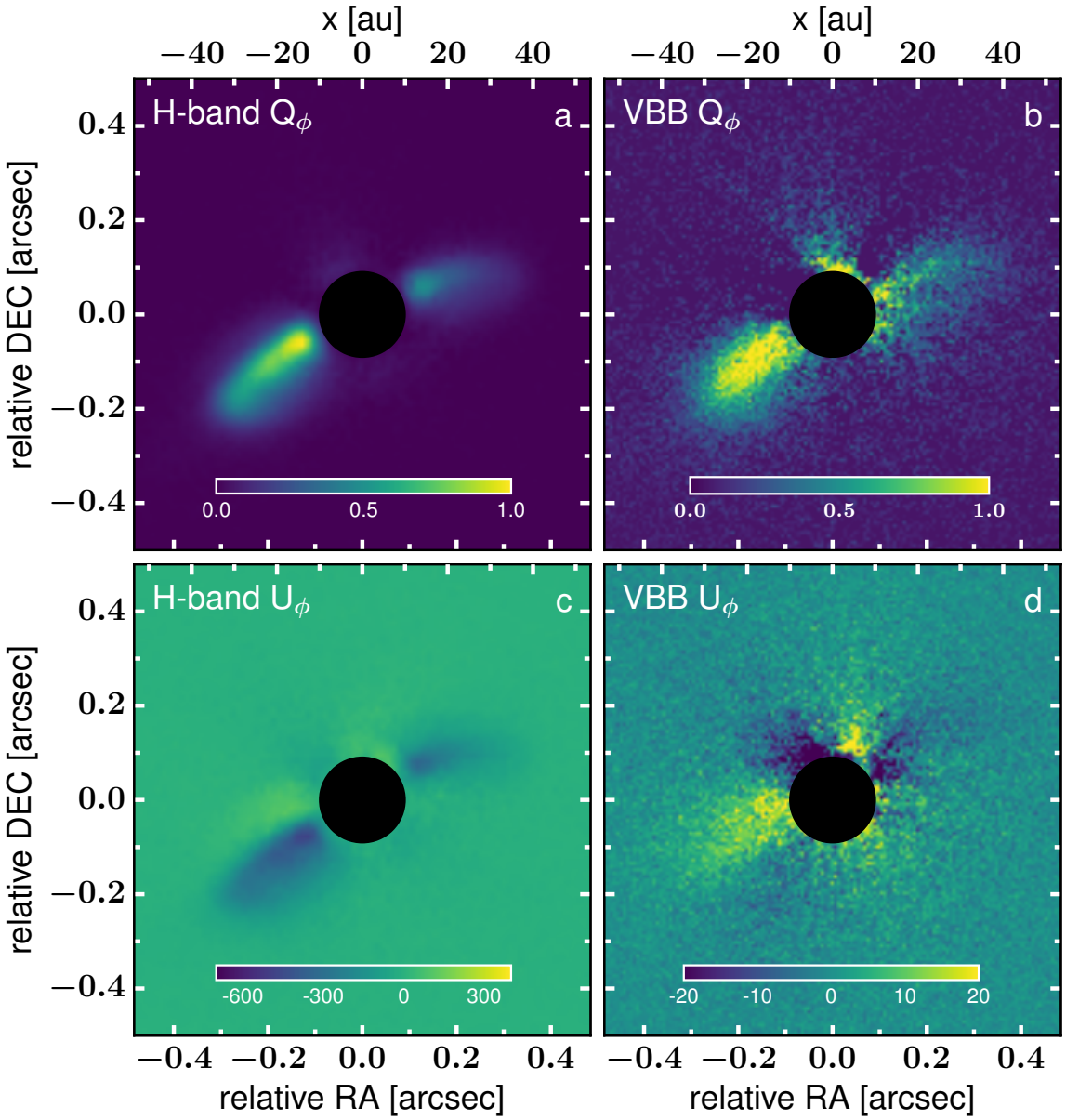

Figure 6.1: IRDIS-DPI H-band and ZIMPOL P2 VBB-filter Q_ϕ (top row) and U_ϕ (bottom row) images. North is up, east is left. The Q_ϕ images are normalized to the highest disk brightness, where the dynamical range for the color scaling is the same (1000). An apodized Lyot coronagraph with a mask diameter of ∼185 mas was used. The inner 0.″18 are masked, represented by the black circular area.

with the model by Huélamo et al. (2015). Scattered light is detected out to a projected distance of ∼0.″39 (∼42 au) from the central star concentrated in a bright arc with, however, a significant difference in brightness between the east and west sides (factor of ∼2.5). This is further discussed in Sects. 6.4.1 and 6.5.3. In the reduced U_ϕ image there is some residual signal left, which has usually been interpreted as instrumental effects or as imperfect centering of the images. However, since the

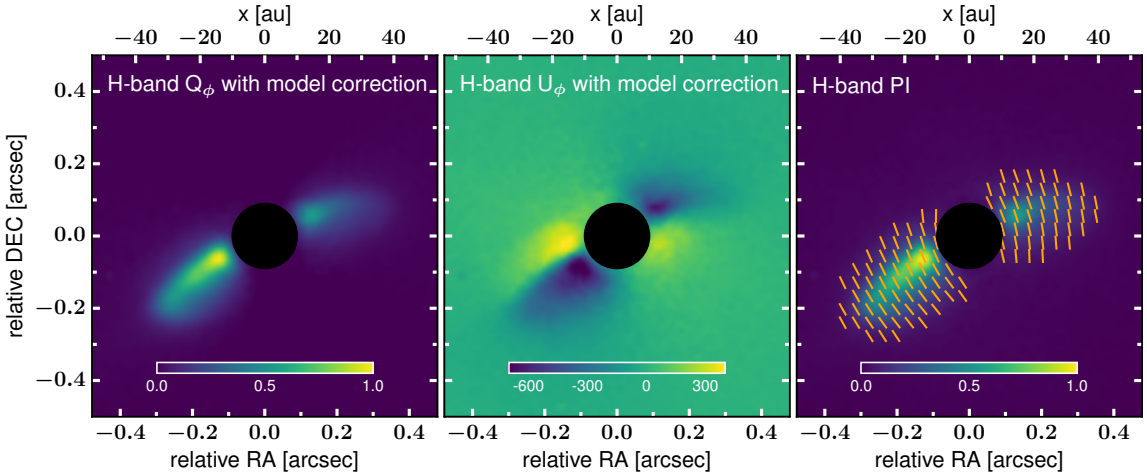

Figure 6.2: Mueller matrix model-corrected IRDIS-DPI Q_ϕ (left), U_ϕ (middle) and polarized intensity $PI = \sqrt{Q^2 + U^2}$ (right) images. North is up, east is left. Note that the Q_ϕ and U_ϕ images are not normalized/saturated here on purpose to emphasize their partially negative signal. The inner 0.″18 are masked, represented by the black circular area. The orange stripes in the right image represent the angle of linear polarization (fixed length, not scaled with the degree of polarization).

U_ϕ/Q_ϕ peak-to-peak value amounts to 9% and owing to the high inclination of the disk around T Cha (69 deg is determined from the total intensity image modeling, see Sect. 6.4.1), multiple scattering (e.g., Bastien & Menard, 1990; Fischer et al., 1996; Ageorges et al., 1996), that is, scattering of already polarized light, in the inner disk might be the prime contributor to this signal. This is consistent with a theoretical study by Canovas et al. (2015), who found that even for moderate disk inclinations multiple scattering alone can produce significant non-azimuthal polarization above the noise level in the U_ϕ images. They showed that the U_ϕ/Q_ϕ peak-to-peak value can even go up to 50% for a disk inclination of 70 deg depending on the mass and grain size distribution of the disk model. We note that the exact geometrical structure of the U_ϕ signal might be influenced by the reduction method described in Sect. 6.2.1 (correction for the instrumental crosstalk by minimizing U_ϕ). Therefore, we are not going to force our model to also fit the U_ϕ in addition to the Q_ϕ. However, in order to prove that the U_ϕ signal is indeed real, we evaluate our IRDIS-DPI data with a newly developed reduction method, independent of the one presented in Sect. 6.2.1. By using the detailed Mueller matrix model of van Holstein et al. (in prep.) and de Boer et al. (in prep.) we correct our measurements for instrumental polarization effects. This model describes the complete optical path of SPHERE/IRDIS, i.e. telescope and instrument, and has been fully validated with measurements using SPHERE's internal source and observations of unpolarized standard stars (van Holstein et al., in prep.). The images of Stokes Q and U incident on the telescope are computed by setting up a system of equations describing every measurement of Q and U and solving it – for every pixel individually – using linear least-squares. The resulting Q_ϕ image (Fig. 6.2, left panel) is very similar to the one from the first reduction

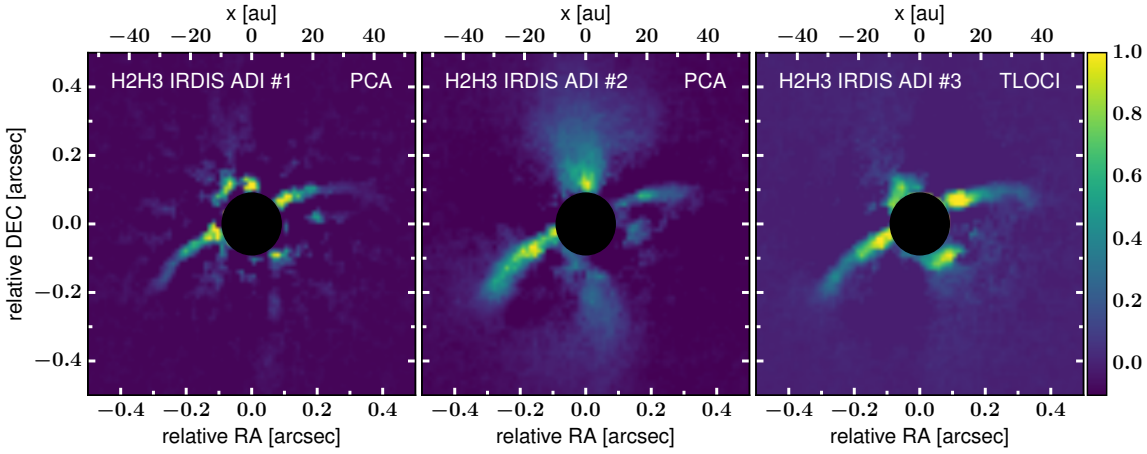

Figure 6.3: IRDIS-ADI *H2H3*-band images (mean across the wavelengths) based on three different reduction pipelines (#1: MPIA-PCA, #2: SpeCal-PCA and #3: SpeCal-TLOCI). North is up, east is left. The images are normalized to the highest disk brightness and the color scales consider the same dynamical range. The inner 0.″18 region masked by the coronagraph is represented by the black circular area.

(Fig. 6.1, top left panel). The new U_ϕ image (Fig. 6.2, middle panel) has a higher accuracy than the one from the reduction that minimizes U_ϕ (Fig. 6.1, bottom left panel), in particular because no assumptions about the angle of linear polarization of the source are made to correct for the instrumental polarization. The U_ϕ image is cleaner and shows more symmetry in the sense that there is also a strong signal to the south-west. On the top right, the positive U_ϕ signal from Fig. 6.1, bottom left, is not visible anymore. The right panel of Fig. 6.2 shows the polarized intensity overplotted with polarization vectors representing the angle of linear polarization. This strengthens that there is a clear departure from azimuthal polarization. For the model-corrected images the U_ϕ/Q_ϕ peak-to-peak value increases from 9% to 14%, suggesting that some of the actual physical U_ϕ signal has been removed in the original reduction method due to the U_ϕ minimization procedure. A detailed comparison between different reduction methods and the specific influence on the left-over U_ϕ signal will be the topic of the two follow-up SPHERE papers.

The optical images obtained with ZIMPOL (Fig. 6.1, right panel) corroborate the disk geometry, but the bad weather conditions and low Strehl ratio (43% at 0.65 μm) of this observation lead to a rather blurred structure. Again, positive and negative patterns (dark and bright color) alternate in the U_ϕ image, where these negative patterns are practically at the same location as in the IRDIS U_ϕ image.

6.3.2 Total intensity images

In addition to the polarimetric images, the IRDIS-ADI *H2H3* intensity images in Fig. 6.3 also clearly show the inclined disk around T Cha. It even more strongly

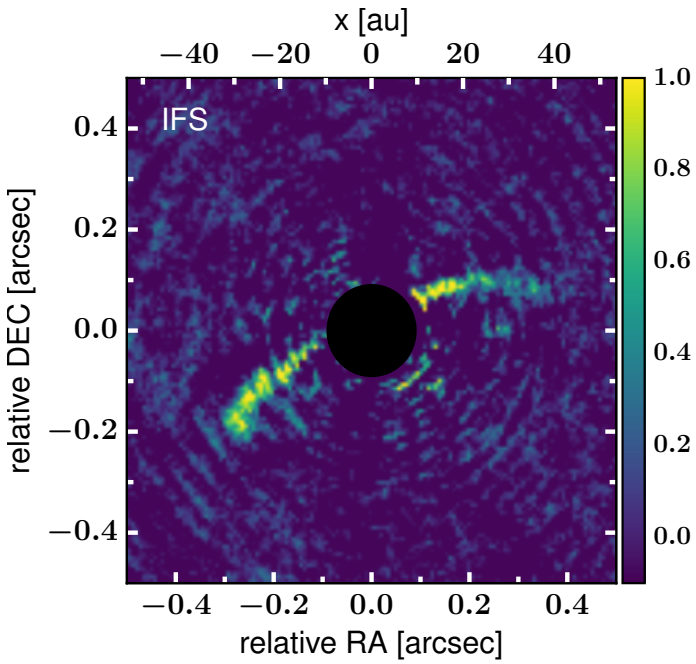

Figure 6.4: IFS image after PCA+SDI reduction with 100 modes: median across the entire wavelength range *YJ*. North is up, east is toward the left; the image is normalized to the highest disk brightness and the color scale considers the same dynamical range as in Fig. 6.3. The inner 0.″18 region masked by the coronagraph is represented by the black circular area.

brings out the inner rim of the outer disk on the far side, visible as a faint arc below the coronagraph. The double-arch structure is a recurrent new form of features that have been detecting with high contrast imaging instruments such as SPHERE (cf. Janson et al., 2016; Garufi et al., 2016). We note that because of the ADI processing this image may have been biased and is not a faithful representation of the true intensity and geometry. The residual signal northeast of the image center is likely due to stellar residuals. However, this signal is almost aligned with the near minor axis, so the possibility that it is real cannot be completely excluded. In fact, it could be the marginal detection of some material outward of the ring with high scattering efficiency. The brightness asymmetry between the west and east disk wings is as pronounced as in the polarimetric images, especially for reduction #2. Figure 6.4 illustrates the median IFS image across the wavelength range from *Y*- to *J*-band. The disk is nicely resolved, confirming the disk geometry and surface brightness extension stated above.

6.4 Analysis

6.4.1 Radiative transfer modeling of the disk

We build a radiative transfer model for T Cha aiming to reproduce the basic structure of its disk. Earlier efforts (Olofsson et al., 2011, 2013; Huélamo et al., 2015) are taken as a starting point for independent 3D radiative transfer calculations using the Monte Carlo code RADMC-3D (Dullemond et al., 2012). We aim to complement the current understanding of the disk geometry by also taking into account our new SPHERE data. RADMC-3D is used to calculate the thermal structure of the dust disk and ray-traced synthetic scattered light images in the NIR.

Modeling approach

The disk around T Cha is parametrized using constraints obtained from previous analyses of data sets (cf. Olofsson et al., 2011, 2013; Huélamo et al., 2015) and from the new SPHERE observations presented in this work. The disk is assumed to be composed of two spatially separated zones with an inner (r_{in}) and outer radius (r_{out}) each, a narrow inner disk close to the central star that is responsible for the NIR excess and a more extended outer disk. Inner and outer disks are assumed to be coplanar, since there is no significant evidence for a misaligned inner disk, which would cast shadows onto the outer disk (cf. the cases of HD142527, Marino et al. 2015 and HD100453, Benisty et al. 2017). The surface density structure is defined by a power-law profile and an exponential taper at the outer edge of the outer component,

$$\Sigma(r) = \Sigma_0 \left(\frac{r}{r_c}\right)^{-\delta} \exp\left[-\left(\frac{r}{r_c}\right)^{2-\delta}\right], \tag{6.1}$$

where r_c corresponds to a characteristic radius and δ denotes the surface density index. For the sake of simplicity, we assume a uniform distribution along the azimuth in our model and concentrate on the radial disk structure. The disk scale height is parameterized radially as $H(r) = H_0\,(r/r_0)^{\beta}$, where H_0 is the scale height at a reference radius r_0 and β is the flaring index. The vertical density distribution follows a Gaussian profile, so that the dust volume density is given by

$$\rho(R, \phi, z) = \frac{\Sigma(R)}{\sqrt{2\,\pi}\,H(R)} \exp\left(-\frac{z^2}{2\,H^2(R)}\right), \tag{6.2}$$

where the cylindrical coordinates R and z can be converted into spherical coordinates with $R = r\,\sin(\theta)$ and $z = r\,\cos(\theta)$, where θ is the polar angle. We consider a power-law grain size distribution with an index $p = -3.5$, $\mathrm{dn(a)} \propto \mathrm{a}^p\,\mathrm{da}$ between a minimum (a_{min}) and maximum grain size (a_{max}). During our modeling process different values for the parameters a_{min} and a_{max} are used, where two distributions are eventually find to give an equally good match for the total intensity image (cf.

Sect. 6.4.1). The dust is assumed to be a mixture made of silicates (Draine, 2003), carbon (Zubko et al., 1996), and water ice (Warren & Brandt, 2008) with fractional abundances of 7%, 21%, and 42%, consistent with Ricci et al. (2010b). The remaining 30% is vacuum. The opacity of the mixture is determined by means of the Bruggeman mixing formula. The absorption and scattering opacities, $\kappa_{\rm scat}$ and $\kappa_{\rm abs}$, as well as the scattering matrix elements Z_{ij} are calculated for spherical, compact dust grains with Mie theory considering the BHMIE code of Bohren & Huffman (1983).

Table 6.2: Overview of the best RADMC-3D model parameters.

Parameter	Inner disk	Outer disk
$r_{\rm in}$ [au]*	0.07[a]	30
$r_{\rm out}$ [au]*	0.11[a]	60
$r_{\rm c}$ [au]	–	50[b]
$M_{\rm dust}$ [$M_\odot$]	2×10^{-11} [a]	9×10^{-5} [b]
δ	1	1
H_0/r_0	0.02/0.1[a]	4/50[b]
β	1	1
$\{a_{\rm min},a_{\rm max}\}$ [μm]*	{0.01,1000}	{0.01,1000}
	∼10	∼10
p	-3.5	-3.5
incl [deg]*	69	69
PA [deg]*	114	114

Notes. δ denotes the exponent of the surface density power-law and β corresponds to the disk flaring index. For the radiation source we take the following star parameters: $T_{\rm eff} = 5400\,{\rm K}$, $M_\star = 1.5\,M_\odot$, $R_\star = 1.3\,R_\odot$, where the star is assumed to be spherical. All parameters marked with an asterisk symbol (*) were varied during the radiative transfer modeling. The grain size distributions as well as inclination (incl) and PA were taken to be the same for the inner and outer disk. References: [a] Olofsson et al. (2013); [b] Huélamo et al. (2015).

The radiative transfer calculations start with computing the dust temperature consistently by means of a thermal Monte Carlo simulation using 10^7 photon packages. Hence, an equilibrium dust temperature is calculated considering the star as the source of luminosity. The main inputs for the radiative transfer modeling are the dust density structure from Eq. 6.2 and the dust opacities (see Sect. 2.4). Full non-isotropic scattering calculations are performed that take multiple scattering and polarization into account. To compare with the observations, synthetic Stokes I intensity images, and Stokes Q and U polarized intensity images are produced at H-band (1.6 μm) using 10^8 photon packages. These theoretical images are

then convolved with a Gaussian PSF with a FWHM of 0.″04 assuming the object to be at 107 pc. Moreover, the synthetic total intensity images are run through the MPIA-PCA and SpeCal-PCA processing described in Sect. 6.2.3 to have a proper comparison. The polarimetric Stokes Q and U images are eventually converted into their azimuthal counterparts Q_ϕ and U_ϕ. All synthetic images are normalized to the highest disk surface brightness and displayed using the same dynamical range as for the observational data. The coronagraph used in our IRDIS observations is mimicked by masking the inner 0.″18 of the disk (19.3 au at 107 pc distance).

Best model

The inner disk geometry parameters are adopted from Olofsson et al. (2013) and are kept fixed in the modeling process. By adjusting the parameters from Huélamo et al. (2015) we generate the outer disk and run a grid of models exploring a pre-defined parameter space for $r_{\rm in}$, $r_{\rm out}$, $a_{\rm min}$, $a_{\rm max}$, incl and PA. The fiducial model is defined by the set of parameters that causes a minimization in the residuals between observations and model within the paramater ranges set. For this determination the images of both, data and models, are normalized to the highest flux value outside of the coronagraph. There is, however, no automatic fitting routine since computing tens of thousands of 3D models for the T Cha system is computationally far too expensive. The best parameters are summarized in Table 6.2. The modeling approach taking into account the new high contrast SPHERE images allow us to better constrain the position of the inner rim of the outer disk, which we find to be at a significantly larger radius of ∼30 au (∼0.″28) compared to earlier work. Hence, the cavity size between the inner and outer disk is correspondingly larger than previously thought (Olofsson et al., 2013). We note, however, that the gap and emission ring properties are sensitive to the grain size, and thus vary with the observing wavelength. Furthermore, the polarimetric measurements provide us better estimates of the grain sizes.

Synthetic total intensity images

Figure 6.5, left panel, shows the synthetic Stokes I image at H-band from the first of our two radiative transfer models. It is produced at a disk PA of 114° and an inclination angle of 69°, which are similar to those values derived in Huélamo et al. (2015). Our disk model gives a qualitatively good match with the IRDIS total intensity images from Fig. 6.3. The bright arc as the dominant source of scattered light is well reproduced and corresponds to forward scattered light from the near side of the inclined disk. The ADI images may, however, be significantly altered by the software processing, which was already shown by Garufi et al. (2016) for the case of HD100546. This ADI bias is especially important for T Cha, since the self-subtraction is strong due to the small field rotation and high inclination. Thus, we apply the ADI processing routines to the model image. To do so we process the model image rotated by 70 deg with the raw data considering the same PCA pa-

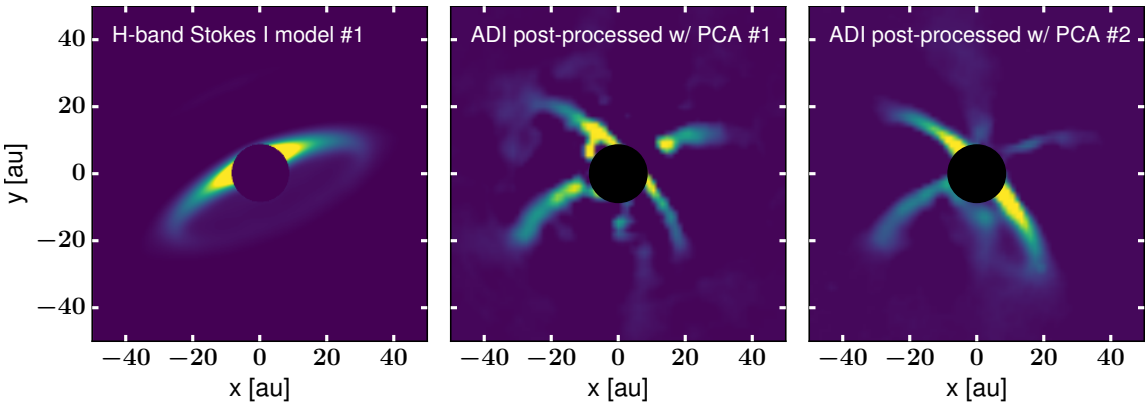

Figure 6.5: Synthetic total intensity images from our radiative transfer model #1 considering a MRN-like power-law grain size distribution with $a_{\rm min} = 0.01\,\mu$m and $a_{\rm max} = 1000\,\mu$m. The left panel shows the theoretical Stokes I image convolved with a Gaussian PSF with FWHM of 0.″04 (at 107 pc distance). The middle and right panels show the theoretical model image at 70° processed together with the raw DBI data by the different PCA methods as described in Sect. 6.2.3. The central 0.″18 of the image are masked to mimic the effect of the coronagraph on the observations. The units are arbitrary, but the dynamical range of the color bar is taken the same as in Fig. 6.3.

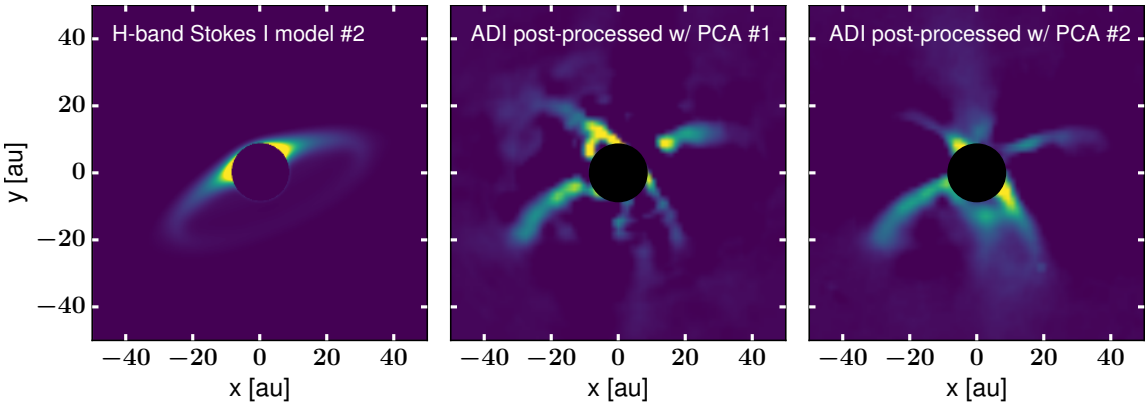

Figure 6.6: Synthetic total intensity images from our radiative transfer model #2 considering a grain size distribution narrowly peaked around ∼10 μm. The layout and color scale is identical to Fig. 6.5.

rameters. The middle and right panels of Fig. 6.5 show the resulting post-processed images depending on the PCA reduction method. The ADI procedure damps the signal of the backside of the disk and introduces a brightness asymmetry along the disk surface. Thus, an original azimuthally symmetric feature can be seen as an asymmetric double-wing structure for a specific disk geometry and orientation. We note here that we additionally favor a physical reason for this asymmetry, since this is also seen in the polarimetric images (cf. Sect. 6.5.3). The ADI processed model image supports that the geometrical parameters used in our model, in particular the gap size, reproduce the observations nicely.

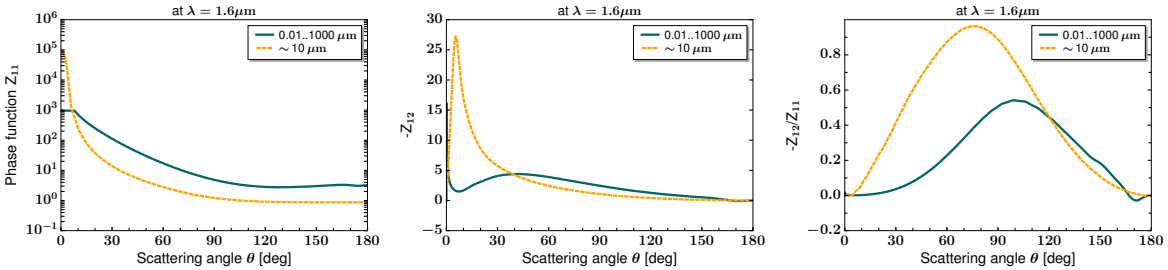

Figure 6.7: Phase functions Z_{11}, $-Z_{12}$ and degree of polarization $-Z_{12}/Z_{11}$ of the dust grains dependent on the scattering angle θ and calculated at $\lambda = 1.6\,\mu$m. Model #1 is represented by the dark green line, model #2 by the orange curve.

The fraction of star light scattered off the disk surface layer towards the observer depends on the disk properties (e.g., mass and scale height), but also on dust grain properties that determine the phase function. Dust grains, which are large compared to the wavelength, have strongly forward peaking scattering phase function, while small grains scatter photons almost isotropically. When keeping the minimum dust grain size fixed at $0.01\,\mu$m, a maximum grain size of at least $100\,\mu$m is requested to match the observations. This serves to reduce the influence of the small grains that are in the Rayleigh limit and absorb radiation much more efficiently than they scatter it. Except for very turbulent disks, one would, however, expect very large grains ($\gg 10\,\mu$m) to settle below the scattering surface. The need for large grains in the disk surface can be avoided by removing the smallest grains. Hence, the minimum and maximum values for the dust grain size distribution in our model are somehow degenerate. An equally good image, that also achieves the desired brightness contrast of the arc with respect to the disk backside, is obtained by using a narrow distribution around $10\,\mu$m. Grains of about ten microns in size are strong forward scatterers in the H-band. If even larger particles were primarily present, the forward scattering efficiency would be too strong, and the brightness of the disk's far sides would be too faint. The corresponding synthetic intensity images for the second model and their appearance after the ADI post processing with PCA can be found in Fig. 6.6.

Synthetic polarimetric images

Our results so far demonstrate that we find a quite good model to match the disk geometry of T Cha. The goal is, however, to also analyze the grain properties compatible with the polarimetric data. For scattering in the Rayleigh and Mie regime, that is, for grains with sizes smaller than or approximately equal the wavelength ($2\pi a \lesssim \lambda$), maximum polarization is expected along a scattering angle of 90 deg. The phase function Z_{11}, the scattering matrix element $-Z_{12}$ and the degree of polarization $-Z_{12}/Z_{11}$ of the dust grains used in our radiative transfer models are shown as a function of the scattering angle θ in Fig. 6.7. Comparing those quantities for

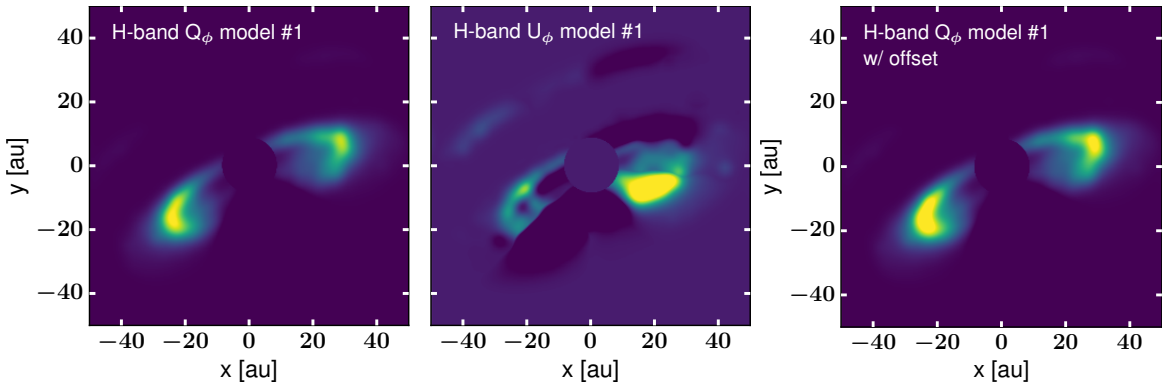

Figure 6.8: Q_ϕ (left) and U_ϕ (middle) images of model #1 at H-band. The right panel considers the same model, but the star is slightly offset from its original central position along the semi-major axis. The images are convolved with a Gaussian PSF with FWHM of 0.″04 (at 107 pc distance). The color scale considers the same dynamical range as for the previous synthetic images.

both models allows us to rule out the first model covering a wide range of grain sizes from 0.01 to 1000 μm. This, rather, produces maxima in polarized intensity along the semi-major axis (see Fig. 6.8), which is clearly not observed in the SPHERE PDI data from Fig. 6.1. Although one can recognize an extreme forward peak in $-Z_{12}$, the resulting peak in polarized intensity is hidden behind the coronagraph. For our second model with grains of $\sim$10 μm the phase function is also dominated by small-angle scattering as seen in the Z_{11} plot, but the $-Z_{12}$ curve has a strong peak at small angles of $\sim$10°. This leads to the spatial shift of brightness maxima away from the semi-major axis (i.e., scattering at 90 deg), meaning that the maximum polarized intensity occurs at the forward scattering position. This is in good agreement with our polarimetric SPHERE observations.

Figure 6.9 shows the synthetic Q_ϕ and U_ϕ images at H-band for the second model, with a disk PA of 114° and an inclination of 69°; both determined from the fit to the total intensity image. The Q_ϕ image is dominated by large positive signal, which is consistent with forward scattering from the close edge of the disk. The small-scale brightness blobs could be due to self-scattering of thermal emission or the result of multiple scattering treatment in the radiative transfer calculations. Monte Carlo noise can be ruled out as the source of these features since the best models were also run with a higher number of photon packages (10^9) for testing, confirming that our calculations are converged. Similar to the observed U_ϕ image, the U_ϕ model image shows an alternation of positive (white) and negative (dark blue) signal, although the exact geometry appears different. The extension of the south-east lobe with negative signal is comparable to that in the observational image in Figs. 6.1 (bottom left panel) and 6.2. The positive signal is a bit less pronounced in our calculated model. Since the U_ϕ signal in the observational image can be substantially influenced by noise, instrumental effects, and the data reduction procedure,

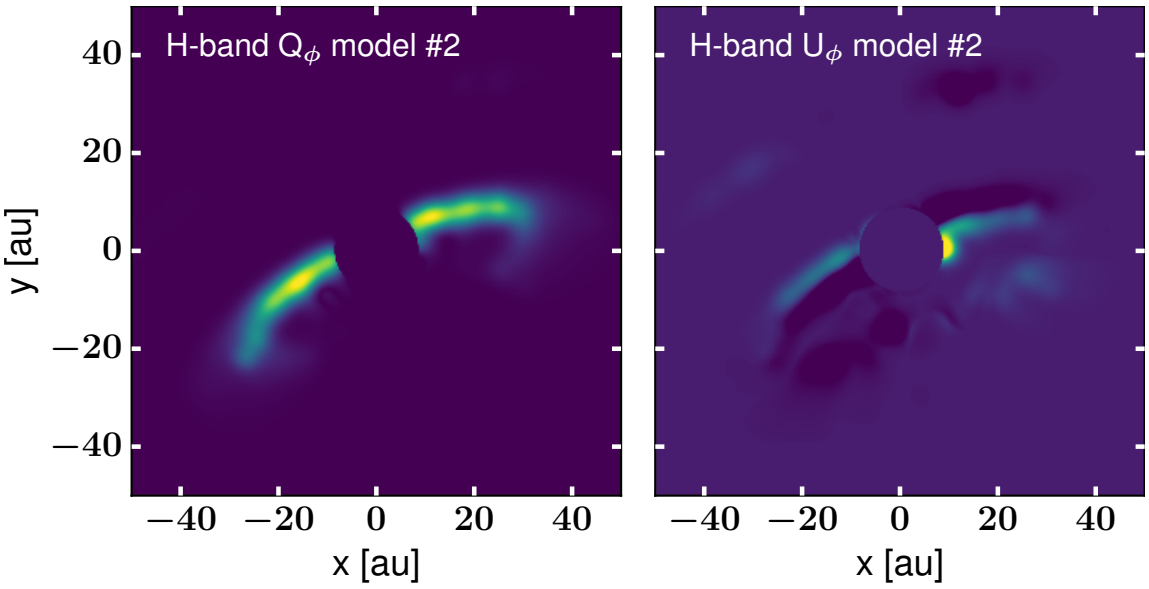

Figure 6.9: Synthetic Q_ϕ (left) and U_ϕ (right) images of model #2 at H-band. They are convolved with a Gaussian PSF with FWHM of 0.″04 (at 107 pc distance). The color scale is arbitrary, the dynamical range is similar as in Fig. 6.1. Negative values are saturated at dark blue color.

which is not included in our modeling, such a deviation was to be expected. The U_ϕ/Q_ϕ peak-to-peak value for the best model is about 15%, which is still in very good agreement with the observations (9% and 14%), but lower than calculated in the study by Canovas et al. (2015) on non-azimuthal linear polarization. For their models and in our RADMC-3D calculations we consider a full treatment of polarized scattering off randomly oriented particles. Due to the absence of any instrumental influence on the polarization, the U_ϕ signal visible in the model images should be primarily connected to multiple scattering events happening in the disk. However, the contribution of multiple scattering strongly depends on the disk inclination, the grain population and the mass of the disk. In Canovas et al. (2015) the signal in U_ϕ reaches up to 50% of the Q_ϕ, but only for an inclination of 70 deg, a grain size distribution with $a_{min,max} = (5, 1000)\,\mu$m, and a disk significantly more massive than assumed for our T Cha model. A higher disk mass produces more scattering events as simply more scattering particles are available. Furthermore, the higher scattering efficiency of the grains relative to their absorption efficiency results in stronger multiple scattering signature in the models of Canovas et al. (2015). These effects can explain the discrepancy to our U_ϕ/Q_ϕ peak-to-peak value of only 15%.

East-west brightness asymmetry

The clear asymmetry in brightness along the inner edge of the outer disk from the observations is naturally not produced with our symmetric disk model with spatially invariant dust properties. A slightly offset disk is one possibility for explaining the

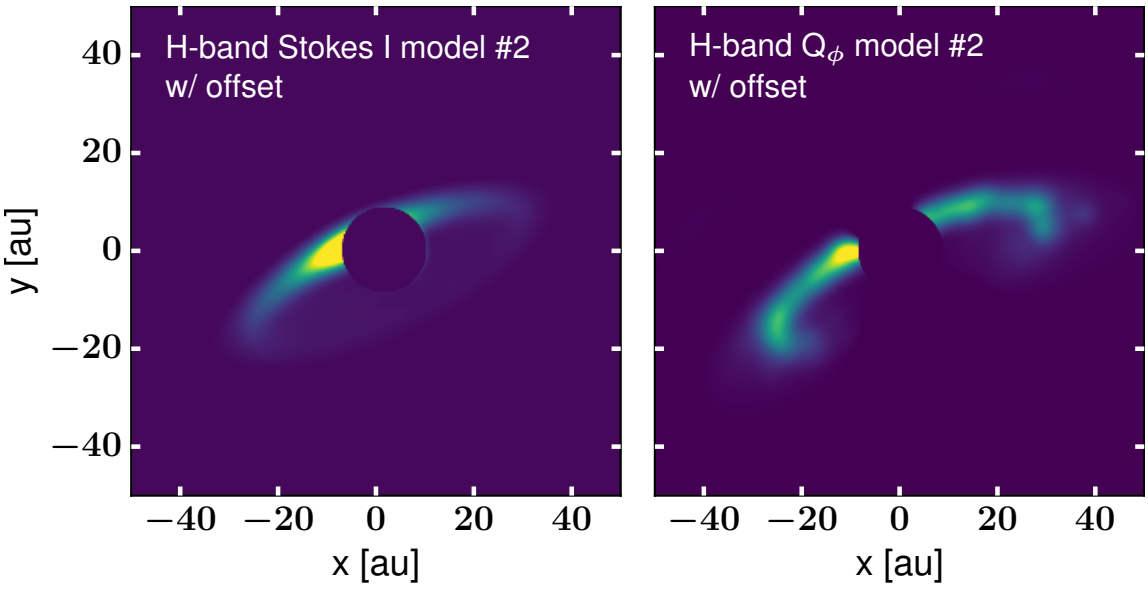

Figure 6.10: Synthetic Stokes I (left) and Q_ϕ (right) images of model #2 at H-band, where the star is slightly offset from its original central position along the semi-major axis. The images are convolved with a Gaussian PSF with FWHM of 0.″04 (at 107 pc distance). The color scales are identical to Figs. 6.5 and 6.9, respectively.

origin of the asymmetry and we explore this scenario in the following. We take our best axisymmetric model and slightly displace the star along the semi-major axis with respect to its original central position, while keeping the general disk structure unchanged. This is directly implemented into the radiative transfer code and not performed in a post-processing manner. A grid of additional models is computed, where the magnitude of the physical offset between the center of the T Cha disk and the position of its host star is changed between 0.5 and 2.5 au. We are only interested whether such a scenario is principally reliable, so we abstain from a fitting procedure. A value of $x = 2.1$ au, where x is measured along the disk's semi-major axis, represents a reasonable match. The offset we apply is equivalent to a disk eccentricity of $e \approx 0.07$. This way a brightness contrast between the east and west sides of 2 (Stokes I) and 3 (Stokes Q_ϕ) can be reached (see Fig. 6.10), consistent with the observational constraints. Other possible scenarios for the brightness asymmetry are discussed in Sect. 6.5.3.

6.4.2 Point source analysis

One companion candidate (CC) is detected in the IRDIS field of view (Fig. 6.11), whereas no point-like sources are found in the IFS image. The speckle pattern is reduced in each frame of the sequence by subtracting an optimized reference image calculated by the TLOCI algorithm (Marois et al., 2010) implemented in SpeCal. We estimate the astrometry and photometry of this companion candidate using the calibrated unsaturated PSF (Galicher & Marois, 2011) to remove biases. First, we

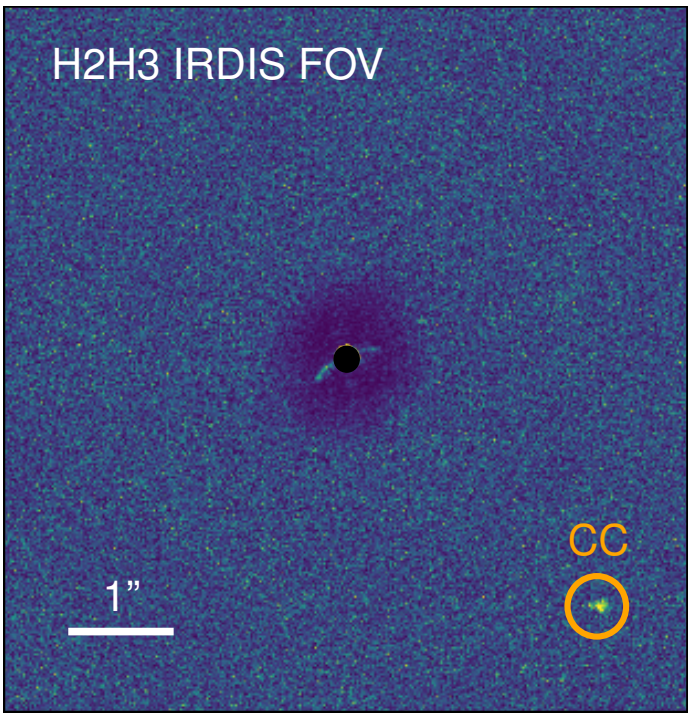

Figure 6.11: Signal-to-noise ratio map of the PCA reduction (#2) of the IRDIS *H2H3* data. The point source considered as a companion candidate (CC) is marked with a circle.

roughly estimate the flux and position of the source in the TLOCI image. The SpeCal pipeline then creates a data cube of frames that only contain the unsaturated PSF at the candidate position on the detector, accounting for the field-of-view rotation in each frame. The TLOCI coefficients used to generate the TLOCI image where the candidate is detected are applied on the candidate data cube. The resulting frames are rotated to align north up. The median of these frames provides the estimation of the candidate image in the TLOCI image. We then adjust the estimated image subpixel position and its flux to minimize the integrated flux of the difference between the real and estimated candidate images. We use a 3×FWHM diameter disk for the minimization. The 1σ error bars are the required excursions in position or in flux to increase the minimum residual flux by a factor of $\sqrt{1.15}$ (cf. Galicher et al., 2016, Galicher et al., in prep.). We empirically determine this factor running tests on sequences, in which we inject known fake planets. Using the calibrated unsaturated PSF, we also estimate the TLOCI throughput in all TLOCI sections following a procedure similar to the one used for the candidate position and flux estimation. The images were thus flux calibrated. The systematic errors for the astrometry of the detected companion candidate include the uncertainties on the pixel scale, north angle, frame centering using the satellite spots, accuracy of the IRDIS dithering procedure, anamorphic correction and SPHERE pupil offset angle in pupil-tracking mode (Vigan et al., 2016; Maire et al., 2016). The calibration uses pixel scales of (12.255 ± 0.009) mas/pix and (12.251 ± 0.009) mas/pix for the *H2* and

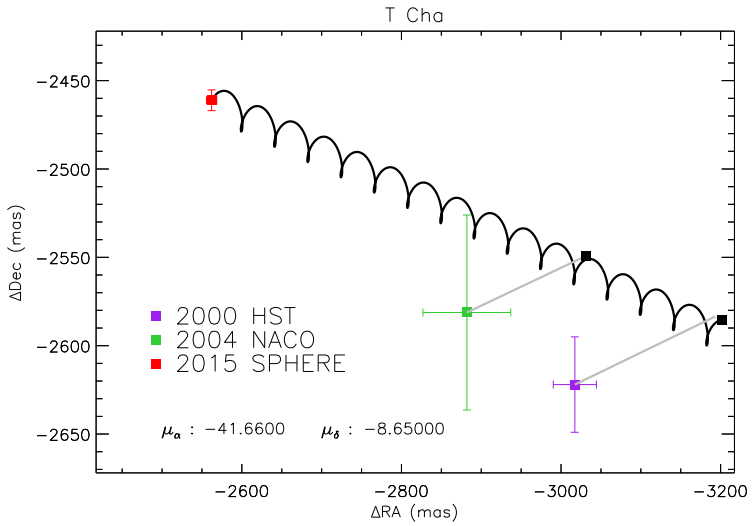

Figure 6.12: Relative astrometry of the companion candidate labeled as CC in Fig. 6.11 measured in SPHERE, NACO and HST data. The black solid line displays the motion of the companion if co-moving and the black squares are the positions expected at the time of HST and NACO observations.

H3 filters, respectively, and a true North offset of $(-1.712 \pm 0.063)^\circ$ is considered (Maire et al., 2016).

CC is located at a separation of $(3.55 \pm 0.01)''$ with contrast ($\Delta m_H = 11.63 \pm 0.04$) mag (see Table 6.3). This same companion was already detected by Chauvin et al. (2010) with $m_K = (11.4 \pm 0.1)$ mag and is also present in HST data taken in coronagraphic mode with STIS in March 2000. Combining the new position measured from SPHERE with the old data (Table 6.4) we rule out this object as being gravitationally bound to T Cha, because the motion observed over these 15 years is too large to be explained by a Keplerian orbit around this star; it is therefore a contaminant object. For completeness, given that the T Cha proper motion is $\mu_\alpha = (-41.66 \pm 0.2)$ mas/yr and $\mu_\delta = (-8.65 \pm 0.19)$ mas/yr (Gaia Collaboration et al., 2016), we also notice that CC has a high relative proper motion with respect to a background object (Fig. 6.12). For completeness, we show the color-magnitude diagram (CMD) in Fig. 6.13. We note that this plot assumes that CC is at the same distance as T Cha, since its actual distance is unknown. This is rather unlikely based on our previous conclusion that it is not physically associated with T Cha. CC is likely located much further, and thus, likely intrinsically much brighter than an object at the L-T transition. Given the H2-H3 color ∼0, it is concluded that this object could be either a floating brown dwarf or a low mass star of the galactic thick disk or halo.

Table 6.3: Astrometry and photometry relative to the star of the companion candidate in the T Cha system.

IRDIS companion candidate		
Filter	*H2*	*H3*
λ [μm]	1.593	1.667
Contrast [mag]	11.65 ± 0.04	11.60 ± 0.04
SNR	31.1	31.4
RA [mas]	-2560.3 ± 6.1	-2562.8 ± 6.0
DEC [mas]	-2460.1 ± 5.7	-2461.29± 5.7
Separation [mas]	3551.9 ± 8.2	3552.1 ± 8.1
PA [deg]	226.14 ± 0.18	226.16 ± 0.18

Table 6.4: Relative astrometry of the companion candidate for different instrumental data.

	NACO	SPHERE
Date	5 March 2004	30 May 2015
JD	2453070	2457173
Separation [mas]	3868.9±55.0	3552.0±8.2
PA [deg]	228.2±0.8	226.15±0.18

Notes. The NACO data was published in Chauvin et al. (2010).

6.4.3 Detection limits on substellar companion candidates

The IRDIS detection limits for point sources are determined using the TLOCI data reduction. We estimate the 5σ noise level, where σ is the azimuthal robust deviation of the residual flux in annuli of λ/D width rejecting pixels with no flux. Finally, the 5σ noise levels are divided by the stellar flux estimated from the unsaturated images. The maximum contrast reached with IFS is obtained by applying the PCA technique. The contrast limits are estimated by an azimuthal standard deviation, that is, between pixels at the same separation from the star, for each angular separation, corrected by the star flux (obtained from the off-axis PSF images taken immediately before and after the coronagraphic observations) and the algorithm throughput (using synthetic companions injected into the data before the data processing as described above).

In Fig. 6.14 the contrast curves obtained for the different data sets are shown. The IRDIS data give a 5σ contrast for a separation larger than 1.0″of greater than 12.5 mag in the *H2* and *H3* bands. Compared with NACO K_s-band results (cf. Chauvin et al., 2010), these observations are deeper by more than three magnitudes at a separation of 0.″7, that is, at the outer edge of the NACO coronagraph, while

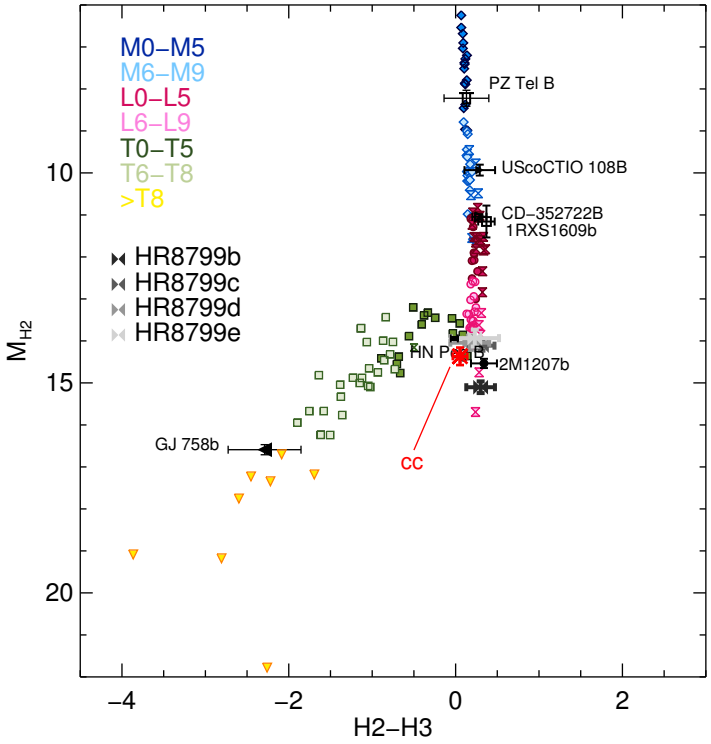

Figure 6.13: Color-magnitude diagram displaying our candidate companion, which is marked in red and labeled as CC, compared to known substellar field (colored symbols) and young objects. Note that this plot assumes that CC is at the same distance as the star. Since CC is eventually classified as a background object based on a common proper motion test (cf. Fig. 6.12), it is likely located much farther.

the contrast values at wider separations are comparable. IFS is deeper in contrast for separations closer than 0.″6 and gives ∼12 mag in the YJ-band at a separation of ∼0.″7, assuming a gray contrast between the two objects.

Using the theoretical atmospheric models AMES-COND (Allard et al., 2003) we convert the contrast limits into upper limits on the mass of possible objects orbiting around T Cha. These models are valid for $T_{\rm eff} < 1400$ K and consider that the dust immediately rains out from the photosphere after its formation. We assume a system age of 7 Myr (Torres et al., 2008). This leads to a mass limit of $\sim 8.5\,M_{\rm jup}$ in the innermost regions (∼0.″1–0.″2), decreasing to $\sim 2\,M_{\rm jup}$ for a separation between 0.″4 and 5.0″. Our new SPHERE observations, therefore, improve the NACO mass limits especially up to ∼1.5″. Both, the contrast and mass curve are cut at 0.″12. The whole coronagraph system (apodizer, mask, stop) produces a radial transmission profile, which has not been accounted for in the derivation of the detection limits. The effect is visible at the region near the edge of the mask plus λ/D, thus, we exclude the inner 0.″12. Furthermore, we note that the detection limits represent an average

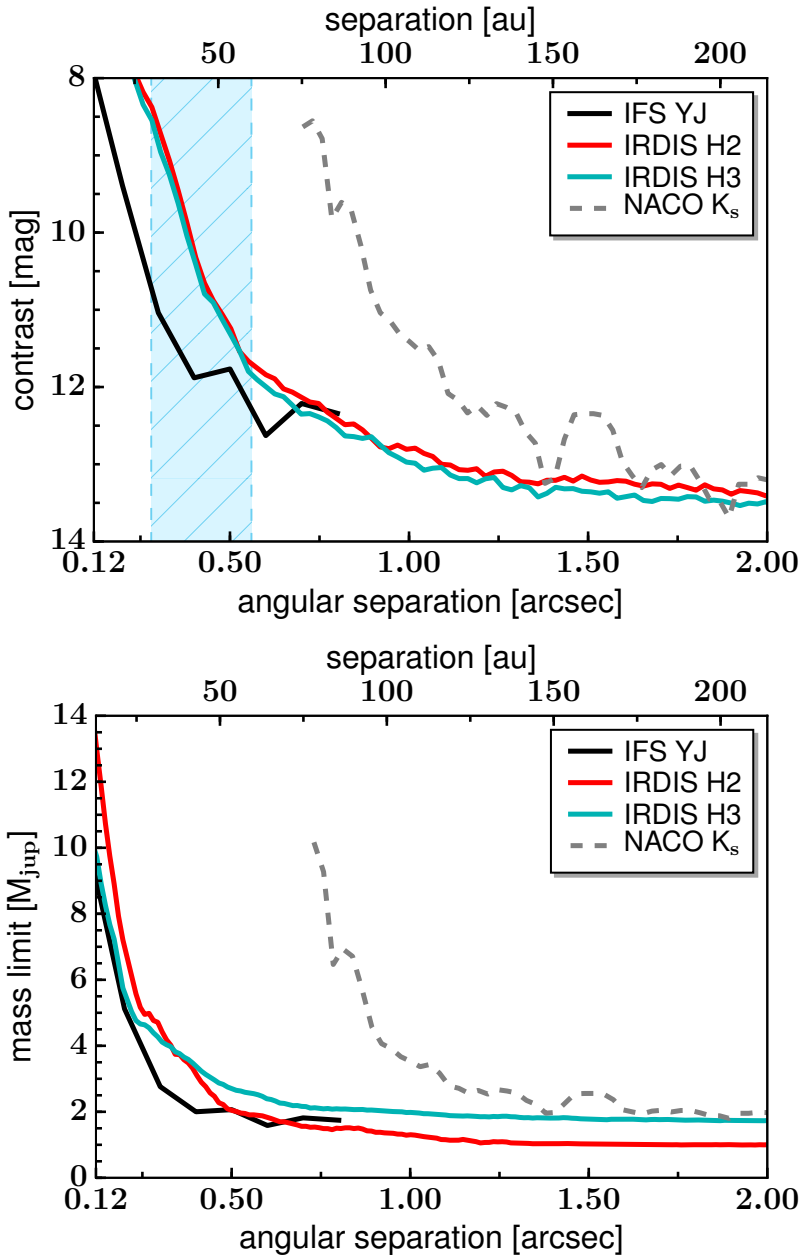

Figure 6.14: Contrast curves and companion mass limits derived for IFS (black) after applying PCA, and for IRDIS *H2* and *H3* bands (red and blue, respectively) from the TLOCI reduction (#3). Both curves have a lower cut at 0.″12. The detection limits from NACO K_s-band data are given for comparison (gray dashed line, inner cut at 0.″7). The blue striped rectangle denotes the area for which the contrast values might be slightly affected by the presence of the disk in scattered light.

value around the star, which might be affected by the disk signal at the location of the disk. However, we expect this effect to be small given the rather compact nature of the disk around T Cha.

6.5 Discussion

6.5.1 Disk geometry

Our analysis and modeling of the SPHERE data set confirms that the disk around T Cha consists of an inner disk part and an outer disk part, separated by a cavity. Compared to the previous study by Olofsson et al. (2013) we find the small dust cavity size to be larger by a factor of ∼2. Besides, it is even larger than the mm dust cavity of 20 au estimated in Huélamo et al. (2015). This is rather unexpected, as the dust trapping scenario for transition disks in the context of planet-disk interactions is supposed to work such that bigger dust is trapped at a ring located outside of the small dust/gas cavity edge (see e.g., Pinilla et al., 2012b; van der Marel et al., 2015). This possible contradiction could be, however, due to uncertainties in the model fitting of data with low resolution by Huélamo et al. (2015). An inclination angle of ∼69° and PA of ∼114° best match our SPHERE observations, which is in agreement with Huélamo et al. (2015). Our new optical and NIR data do, however, not help us to constrain the outer disk radius. In our radiative transfer model we considered a tapered density profile for the dust density description of the outer disk, meaning that the surface density falls off gradually and hence, there is a smooth decrease of the dust mass per radius bin. However, simultaneously reproducing the gas and dust components of the disk remains challenging, and including this in our modeling effort is beyond the scope of this work.

6.5.2 Grain properties

To simultaneously match the total intensity and polarimetric images obtained during our SPHERE observations, intermediate sized grains of ∼10 μm must be present in the disk's surface layers. This provides a better match with the observed properties of the disk than dust distributions covering several orders of magnitudes in size or a narrow distribution peaking at (sub-)micron size. This is in accordance with current grain growth models producing systematically larger grains, although we cannot guarantee that ∼10 μm grains are located at the upper surface layer. By means of scattered light observations in the NIR we only trace the disk surface where the micron-sized grains are located for sure. Compact grains of a few tens of microns are expected to start settling down toward the disk midplane. The efficiency and timescale of vertical mixing depends, however, on the level of turbulence in disks which is still uncertain. With strong turbulence (high α-viscosity, Shakura & Sunyaev, 1973) all grain sizes are better mixed. Thus, even larger grains can be present in the disk surface where they can contribute to the scattering. Furthermore, the amount of porosity of dust grains is unknown and still debated (e.g., Ossenkopf, 1993; Dominik & Tielens, 1997; Kataoka et al., 2014). For fractal aggregates with high porosity the phase function is supposed to differ (Tazaki et al., 2016), which might alter our grain picture for T Cha. A larger porosity for the same grain size might reduce the settling, where the size of the monomers still determines the absorption

and scattering opacities. As shown by Min et al. (2012), the appearance of a disk in scattered light could be different depending on the fraction of fluffy aggregated dust particles compared to compact grains contained in the disk. We also note that very large grains (mm size) are indeed also expected to be present in the midplane in order to match the (sub-)mm data (cf. Huélamo et al., 2015).

6.5.3 Brightness asymmetry along the disk surface

The intensity and polarized intensity distributions observed for T Cha are asymmetric with respect to the minor axis of the disk. Similar brightness variation has also been detected in other disks, such as RY Tau (Takami et al., 2013) and AK Sco (Janson et al., 2016). In our radiative transfer modeling we explored the origin of the east-west asymmetry seen along the semi-major axis in the SPHERE observations by looking into the simplest possibility of a slightly offset disk. We approximate such an eccentric disk by calculating scattered light images of an azimuthally symmetric disk, but introducing an offset between the disk center and the star. A planetary companion on an eccentric orbit could shape the outer disk into an eccentric disk, causing the offset. Keeping T Cha's stellar properties as the photon source in the radiative transfer code, but adding a positional offset, already reproduces well the observed asymmetry.

However, alternative explanations for the east-west brightness difference cannot be ruled out, and several effects may interact. Another idea is that an asymmetry in the inner disk or at the gap edges can lead to illumination effects helping to explain the dips in scattered light. The circumstellar disk around T Cha may be actually still in an early stage of planetary formation. Thus, a dense dust clump formed in the inner, densest parts of the disk, or an already formed yet undetected planetary perturber below the detection limit, could cause this asymmetry. However, this scenario also raises the question of whether such an anisotropy is indeed stationary or moves with the local Keplerian velocity. A third scenario deals with spatially variant dust properties leading to a different scattering efficiency, which is especially related to grain size, structure, and composition. A possibility would be that unequal dust grain size distributions are present in the east and west wings of the disk, whose origin, however, remains unexplained. A fourth possible scenario leading to shadows in the outer disk is an inner disk significantly tilted with respect to the outer disk's plane. However, we find this scenario unlikely, since this arrangement would rather lead to relatively sharp, dark lanes, which are not apparent in our T Cha images.

6.6 Conclusions and outlook

We have carried out VLT/SPHERE optical and NIR observations in polarimetric differential imaging mode with SPHERE/ZIMPOL in *VBB* and SPHERE/IRDIS in *H*-band of the evolved transition disk around the T Tauri star T Cha. Alongside the

polarimetric observations, intensity images from IRDIS *H2H3* dual-band imaging with simultaneous spectro-imaging with IFS in YJ-band were obtained. The disk is clearly detected in all data sets presented in this work and resolved in scattered light with high angular resolution, allowing us to review the current understanding of the disk morphology and surface brightness. The basic structure of a classical transition disk previously reported by interferometric and sub-mm studies, has been confirmed. We developed a radiative transfer model of the disk including a truncated power-law surface density profile. The conclusions of this work are summarized below.

1. Our RADMC-3D radiative transfer model with updated disk parameters accounts well for the main geometry of the disk, the cavity, and the outer disk with its bright inner rim located at $0\farcs28$ ($\sim$30 au). This is significantly further out than previously estimated. A disk inclination of $\sim$69° and a PA of $\sim$114° matches the SPHERE data sets best.

2. We confirm that the dominant source of emission is forward scattered light from the near edge of the disk, given the high disk inclination. While small grains in the Rayleigh limit scatter photons rather isotropically and absorb very efficiently, large dust grains with sizes ($2\pi a > \lambda$) have strong forward scattering properties. This demands a certain range of grain sizes to be present in the disk. We found that a power-law distribution with $a_{\rm min} = 0.01\,\mu$m and $a_{\rm max} = 1000\,\mu$m reproduces the total intensity observations well, but fails to be consistent with the polarimetric images. Thus, we propose a dominant grain size in the disk of $\sim$10 μm. Such grains bring the desired amount of forward scattering and lead to a model that is in accordance with the complete SPHERE data set presented. We note that we restricted ourselves to the analysis of Mie theory and spherical compact grains. However, for aspherical aggregates with high porosity the phase function is supposed to differ, which might alter our grain picture for T Cha.

3. Our highly inclined disk model shows a significant U_ϕ signal at H-band, which is in accordance with the observational U_ϕ/Q_ϕ peak-to-peak value of 14% and theoretical studies on multiple scattering events. The exact geometrical U_ϕ pattern observed with IRDIS is not reproduced, but the alternating structure of positive and negative lobes is well recognizable.

4. The brightness asymmetry between the east and west sides can be reproduced with a slight offset of the star's position, representing a disk eccentricity of $e \approx 0.07$. A planetary companion on an eccentric orbit could force the outer disk to become eccentric, causing this offset. However, a locally different grain

size distribution and therefore a change of the scattering properties, or illumination effects due to asymmetric structures in the inner disk could also contribute to the brightness contrast observed.

5. A previously known companion candidate is detected in the IRDIS field of view at a separation of $(3.54 \pm 0.01)''$ with contrast $m_{\mathrm{H2}} = (11.63 \pm 0.04)$ mag. We, however, rule out the possibility that this object is bound and, thus, conclude that it is not part of the T Cha system.

6. Our analysis rules out the presence of a companion with mass larger than $\sim$8.5 $\mathrm{M_{jup}}$ between $0\farcs1$ and $0\farcs3$ from the central star, and larger than $\sim$2 $\mathrm{M_{jup}}$ for wider separations. There could still be lower-mass planets in the outer disk regions and/or planets in the very inner disk.

   Previous observations with ALMA at 850 μm could not resolve the gap, and only identify two emission bumps. New mm dust continuum and gas line observations will help to understand the origin of the detected disk structures. Particularly, for further studies, one of the main goals is to investigate the wavelength, and thus grain size, dependence of the gap width and the ring-like disk emission. According to particle trapping theory in a disk that has active planet-disk interaction, mm-sized grains are expected to be located further away from the central star than micron-sized grains. On the other hand, in the case of a dead zone, the NIR and mm cavity sizes are supposed to be similar (Pinilla et al., 2016). Moreover, it has to be tested whether there is still dusty material close to the star or whether the disk hosts a full inner cavity. The activity of star-driven photoevaporation or MHD winds remove mass from the inner disk, which would vote for a cavity character. Furthermore, the search for planetary companions within the disk will be continued, which is, however, challenged by the high disk inclination.

7 | The circumstellar disk HD 169142: gas, dust and planets acting in concert?

The content of this chapter is based on Pohl et al. (2017) published in *The Astrophysical Journal (ApJ), 850, 1.* The observational data presented are part of the SPHERE GTO program and based on observations collected at the European Organisation for Astronomical Research in the Southern Hemisphere under ESO program 095.C-0273.

Details of authorship: The text was written by me, with contributions from Myriam Benisty and Paola Pinilla. Henning Avenhaus produced the final data reduction products. Paola Pinilla provided the dust evolution runs. The interpretation section benefited from discussions with my co-authors.

7.1 Motivation

The presence of one or more rings and gaps in protoplanetary disks seems to be quite a common feature, they are found in both young (e.g., HL Tau: ALMA Partnership et al., 2015; Carrasco-González et al., 2016) and rather old systems (e.g., TW Hya: Andrews et al., 2016; Tsukagoshi et al., 2016; Rapson et al., 2015; van Boekel et al., 2017), and around stars of very different spectral types (e.g., HD 100546: Garufi et al. 2016; Walsh et al. 2014; HD 97048: Ginski et al. 2016; van der Plas et al. 2017; RXJ1615.3-3255: de Boer et al. 2016). This set of observations suggests that if the origin of the multiple ring-like structures is the same for all systems, it should be a universal and long-lived mechanism. Various mechanisms have been proposed in the literature that can be assigned to three main categories: structures caused by fluid dynamics, dust evolution effects, and planet-disk perturbations. More precisely, these possibilities include zonal flows from MRI (e.g., Simon & Armitage, 2014; Béthune et al., 2016), gap/bump structures in the surface density close to the dead-zone outer edge (e.g., Flock et al., 2015; Ruge et al., 2016; Pinilla et al., 2016), efficient particle growth at condensation fronts near ice lines or a depletion of solid material between ice lines (Zhang et al., 2015; Pinilla et al., 2017; Stammler et al., 2017), aggregate sintering zones (Okuzumi et al., 2016), secular gravitational

instabilities (Youdin, 2011; Takahashi & Inutsuka, 2014), or planet-disk interactions (e.g., Zhu et al., 2011, 2012; Dipierro et al., 2015; Dong et al., 2015b, 2016a; Rosotti et al., 2016). Finally, dips or dark regions can be interpreted as shadows by inner disk material (Marino et al., 2015; Pinilla et al., 2015b; Stolker et al., 2016; Canovas et al., 2017, e.g.,).

7.1.1 The target: HD 169142

We focus on a multiple ring system in this study, more specifically, the $\sim 6^{+6}_{-3}$ Myr old Herbig A5/A8 star HD 169142 (Dunkin et al., 1997; Grady et al., 2007), located at a distance of d=117±4 pc[8] (Gaia Collaboration et al., 2016). With this new distance of 117 pc, the star is intrinsically less luminous by a factor of ∼0.65. The age estimate by Grady et al. (2007) is based on Hertzsprung-Russell (HR) placement of the companion 2MASS 18242929–2946559. Moving this star down in the HR diagram (Fig. 9 in Grady et al., 2007) leads to a revised age estimate of ∼10 Myr. Its SED shows a strong infrared excess indicating a young gas-rich disk with many emission line features (Riviere-Marichalar et al., 2016; Kama et al., 2016; Seok & Li, 2017), and a clear dip of emission in the infrared regime (Grady et al., 2007; Meeus et al., 2010), qualifying it as a transition disk. The NIR flux indicates the presence of hot dust close to the sublimation radius, resolved by NIR interferometric observations (Lazareff et al., 2017). HD 169142 still experiences gas accretion onto the star, with estimates of the mass accretion rate varying between 0.7 and $2.7 \times 10^{-9}\,M_\odot\,yr^{-1}$ (Grady et al., 2007; Wagner et al., 2015b). Garufi et al. (2017a) noted that HD 169142 has a reduced NIR excess compared to continuous Herbig disks or those hosting spirals. The NIR and MIR fluxes were also found to vary by up to ∼45% over a temporal baseline of ten years, indicating strong variability in the innermost regions (Wagner et al., 2015b).

The outer disk has a low inclination (i=13°, PA=5°) as derived by CO mm observations (Raman et al., 2006; Panić et al., 2008) and confirmed with high contrast imaging in the NIR (Quanz et al., 2013; Momose et al., 2015; Monnier et al., 2017). These images show, from small to larger separations from the star, a wide inner cavity, a bright (unresolved) ring, a second wide gap, and an outer disk that extends up to 1.7″. The inner cavity appears devoid of small dust grains, while the second gap is not. Observations with ALMA at 1.3 mm, obtained with a resolution of 0.″28×0.″18, also show two rings (0.″17–0.″28 and 0.″48–0.″64) and a gap between them (Fedele et al., 2017). The mm continuum extends up to 0.″64 while the gas extends up to twice as far. The channel maps of the 2–1 line transition of the three CO isotopologues reveal the presence of gas inside the dust gaps. Model fitting provides a drop in the gas surface density by a factor of 30–40. The two rings are also detected in VLA observations at longer wavelengths (7 mm; Osorio et al., 2014; Macías et al., 2017) and the azimuthally averaged radial intensity profiles indicate the marginal detection

[8]Note that we are using the revised value by GAIA while most of the papers in the literature use d=145 pc.

of a new gap at ∼0.″7, very close to the CO ice line (Macías et al., 2017). In addition to the disk features, a candidate massive companion was proposed, slightly inside the inner ring, at a separation of ∼0.″11 and ∼0.″16, respectively (Biller et al., 2014; Reggiani et al., 2014). Osorio et al. (2014) report the detection of a compact 7 mm emission source with VLA external to the inner ring. The detection of point-like structures in the context of potential planetary companions is discussed further in Ligi et al. (2018).

7.1.2 Outline

In this work, we report new polarized differential images of HD 169142 obtained in the J-band with the SPHERE instrument at the VLT, complemented with ALMA continuum data from Fedele et al. (2017). We investigate whether the observed rings can be explained by the trapping of dust particles as a consequence of the presence of two planets. This study on HD 169142 serves as a prototype in which it is demonstrated that multi-wavelength observations are needed to constrain the dust size distribution and physical mechanisms at work in the disk. This chapter is organized as follows. Section 2 describes the observations and the data processing. Section 3 reports on the detected disk features, Sect. 4 provides a physical disk model, and in Sect. 5 we discuss our findings.

7.2 Observations and data reduction

The observations were obtained at the VLT at Cerro Paranal, Chile, on 2015 May 02 with the SPHERE instrument as part of the GTO program. HD 169142 was observed in the J-band filter (λ_0=1.258, $\Delta\lambda$=0.197 μm) using the polarimetric imaging mode of IRDIS, with a plate scale of 12.25 mas per pixel (Maire et al., 2016), and a 145 mas-diameter coronagraphic focal mask (N_ALC_YJ_S, IWA of 0.″08, Boccaletti et al. 2008). HD 169142 was observed for ∼53 minutes on-source under moderate AO conditions (seeing of 0.″9). The analysis of the reference PSF that is estimated from a non-coronagraphic total intensity measurement shows that the observations reach a 33.8 mas × 40.8 mas resolution (FWHM along the x and y directions) and a Strehl ratio of 56%.

HD 169142 is observed using the PDI technique (e.g., Kuhn et al., 2001; Apai et al., 2004) that measures the linear polarization of the light scattered by dust grains in the disk and enables one to efficiently remove the unpolarized contribution, including that from the star. This allows to image, with high contrast, the polarized signal from the disk. In this mode, the instrument splits the beam into two orthogonal polarization states. The control of the polarization orientation is performed with a HWP that was set to four positions shifted by 22.5° in order to construct a set of linear Stokes images. We reduce the data according to the double difference method (Kuhn et al., 2001), and obtain the Stokes parameters Q and U. It is convenient to describe the polarization vector field in polar coordinates (Schmid et al., 2006;

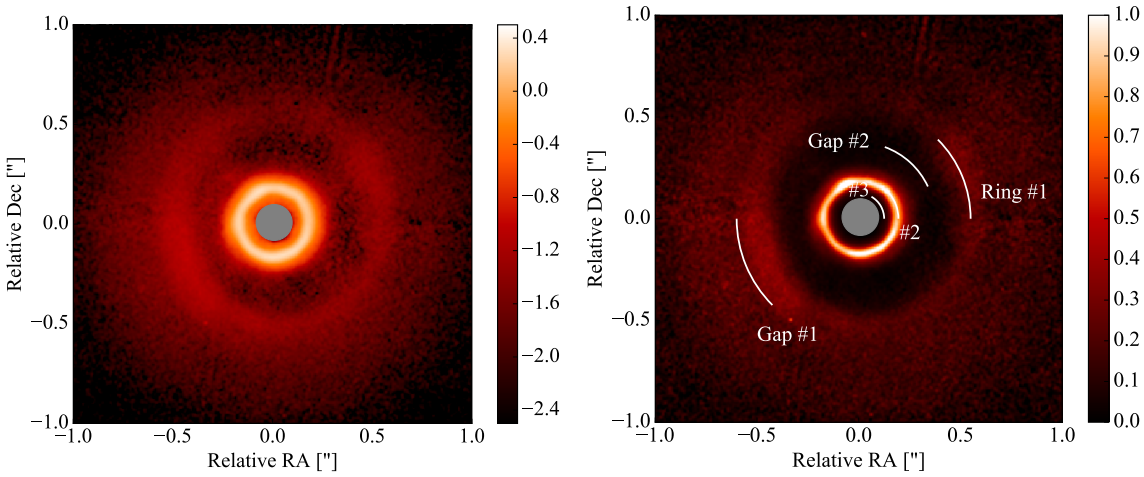

Figure 7.1: *Left:* J-band azimuthally polarized intensity image Q_ϕ in logarithmic scale for better visualization. *Right:* $Q_\phi \times r^2$ in linear scale with annotations for the gap and ring structures. Each image pixel is multiplied with the square of its distance to the star, r^2, to compensate for the stellar illumination drop-off with radius. All flux scales are normalized to half of the brightest pixel along the inner ring. The region masked by the coronagraph is indicated by the gray circle. North is up, east points towards left.

Avenhaus et al., 2014) as Q_ϕ and U_ϕ (Eq. 1.47).

In this coordinate system, under the single scattering assumption the azimuthally polarized flux appears as a positive signal in the Q_ϕ image, whereas the U_ϕ image remains free of disk signal and can be used as an estimate of the residual noise in the Q_ϕ image (Schmid et al., 2006). This is only valid for disks with face-on geometry since multiple scattering effects in inclined disks can cause a considerable physical signal in U_ϕ (e.g., T Cha: Pohl et al., 2017). The correction for instrumental polarization is done using a U_ϕ minimization by subtracting scaled versions of the total intensity frame from the Stokes Q and U frames. The final data images are corrected for the true north (by rotating them by 1.775° in the counterclockwise direction, Maire et al., 2016). We do not attempt to perform an absolute flux calibration of our images due to the inherent problems with measuring flux in PDI images.

7.3 Polarized intensity images

Figures 7.1 and 7.2 show the polarized scattered light images Q_ϕ and U_ϕ, respectively, obtained in the J-band. The U_ϕ image contains very low signal, suggesting that the assumption of single scattering is valid (c.f. Canovas et al., 2015). Figure 7.1 is similar to previously published scattered light images of HD 169142, in particular those of Momose et al. (2015) and Monnier et al. (2017), but it brings the highest SNR view of the inner ring. It shows a number of features. We detect from outside in:

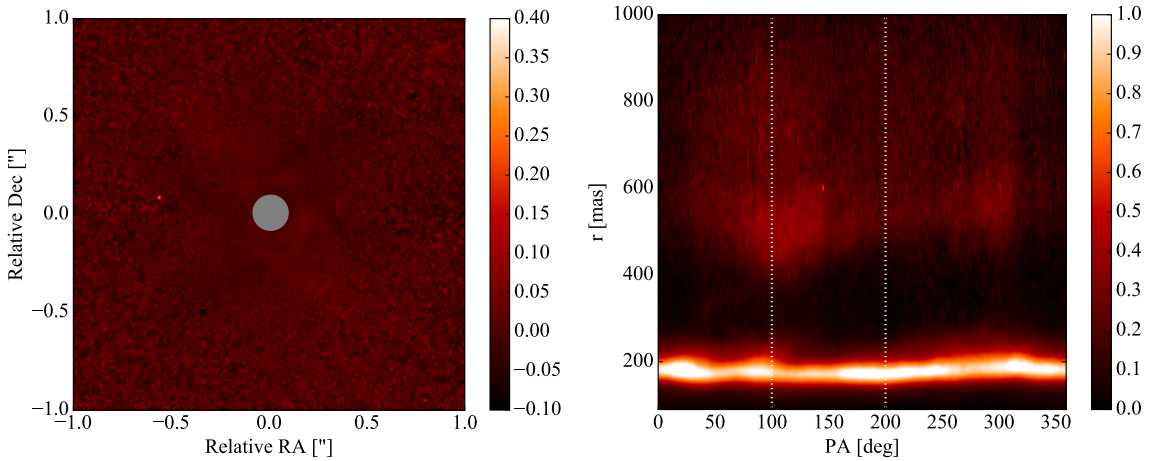

Figure 7.2: *Left:* J-band $U_\phi \times r^2$ image in linear scale. Each pixel is multiplied by the square root of its distance to the star, r^2, to compensate for the stellar illumination drop-off with radius. The normalization is similar to the Q_ϕ image, but the dynamical range of the color bar is adjusted. The region masked by the coronagraph is indicated by the gray circle. North is up, and east is toward the left. *Right:* Polar map of the $Q_\phi \times r^2$ image in linear scale. The vertical dotted lines indicate PA=100° and 200°.

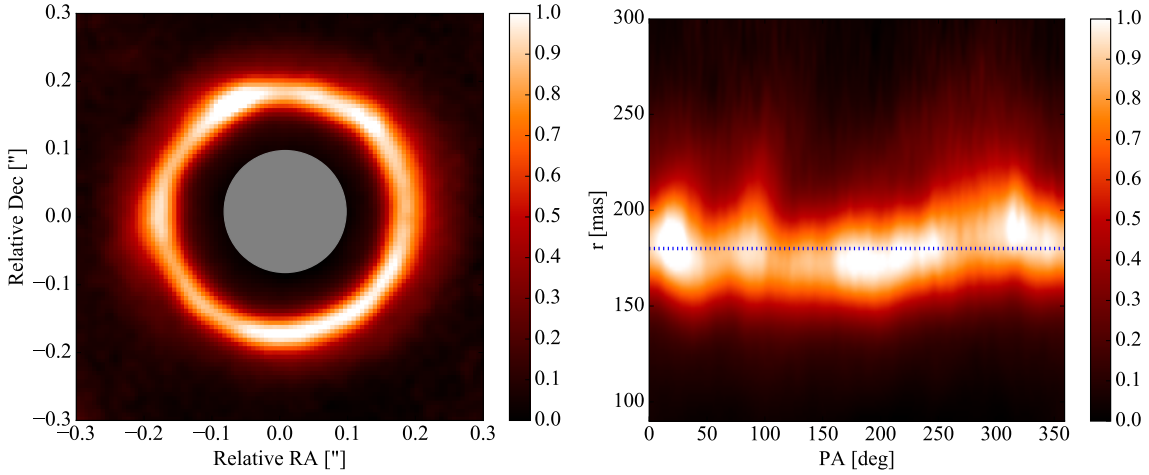

Figure 7.3: *Left:* zoom-in on the central 0.″3 of the J-band $Q_\phi \times r^2$ image. *Right:* polar map of the $Q_\phi \times r^2$ image. The flux scales are normalized to half of the brightest pixel along the ring. The horizontal dashed line indicates a radius of 0.″18.

(a) A faint gap (Gap #1) at ∼0.″70-0.″73 (81–85 au). Beyond this radius, the image shows diffuse scattered light up to ∼1.5″(∼176 au). The marginal detection of this gap can be seen in the normalized, azimuthally averaged radial profile of the surface brightness, obtained after deprojection and azimuthally averaging the image (Fig. 7.4, left).

(b) A ring (Ring #1) peaking at 0.″56 (∼66 au) with an apparent width of ∼0.″16 (∼19 au, at PA∼100°). This outer ring also shows some azimuthal brightness varia-

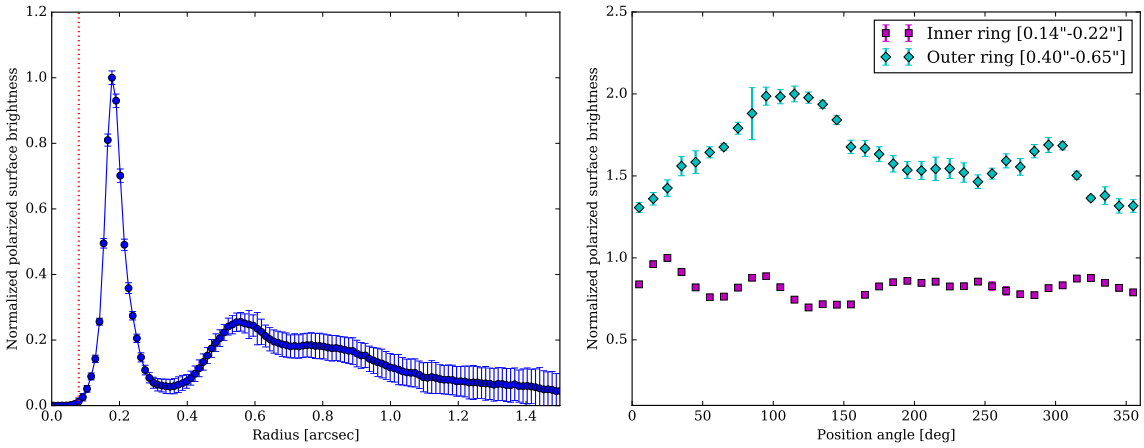

Figure 7.4: Normalized radial (*left*) and azimuthal intensity profiles (*right*) obtained after deprojection of the r^2-scaled J-band Q_ϕ image. The radial cut is obtained after azimuthally averaging and normalized to the maximum brightness of the inner ring. The red vertical dotted line is the limit of our IWA. The normalized azimuthal cuts are obtained after averaging radially between 0.″14 and 0.″22 (inner ring, purple squares) and between 0.″4 and 0.″65 (outer ring, green diamonds). The green curve is shifted vertically for clarity. The plotted error bars are the standard deviation in each bin in the U_ϕ image on a pixel basis.

tion with a dip in scattered light along PA∼-15°to 30°. This is also detected in the H- and J-band images of Momose et al. (2015) and Monnier et al. (2017).

(c) A wide off-centered gap (Gap #2), the width of which ranges from 0.″13 (∼15 au) along PA∼100° to 0.″24 (∼28 au) along PA∼ 200°. In the left panel of Fig. 7.4, it is also evident that this gap is not empty of scattering material with a lowest value of 1–2% of the peak value at 0.″35 (∼41 au). We note, however, that it could actually be emptier, with light from the adjacent rings inside and outside being convolved into the gap. An additional polar map of the full image showing the various gap widths against PA is available in Fig. 7.2.

(d) A resolved bright and narrow ring (Ring #2), located at 0.″18 (∼21 au) with an apparent width of 40-50 mas (∼5-6 au). Its brightness varies azimuthally by up to ∼25%, as evidenced by the zoom displayed in the left panel of Fig. 7.3. The regions at PAs ∼23°, 90°, 200°, and 315° are brighter than the regions at PAs ∼0°, 60°, 130°, and 275°. Figure 7.3 (right panel) shows the image in polar coordinates after deprojecting it with the inclination and PA derived from the observed kinematic pattern and line profiles at mm wavelength (i∼13°, PA∼5°, respectively). One can see that the ring does not lie on a perfectly horizontal line (at a radius of 0.″18 in the plot). This suggests that the ring is intrinsically asymmetric or could be asymmetrically illuminated due to shadowing by the inner disk. The ring might also have a non-negligible vertical extent in the image, although this is rather unlikely due to the face-on disk configuration. A detailed analysis on the geometry of this inner ring based on optical SPHERE-ZIMPOL data can be found in Bertrang et al., subm.

Table 7.1: Ellipse parameters fitted to the two rings and Gap #2 in our scattered light images.

	Ring #1	Gap #2	Ring #2
Δ RA [mas]	28.4±5.5	12.4±5.3	4.4±2.9
Δ Dec [mas]	18.9±5.7	33.5±5.4	5.3±2.8
Semi-major axis [mas]	536.4±18.2	375.2±14.5	173.8±9.1
Semi-major axis [au]	62.8±2.1	43.9±1.7	20.3±1.1
Semi-minor axis [mas]	522.7±1.2	365.6±1.5	169.3±2.0
Semi-minor axis [au]	61.2±0.1	42.8±0.2	19.8±0.2
H_s [au]	17.7±4.2	18.6±4.0	3.6±2.1

Notes. The PA of the disk is fixed to 5 deg and the inclination to 13 deg. The offset of the ellipses from the star position as well as the size of the semi-major and -minor axes are given for each fitted feature.

(e) A region with a deficit of scattered light (Gap #3) outside of our IWA (0.″08). This inner gap appears devoid of scattered light flux, but there is an unresolved inner disk with accretion as discussed in Grady et al. (2007) and Wagner et al. (2015b).

Fig. 7.4 (right panel) shows the azimuthal cuts along the two rings after deprojecting the Q_ϕ image and radially averaging over their apparent widths (between 0.″14 and 0.″22, and between 0.″40 and 0.″65, respectively). One can see that both the inner and outer rings host clear azimuthal variations. The outer disk appears brighter along PA∼110-120°, i.e. close to the minor axis of the disk. To better characterize the rings and Gap #2, we attempt to fit ellipses to the image. We follow the procedure described in detail in de Boer et al. (2016) and Ginski et al. (2016): we consider 10^6 annuli for each feature and find the annulus for which the flux is maximized (for the rings) or minimized (for the gap). To reduce the number of free parameters, we fix the inclination and PA of the ellipses to the values inferred from sub-mm interferometry (Panić et al., 2008). Our best fit result is shown in Tab. 7.1. We give the offset of the ellipses from the star position (ΔRA and ΔDec), as well as the size of the semi-major and -minor axes for each fitted feature. Our error bars are estimated as the standard deviation of the best 1% fits (i.e. the 1% fits with the highest flux in the resulting aperture for the rings). Figure 7.5 shows a schematic view of a disk/ring system to show the basic principle on estimating the scattering surface height $H_{s,\tau=1}$ from the offsets derived. It can be determined via

$$H_{s,\tau=1} = \frac{r_{proj}}{\sin(i)} \tag{7.1}$$

where i is the ring inclination with respect to the line of sight and r_{proj} is the projected distance of the ellipse center to the star center position. All of the offsets that we

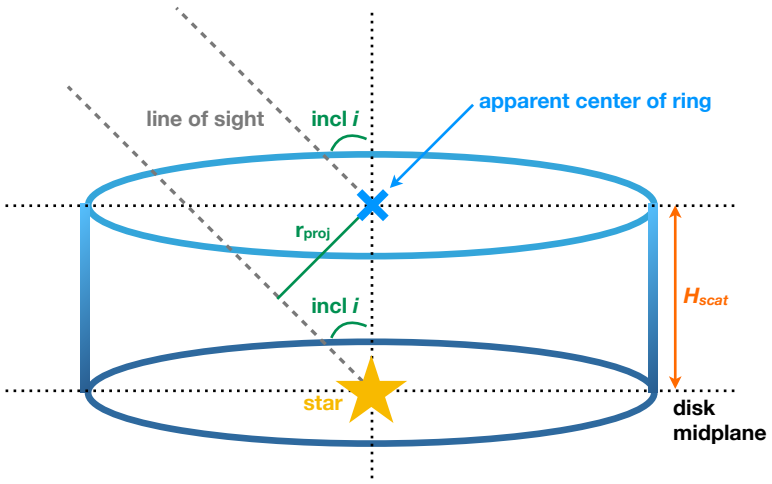

Figure 7.5: Schematic view of the scattering surface height H_s of a circular ring observed at an inclination i.

measure for the best ellipse fits are toward the northwest direction (as in Momose et al., 2015), which suggests that the southeast side of the disk is the near side of the disk. We note that the direction of the offsets is not solely perpendicular to the semi-major axis. Hence, assuming that the used inclination and PA are correct, these offsets do not only trace geometrical effects. That means only the component of the offset along the minor axis can be considered to compute the disk surface height (Table 7.1). The remaining offset could then be led back to an actual disk eccentricity.

Comparison to previous observations

The SPHERE/IRDIS J-band image is very similar to the H-and J-band images obtained by Momose et al. (2015) with Subaru/HiCIAO and by Monnier et al. (2017) with Gemini South/GPI three years and one year before our observations, respectively. This suggests that the observed azimuthal asymmetries are not due to shadowing from the innermost disk. Dynamical structures in the inner disk would evolve significantly on timescales of years (cf. discussion in Sect. 7.5.6). The two rings in our image are approximately co-located with the two rings detected in the ALMA mm dust continuum (Fedele et al., 2017) as shown in Figs. 7.6 and 7.13. More precisely, the peaks of the two rings at mm are slightly further out than in our SPHERE scattered light data (∼28 au and ∼70 au versus ∼21 au and ∼66 au), consistent with current dust trapping scenarios for planet-disk interactions. Although Gap #2 does not appear devoid of small dust grains, the ALMA image shows no continuum detection in both the inner (Gap #3) and wide (Gap #2) gaps. This indicates that dust particles, independently of their sizes, are filtered out in the inner gap, but that the filtering mechanism at play in the outer gap affects small and large dust grains

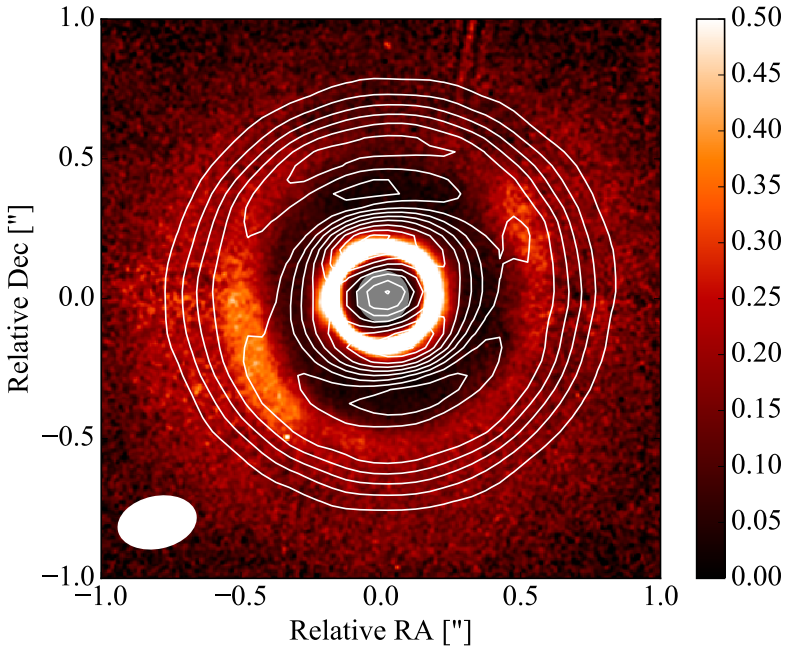

Figure 7.6: SPHERE/IRDIS r^2-scaled J-band Q_ϕ image overlaid with contours of the ALMA 1.3 mm continuum image (from Fedele et al., 2017). The white ellipse in the bottom left corner shows the ALMA beam with a size of $0\farcs28 \times 0\farcs18$. The Q_ϕ image is normalized in the same way as in the right panel of Fig. 7.1, but the color scale is chosen such that the structures in the outer disk are enhanced and the inner ring is saturated.

differently. The inner ring (Ring #2) is also well detected in VLA 7 mm and 9 mm observations (Osorio et al., 2014; Macías et al., 2017), although at a slightly larger radius of ∼25 au compared to ∼21 au in scattered light). Furthermore, Macías et al. (2017) also report on the detection of a third gap at ∼85 au, consistent with the marginal detection in the SPHERE polarized intensity data.

7.4 Disk modeling

We start our models by introducing planet-induced depressions in a uniform disk gas density profile to mimic the position and shape of the observed gaps. We present physical simulations including dust evolution and trapping processes to constrain the disk dust distribution and to investigate whether planet-disk interactions are responsible for the detected substructures. We take the approach of fixing as many parameter values as possible and do not attempt a best-fitting procedure. Because of the high parameter degeneracy when physical processes related to dust evolution are involved, we do not explore a large grid of these models. Our concept is complementary to the one presented by Monnier et al. (2017), who showed a parameterized model without connecting the gap and ring structures to a planetary origin or dust evolution. In their model, the scale height of an inner and outer disk region, and the

density scaling factor for the outer gap are determined via a fitting process.

7.4.1 Model set-ups

In our models, we consider two spatially separated planets that are massive enough to open a gap in the gas surface density. The planet cores are assumed to be at fixed orbits and are not allowed to migrate. We note that we constrain the total number of planets to two, although multiple low mass planets in close-by resonances could exist to cause the second, wide gap (Gap #2). The perturbed gas surface density profiles Σ_g depend on the planet masses and on the disk viscosity. To derive Σ_g, the analytical solution of Crida et al. (2006) is considered, in which the gravitational and pressure torques are assumed to be zero very close to the planet. For this reason, a correction for the depth of the gap is implemented using the empirical relation from Fung et al. (2014). The details on analytical gap profiles can be found in Sect. 1.2.3. The resulting gas surface density distributions are used as inputs to model the dust evolution considering the dust dynamics, including the processes of coagulation, fragmentation, and erosion of dust particles (Birnstiel et al., 2010; Pinilla et al., 2015a). For the background surface density profile we use an exponentially tapered power law with a power index of 1 and a tapered radius of six times the location of the inner planet. As the inner gap appears relatively devoid of scattering material and free from larger grains, we consider a planet-to-stellar mass ratio of 2×10^{-3} ($3.5\,M_{jup}$) for the inner planet, such that the gap is deep enough to lead to a filtration of particles of all sizes. For the second gap being filled with small particles, we consider the mass of the outer planet close to the mass estimate obtained in Osorio et al. (2014) in this region, and we choose 0.7 and $0.3\,M_{jup}$, the latter being the minimum mass needed to open a gap in the gas surface density (and hence to have a pressure trap at the outer edge of the gap) under our assumptions. The locations of the planets are chosen to be $r_1 = 14$ au and $r_2 = 53$ au, such that the pressure maxima are close to the observed peaks of the mm emission. The companion masses considered in our simulations are compatible with the detection limits obtained in total intensity with IRDIS and IFS of SPHERE. These data will be presented in detail in the F100 SHINE data analysis and detection performance paper (Langlois et al., in prep.). The disk temperature profile is a power law ($\sim r^{-0.5}$, cf. Eq. 25 in Birnstiel et al., 2010) such that at 1 au the temperature is ∼230 K. An α-viscosity of 10^{-3} is assumed throughout the disk and we note that this choice also influences the planet masses assumed (cf. Sect. 1.2.3). Furthermore, a disk mass of $5 \times 10^{-3}\,M_\odot$ is considered which is consistent with the value range reported by Panić et al. (2008), and a disk radial extension from 1 to 300 au. The initial gas-to-dust ratio is 100 and particles are initially 1 μm in size. The model follows the evolution of 180 grain sizes (from 1 μm to 2 m) and calculates the dust density distribution at each radius for time scales from 10^4 to 10^7 yr. We do not consider the effect of ice lines on the dust dynamics.

To compute synthetic images, the resulting dust distribution is considered as input to the radiative transfer code RADMC-3D (Dullemond et al., 2012). From the

vertically integrated dust density distribution, we derive the dust density for each grain size $\Sigma_d(r, a)$. From the temperature profile $T(r)$ used in the dust evolution, the pressure scale height $H_p(r)$ is determined. We take the approach in Pohl et al. (2016) and calculate the dust scale height for each grain size a following Birnstiel et al. (2010) as

$$H_d(r, a) = H_p(r) \times \min\left(1, \sqrt{\frac{\alpha}{\min(\mathrm{St}, 1/2)(1 + \mathrm{St}^2)}}\right), \tag{7.2}$$

where α is the turbulent viscosity and St is the Stokes number (cf. Eq. 1.26), a dimensionless parameter that indicates how well a dust grain is coupled to the gas. In the Epstein regime, valid for most regions of protoplanetary disks and where the molecular hydrogen mean free path is larger than 4/9 times the grain size, the Stokes number at the midplane is given by Eq. 1.27, with ρ_s the volume density of the dust grain, typically $\sim 1.2\,\mathrm{g\,cm^{-3}}$ according to the averaged values of the volume density for silicates. Dust grains with sizes corresponding to St$\sim$1 are subject to the strongest gas drag and move fast to the regions of pressure maxima (see Sect. 1.2.1). From the dust surface density and scale height, we compute the volume density profile for each grain size as

$$\rho(R, \phi, z, a) = \frac{\Sigma_d(R, a)}{\sqrt{2\pi} H_d(R, a)} \exp\left(-\frac{z^2}{2 H_d(R, a)^2}\right), \tag{7.3}$$

where $R = r\sin(\theta)$ and $z = r\cos(\theta)$ are cylindrical coordinates and θ the polar angle. The opacity calculation of each grain size bin takes into account porous spheres with a dust mixture composed of astronomical silicates (Draine, 2003), carbonaceous material (Zubko et al., 1996), and water ice Warren & Brandt (2008). The fractional abundances of 7%, 21% and 42% (amount of vacuum is 30%) are adopted from Ricci et al. (2010b). The temperature structure of each dust grain size is determined with a Monte Carlo radiative transfer simulation and synthetic scattered light images are computed including the full treatment of polarization. Mie theory is used to compute the Mueller matrix elements. These images are convolved by an elliptical Gaussian PSF ($0\farcs034 \times 0\farcs041$), chosen to mimic the angular resolution of our SPHERE observations, and each pixel is multiplied by the square of its distance to the star to compensate for the stellar illumination drop-off with distance. For the synthetic mm observations, a beam size of $0\farcs3 \times 0\farcs2$ is considered (Fedele et al., 2017).

For comparison reasons, we additionally perform simplified models by neglecting the self-consistent dust evolution, that is, the dust growth and its dynamics. However, there are mm grains in these models, so significant evolution has taken place here as well. In this second approach, we consider the same initial gas density profile perturbed by the two giant planets and assume a fixed gas-to-dust ratio exploring the range from 50 to 100, a simple approach typically used to compare scattered

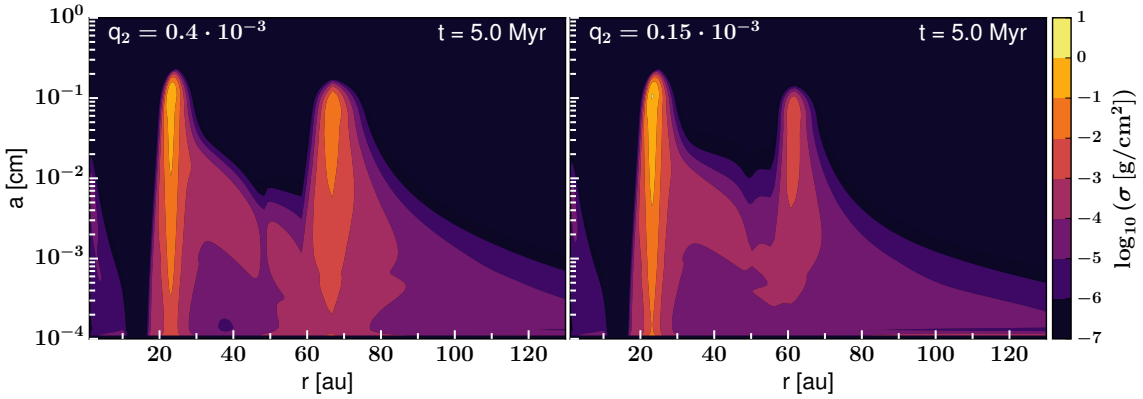

Figure 7.7: Vertically integrated dust density distribution after 5 Myr of evolution, when two massive planets (*left:* 3.5 and 0.7 M_{jup}, *right*: 3.5 and 0.3 M_{jup}) are embedded in the disk at 14 au and 53 au, respectively.

light images with hydrodynamic simulations of planet-disk interaction (e.g., Dong & Fung, 2017). This approach is valid as long as the micron-sized particles are well coupled to the gas and no self-consistent dust settling is included. However, these simplified models are expected to differ from dust evolution models because several processes, such as growth and fragmentation, can change the dust distribution in the disk, which at the same time changes the dynamics, in particular when pressure maxima are present (cf. Fig. 7.7). In these simplified models, an average opacity is used considering a power-law distribution for the grain size, where the number density follows $n(a) \propto a^{-3.5}$ with $a_{\rm min} = 0.01\,\mu$m and $a_{\rm max} = 1$ mm. For all models, the following stellar parameters are considered: $T_{\rm eff} = 8400$ K, $M_* = 1.65\,M_\odot$ and $R_* = 1.5\,R_\odot$, hence $10\,L_\odot$ (Dunkin et al., 1997; Blondel & Djie, 2006; Fedele et al., 2017). The stellar luminosity adopted in Fedele et al. (2017) is based on the new distance estimate from Gaia (d=117 pc). For the stellar spectrum a Kurucz spectrum of a star with metallicity [Fe/H]=0 and a surface gravity of $\log g = 4.5$ is taken into account (cf. Folsom et al., 2012).

In addition, as we do not know the shape of the innermost disk (masked by the coronagraph), and because the presence of a tiny amount of dust could alter the brightness signal close to the inner peak, we set the dust density to a floor value within 10 au and apply a smooth Gaussian taper to create a rounded inner rim for the inner ring. This step is especially needed in the simplified models, because in the models with dust evolution included, most of the dust particles are filtered out and trapped at the outer edge of the gap opened by the innermost planet, and hence in these models the inner disk is anyway almost empty of grains. However, we note that a tiny inner disk exists as presented in Lazareff et al. (2017).

7.4.2 Results

Figure 7.7 (left panel) shows the dust density distribution after 5 Myr of evolution for planet masses of 3.5 M_{jup} and 0.7 M_{jup} located at 14 au and 53 au, respectively.

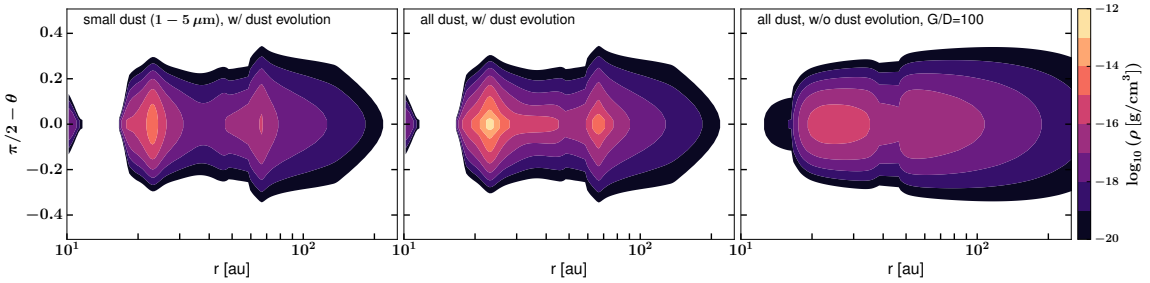

Figure 7.8: Vertical disk density structure assumed for the radiative transfer calculations following Eq. 7.3 for an outer planet mass of $0.7\,M_{jup}$. The cumulative density distribution for small dust grains only from $1-5\,\mu$m (*left*), for all dust grains (*middle*) and for the simplified parametric approach (*right*) are shown. Note that the radial scale is logarithmic for a better visualization.

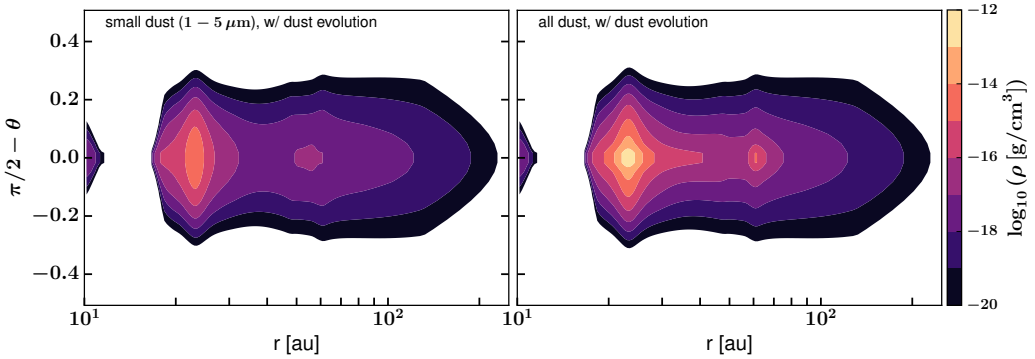

Figure 7.9: Vertical disk density structure assumed for the radiative transfer calculations following Eq. 7.3 for an outer planet mass of $0.3\,M_{jup}$. The cumulative density distribution for small dust grains only from $1-5\,\mu$m (*left*) and for all dust grains (*right*) are shown. Note that the radial scale is logarithmic for a better visualization.

A pressure bump is formed at the outer edge of each gap that acts as a particle trap and helps to reduce the radial drift. The higher the mass of the planet, the more efficient is the trapping and the higher is the mm flux (Pinilla et al., 2012b, 2015b). This trend is also seen in Fig. 7.7 (right panel), where the second planet has a lower mass ($0.3\,M_{jup}$), leading to less efficient trapping there. Although the trapping of mm grains is effective, the values for the planet mass (at the considered disk turbulence) are chosen such that the small grains are not fully filtered out. Note that there is a degeneracy between the choice of disk mass, temperature, $\alpha-$turbulence, and planet mass, thus, we do not claim to infer mass limits for potential planets. The density contrast between the two rings also depends on whether the planets formed simultaneously or sequentially (Pinilla et al., 2015a) and whether they migrate. Applying Eq. 7.3 to the dust density distributions results in the vertical density structure illustrated in Fig. 7.8 (left and middle panels) and 7.9. While the small grains are distributed radially over the disk extension and all the way up to the disk surface layers according to their dust scale height, the large grains are concen-

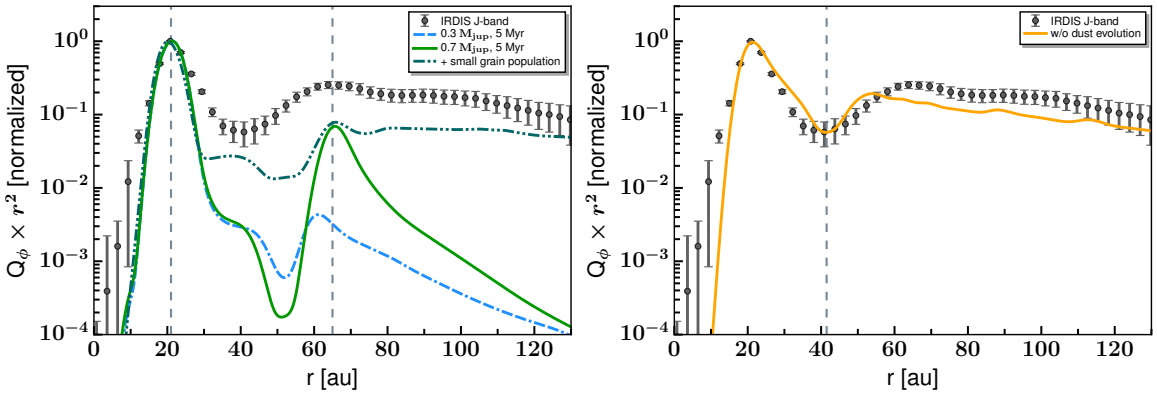

Figure 7.10: Comparison of surface brightness radial profiles of the $Q_\phi \times r^2$ model image at J-band. The values are scaled by the square of the distance from the central star in order to compensate for the falloff of the stellar irradiation. Models with self-consistent dust evolution are shown in the left panel, and that with a simplified parametric grain size distribution is shown in the right panel. The vertical dashed lines mark the positions of the brightness peaks (*left*) and the location of Gap #2 (*right*), respectively.

trated at the pressure bump regions close to the midplane. For comparison, Fig. 7.8 (right panel) shows the vertical density structure of our simplified approach, where no grain growth model is involved and a fixed gas-to-dust ratio of 100 is considered. In this case, a larger amount of dust is still present within the two gap regions and in the outer disk because the dust radial drift is neglected.

Scattered light

Figure 7.10 shows the radial surface brightness profiles of the $Q_\phi \times r^2$ model images compared to the observational radial profile (also shown in Fig. 7.4). All profiles are normalized to the peak flux of the inner ring (Ring #2). The brightness of this ring in scattered light is highest because of the geometry of the disk scattering surface. The incidence angle of stellar radiation is steepest here so that the disk receives and scatters the most light per unit surface area. This is due to density effects given the large amount of dust there and the temperature profile. The curves in the left panel are based on our dust evolution modeling approach. The solid green curve representing the model with a higher outer planet mass well reproduces the two main ring locations observed with SPHERE, but there is a discrepancy for the brightness contrast between the rings. Although the overall width of Gap #2 matches the observations, a gap much deeper and with sharper edges than observed is produced by our model. Reducing the mass of the outer planet helps to create a slightly shallower outer gap edge (dash-dotted blue curve). However, in this case, the amount of dust that is trapped in the outer disk is lower, and consequently, the brightness of Ring #1 decreases. In addition, the peak of this outer ring moves slightly inward when the planet mass is reduced, differing from the observations. In both cases, the outer disk in our models appears too faint in scattered light, as

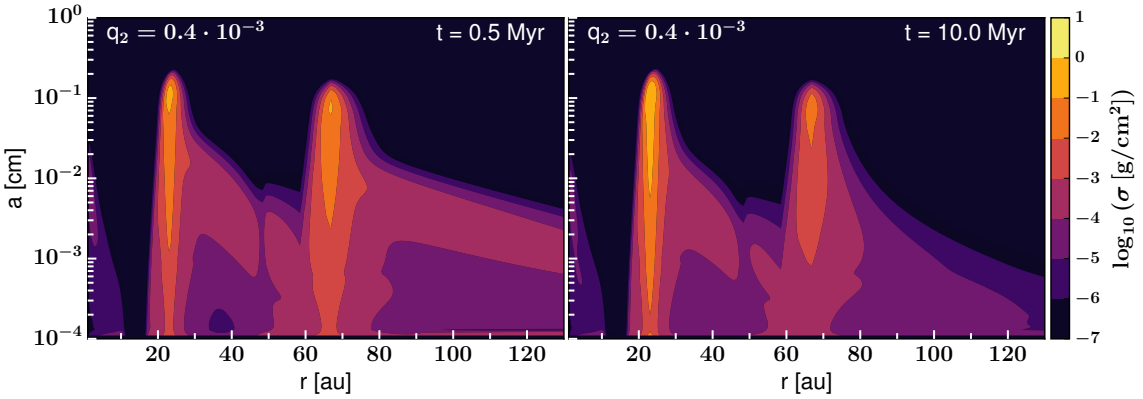

Figure 7.11: Vertically integrated dust density distribution after 0.5 Myr (left) and 10 Myr (right) of evolution, when two massive planets (3.5 and 0.7 M_{jup}) are embedded in the disk at 14 au and 53 au, respectively.

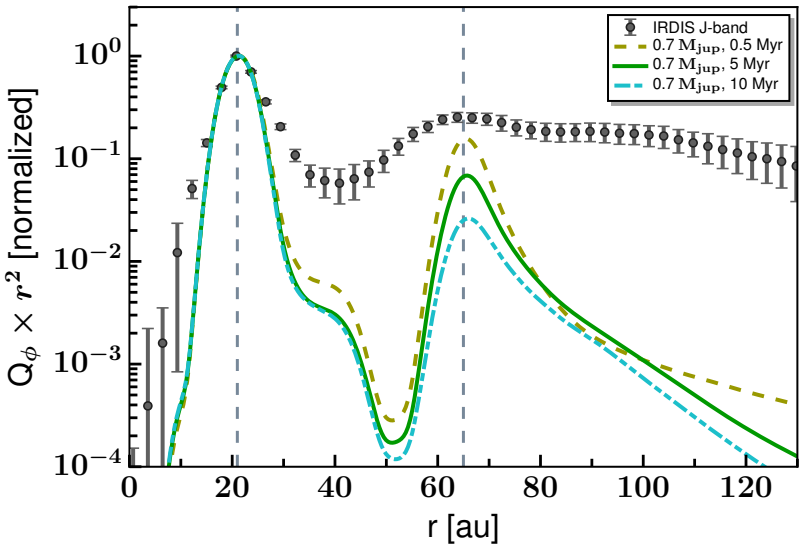

Figure 7.12: Comparison of surface brightness radial profiles of the $Q_\phi \times r^2$ model image at J-band for different dust evolution timescales. The values are scaled by the square of the distance from the central star in order to compensate for the falloff of the stellar irradiation. The vertical dashed lines mark the positions of the brightness peaks.

all dust grains originally located in the outer disk have already grown and drifted inward, even after an evolutionary time of 0.5 Myr (see Fig. 7.11 and dashed olive curve in Fig. 7.12).

The orange line in the right panel illustrates a good match for our simplified approach that ignores dust growth and fragmentation processes and assumes a power law for the dust size distribution. The gap location between the two main rings can be reproduced well when moving the second planet position further in from 53 au to 42 au. The reason why the planet position needs to be different between the dust evolution models and the simplified approach is as follows. The gap in the small

grains is similar in shape to that of the gas surface density, since the small grains are well coupled to the gas. Contrarily, in the dust evolution models, there is a dominating peak of emission at the pressure maximum, which is further out from the outer edge of the gas gap and where small grains are continuously reproduced by fragmentation due to turbulent motions (Pinilla et al., 2012b). The shallowness of the gap better matches compared to the dust evolution approach. However, a simultaneous fit of gap depth and ring positions is not possible either. This trend is also seen in the HD 169142 model-fitting results by Monnier et al. (2017), where either the gap depth or the outer ring position is off compared to the GPI J- and H-band profiles.

Mixed midplane-surface dust models

At this point of the analysis, it seems that the model without dust evolution does a significantly better job in reproducing the SPHERE scattered light observations, which is, however, not the case for the mm dust continuum as demonstrated later in Sect. 7.4.2. One has to keep in mind that dust evolution assumptions are developed for the disk midplane, where dust growth is quite efficient due to the high densities. Since the dust evolution models are only 1D, the vertical disk structure chosen influences the situation at larger height. More precisely, the coagulation equation itself is not only calculated in the midplane, but it averages the processes with presumed weights over the vertical structure. Then, it assumes that the size distribution at a given location develops as a whole, followed by a redistribution of the grains. There is also a reservoir of small grains produced that are going through the growth and fragmentation cycle. It might be that the vertical exchange in the dust evolution is not working properly and that there are small grains at the disk surface that do not grow quickly at high altitude where the densities are lower. If this population at the top layer is indeed isolated, its coagulation compared to the midplane situation will also be on a different time scale. Moreover, charging effects could play a role for dust evolution processes at the disk surface, which would keep the particles very small.

Hence, as a test, a new population of small grains (0.01–0.5 μm) is introduced that follow the initial gas density distribution of the dust evolution model with a mass fraction of $8 \times 10^{-4}\,\Sigma_{\rm disk,gas}$. The mass in the other size bins is reduced correspondingly to keep the same dust mass as that for the original dust evolution simulation. This model is displayed in Fig. 7.10 with the dash-dotted dark green line. It helps to decrease the gap depth and to increase the scattered light in the outer disk.

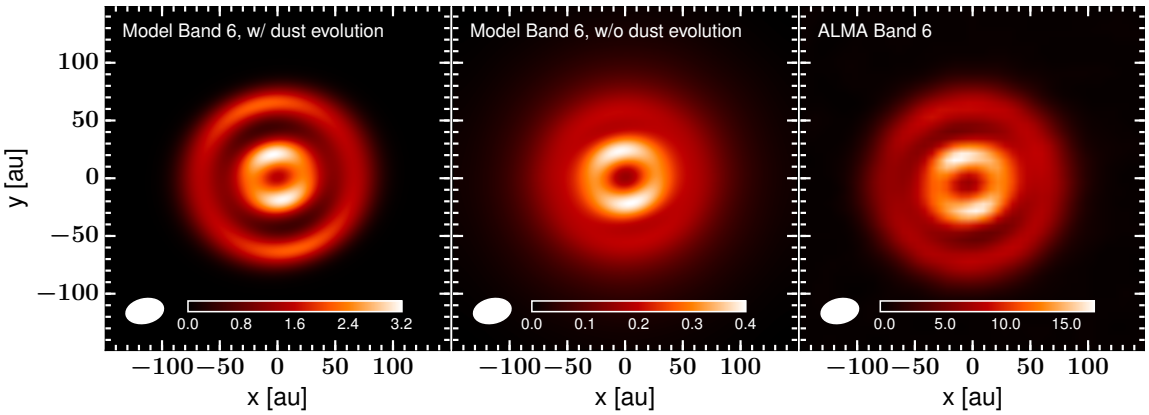

Figure 7.13: Simulated intensity images of HD 169142 for ALMA Band 6 (1.3 mm) based on the radiative transfer models. The images are smoothed to the same angular resolution as in Fedele et al. (2017). The intensity units are mJy/beam.

Millimeter dust continuum emission

Figure 7.13 shows synthetic mm continuum images at 1.3 mm for our two representative models (solid lines in Fig. 7.10) alongside the ALMA data from Fedele et al. (2017). The left panel considers our self-consistent dust growth model. This results in an inner dust cavity, an inner ring between ∼15 and 35 au (0.″13 and 0.″3), and an outer ring between ∼55 and 80 au (0.″47 and 0.″68), with a gap in between. Both the inner cavity and the gap are depleted in mm-sized dust particles. Our model is qualitatively consistent with the ALMA dust continuum image showing rings at ∼20–35 au and ∼56–83 au. This agreement supports the view that the efficient dust trapping scenario by means of the two giant planets may be at work in HD 169142. The relatively sharp outer edge of the continuum map gives further evidence of large dust grains radially drifting inward (cf. Birnstiel & Andrews, 2014; Facchini et al., 2017). For completeness, the synthetic image for our simplified fixed gas-to-dust ratio model without dust evolution treatment is also shown. The clear depletion of dust particles within the gap region is not seen in this case. Furthermore, the outer ring is more extended and both the inner and outer edges are less well defined, leading to a fuzzier overall disk structure. We note that the flux is underpredicted in both model scenarios compared to the actual ALMA measurement.

Spectral energy distribution

The SED predictions for our different simulations with and without self-consistent dust evolution are compared to the measured fluxes (from Dent et al., 2006; Fedele et al., 2017) in Fig. 7.14. The impact of dust and disk structure parameters on the SED is large, making the fit very degenerate (e.g., Thamm et al., 1994). The photometry in the sub-mm and mm regime within its uncertainties is reproduced with both the dust evolution model (solid green) and the simplified parametric model (dashed blue), indicating a relatively good model value for the outer disk mass, the

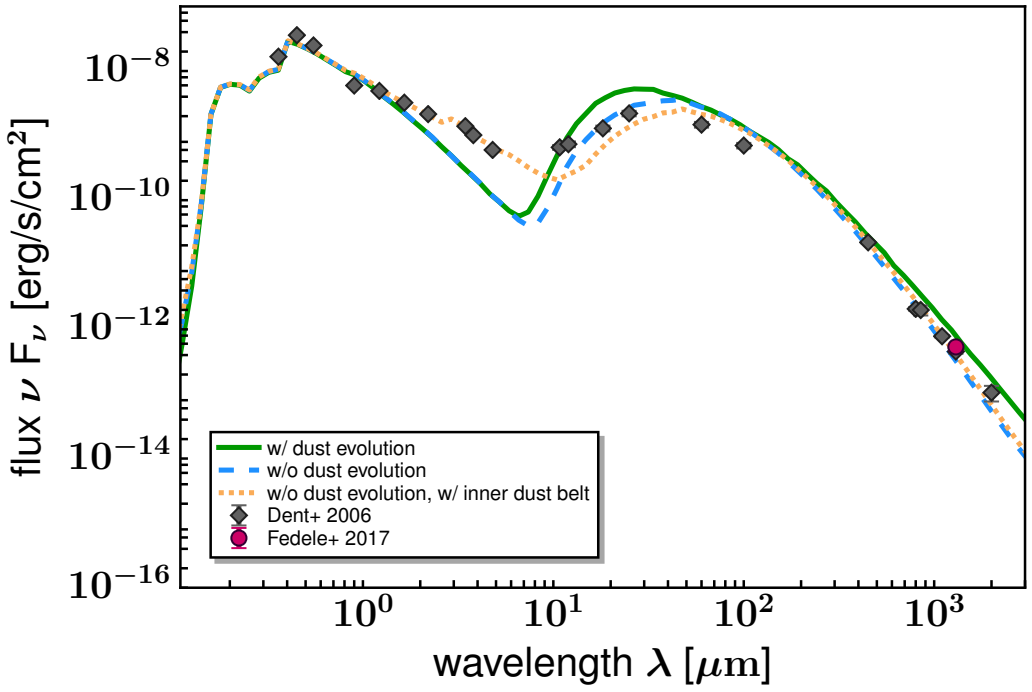

Figure 7.14: SED models for HD 169142 with (solid green) and without (dashed blue) self-consistent dust evolution, where the inner disk material up to 10 au is removed. The dotted orange line corresponds to the simplified model without dust evolution, where an inner dust belt is included. The flux density measurements are taken from the compilations of Dent et al. (2006) and Fedele et al. (2017).

maximum grain size and the grain size distribution. We remind here that the models without self-consistent dust evolution also include mm grains, so significant evolution has taken place. A model that is really without any evolution would be a model with small grains only, and that does not give a good fit at all.

However, both models underestimate the NIR excess and overestimate the MIR to FIR excess. Decreasing the disk scale height affects the SED especially at wavelengths between 10 and 200 μm. With a smaller scale height the disk intersects less stellar light, which produces a colder disk interior and less thermal radiation. As shown in Woitke et al. (2016) alternative possibilities exist to reduce the MIR and FIR emission, such as reducing the flaring index. As expected, our models without dusty material in the very inner disk fail to reproduce the NIR excess. We acknowledge that the presence of an accretion disk is already known, but determining its exact morphology cannot be achieved with our scattered light measurement and is beyond the scope of this work. In the case of HD 169142, Monnier et al. (2017) introduced a coplanar inner disk ranging from 0.2 to 0.5 au with an inner edge scale height of 0.006 au in order to fit the NIR excess. Instead, Wagner et al. (2015b) added an optically thin inner spherical halo. In this way, optically thin material at high altitude can reprocess a significant fraction of the stellar light. We exemplify that even a narrow dust belt improves the agreement at NIR considerably. It also

reduces the too high excess in the 10–100 micron regime as the inner disk casts a shadow on the outer disk, which will decrease the latter's scale height. The dotted orange line in Fig. 7.14 considers our simplified model and additionally, an inner dust belt from 0.05 – 0.09 au (Chen et al., 2017). The scale height is proportional to $r^{1.1}$, where the scale height at the inner rim is set to 0.005 au. The inner disk radial density is proportional to $r^{-1.0}$ and the dust mass is chosen to be $5 \times 10^{-11}\,M_\odot$. The overall dust mass of the disk has to be increased by a factor of 1.4 in order to counteract the decrease in FIR flux due to the significant shadow effect of the inner on the outer disk. We note that to not be seen in our scattered light model predictions, any dusty material in the inner disk must be confined within ∼0.09 au.

7.5 Discussion

7.5.1 Fragmentation and trapping efficiency

The main reason for the discrepancy between the dust evolution models and the simplified approach is the fact that, in the dust evolution models, micron-sized particles efficiently grow to larger sizes already at early times of evolution. The growth changes their coupling to the gas (i.e. their Stokes number) and hence their dynamics (e.g., their drift velocities increase when they grow). In these models, small grains are continuously reproduced thanks to destructive collisions that can occur because of turbulent motions and radial drift. In the particular case of two planets embedded in the disk presented in this study, the radial drift is reduced at the pressure bumps, and fragmentation occurs due to turbulence that replenishes these regions with small grains. These small grains are more affected by turbulent motions and more difficult to trap, and thus they can be dragged along with the gas. For this reason, a small amount of micron-sized particles can still flow through the gap (cf. Fig. 7.7). This amount of small grains is, however, not enough to reproduce the observed surface brightness profile inside the gap (as it is in the case of a constant gas-to-dust ratio). For sub-micron grains, this amount would be significantly higher, and these smaller grains scatter more efficiently in our direction, too. A possible solution for this discrepancy is to make fragmentation more efficient, for example, by increasing the turbulent motions of the grains, that is, increasing the α-viscosity. However, when α increases, a more massive planet is needed to open a gap (Crida et al., 2006), which can lead to a new discrepancy with the gap width. Moreover, the higher the turbulent motions, the more difficult it is to trap the mm-sized particles, because of the high dust diffusion that allows particles to escape from pressure bumps (de Juan Ovelar et al., 2016). As an alternative, in order to have less growth and more fragmentation, the maximum fragmentation velocity threshold of the particles can be decreased, which mainly depends on the grain composition and its structure. Nonetheless, while having more fragmentation might help to increase the surface brightness inside the gap, this can also lead to less dust trapping, which can create differences with the current mm observations. Note that decreasing the

initial minimum grain size in our current dust evolution models would not help us to have a better match with observations, because small grains quickly grow regardless of their initial size.

7.5.2 Dust evolution as a function of z

Following the analysis in Sect. 7.4.2, it becomes clear that the assumptions in current 1D dust evolution models are tuned for coagulation processes happening in the disk midplane. The evolution of gas and dust is modeled in a vertically integrated way assuming a steady-state disk model, although there might actually be a strong dependency on the vertical disk height. Hence, our treatment of vertical exchange and vertical settling might also be inaccurate. For instance, if there is indeed a population of small grains isolated at the top layer, this would suggest very weak turbulence. This provokes quite efficient settling, even for small grains. What might work is a population of small, charged grains that is kept from settling by, for example, magnetic fields. Hence, these small grains would be unaffected by efficient dust growth and could be permanently present at the disk surface. As a consequence, scattered light detections at optical and NIR wavelengths would not be affected by significant dust growth. Contrarily, the surface layers might have higher turbulence, which is expected because they are hotter and highly ionized (e.g., Dzyurkevich et al., 2013). However, with only higher turbulence, grains are also mixed downward and get into contact with the lower turbulence regions deeper in the disk, where they settle and take part in the coagulation there. Thus, a locally higher turbulence is not a way to isolate grains, it is a way to move them faster. Consequently, it could be that the gas velocities at very high altitude are such that fragmentation also works in a thin surface layer to locally replenish the reservoir of even sub-micron grains.

7.5.3 Mass of gap opening planets

As shown in Sect. 7.4.2, planets with masses of $3.5\,\mathrm{M_{jup}}$ and $0.7\,\mathrm{M_{jup}}$ located at 14 au and 53 au are needed in our dust evolution models in order to create effective pressure bumps that trap particles at the location of the rings seen in scattered light. Note that these values are compatible with the mass detection limits derived from contrast curves in total intensity SPHERE IRDIS and IFS data. The minimum planet mass limit in our model is chosen such that the planet perturbs the gas profile and efficient trapping can be generated ($M_\mathrm{p} \gtrsim 0.3\,\mathrm{M_{jup}}$). While a planet mass of $0.3\,\mathrm{M_{jup}}$ is too low to clear the full extent of Gap #2, the $0.7\,\mathrm{M_{jup}}$ planet is able to reproduce the gap width. The presence of multiple planets below this mass whose gaps overlap is an alternative possibility (e.g., Dodson-Robinson & Salyk, 2011). Numerical studies have shown that less massive planets do not open a gap in the gas but effectively open a gap in the dust (Paardekooper & Mellema, 2004, 2006; Picogna & Kley, 2015; Rosotti et al., 2016; Dipierro et al., 2016; Dipierro & Laibe, 2017). The gas azimuthal velocities can be perturbed such that the drift velocities of the particles are reduced, leading to a traffic jam effect without creating local pressure maxima.

In addition to the gas viscous forces, Dipierro et al. (2016) and Dipierro & Laibe (2017) also include the contribution from the tides of an embedded planet and show that a low mass planet can open a gap in the dust only if the tidal torque exceeds the drag torque outside the planetary orbit. In this scenario, a shallow gap can be carved out, but it is rather unlikely that this effect can create the strong rings in the distribution of small and large grains in HD 169142. It should be tested whether a combination of pressure bumps, self-consistent dust evolution, and the consideration of disk-planet tidal interactions can lead to a coherent picture for the gap and ring appearances.

Pioneering studies from Kanagawa et al. (2015), Rosotti et al. (2016), and Dong & Fung (2017) look at the inverse problem, meaning to derive planet masses from observed gap profiles. For this method, a number of assumptions about the disk structure and dynamics are made when simulating the gap shape and deriving the correlation with planet mass. The mass of the putative second planet in our HD 169142 model is consistent with the numerical analysis by Dong & Fung (2017), who derived disk and planet properties based on the morphology of gaps in NIR scattered light images. They estimate a mass between 0.2–2.1 M_{jup} for an α-viscosity varying from 10^{-4}–10^{-2}. Kanagawa et al. (2015) suggest a mass $\gtrsim 0.4\,M_{jup}$ by measuring the gap depth in VLA 7 mm data. Although this is principally consistent with the other estimates, a measurement based on mm data only is complicated due to dust/gas coupling effects (Rosotti et al., 2016). This makes an exact definition of the gap width difficult and its value depends on the disk lifetime. As discussed in Rosotti et al. (2016) a more robust indicator of the planet mass from (sub-)mm images is the location of the bright ring tracing the gas pressure maximum. This is the reason why we intend to reproduce the ring positions rather than the gap locations with the modeling approach in this work. The inclusion of dust growth and fragmentation processes would certainly change the conclusions from Rosotti et al. (2016) and Dong & Fung (2017) as dust evolution dynamics affects the gap depth, the slope of the gap edges, the position of the rings and their contrast.

7.5.4 Dust evolution timescale

All of our results based on the dust evolution modeling consider a dust evolutionary timescale of 5 Myr and that the giant planets embedded were formed simultaneously. The disk and planet age can affect the appearance of the radial profiles in polarized intensity at the NIR (see Fig. 7.12) and in total intensity at mm wavelength. On the one hand, the outer ring (Ring #1) becomes narrower at longer times of evolution, which produces a rather sharp outer disk edge and shifts it toward smaller radii. This in turns lowers the brightness signal in the outer disk. While this is consistent with the mm data, the amount of small dust particles decreases with time, and the NIR observations cannot be reproduced. If longer times of evolution are taken ($\sim$10 Myr, which is consistent with the revised age of the system), there would be a higher discrepancy between the dust evolution models and the NIR observations unless additional trapping mechanisms play a role all across the disk. In contrast, at very

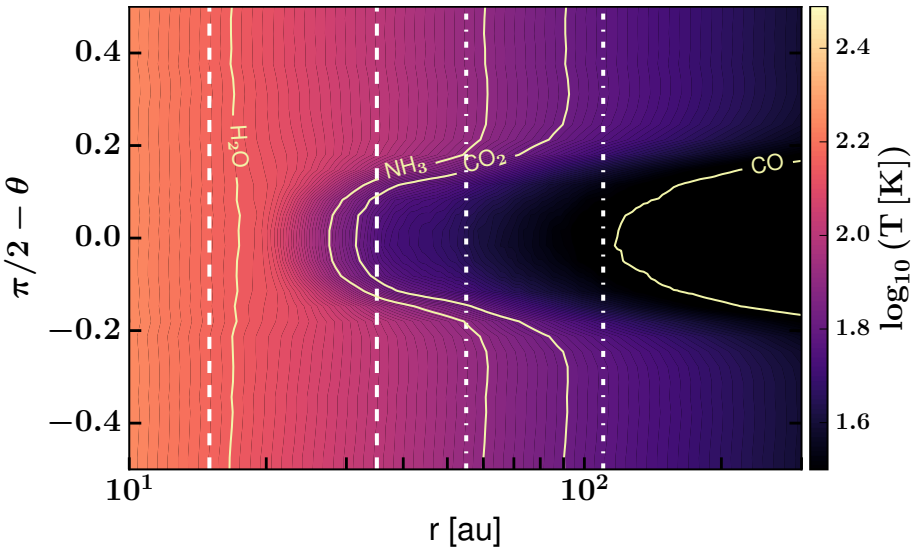

Figure 7.15: Temperature map as a function of radius and polar angle in spherical coordinates for the simplified model. The ice lines for H_2O, NH_3, CO_2 and CO are indicated with yellow contours. The vertical dashed lines illustrate the edges of the two bright rings in mm dust emission.

early timescales of 0.1–0.5 Myr, when all grains are not yet at the pressure maxima, the wide gap (Gap #2) remains shallower. On the other hand, analogous to the sequential planet formation scenario presented in Pinilla et al. (2015b), it could be also possible that the outer planet forms earlier than the inner planet (or vice versa). This can affect the amount of dust in both traps and adjust the contrast between the two rings. However, there is no constraint on whether the two planets have been forming at the same time or consecutively. Together with the uncertainty when the putative planets have been forming at all, this means that the dust evolution after 5 Myr could still be a good proxy for the situation in the HD 169142 system.

7.5.5 Gaps and rings in the context of ice lines

Although observational signposts of embedded planets are the most widely used explanation to interpret ring structures in disks, the relation to ice lines of various materials is another possible scenario (Zhang et al., 2015; Okuzumi et al., 2016). Ice lines of different volatile species can significantly affect the dynamics of dust evolution processes including growth and fragmentation, which in turn has an effect on the observational appearance of rings and gaps at different wavelengths (see Chapter 8). The freeze-out temperatures of the main volatiles, such as water (H_2O), ammonia (NH_3), carbon dioxide (CO_2), and carbon monoxide (CO), are estimated to have average values of ∼142 K, ∼80 K, ∼66 K and ∼26 K, respectively (Zhang et al., 2015).

Our radiative transfer models show that the midplane temperatures at the inner ring position are such that the H_2O and NH_3/CO_2 ice lines are located close to the inner and outer edges of this ring, respectively, at mm emission. It is recognizable

that the gap at scattered light lies between the ice lines of H_2O and CO_2 when comparing the surface layer temperatures with the volatile freeze-out temperatures. Thus, the H_2O, NH_3 and CO_2 ice lines nearly coincide with the scattered light ring positions. Furthermore, the CO ice line at the midplane is located at ∼110 au, which is close to the outermost gap at ∼85 au, consistent with DCO^+(3–2) and $C^{18}O$(2–1) ALMA observations presented in Macías et al. (2017). In Fig. 7.15, there is an uncertainty for the specific location of these ice lines that depends on the freezing temperatures that we assume, and for the CO ice line, it could be between ∼95 and 145 au. The current observations suggest that the accumulation of large dust grains close to the CO ice line is a possible mechanism to explain the origin of this outermost gap.

7.5.6 Shadowing effects and time variability

We note that because of the modeling procedure (analytical gas profile coupled with 1D dust evolution) the observational signatures presented in this work are always azimuthally symmetric. This is, for example, not necessarily true for a massive enough planet for which an eccentric gap and vortex formation at its edge are expected (e.g., Ataiee et al., 2013). As mentioned in Sect. 7.2, there are significant asymmetries along both the inner and outer ring regions in polarized intensity. It is noticeable that the maximum polarization of the outer ring is along the minor axis. This is opposite to several other disks showing a brighter polarized intensity along the major axis, expected due to the polarization efficiency being highest for 90° scattering in the Rayleigh and Mie scattering regime. A significant scattering angle effect is also likely not to be expected at the low inclination of HD 169142. Momose et al. (2015) invokes corrugations of the scattering surface in the outer region as a possible origin. Alternatively, asymmetries in the outer disk emission can be caused by shadowing of the inner disk region. For HD 169142 there is a slightly inclined inner disk at sub-au distance (i=21°, PA=100–130°, Lazareff et al., 2017) that is known to be variable and might contain an extended dust envelope, as suggested by Wagner et al. (2015b). Azimuthal brightness variations in the inner ring of the scattered light could be caused, for example, by perturbations by a protoplanet, by optical depth variations through the suggested dust envelope, by accretion flows, or turbulence in the inner disk. The local brightness enhancements along the innermost scattered light ring at different time epochs are discussed in Ligi et al. (2018). The azimuthal inhomogeneities in the inner ring (Ring #2) could in turn cause radial shadowing on Ring #1 and the remaining outer disk. The pace of variations in the illumination pattern of the outer disk depends on the precession timescale of the inner disk material. Given that there is no apparent difference in the rings' brightness asymmetries in the three observational data sets in polarized intensity (Subaru/HiCIAO: Momose et al. 2015, Gemini South/GPI: Monnier et al. 2017, VLT/SPHERE: this work) that span a time period of three years, the shadowing scenario for the outer disk seems rather unlikely. However, it cannot be ruled out either, as the precession time scale for the inner disk, for example, in the context

of a hypothetical star-companion system, can be rather long (several hundred to thousand years).

7.6 Conclusions

In this work, we present scattered light observations of the protoplanetary disk around the Herbig Ae star HD 169142 obtained with the VLT/SPHERE at the J-band, and compare our results with recent ALMA data of this target. Together with TW Hya, HD 163296, and HD 97048, it is one of a handful of disks around young stars that have been observed at very high angular resolution at NIR and mm wavelengths, where in each case both images show similar substructures even if their scales differ but also show different morphologies. For HD 169142, we confirm the previous detection of two ring-like features separated by a wide gap, of an additional inner gap, and report on the marginal detection of a third gap in the outer disk, as well as azimuthal brightness variations along both rings. We present azimuthally symmetric radiative transfer models based on planet-disk interaction processes that account for the main observational features and discuss the influence of dust evolution and particle trapping on the gap and ring properties. We place our findings in the context of planet masses inferred from the gap-opening process and ice line chemistry. Our measurements and modeling results suggest the following:

1. The location and width of the gap, as well as the peak positions in polarized scattered light, of HD 169142 are reproduced with our model based on dust evolution processes when two giant planets of 3.5 and 0.7 M_{jup} are embedded in the disk. The observed gap, however, possesses a shallower outer flank than expected for planet-disk interaction signatures. There is also a significant discrepancy in the gap depth, as micron-sized particles rapidly grow in the presence of pressure bumps. Small grains distributed all over the disk wherever there is gas, as in our simplified approach, decreases the gap depth such that there is a good agreement with the observed shape. This also helps to increase the scattered light flux in the outer disk. A more efficient fragmentation by adjusting the fragmentation velocities could help to overcome this deficit in small grains. Including the contribution from the tides of an embedded planet can lead to a shallower dust gap, in case the planet hypothesis is correct at all.

2. The assumptions in current dust evolution models are tuned for the disk midplane, and the vertical exchange does not work properly; thus, the coagulation timescale might be different at higher disk altitudes. A population of small (sub-)micron-sized grains might exist in the upper surface layers that is unaffected by quick growth due to lower densities, different turbulence, or charging effects there. Thus, the vertical disk structure and its consequence for dust evolution processes also have a significant role for interpreting scattered light images.

3. In order to obtain a consistent picture with the mm observations, the accumulation of large grains in the dust trap of a pressure bump is needed. This generates the bright emission rings and the sharp outer disk edge as detected in the mm continuum image of HD 169142. A simplified parameterized dust size distribution is not able to reproduce the high dust depletion factor required.

4. A scenario with a grain size dependent gap opening that still allows a perturbation in the radial pressure gradient is required. We emphasize that inferring the mass of gap-opening planets from simplified models is degenerate and depends on the choice of the disk mass, temperature, and $\alpha-$turbulence. Constraining planet masses becomes even more uncertain when including more physical processes that are expected to occur in planet-forming disks, such as grain growth, fragmentation, and vertical disk instabilities.

5. Observing the total amount of gas and using different techniques that allow us to get better constraints on the grains sizes in disks, such as mm-wave dust polarization (see Chapter 10), may allow us to further explain the origin of the gaps and derive the properties of potential embedded planets.

Eventually, 2D dust evolution models are needed in order to have a self-consistent treatment of radial transport and vertical settling and consider turbulence changes across the vertical direction of the disk. In principle, we can start to use multi-wavelength analyses, such as the one presented in this work, to provide feedback on the model assumptions and to calibrate our understanding of microphysical dust processes (sticking, fragmentation, compact versus fluffy grains, etc.).

8 | Imaging analysis of different ice lines in circumstellar disks

The content of this chapter is based on Pinilla, Pohl, Stammler, & Birnstiel (2017) published in *2017, ApJ, 845, 68*.

Details of authorship: The main author is Paola Pinilla, who is also responsible for the dust evolution models. I performed the radiative transfer modeling and contributed to the text, especially for Sects. 8.2.2 and 8.3.2. The interpretation of the simulations was done in close collaboration with Paola Pinilla.

8.1 Introduction

As summarized in Chapter 7, recent high angular resolution observations of protoplanetary disks revealed several examples of multiple ring-like structures. These objects have a large range of properties, including different stellar types and ages, from very young $\lesssim 1$ Myr to very old $\sim$10 Myr. The current literature for explaining dust rings and gaps in protoplanetary disks is very rich, and includes zonal flows from the MRI (e.g., Johansen et al., 2009; Uribe et al., 2011; Dittrich et al., 2013; Simon & Armitage, 2014), spatial variations of the disk viscosity (e.g., Kretke & Lin, 2007; Regály et al., 2012; Flock et al., 2015; Pinilla et al., 2016), secular gravitational instability (e.g., Youdin, 2011; Takahashi & Inutsuka, 2014), instabilities originating from dust settling (Lorén-Aguilar & Bate, 2015), self-sustained recycling of inner dust rings (Husmann et al., 2016), particle growth by condensation near ice lines (Saito & Sirono, 2011; Ros & Johansen, 2013; Stammler et al., 2017), sintering of dust particles that inhibits dust growth near the ice lines (Okuzumi et al., 2016), and planet-disk interaction (e.g., Rice et al., 2006; Zhu et al., 2011; Gonzalez et al., 2012; Pinilla et al., 2012a; Dipierro et al., 2016; Rosotti et al., 2016; Dong & Fung, 2017). Although the latter explanation is the most widely used to interpret current observations, it is not a unique possibility and several of the listed processes can play an important role during the disk evolution.

To differentiate between all these models for the origin of rings and gaps, it is crucial to predict the behavior of the gas, as well as dust particles of different size, and compare with current observations of disks that cover wavelengths from optical

to mm emission. In this work, the effect that different ice lines have on the dust evolution is further investigated. We predict the distributions of small (micron-sized) particles versus the distribution of large (mm-sized) grains and give imaging diagnostics to consider or exclude this scenario as the cause of the seen structures.

In this work, the growth and fragmentation of dust particles during the disk evolution is considered. The growth from micron-sized particles to larger bodies occurs as a result of sticking collisions (cf. Sect. 1.2.1). The sticking efficiency between pairs of dust grains depends on the Van der Waals forces, which are attractive forces between permanent, induced, or fluctuating dipoles. Hamaker (1937) calculated the resulting Van der Waals force between two spherical particles as a function of their diameters and the distance separating them, such that the total attractive force is given by $\sim -C_{\rm H}/r^6$. The Hamaker constant ($C_{\rm H}$) is the sum of the dispersion, polarizability, and orientation coefficients of the pairs in the interaction. Dispersion forces are exhibited by non-polar molecules because of the fluctuating moments of the nucleus and electrons of the atoms or molecules. For non-polar molecules, the higher the contribution of the dispersion force to the Van der Waals force, the lower is the magnitude of the net Van der Waals force. For instance, CO_2 is a nonpolar molecule, and therefore the only contribution to the Van der Waals force is the dispersion force (French et al., 2007). As a consequence, when the mantle of two dust particles is composed mainly by CO_2 ice (or another molecule with very low dipole moment, e.g. CO or silicates) the net attractive force between the two grains is weaker compared to the net attraction of particles constituted by other polar molecules, such as water or ammonia. The total contribution of the dispersion force to the Van der Waals force is 24% and 57% for water and ammonia respectively (e.g., Kohler, 1977; Israelachvili, 1992).

To reassemble the dependence of the dipole moment of the constituents on the net attractive force between dust particles, it is simply assumed that the threshold of the dust collision velocity to cause fragmentation of particles (the fragmentation velocity, $v_{\rm frag}$) accordingly changes radially at the location of one, two, or three ice lines. Specifically, changes at the radial location are assumed, where H_2O, NH_3, and CO_2 are expected to freeze out. In these models, we assume that the mantle of dust grains is mainly composed by the volatile that freezes out at a given location. It is analyzed how the changes of the fragmentation velocity affect the final dust distribution of particles with one micron to mm sizes. In order to compare with current multi-wavelength observations of protoplanetary disks, we include radiative transfer calculations and calculate the radial profile of synthetic images at different wavelengths.

The organization of this work is as follows. In Sect. 8.2, the details and assumptions of our dust evolution and radiative transfer models are assumed. Sections 8.3.1 and 8.3.2 present the results of the dust density distribution and radial profiles of synthetic images from different models. Sections 8.4 and 8.5 provide a discussion and conclusions, respectively.

8.2 Models and assumptions

8.2.1 Dust evolution models

Our models follow the radial evolution of a dust density distribution and calculate the growth, fragmentation, and erosion of dust particles, covering objects from 1 μm to 2 m in size. Bouncing of particles is not taken into account. The sticking probability depends on the relative velocities before collision. For this velocity, Brownian motion, vertical settling, turbulent diffusion, radial and azimuthal drift is taken into account. For larger particles, the relative velocities increase (e.g., Windmark et al., 2012a). The motion of the particles is determined by the interaction with the gas, and it is calculated according to their size (Birnstiel et al., 2010).

Parameters of a disk around a Herbig star are taken, specifically $T_\star = 9300\,\mathrm{K}$, $R_\star = 2\,\mathrm{R}_\odot$, and $M_\star = 2.5\,\mathrm{M}_\odot$. The gas surface density is assumed to remain constant with time, which is a power-law with an exponential cut-off (e.g., Lynden-Bell & Pringle, 1974), that is,

$$\Sigma_g(r) = \Sigma_\mathrm{c} \left(\frac{r}{r_\mathrm{c}}\right)^{-\delta} \times \exp\left[-\left(\frac{r}{r_\mathrm{c}}\right)^{2-\delta}\right] . \tag{8.1}$$

The cut-off radius r_c is taken to be 120 au, and $\delta = 1$. The total disk mass is $M_\mathrm{disk} = 0.08\,\mathrm{M}_\odot$. We assume a simple parametrization for the disk temperature that depends on the stellar parameters and is given by (Kenyon & Hartmann, 1987)

$$\begin{aligned} T(r) &= T_\star \left(\frac{R_\star}{r}\right)^{1/2} \varphi_\mathrm{inc}^{1/4} \\ \text{or} \quad T(r) &\simeq 426\,\mathrm{K} \left(\frac{r}{1\,\mathrm{au}}\right)^{-1/2} , \end{aligned} \tag{8.2}$$

where φ_inc is the angle between the incident radiation and the local disk surface, taken to be $\varphi_\mathrm{inc} = 0.05$. The radial grid is logarithmically spaced from 1 to 500 au with 500 steps. The initial gas-to-dust ratio is 100, and all the dust particles are assumed to be 1 μm in size at the initial time.

A simplified prescription of the fragmentation velocity threshold is used, which is assumed to change radially at the location of the ice lines. We assume that for grains whose mantle composition is dominated by nonpolar molecules (or with very low dipole moment), such as CO, CO_2, or silicates, the fragmentation velocity is of the order of $1\,\mathrm{m\,s^{-1}}$, in agreement with results from numerical simulations and laboratory experiments (Blum & Wurm, 2000; Poppe et al., 2000; Paszun & Dominik, 2009; Gundlach & Blum, 2015; Musiolik et al., 2016a,b). Under the assumptions of our models, assuming the CO or CO_2 ice line does not make any difference, except that the location of the CO ice line is farther out, and v_frag would be $1\,\mathrm{m\,s^{-1}}$ for both

ice lines. In this work, the CO_2 ice line is assumed, but results would be similar if we were to assume the CO ice line.

In the cases where the grain mantle is composed by molecules with permanent electrical dipoles, such as H_2O and NH_3, the fragmentation velocity is assumed to have a higher value. For H_2O, it is assumed to be $10\,\mathrm{m\,s^{-1}}$ as suggested by numerical and laboratory experiments (Wada et al., 2009, 2011; Gundlach & Blum, 2015). For NH_3, a fragmentation velocity of $\sim 7\,\mathrm{m\,s^{-1}}$ is assumed. This is an estimate as there are no data on NH_3 fragmentation, but it is in correspondence to the contribution of the dispersion force to the total Van der Waals force between dust grains, which is 24% and 57% for H_2O and NH_3, respectively (Israelachvili, 1992). For simplicity we assume the particles to be layered with a silicate core and mantles of water, ammonia, and carbon dioxide depending on their location relative to the ice lines.

At the ice lines of H_2O, NH_3, and CO_2, the fragmentation velocity is assumed to change as a smooth step function, for which we use

$$H(x) = \begin{cases} \dfrac{1}{2}\exp\left(\dfrac{x}{\Delta x}\right) & \text{for } x \leq 0 \\ 1 - \dfrac{1}{2}\exp\left(-\dfrac{x}{\Delta x}\right) & \text{for } x > 0 \end{cases} , \tag{8.3}$$

where $x = r - r_{\mathrm{ice}}$, with r_{ice} being the radial position of a given ice line. These positions are assumed at the locations where the disk temperature has the values of the averaged freezing temperatures of H_2O, NH_3, and CO_2, in agreement with the values reported in Zhang et al. (2015) (Table 8.1). Notice that for CO_2, a freezing temperature of 44 K is taken, which is an average value for CO_2 and CO. The factor Δx in Eq. 8.3 is a smoothing parameter for the radial change of the fragmentation velocity at a given position and is taken to be $\Delta x = 0.5\,\mathrm{au}$. Depending on how many ice lines are assumed, the fragmentation velocity is taken to be a composition of different smooth step functions (Eq. 8.3). For instance, for the simplest case where only the water ice line is considered (as in Birnstiel et al., 2010), the fragmentation velocity is given by

$$v_{\mathrm{frag}} = \left(100 \times 10^{H(x)}\right) \frac{\mathrm{cm}}{\mathrm{s}} \quad \text{with} \quad x = r - r_{\mathrm{ice,H_2O}}\,. \tag{8.4}$$

In this work, three different cases are assumed: the fragmentation velocity only changes at H_2O ice line (model I), when the fragmentation velocity changes at the H_2O and CO_2 ice lines (model II), being $1\,\mathrm{m\,s^{-1}}$ inside the H_2O ice line and beyond the CO_2 ice line, and when H_2O, NH_3, and CO_2 ice lines are assumed for the changes of the fragmentation velocity (model III). Figure 8.1 shows the profiles of the fragmentation velocity for these three cases. With the disk and stellar properties of our models, the first case recreates the results already presented in Banzatti et al. (2015). In this work, we add the proper radiative transfer calculations to predict images at scattered light and mm wavelengths.

Table 8.1: Assumed freezing temperatures for H_2O, NH_3, and CO_2.

	H_2O	NH_3	CO_2
$T_{\rm cond}$ [K]	150	80	44
$r_{\rm ice}$ [au]	8.1	28.5	92.0

Notes. According to the averaged values reported in Zhang et al. (2015) and based on Mumma & Charnley (2011) and Martín-Doménech et al. (2014).

In our models, the ice line locations and gas surface density remain constant with time. It is, however, expected that dust dynamics, in particular radial drift and vertical settling, can change the gas surface density and the location of ice lines (Piso et al., 2015; Cleeves, 2016; Krijt et al., 2016; Powell et al., 2017; Stammler et al., 2017). In addition, the disk temperature can vary by different effects, such as disk dispersal, which can also change the ice line locations (Panić & Min, 2017). Our models are a simplification assuming that the viscous evolution timescales are longer than the dust growth timescales, and that any material that evaporates from the grains does not contribute significantly to the gas surface density, which is a reasonable assumption for the low dust-to-gas ratios that we have at any time of evolution in our models.

For the collisional outcome, the fragmentation probability ($P_{\rm frag}$) is assumed to be unity when the relative velocity ($v_{\rm rel}$) is above the fragmentation velocity ($v_{\rm frag}$) and zero when $v_{\rm rel}$ is between 0 and $0.8\,v_{\rm frag}$. For intermediate values (between 0.8 and $1.0\,v_{\rm frag}$), a linear transition of the fragmentation probability is assumed, such that $P_{\rm stick}$=1-$P_{\rm frag}$ (Birnstiel et al., 2011). When the collision velocity is only determined by turbulence, the maximum grain size is given by (Birnstiel et al., 2012),

$$a_{\rm frag} = \frac{2}{3\pi}\frac{\Sigma_g}{\rho_{\rm s}\alpha}\frac{v_{\rm frag}^2}{c_{\rm s}^2}\,, \tag{8.5}$$

which is usually known as the fragmentation barrier. In Eq. 8.5, $\rho_{\rm s}$ is the volume density of dust grains, which is taken to be $1.2\,{\rm g\,cm^{-3}}$, α parameterizes the disk viscosity ν (see Eq. 1.21), and $c_{\rm s}$ is the sound speed.

Particles can reach large sizes drifting toward the star in timescales shorter than the collision timescales (mainly in the outer parts of the disk). This barrier to further growth is the drift barrier, and it is given by

$$a_{\rm drift} = \frac{2\Sigma_d}{\pi\rho_{\rm s}}\frac{v_K^2}{c_{\rm s}^2}\left|\frac{d\ln P}{d\ln r}\right|^{-1}\,, \tag{8.6}$$

where Σ_d is the dust density distribution, $v_{\rm K}$ is the Keplerian angular velocity (i.e., $v_{\rm K} = r\Omega$), and P is the disk pressure $P = \rho\, c_{\rm s}^2$, with ρ being the total gas density.

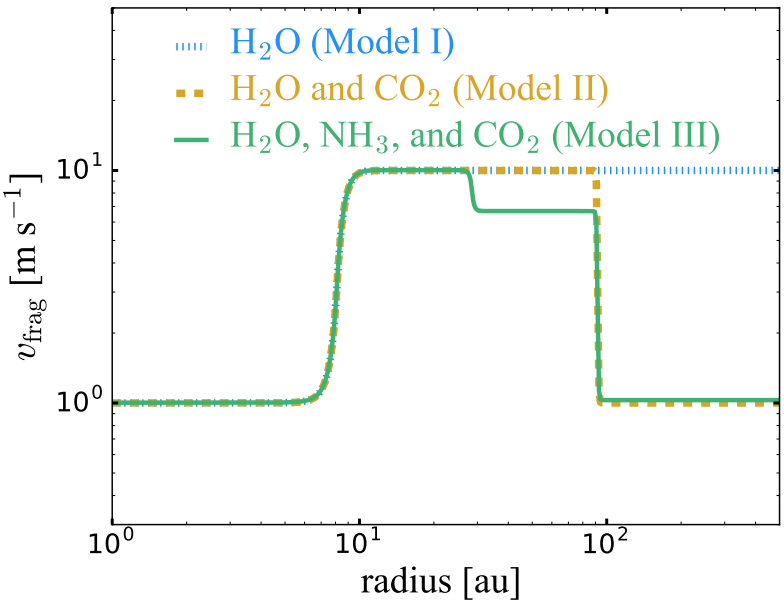

Figure 8.1: Profile of the fragmentation velocity for three different cases: (I) When only the H_2O ice lien is assumed (dotted line); (II) When H_2O and CO_2 ice lines are assumed (dashed line); (III) When H_2O, NH_3, and CO_2 ice lines are assumed (solid line).

Okuzumi et al. (2016) modeled the dependency of the fragmentation velocity of dust particles on the sintering. We do not take this particle fusion process into account, which can also affect the fragmentation velocity and create gaps and rings in the dust surface density.

8.2.2 Radiative transfer models

For the radiative transfer calculations with RADMC-3D, we follow the same procedure presented in Pohl et al. (2016). However, for the NIR predictions, we do not calculate images in the full Stokes vector, but concentrate on the total intensity. In addition, we assume the temperature as in the dust evolution models. The models are 3D, but the azimuth is treated with only one grid cell since our dust evolution models are azimuthally symmetric. The total dust density is calculated assuming the dust density distribution from the dust evolution models, such that

$$\rho_\mathrm{d}(R,\phi,z) = \frac{\Sigma_\mathrm{d}(R)}{\sqrt{2\,\pi}\,H_\mathrm{d}(R)}\,\exp\left(-\frac{z^2}{2\,H_\mathrm{d}^2(R)}\right)\,, \tag{8.7}$$

where R and z are cylindrical coordinates, that can be converted to spherical coordinates by $R = r\,\sin(\theta)$ and $z = r\,\cos(\theta)$, with θ being the polar angle. In order to include the effect of settling on the models, the dust scale height $H_\mathrm{d}(R)$ depends on the grain size and the disk viscosity (Youdin & Lithwick, 2007; Birnstiel et al.,

2010), and is given by (cf. derivation in Eq. 9.5)

$$H_{\rm d} = H \min\left(1, \sqrt{\frac{\alpha}{\min(\mathrm{St}, 1/2)(1+\mathrm{St}^2)}}\right) , \tag{8.8}$$

where H is the gas scale height and St is the Stokes number given by Eq. 1.27.

For the synthetic images, a face-on disk with a distance of 140 pc is assumed. For the convolved synthetic images, a Gaussian is used for the PSF with a FWHM of 0.″04 for the total intensity at 1.6 μm, as a realistic value for observations with VLT/SPHERE or GPI. For images at the continuum mm emission, we consider two wavelengths, 0.87 and 3 mm, and we convolve the images with a Gaussian beam of 0.″04, in order to have the same resolution as at short wavelength and to mimic ALMA observations with high resolution.

For the dust optical properties, a dust composition as in Ricci et al. (2010b) is assumed, that is a mixture between silicate, carbonaceous, and water ice. In Banzatti et al. (2015), it was investigated how different fractions of water ice at the snow line could affect the resulting dust density distributions and hence the observational predictions. The effect on the results is found to be weak, and for this reason the dust composition in this work is kept fixed for all the models.

8.3 Results

8.3.1 Dust density distributions

Figure 8.2 shows the vertically integrated dust density distribution at 1 Myr of evolution when one, two, or three ice lines are considered (see Fig. 8.1, for reference). Results are shown for three different values of α-viscosity, specifically $\alpha = \{10^{-4}, 10^{-3}, 10^{-2}\}$. Figure 8.3 shows the dust density distribution for small ($a \in [1-10]\,\mu$m) versus large grains ($a \in [1-10]$ mm) for the same cases as Fig. 8.2. In this section, we describe the radial variations of the dust density distribution for each value of α-viscosity. In the appendix, the vertical dust density distribution (Eq. 8.7) is shown for each case. These distributions are assumed for the radiative transfer calculations.

Case of $\alpha = 10^{-2}$

In the case of high viscosity, the maximum grain size is determined by fragmentation. In this case $a_{\rm frag} < a_{\rm drift}$ for the entire disk in all models (I, II, and III), which is illustrated by the cyan line that is well below the white line in the top panel of Fig. 8.2. As a consequence, the radial changes of $v_{\rm frag}$ have a direct effect on the resulting dust density distributions (Eq. 8.5).

In the case when only the water ice line is included (model I), the maximum grain size decreases smoothly with radius beyond the water ice line at ∼8 au, where the

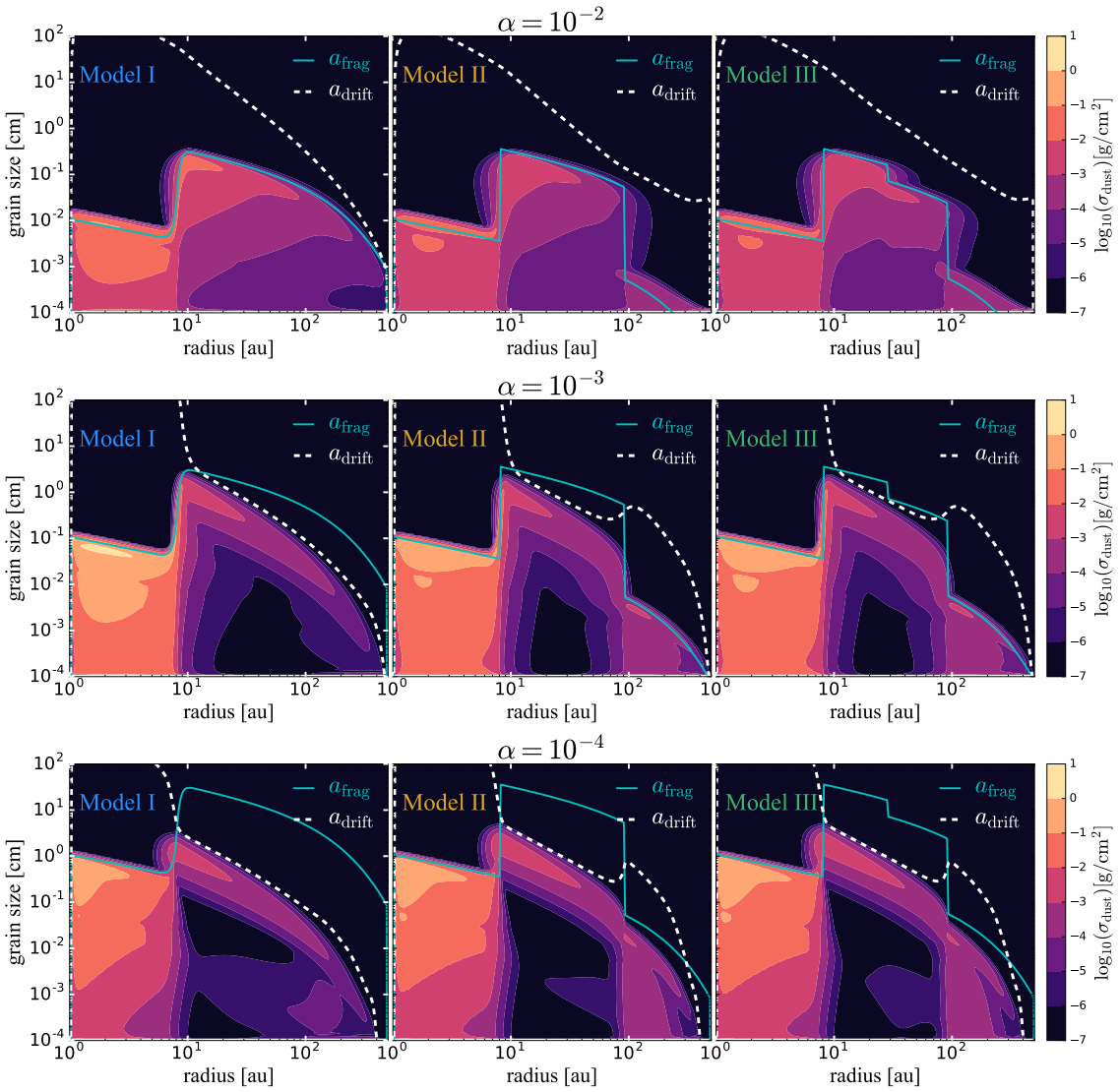

Figure 8.2: Vertically integrated dust density distribution at 1 Myr of evolution when one, two, or three ice lines are considered (see Fig. 8.1, for reference). Results are for $\alpha = 10^{-2}$ (top panels), $\alpha = 10^{-3}$ (middle panels), and $\alpha = 10^{-4}$ (bottom panels). The solid cyan line represents the maximum grain size set by fragmentation (Eq. 8.5), and the dashed white line corresponds to the maximum grain size set by radial drift (Eq. 8.6).

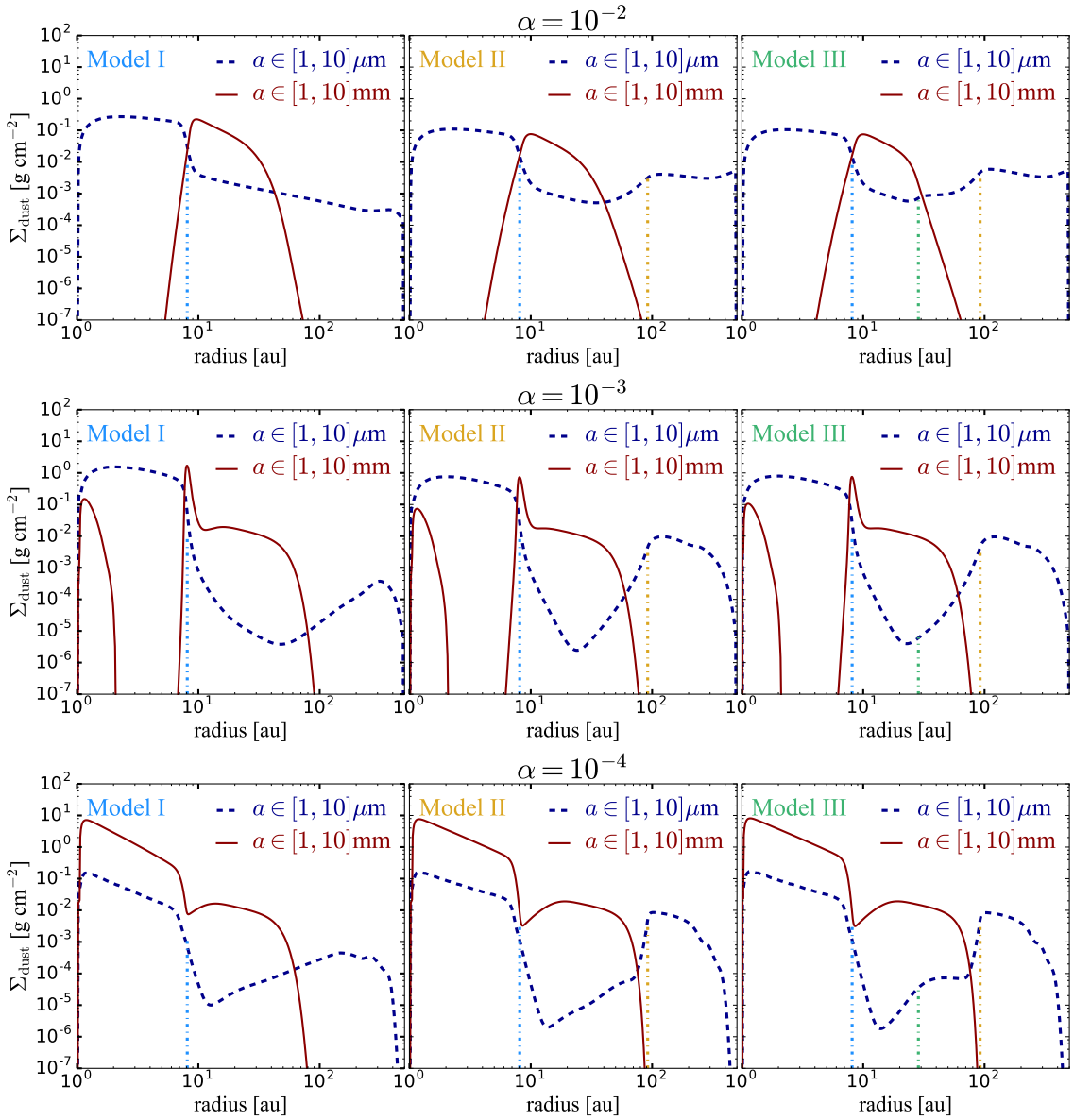

Figure 8.3: Dust density distribution for small ($a \in [1 - 10]\,\mu$m) versus large grains ($a \in [1 - 10]\,$mm) at 1 Myr of evolution when one, two, or three ice lines are considered (see Fig. 8.1 for reference, and vertical lines that represent the ice line locations according to Table 8.1). Results for $\alpha = 10^{-2}$ (top panels), $\alpha = 10^{-3}$ (middle panels), and $\alpha = 10^{-4}$ (bottom panels).

maximum grain size is around 3 mm. In the outer disk, the distribution of small grains is as extended as the gas density. Due to the effective destructive collisions when the fragmentation velocity is taken to be $1\,\mathrm{m\,s^{-1}}$, that is for $r \lesssim r_{\mathrm{ice,H_2O}}$, there is an enhancement of the dust density for small grains within this region (see Figs. 8.2 and 8.3). In these inner locations, the maximum grain size is around 0.1 mm. Hence, the surface density of mm-sized particles shows a depletion because particles do not grow to these large sizes. However, outside the water ice line, where the fragmentation velocity is higher ($10\,\mathrm{m\,s^{-1}}$), the dust density distribution for mm grains first increases and at ∼30 au starts to decrease outwards. The outer radius for the dust density of the mm grains, this is where the dust density drops below $10^{-7}\mathrm{g\,cm^{-2}}$, is around 70 au, while the gas outer radius is 500 au. This is because of radial drift as shown by Birnstiel & Andrews (2014).

When the H_2O and CO_2 ice lines are both included for the calculation of v_{frag} (model II), there is a re-creation of small grains at $r \gtrsim r_{\mathrm{ice,CO_2}}$. As a consequence, a gap-like shape in the dust surface density distribution of small grains is formed within the region between the ice lines of H_2O and CO_2, and surrounded by two ring-like shapes. In this case, the dust density decreases by ∼1-2 orders of magnitude for small grains, while the dust density for mm-sized particles is enhanced within the same region. The outer radius of the dust density of the mm grains is slightly further out than in model I because at the same time of evolution (1 Myr), there is a higher replenishment of small grains in the outer part of the disk, for which the drift velocities are lower, and it takes longer times for the particles to reach the locations where they can grow to larger sizes, that is $r \lesssim r_{\mathrm{ice,CO_2}}$.

The inclusion of the NH_3 ice line does not have a significant effect on the final dust density distribution compared to model II (Fig 8.1). In this case the fragmentation velocity decreases at $r_{\mathrm{ice,NH_3}}$ from $10\,\mathrm{m\,s^{-1}}$ to $7\,\mathrm{m\,s^{-1}}$, and there is a more effective fragmentation at $r_{\mathrm{ice,NH_3}}$ than in model II from $r_{\mathrm{ice,NH_3}}$. This is reflected in a small increment of the dust density of small grains at such location (Fig. 8.3). The shape of the dust density distribution for large mm-sized particles remains similar as in models I and II. The growth due to the sticking properties of particles lead to a distribution of the mm-sized particles with a ring-shaped structure in the region between the H_2O and CO_2.

Case of $\alpha = 10^{-3}$

In the case where the viscosity has an intermediate value, there are regions in the disk where the maximum grain size is determined by fragmentation and where it is determined by drift (Fig. 8.2). Because the α-viscosity is lower, particles can reach larger sizes (Eq. 8.5).

In model I, inside the water ice line $a_{\mathrm{max}} = a_{\mathrm{frag}}$ as in the case of $\alpha = 10^{-2}$. The maximum grain size in this region is ∼1 mm (one order of magnitude higher than in the case of $\alpha = 10^{-2}$), but it remains depleted of larger grains and there is an enhancement of the distribution of small grains as before. For $r \gtrsim r_{\mathrm{ice,H_2O}}$, a_{max} is determined by drift, the growth is more effective and particles reach sizes

of $1\,\mathrm{mm} \lesssim a \lesssim 3\,\mathrm{cm}$, depleting this region in small grains. At $r_{\mathrm{ice,H_2O}}$, there is a narrow ring-like accumulation of mm grains, where v_{frag} changes from 1 to $10\,\mathrm{m\,s^{-1}}$. This happens just at the location where $a_{\mathrm{frag}} < a_{\mathrm{drift}}$. Beyond this peak of the density of large grains, the distribution of the mm-sized particles is uniform up to 60 au where the dust density sharply decreases with radius. For this case, the dust density distribution of large grains reassembles similar profiles than in the case of dust trapping by a broad pressure bump (e.g., created by a planet or at the outer edge of a dead zone, Pinilla et al., 2012b, 2016). In model I, the small grains also show a gap in the outer regions, which is a result of inefficient fragmentation of dust particles as shown by Birnstiel et al. (2015).

In model II, due to the changes of v_{frag} at $r_{\mathrm{ice,CO_2}}$, the maximum grain size in the outer parts of the disk ($r \gtrsim r_{\mathrm{ice,CO_2}}$) is again determined by fragmentation. In this region there is effective fragmentation of particles and the dust density distribution of small grains again increases in the outer disk, creating a clear gap where the dust density for $a \in [1 - 10]\,\mu$m decreases around four orders of magnitude (Fig 8.3). The distribution of large grains does not significantly change compared to model I. The small bump at the location of the water ice line is a traffic jam effect where particles, for which the maximum size is determined by radial drift, reduce their radial velocities because they fragment.

In model III, although there is a change of v_{frag} at $r_{\mathrm{ice,N_3H}}$, there is no effect on the final dust density distribution (Fig. 8.2). This is because at these locations $a_{\mathrm{max}} = a_{\mathrm{drift}}$ and hence changes of v_{frag} do not influence the distribution of small grains as in the case of model III with $\alpha = 10^{-2}$.

Summarizing, for this case of $\alpha = 10^{-3}$, in all models there is a narrow ring-like accumulation of mm-sized particles in the dust density distribution at $r_{\mathrm{ice,H_2O}}$ where v_{frag} changes from 1 to $10\,\mathrm{m\,s^{-1}}$. Beyond that accumulation, the distribution of large grains is uniform and the outer radius for the large grains is around 80-90 au. For small grains, there is a decrease of the distribution of small grains due to inefficient fragmentation. When v_{frag} changes again to $1\,\mathrm{m\,s^{-1}}$ in the outer disk, because CO_2 ice behaves like silicates in terms of collisions, there is an enhancement for the dust distribution of small particles, creating a distinct gap.

Case of $\alpha = 10^{-4}$

In the case of low viscosity, there are regions in the disk where the maximum grain size is determined by fragmentation and where it is determined by drift as in the case of $\alpha = 10^{-3}$ (Fig. 8.2). Because of the lower viscosity a_{frag} increases by one order of magnitude and thus the maximum grain size where $a_{\mathrm{max}} = a_{\mathrm{frag}}$. This is the case inside the water ice line, where a_{max} is around 1 cm. This implies that there is no depletion of mm-sized grains inside the water ice line because a_{frag} is large enough to allow mm grains, but an enhancement of these particles. An enhancement of the dust surface density beyond the water ice line only occurs for the very large grains ($a > 1\,\mathrm{cm}$).

In model I, beyond the water ice line $a_{\mathrm{max}} = a_{\mathrm{drift}}$ and the maximum grain size

only increases by a small factor. Although the particles reach larger sizes, there is not a broad ring-like accumulation of grains with size of 1-10 mm as in the case of $\alpha = 10^{-3}$. Instead there is a small depletion of the mm-sized grains at $r_{\mathrm{ice,H_2O}}$. This is because fragmentation is too inefficient in this region, creating gaps for the dust surface density of large and small grains. Beyond this gap, there is a uniform distribution of mm-sized particles. The dust diffusion is slower because the viscosity is lower and therefore it takes longer times for the small particles to diffuse outwards. As a result, the gap is slightly narrower in small grains than in the previous case of $\alpha = 10^{-3}$.

In model II, as in the previous cases due to the changes of v_{frag}, $a_{\mathrm{max}} = a_{\mathrm{frag}}$ for locations beyond the CO_2 ice line. This makes the gap of the small grains deeper, with a depletion factor of around four orders of magnitude. The distribution of mm-sized particles does not remarkably change between models I and II.

In model III, the distributions of small and large particles are similar as in models I and II. There is a small enhancement in the distribution of small particles close to $r_{\mathrm{ice,NH_3}}$. This is the result of the slower diffusion of small grains, which take longer times to diffuse outwards. In this case, at around 1.5 Myr, this enhancement disappears.

8.3.2 Radial intensity profiles

With the radiative transfer calculations described in Sect. 8.2.2 images at NIR and (sub-)mm emission are obtained, specifically at 1.6 μm, 0.87 mm, and 3 mm. Figure 8.4 shows the radial profiles of the intensity from the synthetic images. Figure 8.5 shows the same profiles after convolving with a circular PSF with a FHWM of 0.″04, which corresponds to 5.6 au for the assumed distance of 140 pc. The intensity profiles at 1.6 μm are multiply by r^2, to compensate for the r^{-2} dependency of the stellar illumination.

The intensity profiles reveal different kinds of structures depending on the assumed value for the α-viscosity and the number of ice lines that are assumed in the models. In our models the radial structures at scattered light and mm emission originate from variations (radial and vertical, see figures in Appendix) of the total dust density distribution, and not from temperature variations. The temperature that is assumed is a simple power law (Eq. 8.2), as in the dust evolution models. As a test, we checked if the obtained intensity profiles change when the dust temperature is calculated within the radiative transfer models, and we do not find significant changes. This is because the temperature values are not very different from the power law assumption, and the only significant variations are in the very inner disk ($\sim$1 au), where the maximum temperature is higher from the radiative transfer calculations.

When only the water ice line is assumed (model I), the general trend is a dip of emission near the location of the water ice line at all wavelengths. The dip is deeper at 1.6 μm than at (sub-)mm emission, and for lower viscosity the depression of the dip is higher. These results are similar to Birnstiel et al. (2015), who found dips of emission in the outer parts of a protoplanetary disk at scattered light due to inefficient

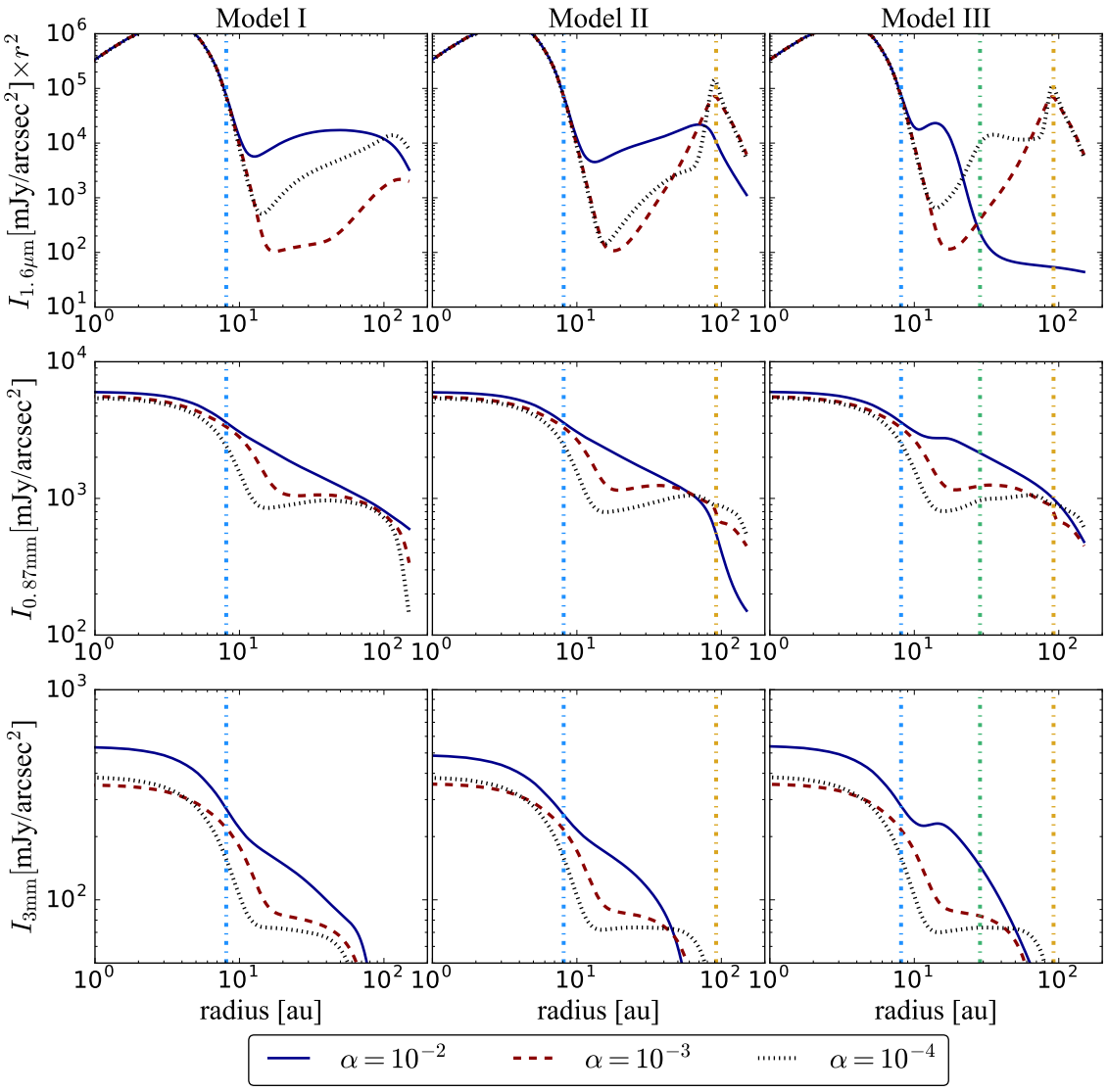

Figure 8.4: Radial intensity profiles of the synthetic images after radiative transfer calculations assuming the dust density distributions from Fig. 8.2. The intensity profiles are obtained at 1.6 μm (top panels, which are multiply by r^2), 0.87 mm (middle panels), and 3 mm (bottom panels), for the cases where one, two or three ice lines are considered (from left to right panels), and assuming different values for α. The vertical lines represent the ice line locations (Table 8.1).

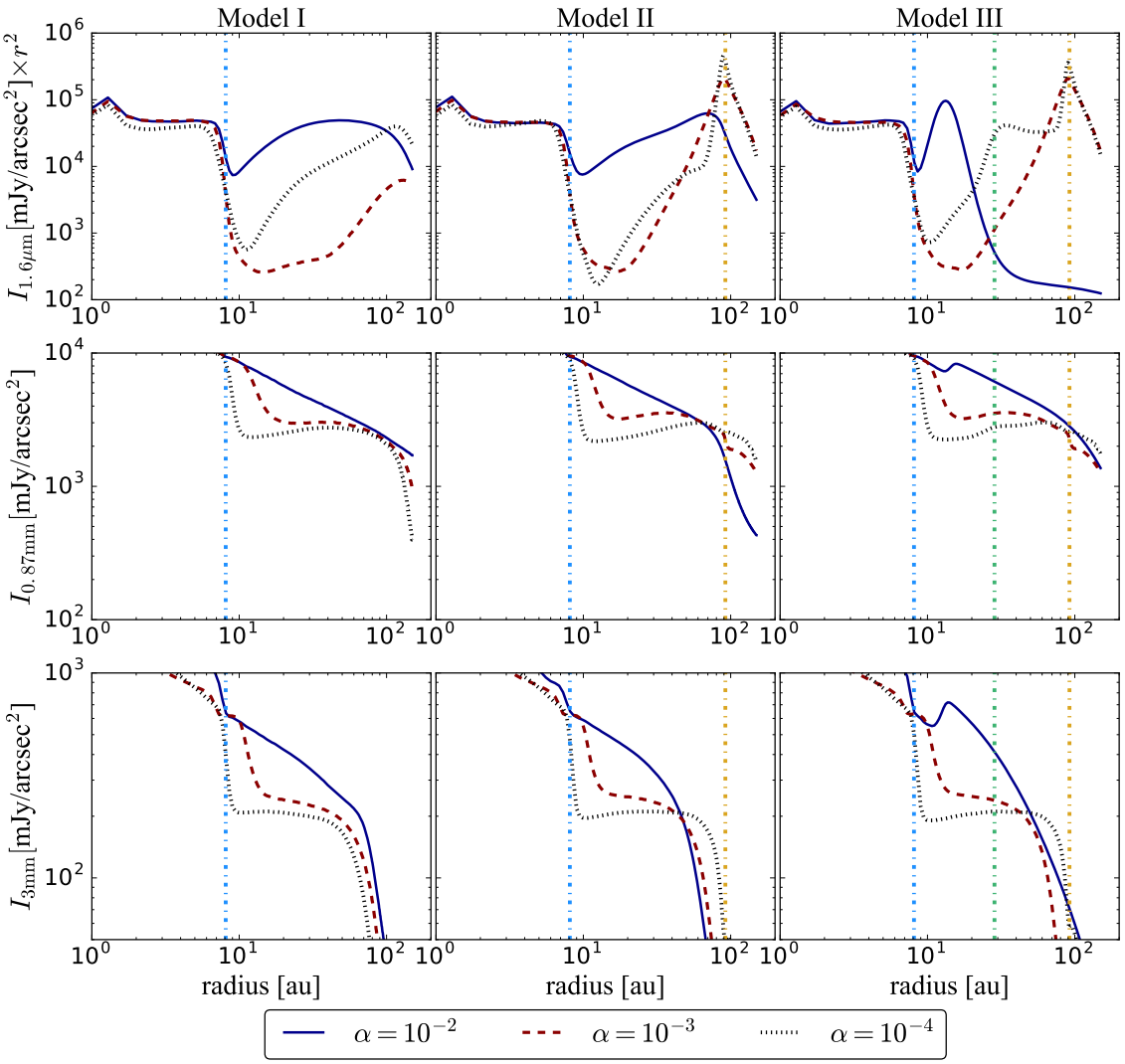

Figure 8.5: As Fig. 8.4 but convolved with a circular PSF with a FHWM of 0.″04 for all profiles.

fragmentation of dust particles. The main difference with the present models, is that the dip is located closer-in, near the water ice line, where the fragmentation velocity is expected to change, and not in the outer disk. Although the resulting dust surface density distribution in model I shows a depletion of mm grains inside the water ice line and a ring-like structure just beyond, the (sub-)mm intensity does not show such a ring-like structure, and instead it also shows a dip of emission. This is because inside the water ice line there is an enhancement of all grain sizes below the maximum grain size, which is determined by fragmentation $a_{\rm frag}$. All these grains contribute to the emission at (sub-)mm wavelengths, and when fragmentation becomes less efficient beyond the water ice line, there is a depression in the total intensity because grain growth and drift are more efficient. This is opposite to the case of particle trapping by a planet or at the outer edge of a dead zone, where only the dust grains inside the trap emit at (sub-)mm wavelengths.

For models II and III, when CO_2, and NH_3 ice lines are included in addition to the water ice line, there are changes in the radial profile of the intensity. The main difference is for the intensity at 1.6 μm, where a clear gap of emission is formed, becoming deeper when α has values of 10^{-3} and 10^{-4}. At the outer edge of that gap, a ring-like structure is also formed, and in the case of three ice lines and low viscosity, there are multiple ring- and gap-like structures. For the case of $\alpha = 10^{-2}$, the gap in micron-sized particles is shallower than in the other two cases because when α decreases, the growth is more efficient between the water and the other ice lines. As a result, there is a high depletion of micron-sized particles creating a deep gap in the intensity profile, whose depletion factor is around four orders of magnitude when comparing to the inner part of the disk. The (sub-)mm emission in the case of multiple ice lines remains similar to that in the case when only the water ice line is included. This is because the mm-/cm-sized particles are not affected by the changes of the fragmentation velocity when more than one ice line is included in the outer disk. In model III and $\alpha = 10^{-2}$, there is a sharp decrease of the intensity at 1.6 μm after the gap and ring located near the water ice line. This is the result of a more flared inner disk with high density of small grains that can block the light from the central star, preventing the light to be scattered in the outer surface layers.

In summary, the general trend in all models is just a dip of emission (or shallow gaps) at (sub-)mm emission near the ice lines. The width of the gap or the separation between the ring-like shapes is smaller at longer wavelength. The depression of such a dip or gap at (sub-)mm is less than one order of magnitude and thus much more shallower than at 1.6 μm. It is important to note that at longer wavelengths, that is 3 mm, the outer disk radius is smaller than at shorter wavelengths as expected from radial drift.

The convolved images prove that the structures and depletions that are expected from ice lines can be detected with the current capabilities of different telescopes, such as VLT/SPHERE and ALMA.

8.4 Discussion

8.4.1 The effect of the disk viscosity

The assumed value for the disk viscosity plays an important role on the final dust distributions, and hence on the potential structures. The value of α depends on how angular momentum is transported within the disk, which can have different origins such as MRI and MHD winds (e.g., Balbus & Hawley, 1991; Suzuki & Inutsuka, 2009; Bai, 2016, cf. Sect. 1.1.3). MRI requires disk ionization for the disk gas to be coupled to the magnetic field, and therefore if MRI drives accretion and turbulence, the value of α depends on the ionization environment of the disk (e.g., Dolginov & Stepinski, 1994; Flock et al., 2012; Desch & Turner, 2015).

Observationally, measuring the level of turbulence in protoplanetary disks is quite challenging, although recent efforts with ALMA allowed to measure the turbulent velocity dispersion for a couple of protoplanetary disks (Flaherty et al., 2015, 2017; Teague et al., 2016), revealing values predicted by MRI, but still with large uncertainty ($\alpha \sim 10^{-4} - 10^{-2}$, e.g., Simon et al., 2015).

The value of α is of great importance in the context of dust evolution models because it determines the turbulent velocities of the dust particles and hence the fragmentation limit (Eq. 8.5). After combining our results from the dust evolution models with radiative transfer calculations, we demonstrate that the shape (in particular the depth) of the dips or gaps that formed due to variations of fragmentation dust properties near the ice line depends on α. The depletion factor of the gaps or dips becomes higher for lower values of α, although the main differences are between the results of 10^{-2} and the other two values considered (10^{-4} and 10^{-3}). This is because for $\alpha = 10^{-2}$, the maximum grain size is determined by fragmentation in the entire disk, while for the other two values it is a mixture between fragmentation and drift. Therefore, observationally insights about the turbulence in disks can provide better constraints on whether or not the origin of gaps are due to ice lines.

In the context of our simulations, the number of rings or gaps depend on how many changes of the fragmentation velocity are assumed. In this work, we assume up to three variations corresponding to three main volatiles. It is important to notice that multiple gaps/rings are only obtained at NIR light, while at the mm emission there is only a single dip or gap. Multiple ring structures at scattered light were only obtained in model III with three radial variations of the fragmentation velocity and low values of $\alpha-$viscosity (Figs. 8.4 and 8.5).

8.4.2 Discerning different gap-opening mechanisms

There are several possibilities for the origin of rings and gaps in protoplanetary disk, including radial variations of the disk viscosity and planet disk interaction. However, different observational diagnostics can give insights to distinguish between these scenarios.

Models of planet disk interaction predict that when the planet is massive enough to open a gap in the gas surface density, there is trapping of mm-sized particles at the outer edge of the gap where the density and hence the pressure increases outwards (Rice et al., 2006; Zhu et al., 2011; Pinilla et al., 2012a). Depending on the planet mass (which changes the pressure gradient) and disk viscosity, there is a critical grain size that can be trapped. In general, the micron-sized particles are not effectively trapped and they can be distributed throughout the disk showing a smooth distribution or a shallower and smaller gap at short-wavelength than at mm emission (de Juan Ovelar et al., 2013; Dong et al., 2015c). This is an important difference to our current models of ice lines where a shallower gap is obtained at the mm emission. For instance, there is a dip of emission near the water ice line which is much more depleted at 1.6μm than at 0.87 or 3.0 mm. In addition, in the case of ice lines, the width of the gap or the separation between the rings is smaller at longer wavelengths.

For the gas distribution, in the case of massive planets, a deep gap is also expected in the *total* gas surface density, for which depth and width again depend on the planet mass and disk viscosity. In the case of ice lines, it is not expected that the *total* gas surface density has strong variations (e.g., Ciesla & Cuzzi, 2006; Stammler et al., 2017). The CO molecular line and its isotopologues are usually used to infer the gas surface density distribution, but these can be strongly affected by the CO ice line (e.g., Schoonenberg & Ormel, 2017).

In the case where the planet is not massive enough to open a gap in the gas surface density, the dust can still be shaped in rings and gaps due to changes in the gas velocities near the planet position and which can slow down the radial dust motion (Paardekooper & Mellema, 2004, 2006; Rosotti et al., 2016; Dipierro et al., 2016). As in the case of ice lines, the total gas surface density should not show any strong depletions. Nevertheless, the gaps in the case of low mass planets are expected to be shallower and narrower for smaller grains than for large grains. As a consequence, measuring the depth and width of an observed gap at NIR emission and mm-emission is one of the keys to discern between ice lines and low mass planetary origin.

Alternatives for gap-opening processes are variations of the disk viscosity that can lead to different transport of angular momentum, creating bumps in the gas surface density that can lead to trapping of particles. The trapping mechanism is more effective for large mm grains, while the small grains are expected to be diffused and smoothly disturbed in the disk (Pinilla et al., 2012b), opposite to our current results for the ice lines.

8.4.3 Comparison for TW Hya

We discuss our results in the context of current observations of TW Hya (cf. Fig. 1.9), because it is very well studied in the literature, and the CO ice line has been claimed to be imaged by ALMA. In addition, there are constraints in the level of turbulence, making it an excellent laboratory to discuss our current results.

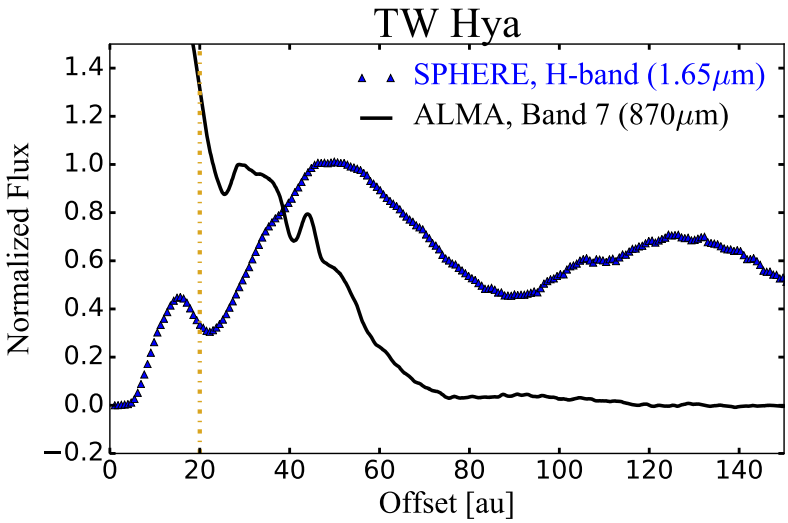

Figure 8.6: Comparison of the radial intensity profile of TW Hya from SPHERE (van Boekel et al., 2017) at 1.65 μm versus the sub-mm emission at 870 μm from ALMA (Andrews et al., 2016). Both profiles are obtained by azimuthally averaging the surface brightness intensity, and normalizing it to one of the peaks of emission (peak at $\sim$0.″8 for the SPHERE profile and peak at $\sim$0.″5 for the ALMA profile). The profile from SPHERE is multiplied by r^2 to compensate for the stellar illumination. The vertical line represents the location of the CO ice line at 20 au (assuming a distance of 59.5 pc, Gaia Collaboration et al., 2016).

In TW Hya, the ionization environment was investigated by Cleeves et al. (2015), suggesting a dead zone extended up to 60 au distance. The level of turbulence was constrained by Teague et al. (2016), finding non-thermal motion from the CO(2-1) emission layer. The CO ice line was suggested to be at 30 au from observations of N_2H^+, which might be a chemical tracer of CO ice (e.g., Qi et al., 2013). However, van't Hoff et al. (2017) demonstrated that the amount of CO in the gas phase can affect the abundance of N_2H^+, such that the N_2H^+ column density peaks further outside the CO snow line. Assuming disk parameters of the TW Hya disk, van't Hoff et al. (2017) found that the CO ice line should be located at 20 au, in agreement with recent ALMA observations (Zhang et al., 2017).

Near 20 au distance there is a distinct gap at scattered light followed by a ring-like emission in the TW Hya disk (see Fig. 8.6, van Boekel et al., 2017), and ALMA observations also reveal a gap at 0.87 mm that is narrower than the one observed at scattered light (see Fig. 8.6, Andrews et al., 2016). This gap at 20 au follows the trend found for the gap shape of our models when the disk viscosity is low ($\alpha = 10^{-3} - 10^{-4}$, see also Fig.10 in Zhang et al., 2017), in agreement with the possibility that the CO ice line is inside a MRI-dead region. It is important to notice that our models are for a disk around a Herbig star and the CO ice line is much further out (close to the outer edge) than in TW Hya. However, the observed shapes of the gap near 20 au are similar to the results of our models at $\sim$8 au, where the fragmentation velocity increases by one order of magnitude. The observed gap,

in particular in the mm emission, is narrower than our prediction. In our models, the width is determined by where the fragmentation velocity changes and this determines whether the maximum grain size is dictated by fragmentation or drift. Our models may be neglecting variations of the fragmentation velocity due to for instance other main volatiles that change the stickiness efficiency near the CO ice line that can make the gap smaller.

Additional observational insights can be obtained if the *total* gas surface density can be inferred. If a deep gap is also detected in the *total* gas surface density at this location, this would suggest that the CO ice line is not responsible of the observed gap.

Because these comparisons are done with polarized light intensity, we run as a test a 3D single scattering model for one of the cases (model III with $\alpha = 10^{-3}$), keeping the same disk parameters to calculate the polarized intensity profile at 1.6 μm. The resulting shape of the radial profile of the polarized intensity is similar to the profile of the total intensity.

8.5 Conclusions

In this work, the effect that different ice lines have on the dust-density distribution at million year time scales is investigated, by including radial variations of the fragmentation velocity at the ice lines of H_2O, CO_2 (or CO), and NH_3. Our findings are:

1. Variations of the fragmentation properties of dust particles near ice lines can lead to visible gaps and rings, in particular at short-wavelengths.

2. The amount of gaps depends on the number of ice lines considered. When only the water ice line is assumed, there is a break of the emission near the ice line at different wavelengths and independent of disk viscosity. The depth of the break or dip is higher for lower viscosity.

3. When the CO_2 (or CO), and NH_3 ice lines are also assumed in the models, there is a clear gap between ice lines. The depth of the gaps depends on the disk viscosity, which is deeper for lower viscosity. In addition, the formed gaps are narrower at longer wavelengths. The total number of rings and gaps can vary with wavelength. For instance, in the case of three ice lines, there are two clear gaps and three bright regions in the emission at 1.6 μm, but only one gap at the (sub-)mm emission.

4. The general trend of our results is that gaps at the (sub-)mm emission are shallower and narrower than at scattered light. Comparing the scattered light and mm observations of TW Hya, where the CO ice line has been observed, there are structures near the CO ice line (at 20 au) that are in agreement

with our findings. This is opposite to the results expected by models of dust trapping by a giant planet embedded in the disk or when trapping is triggered by changes of disk viscosity, where a deeper and wider gap is expected at the (sub-)mm emission.

5. In our models the gap width corresponds to the separation between ice lines, and therefore the gaps are very wide compared to the rings observed in disks around for example TW Hya and HL Tau. However, any other volatile or mechanism that contributes to change the dust fragmentation velocities can lead to closer gaps and rings, or they can have a different origin.

6. In these models, we do not expect a strong change of the *total* gas surface density near the ice lines. Massive planets or dead zones can lead to strong variations (gaps or bumps) in the gas surface density.

Appendix

Figures 8.7, 8.8 and 8.9 show the 2D (r, z) dust density distribution assumed for the radiative transfer calculations and obtained using Eq. 8.7, for small grains $a \in [1 - 10]\,\mu$m), large grains ($a \in [1 - 10]\,$mm), and all grains, assuming different values of α.

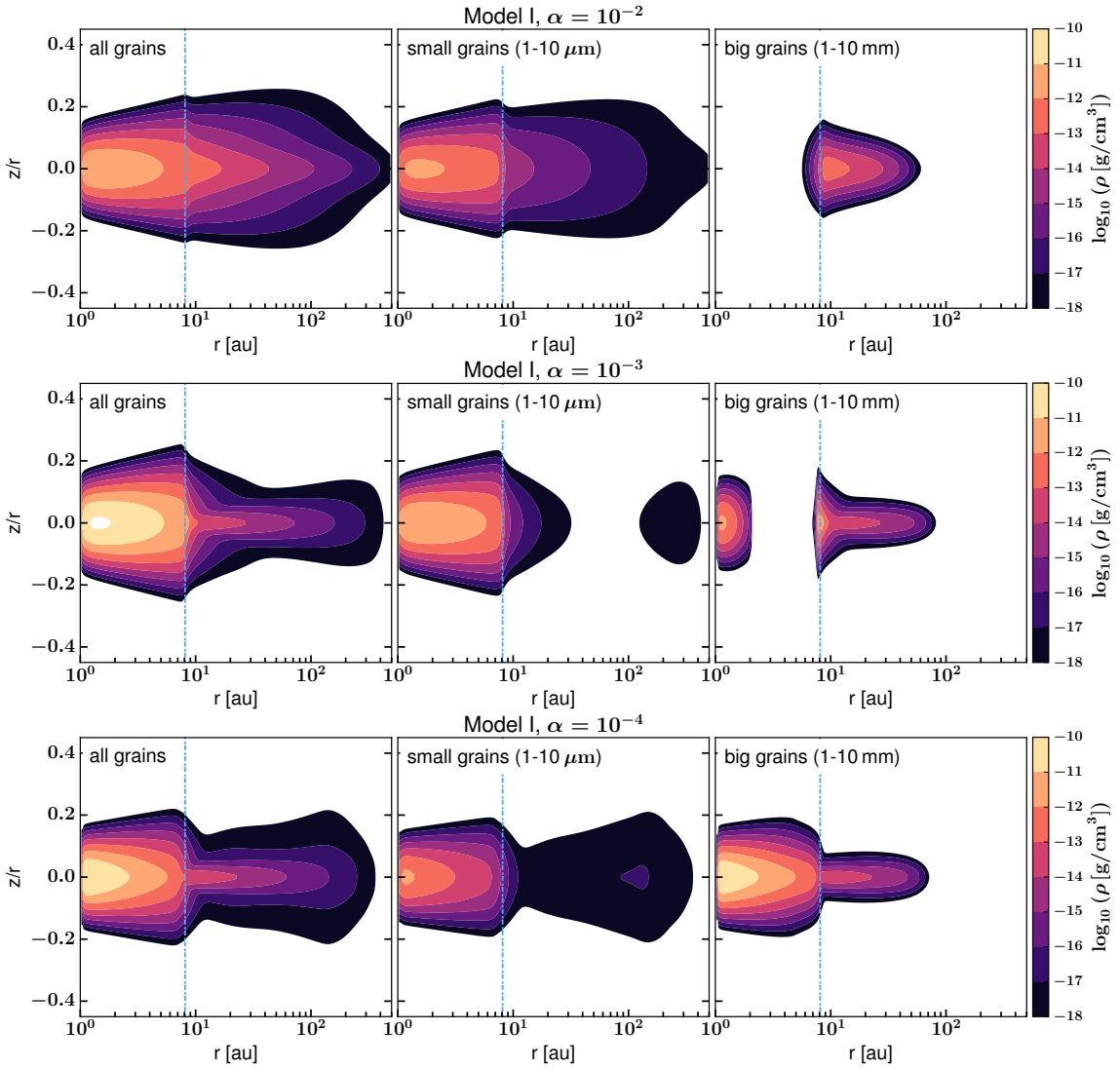

Figure 8.7: 2D dust density distribution assumed for the radiative transfer calculations and obtained using Eq. 8.7. We show the distribution for all the grain sizes (left panels), small grains ($a \in [1-10]\,\mu$m, middle panels), and large grains ($a \in [1-10]\,$mm, right panels). All plots correspond to model I (only H_2O ice line, vertical line) with different values of $\alpha = 10^{-2}$ (top panels), $\alpha = 10^{-3}$ (middle panels), and $\alpha = 10^{-4}$ (bottom panels).

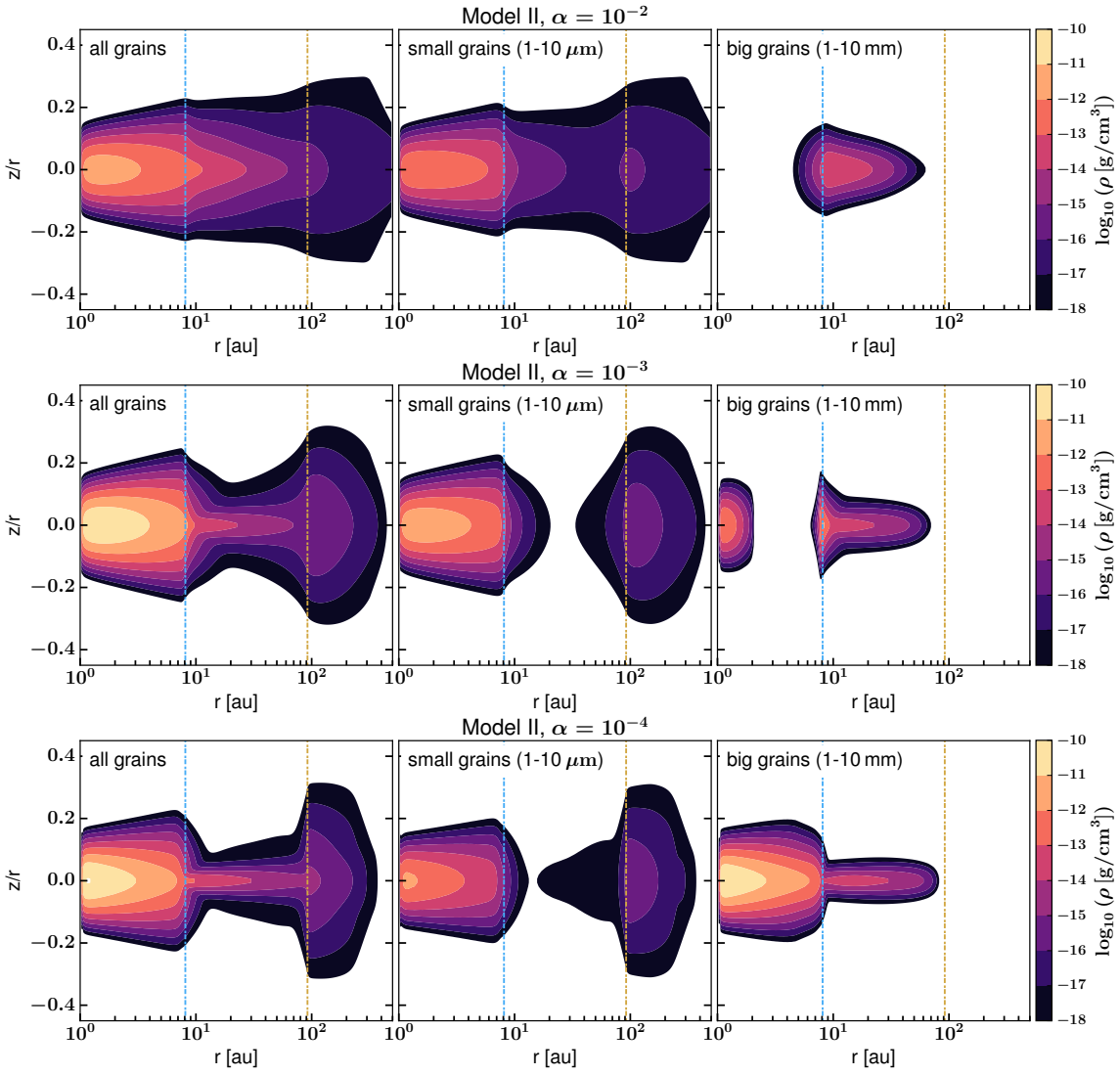

Figure 8.8: As Fig. 8.7, but for model II (H_2O and CO_2 ice lines, vertical lines).

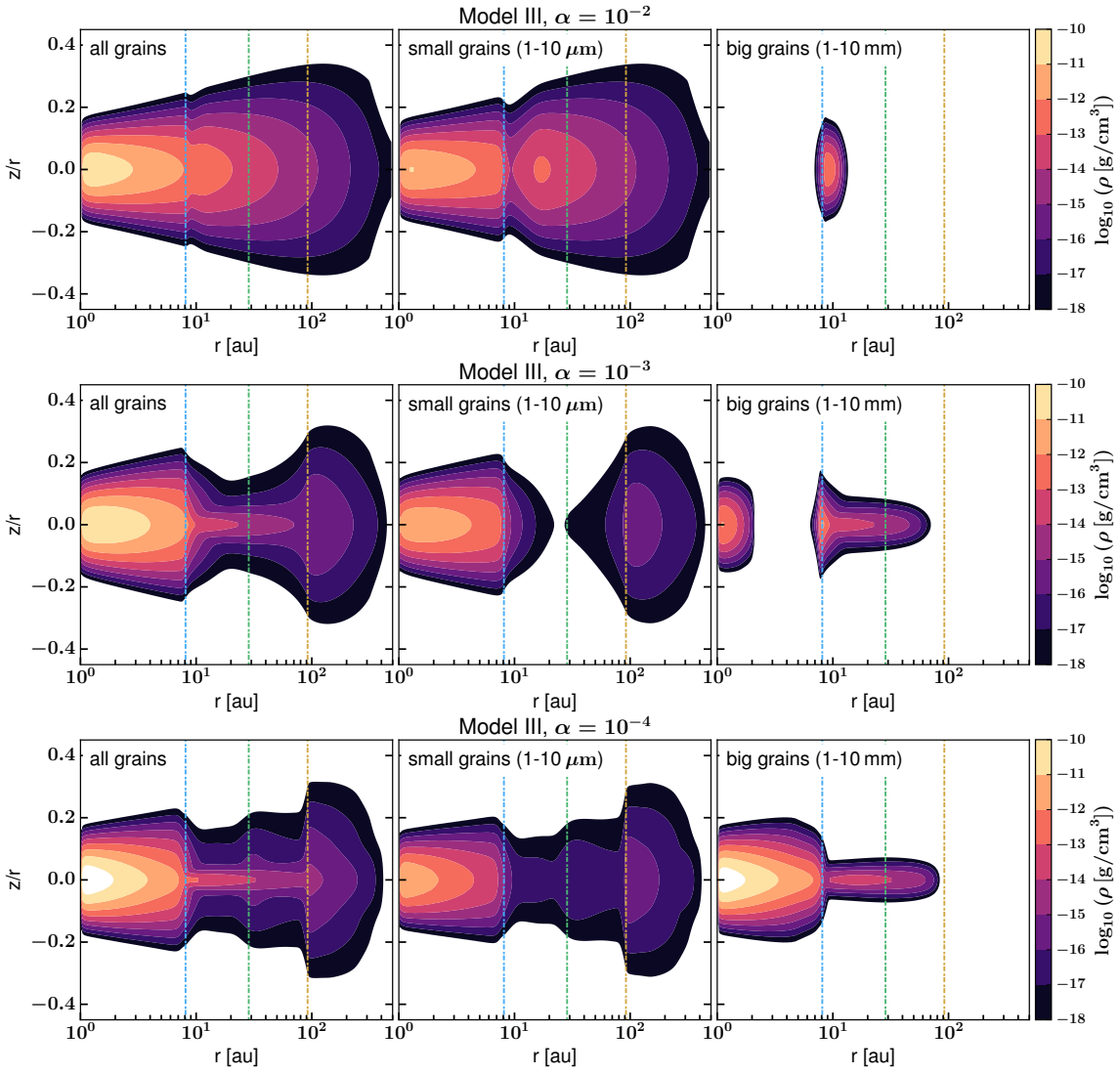

Figure 8.9: As Fig. 8.7, but for model III (H_2O, CO_2, and NH_3 ice lines, vertical lines).

9 | Flaring of scattered light as an independent tracer of the bulk gas distribution

The content of this chapter is based on a paper in preparation by Pohl et al., *in prep.*

9.1 Motivation

9.1.1 Disk mass estimates and their problems

Constraining the spatial distribution of the bulk gas in protoplanetary disks and determining their total mass is fundamental in understanding the processes involved in planet formation. The mass budget of a protoplanetary disk, which is the building material for planets, has a profound impact on the disk evolution, and thus, on the diversity of planetary types and system architectures (e.g., Mordasini et al., 2012). Both the disk dust and gas masses (M_d and M_g) are exceedingly difficult to constrain from observations (cf. Sect. 3.1.3). A dust opacity value at the observed wavelength together with a dust temperature has to be chosen to infer the total dust mass, both quantities involve uncertainties. The dominant constituent of the bulk gas mass, H_2, lacks a permanent dipole moment, and is difficult to observe directly because of its intrinsically weak lines at NIR and MIR wavelengths. Instead, measurements of the disk gas mass are commonly done by tracers such as CO isotopologues.

However, the derived gas mass is particularly sensitive to the conversion of the observed CO mass into total gas mass. Usually, the canonical ISM value of $[\mathrm{CO}]/[\mathrm{H_2}] = 10^{-4}$ is used, which might be underestimated due to processes like CO photodissociation in the upper layers and freeze-out in the disk midplane. Recently, several ALMA surveys used a combination of mm continuum emission and ^{13}CO and C^{18}O line emission to measure disk masses and gas-to-dust ratios for a large sample of disks in different nearby star-forming regions (e.g., Ansdell et al., 2016; Barenfeld et al., 2016; Pascucci et al., 2016; Long et al., 2017a). They all reveal the surprising trend of implausibly low gas masses and gas-to-dust ratios well below the canonical ISM value of 100. This is found even after the effects of CO

freeze-out and isotope-selective photodissociation have been taken into account for the modeling analysis. For example, Ansdell et al. (2016) report on a sample of Lupus disks with a substantially depleted gas content relative to the inferred refractory content with typical disk gas masses that are smaller than M_{jup}. While the reason for these low gas-to-dust ratios is not understood, a proposed solution considers that the CO emission is not tracing the bulk of the H_2. Possibly, there is a depletion of CO through grain evolution with a condensation/sublimation of volatiles onto grains (Krijt et al., 2016), or the sequestering of carbon from CO to more complex molecules (Miotello et al., 2017). Favre et al. (2013) and Schwarz et al. (2016) report on low abundances of CO and other carbon bearing species in the TW Hya system, which suggests that the majority of the volatile carbon has been removed from the gas. The small amount of CO returning to the gas phase inside the surface CO snowline is insufficient to explain the overall depletion.

As an alternative gas mass probe, the fundamental rotational transition of HD has been observed by Herschel, but so far only for three disks (TW Hya: Bergin et al. 2013, DM Tau and GM Aur: McClure et al. 2016). Even this rather low statistics sample shows that the HD mass estimates hint at higher disk gas masses than inferred from the CO surveys. This suggests a depletion of CO rather than of the bulk H_2 gas. However, current methods cannot readily distinguish between these scenarios, demanding an independent measure for the bulk mass distribution.

9.1.2 Scattered light as a solution

A new idea will be presented here that makes use of the flaring of scattered light to estimate the bulk gas mass distribution. It profits from the strong dynamical coupling between the bulk gas and the small dust particles that dominate the scattered light from the disk surface layer at optical and NIR wavelengths.

As introduced in Chapter 1, protoplanetary disks are optically thick in the optical and NIR, thus, the radiation from the star is not able to pass through the disk, but is absorbed in the surface layers of the disk. There is a height above the midplane, where the disk becomes transparent. Referring to the concept of optical depth from Chapter 2 (Eq. 2.2), this scattering surface height H_s is defined where the radial optical depth, τ_r, is about unity. Typically, H_s is a few times the pressure scale height H (e.g., Dullemond et al., 2001), which is in turn related to the dust scale height H_d as derived below in Eq. 9.5. They are sensitive to both the gas surface density and therefore M_g, and the turbulence. This dependency is exploited analytically and with radiative transfer modeling in the following Sects. 9.2 and 9.3. A related approach has been already followed in the case study of TW Hya (van Boekel et al., 2017), where the authors reconstruct the bulk gas surface density profile from the observed scattered light brightness distribution for a fixed turbulence parameter. This method provides independent constraints on the gas distribution at similar spatial resolution as it is feasible with ALMA gas line observations.

9.2 Method

9.2.1 Vertical settling and stirring

Dust grains in the tenuous disk atmosphere settle towards the midplane, but mixing counteracts this downward motion. More precisely, turbulence prevents the dust from settling down below a certain disk height, and therefore determines the final shape of the photospheric surface of the disk.

A particle suspended in gas at a height z above the midplane is subject to the vertical component of the stellar gravity force, $F_{\rm grav} = -m\,z\,\Omega_{\rm K}^2$. As the particle starts to fall towards the midplane, it feels a friction force as defined in Eq. 1.23. By equating these two forces, the equilibrium settling speed for particles in the Epstein regime is set by $v_{\rm sett} = -z\,\Omega_{\rm K}\,{\rm St}$ (Dullemond & Dominik, 2004b). Following Birnstiel et al. (2010), the settling speed is limited to velocities smaller than half the vertically projected Kepler velocity, such that $v_{\rm sett} = -z\,\Omega_{\rm K}\,\min\left(1/2, {\rm St}\right)$. The time scale for settling is defined as

$$t_{\rm sett} = \frac{z}{v_{\rm sett}}\,. \tag{9.1}$$

The turbulent eddies of the gas transport the dust grains up and down in a random manner, which leads to a turbulent diffusion process. Youdin & Lithwick (2007) derived the so-called Schmidt number Sc as the ratio of gas diffusivity $D_{\rm g}$ over dust diffusivity $D_{\rm d}$,

$${\rm Sc} \equiv \frac{D_{\rm g}}{D_{\rm d}} = 1 + {\rm St}^2\,. \tag{9.2}$$

The diffusion coefficient for gas molecules is set to be equal to the turbulent gas viscosity $\nu_{\rm t}$. Using the α-prescription from Eq. 1.21, this leads to

$$D_{\rm g} = \alpha c_{\rm s} H\,. \tag{9.3}$$

The time scale for turbulent diffusion, or vertical stirring, is now given by (Schräpler & Henning, 2004),

$$t_{\rm stir} = \frac{z^2}{D_{\rm d}} = \frac{H_{\rm d}^2\left(1+{\rm St}^2\right)}{\alpha c_{\rm s} H}\,. \tag{9.4}$$

By equating Eqs. 9.1 and 9.4 and by constraining the dust scale height to be at most

equal to the gas scale height, the dust scale height can be derived as

$$H_\mathrm{d} = H \min\left(1, \sqrt{\frac{\alpha}{\min\left(1/2, \mathrm{St}\right)\left(1+\mathrm{St}^2\right)}}\right) . \tag{9.5}$$

Inserting the Stokes number in the case of the Epstein regime ($\mathrm{St} \propto a\,\Sigma_\mathrm{g}^{-1}$, cf. Eq. 1.26), which applies to small grains that are most relevant for this study, and only considering leading exponents, this yields a proportionality of

$$H_\mathrm{d} \propto \alpha^{1/2}\,\Sigma_\mathrm{g}^{3/2}\,a^{-3/2} . \tag{9.6}$$

From Eq. 9.6 it is clear that scattered light can only probe the product of the bulk gas density, the turbulence strength, and grain size. The dependency of the dust scale height and correspondingly of the scattering surface height on α and the gas mass are, however, expected to differ. Moreover, the degeneracy with the turbulent mixing can be broken with kinematic ALMA observations of CO isotopologue emission that are used to estimate the turbulence level (Flaherty et al., 2015, 2017; Teague et al., 2016). The analysis of polarimetric scattered light data is pivotal to constrain the scattering phase function and consequently the properties of the grains.

9.2.2 Disk model

A smooth disk is considered with a surface density distribution that is radially parameterized close to the self-similar solution from Lynden-Bell & Pringle (1974),

$$\Sigma_\mathrm{g,d}(r) = \Sigma_\mathrm{g,d,0}\left(\frac{r}{r_\mathrm{c}}\right)^{-\delta} \exp\left[-\left(\frac{r}{r_\mathrm{c}}\right)^{2-\delta}\right] , \tag{9.7}$$

with a δ of unity and a characteristic tapering-off radius $r_\mathrm{c} = 120\,\mathrm{au}$. The radial grid extends from 1 au to 150 au. The surface density profile is scaled to the total gas and dust mass, respectively, which only differ by a constant gas-to-dust ratio. The disk is considered to be in a state of hydrostatic equilibrium such that the vertical surface density profile obeys a Gaussian profile (see Eq. 1.11),

$$\rho_\mathrm{g,d}(R,z) = \rho_\mathrm{g,d,0}(R)\,\exp\left(-\frac{z^2}{2\,H_\mathrm{g,d}^2(R)}\right) . \tag{9.8}$$

The cylindrical coordinates (R, z) can be converted into spherical coordinates via $R = r\sin\theta$ and $z = r\cos\theta$. The disk's scale height is parameterized radially as $H(R) = H_0(R/R_0)^\psi$, where $H_0 = 5\,\mathrm{au}$ is the scale height at the reference radius

$R_0 = 50\,\mathrm{au}$, and $\psi = 1.25$ is the flaring index. For the dust grain size distribution a power law with exponent $\gamma = 3.5$ and a minimum ($\mathrm{a_{min}} = \{0.1, 10\,\mu\mathrm{m}\}$) and maximum ($\mathrm{a_{max}} = \{10, 20\,\mu\mathrm{m}\}$) grain size is used. The opacities are calculated for compact, spherical particles and a dust mixture of 70% silicates and 30% carbon using the optical constants from Jaeger et al. (1994); Dorschner et al. (1995) and Preibisch et al. (1993). For the stellar parameters of the central luminosity source typical values of a Herbig Ae star are taken ($T_{\mathrm{eff}} = 8400\,\mathrm{K}$, $M_\star = 1.65\,\mathrm{M}_\odot$, $R_\star = 1.5\,\mathrm{R}_\odot$).

As explained above, an observable feature of the disk opacity structure is the scattering surface H_s. In order to verify its dependence on the gas-to-dust ratio, two approaches can be followed: (1) the gas mass is kept constant and the dust mass is changed via different gas-to-dust ratios; (2) the dust mass is kept constant and the gas mass is changed via different gas-to-dust ratios. From the Lupus survey a lack of gas rather than an excess of dust seems to be inferred, thus, the flaring structure of disks over a wide range of different gas masses should be analyzed. Hence, approach (2) has to be eventually followed when applying the method to observations. In order to show the level of degeneracy between α, the gas-to-dust ratio, and the absolute dust and gas masses, approach (2) will be investigated in the following. With Eq. 9.5 the dust scale height is calculated depending on the α-viscosity and the Stokes number.

For each model with a certain set of $\{M_\mathrm{d}, M_\mathrm{g}, \alpha\}$ the radial $\tau_\mathrm{r} = 1$ surface is calculated. For this purpose, the radial optical depth $\tau_\mathrm{r}(r, z)$ across the radial disk extension at a wavelength of $1.2\,\mu\mathrm{m}$ is computed via the dust density $\rho_\mathrm{d}(r, z)$ and opacity κ_ν (cf. Eq. 2.2). Then, for each disk radius the height z where $\tau_\mathrm{r} = 1$ is determined, which corresponds to the scattering surface $H_\mathrm{s}(r)$.

9.3 Results

Figure 9.1 shows the results of approach (2) at a wavelength of $1.2\,\mu\mathrm{m}$ for a fixed disk dust mass of $10^{-4}\,\mathrm{M}_\odot$. The left panels considers two different gas-to-dust ratios of $\{1, 50\}$ colored in orange and blue for three different $\alpha = \{10^{-4}, 10^{-3}, 10^{-2}\}$ values, shown with triangles, circles, and squares, respectively. The scattering surface is higher the larger the gas-to-dust ratio is, that is a higher disk gas mass for a constant dust mass. Moreover, the scattering surface is sensitive to the turbulence parameter giving the highest values for $\alpha = 10^{-2}$. Current turbulence measurements do, however, rule out such a high α-parameter due to the lack of non-thermal broadening. The right panel shows the two lower α cases for three different gas-to-dust ratios, for which the sensitivity of the gas surface density is more prominent. It can be concluded that H_s is sufficiently sensitive to the gas mass given the large spread between the dark blue markers and the yellow/light blue markers for a specific α value.

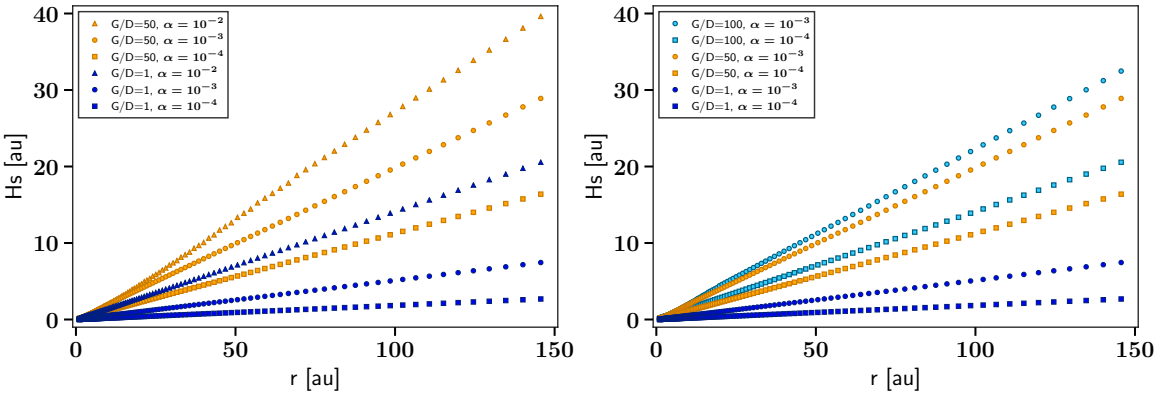

Figure 9.1: Dependency of the scattering surface height at a wavelength of 1.2 μm on the gas-to-dust ratio (here indicated as G/D) and turbulence level (α) computed for models with a constant disk dust mass of $10^{-4}\,M_\odot$. The results are shown for a grain size distribution with $a_{min} = 0.1\,\mu$m and $a_{max} = 10\,\mu$m.

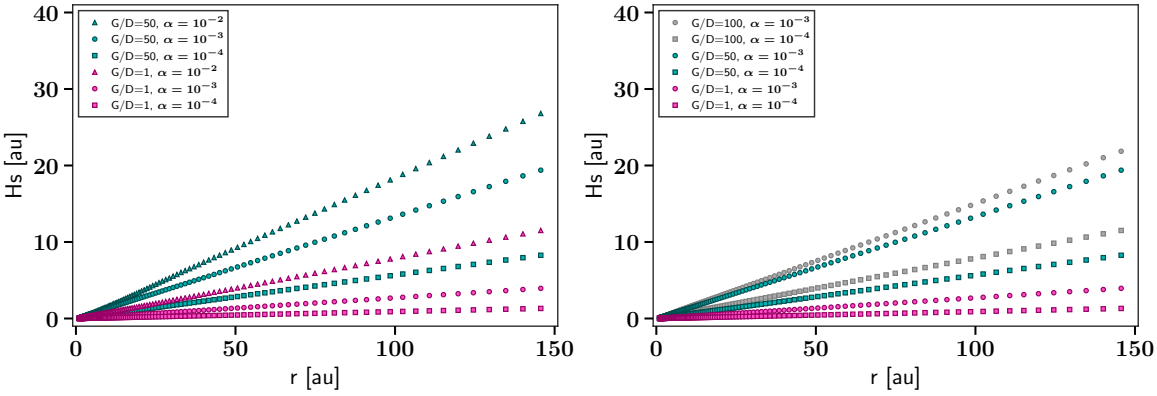

Figure 9.2: Dependency of the scattering surface height at a wavelength of 1.2 μm on the grain size computed for models with a constant disk dust mass of $10^{-4}\,M_\odot$ and specific gas-to-dust ratio and α values. The results are shown for a grain size distribution with $a_{min} = 10\,\mu$m and $a_{max} = 20\,\mu$m.

The larger the grain size the smaller is its dust scale height according to Eq. 9.5, which is consequently also reflected in the scattering surface height. Due to this settling effect, the surface height of the disk is reduced when scattering from larger grains is measured. Hence, the appearance of the disk in the optical and NIR becomes flatter. Figure 9.2 shows this trend for a grain size distribution with $a_{min} = 10\,\mu$m and $a_{max} = 20\,\mu$m. It illustrates that the scattering surface height is significantly lower than expected for the distribution of smaller grains, which is also visible in the comparison plot of Fig. 9.3. The spreads in the gas-to-dust ratio and α are independent of the grain size. Grains with sizes of a few tens of microns are expected to be located below the scattering surface layer of the smallest grains due to the settling effect. Since these particles have higher Stokes numbers, they are no longer efficiently coupled to the gas as it is the case for the smaller grains.

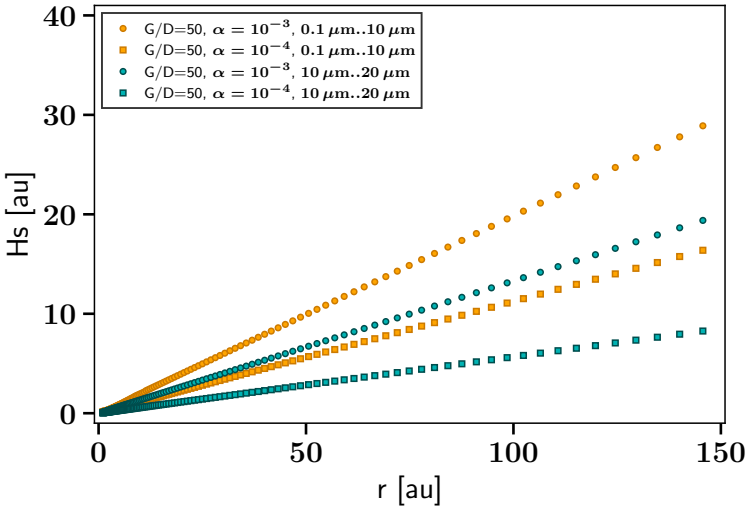

Figure 9.3: Comparison of the scattering surface height at a wavelength of 1.2 μm for different grain size distributions. The orange curves are from Fig. 9.1, the green curves from Fig. 9.2.

Moreover, dust grains that are small compared to the wavelength scatter photons uniformly, while larger grains have strongly forward peaking scattering phase function. Thus, for disks viewed at low-inclination large grains scatter photons mostly into the disk, and only a small fraction reaches the observer. For inclined-disks, the combination of total and polarized intensity images at optical or NIR light help to constrain the dominant grain size (cf. Chapter 6). This way, the possible degeneracy of the dust scattering height with the grain size can be approached.

So far, only the initial vertical structure is taken into account for the calculations of the scattering surface height. This is a valid approach as long as the main interest only lies in a relative comparison of the different parameter effects. In order to apply the approach to observations, for which absolute values are desired, the vertical structure has to be re-calculated in an iterative manner. Again, it is assumed that the gas is in vertical hydrostatic equilibrium. Exemplarily, the left panel in Fig. 9.4 shows the dust density distribution assumed for the radiative transfer calculation for the model with a gas-to-dust ratio of 50 and $\alpha = 10^{-2}$. As a first step, the dust temperature (Fig. 9.4, right panel) is calculated by a Monte Carlo simulation as explained in Sect. 2.3. Then, the gas scale height is re-calculated by following Eqs. 1.5 and 1.8,

$$H = \sqrt{\frac{k_\mathrm{B} T r^3}{\mu m_\mathrm{p} G M_\star}}\,, \tag{9.9}$$

where this calculation implicitly assumes that the dust temperature is equal to the

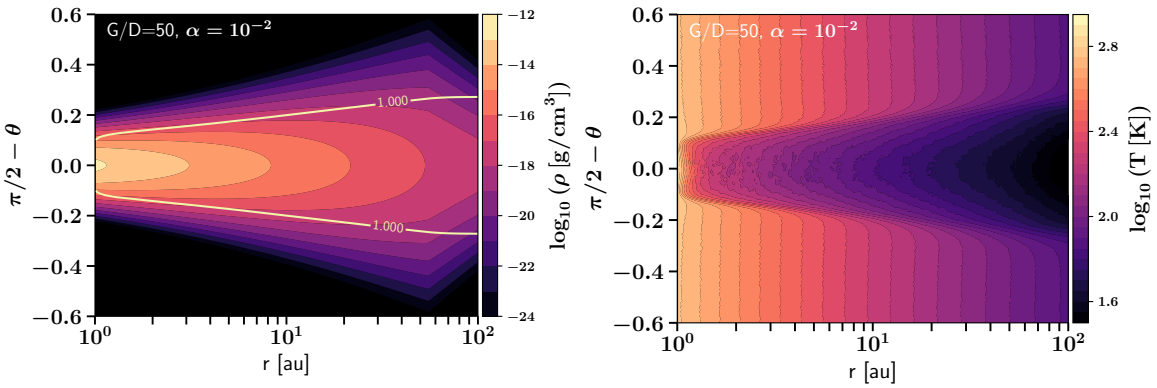

Figure 9.4: *Left:* 2D dust density distribution assumed for the radiative transfer calculation. It is obtained using Eqs. 9.5 and 9.8 for the model with G/D= 50, $\alpha = 10^{-2}$ and a constant disk dust mass of $10^{-4}\,\mathrm{M}_\odot$. The yellow contour line denotes the $\tau_\mathrm{r} = 1$ surface. *Right:* Dust temperature map obtained after the first Monte Carlo simulation run.

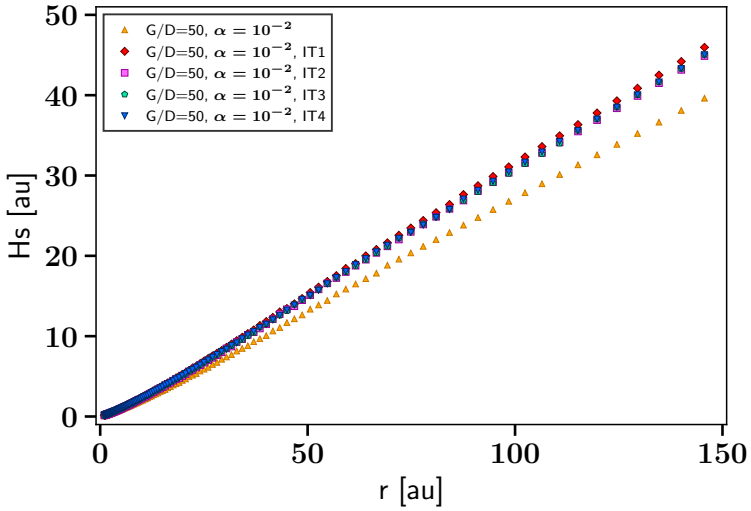

Figure 9.5: Results for the vertical structure of the disk when calculating it in an iterative manner.

gas temperature. By mimicking dust settling the dust scale height is subsequently determined via Eq. 9.5. The recalculated vertical structure deviates from the initial assumption, so that the solution is not yet self-consistent. Thus, a second Monte Carlo simulations is performed in order to calculate the new dust temperature. The process of dust temperature and follow-up vertical structure calculation of the dust is iterated until the density and temperature structure converge to a self-consistent solution. Typically, convergence is reached within five iterations.

Figure 9.5 shows how the scattering surface height changes after each radiative transfer iteration of the physical disk structure. While the orange circles represent the initial condition, it can be recognized that a sufficiently converged solution is already reached after four iterations (blue triangles).

9.4 Summary and outlook

With the simple analytic approach outlined above it is predicted that for a given dust mass, a disk with a low gas-to-dust ratio will be significantly less flared than those with large gas-to-dust ratios. Nowadays, the scattering surface of the disk can be spatially resolved with high angular resolution instruments that work at optical and NIR light, such as VLT/SPHERE. Thus, the connection to high contrast and high angular resolution scattered light observations is as follows. Recent analyses of scattered light images from VLT/SPHERE show that the scattering surface H_s as a function of radius can be determined for intermediate inclined disks (cf. Fig. 7.5 and Eq. 7.1). Due to projection effects, an ellipse fitted to an inclined, flared disk has an offset from the stellar position along the semiminor axis. Such ellipses can be either fitted to brightness isophotes (Lagage et al., 2006), or to substructures in the form of multiple gaps and rings (de Boer et al., 2016; Ginski et al., 2016). For a specific disk, by running a grid of models for various M_g, taking into account measurements of the turbulent velocities, and comparing the results to the observational H_s reconstruction, constraints on the disk gas mass can be set. These findings can be compared to the CO isotopologue and HD gas mass estimates. This is possible under the assumption that the disk dust mass can be constrained from SED fitting, that adequate measurements of the turbulent gas velocities are available, and that the scattered light is dominated by small grains. A further qualitative or quantitative comparison could be made by comparing the scattered light emission morphology rather than directly comparing H_s. Appropriate SPHERE data for inclined disks with substructure will be available in the near future to test our approach. It is also planned to extend the modeling effort by considering more realistic dust distributions instead of the simple power-law size distributions. This way, the scattering surface situation for different evolutionary times of the disk lifetime can be investigated.

10 | Investigating dust trapping in transition disks with millimeter-wave polarization

The content of this chapter is based on Pohl et al. (2016) published in *A&A, 593, A12*, and on a paper in preparation by Pohl et al., *in prep.*

10.1 Motivation

Observational constraints on the size of grains embedded in a protoplanetary disk are crucial to investigate dust coagulation and ongoing planet formation processes. Observations at mm wavelengths have probed large (mm-sized) grains in the disk midplane, through calculation of a low spectral index of the dust opacity (e.g., Beckwith & Sargent, 1991; Testi et al., 2001; Rodmann et al., 2006; Ricci et al., 2010a,b; Guilloteau et al., 2011). For a continuous disk with a monotonically decreasing radial gas pressure, mm dust particles in the outer disk can experience an excessive radial drift toward the star, contradicting observations that revealed the existence of mm-sized particles in the outer disk regions (e.g., Wilner et al., 2005; Andrews & Williams, 2005; Ricci et al., 2010b, 2011). A particle trap caused by a pressure bump might be a solution to prevent this drift problem and to allow the grains to grow efficiently (e.g., Whipple, 1972; Klahr & Henning, 1997; Fromang & Nelson, 2005; Johansen et al., 2009; Pinilla et al., 2012b; Zhu et al., 2012). This bump can for example result from the presence of a massive planet carving a gap in the gas density. Hence, transition disks are excellent targets to study the impact of planet formation on the disk structure. To explain pronounced dust rings in protoplanetary disks there are certainly also other mechanisms (see Chapters 7 and 8). Particle trapping can be probed by measuring low spectral index values inside the trap, however, small opacity index values could be also explained by optically thick emission from compact regions (Ricci et al., 2012). Among other uncertainties, such as the composition and porosity of dust aggregates (Henning & Stognienko, 1996; Kataoka et al., 2014), this shows that only constraining the grain size with opacity index measurements is still problematic.

Recently, Kataoka et al. (2015) introduced an alternative, independent method to constrain the grain size distribution in protoplanetary disks based on dust polarization at mm wavelengths. The classical picture from the optical and NIR, where stellar photons are scattered by small dust in the disk surface layers, is transferred to dust self-scattering[9] in the mm wavelength regime (cf. Sect. 1.3.4). As mentioned above, it is known that dust grains in protoplanetary disks can grow to sizes comparable to mm wavelengths, meaning that they are expected to have a large albedo and, thus, can produce scattered light. When the radiation field is anisotropic, the continuum emission is expected to be partially polarized owing to self-scattering of dust thermal emission. So far, polarized (sub-)mm emission has been observed in the disks around a few YSOs, for example, IRAS 16293-2422B (Tamura et al., 1995; Rao et al., 2014), and L1527 (Segura-Cox et al., 2015). There have been two resolved detections of mm-wave polarization for disks that are Class I or older (HL Tau: Stephens et al. 2014, 2017; Kataoka et al. 2017 and HD 142527 Kataoka et al. 2016b). Commonly, magnetically or radially aligned grains (e.g., Lazarian, 2007, see Sect. 1.3.4) are assumed to be the source of polarization, but dust self-scattering is another important mechanism that needs to be considered. This idea has been explicitly applied to the protoplanetary disk around HL Tau by Kataoka et al. (2016a) and Yang et al. (2016), who successfully reproduced the polarization signatures observed at sub-mm by means of scattered thermal radiation.

Outline

In this work we study the dust trapping scenario when a massive planet is embedded in the disk, and investigate where polarization due to scattering can be detected. We combine 2D hydrodynamic simulations of planet-disk interactions with self-consistent dust growth models (cf., Pinilla et al., 2012a; de Juan Ovelar et al., 2013). These results are used to perform 3D radiative transfer calculations to predict the polarization at ALMA wavelengths due to scattered thermal emission. In contrast to Kataoka et al. (2015), we consider the simulated spatial dust density distribution for each grain size from the dust evolution model instead of a parametrized dust density and a simplified power-law grain size distribution. We compare our results for different dust evolution timescales and analyze the dependence of the polarization degree on the disk inclination, dust composition, the position of the planet, and observing wavelength. Moreover, we discuss whether the polarization is detectable with future ALMA observations.

This chapter is organized as follows. In Sect. 10.2 we describe the numerical methods to obtain a transition disk model and the radiative transfer calculations. Section 10.3 presents our results of the dust growth modeling and the simulated polarization maps. Furthermore, we discuss our findings in terms of disk inclination, dust evolution timescales, dust composition, the position of the planet, and observing

[9]Self-scattering means that the source of incident radiation is the thermal emission of the dust itself, which is then scattered off large dust grains resulting in polarized mm disk emission.

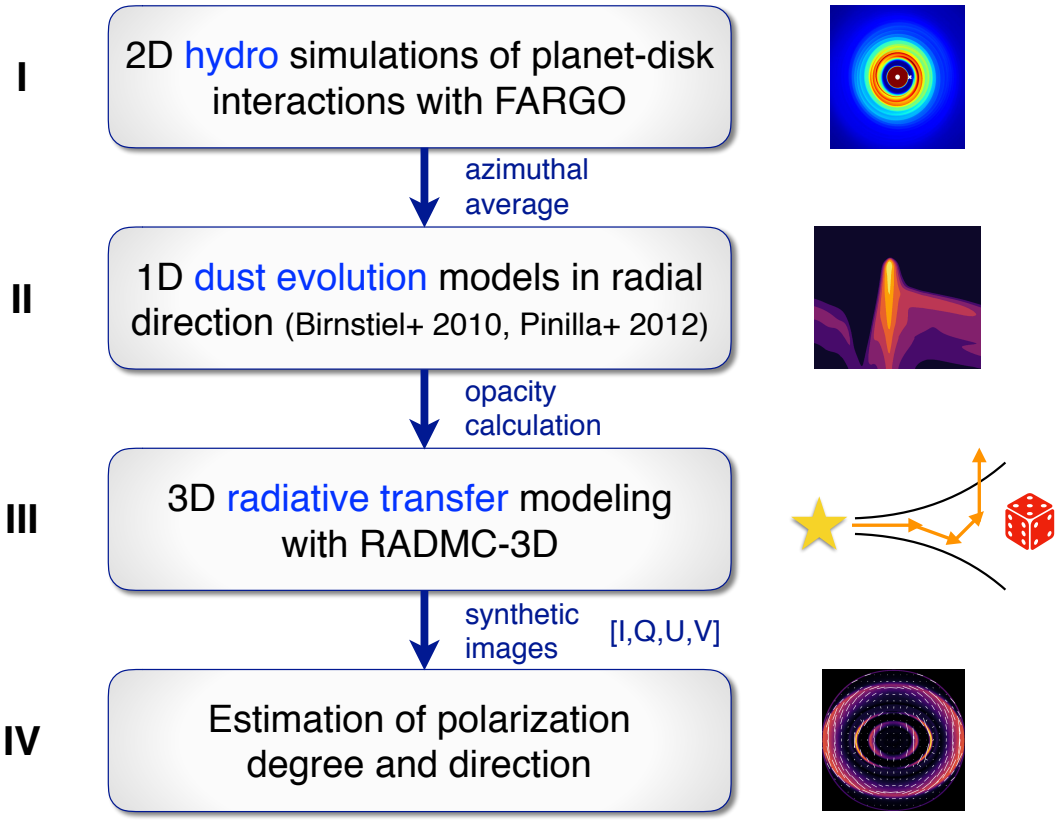

Figure 10.1: Chart illustrating the four basic steps of the modeling workflow.

wavelength. Finally, our results and the conclusions of this work are summarized in Sect. 10.4.

10.2 Numerical methods

Figure 10.1 illustrates the sequence of our different numerical modeling steps. The models start with performing hydrodynamic simulations of planet-disk interactions followed by self-consistent dust growth models, based on the setup from Pinilla et al. (2012a) that is also used in de Juan Ovelar et al. (2013). The resulting dust distributions after different evolution times are taken as input for radiative transfer calculations with the Monte Carlo-based radiative transfer code RADMC-3D (Dullemond et al., 2012). The details of the individual simulation steps are presented in the following Sects. 10.2.1 and 10.2.2.

10.2.1 Planet-disk interaction and dust evolution models

The 2D hydrodynamical grid code FARGO (Masset, 2000) is used to simulate the planet-disk interaction processes. The parameters are similar to the models in Pinilla

et al. (2012a) and can be found in Table 10.1. The basic model consists of a viscous disk with $\alpha = 10^{-3}$ and an embedded massive planet with a planet-to-star mass ratio of 10^{-3} located on a fixed orbital radius at 20 au or 60 au, respectively. Our choice for the α value is motivated by recent results from de Juan Ovelar et al. (2016), who constrained α to be within an order of magnitude of 10^{-3} in order to reproduce the observed structures in transition disks. The radial grid with $N_\mathrm{r} = 512$ is logarithmically spaced between 0.5 and 140 au, while the azimuthal grid considers $N_\phi = 1024$ uniformly distributed cells. Furthermore, a gas surface density profile of $\Sigma_\mathrm{g} \propto r^{-1}$ is chosen, such that the disk bulk mass corresponds to $M_\mathrm{disk} = 0.05\,\mathrm{M}_\odot$. The hydrodynamic simulations are run for about 1000 planetary orbits until the disk gas surface density has reached a quasi-stationary state.

In the next step, the final gas surface density is azimuthally averaged, interpolated to a radial grid of 300 cells, and used as initial condition for the 1D dust evolution code from Birnstiel et al. (2010). Since we are only interested in the radial dust distribution, this simplification is adequate. The code computes the coagulation and fragmentation of dust grains due to radial drift, turbulent mixing, and gas drag. The gas surface density is kept constant during the dust evolution on simulation timescales of a few million years. This is justifiable because the gap opening timescale is much shorter compared to the dust evolution processes. As initial conditions a dust-to-gas ratio of 0.01 with an initial particle size of 1 μm and an intrinsic dust volume density of $\rho_\mathrm{s} = 1.2\,\mathrm{g\,cm^{-3}}$ are assumed. The fragmentation velocity is considered to be $v_\mathrm{f} = 1000\,\mathrm{cm\,s^{-1}}$. Stellar parameters typical for those of T Tauri stars ($T_\mathrm{eff} = 4730\,\mathrm{K}$, $M_\star = 1.0\,\mathrm{M}_\odot$, $R_\star = 1.7\,\mathrm{R}_\odot$) are assumed. The dust grain distribution $n(r, z, a)$ depends on the grain size a, the distance to the star r, and the height above the midplane z. The vertically integrated dust surface density distribution $\sigma_\mathrm{d}(r, a)$ is used to describe the dust grain distribution, since the coagulation processes are concentrated in the disk midplane. The vertically integrated dust surface density distribution per logarithmic bin of grain radius is defined as (see Birnstiel et al., 2010)

$$\sigma_\mathrm{d}(r, a) = \int_{-\infty}^{\infty} n(r, z, a)\, m\, a\, dz\,, \tag{10.1}$$

where m is the mass of a single particle of size a.

The dust coagulation simulations consider 180 different particle sizes from micron size up to two meters. Since the density of grains larger than ∼10 cm is very small and their contribution to the emitted and scattered light is negligible, the grain size and density distributions are binned such that 140 grains with a maximum size of 7 cm are taken into account for further calculations.

Table 10.1: Overview of main simulation input parameters.

Parameter	Variable	Value
Inner disk radius	$r_{\rm in}$	$0.5\,{\rm au}$
Outer disk radius	$r_{\rm out}$	$140\,{\rm au}$
# of radial grid cells	$N_{\rm r}$	512
# of azimuthal grid cells	N_{ϕ}	1024
α-viscosity	α	10^{-3}
Surface density at $r = r_{\rm p}$	$\Sigma_{\rm g,0}$	$1.26 \times 10^{-3}\, M_{\star}/r_{\rm p}^2$
Surface density index	β	-1
Star temperature	$T_{\star}$	$4730\,{\rm K}$
Star mass	$M_{\star}$	$1.0\,{\rm M}_{\odot}$
Star radius	$R_{\star}$	$1.7\,{\rm R}_{\odot}$
Planet-to-star mass ratio	$M_{\rm p}/M_{\star}$	10^{-3}
Planet position	$r_{\rm p}$	$\{20, 60\}\,{\rm au}$
Fragmentation velocity	$v_{\rm f}$	$1000\,{\rm cm/s}$
Solid density of dust particles	$\rho_{\rm s}$	$1.2\,{\rm g/cm^3}$
# of photons for RT	$\rm N_{phot,scat}$	5×10^7
Distance to observer	d	$140\,{\rm pc}$
Disk inclination	i	$\{0, 20, 40, 60, 90\}^{\circ}$

10.2.2 Radiative transfer calculations

The radiative transfer code RADMC-3D is used to calculate the intensity and polarized intensity images of our transition disk model. The code is frequently applied to compare theoretical disk models with observations or to make observational predictions (see recent studies from, e.g., Marino et al., 2015; Casassus et al., 2015; Kataoka et al., 2015; Juhász et al., 2015, and Chapters 3 - 9 in this thesis)). In addition, Kataoka et al. (2015) confirmed the validity of the polarization calculations of RADMC-3D with a benchmark test proposed by Pinte et al. (2009). The intensity images and polarization maps are simulated in this work with 5×10^7 photon packages. The linear polarization degree P can be calculated with $P = \sqrt{\rm Q^2 + U^2}/I$. The radiative transfer calculations require a radiation source, which has typical stellar parameters of a T Tauri star (see Table 10.1), where a blackbody radiation field is assumed for simplicity. Furthermore, the results of the dust evolution models are taken as input, i.e., the corresponding dust density for each grain size $\Sigma_{\rm d}(r)$ extracted from the distribution $\sigma_{\rm d}(r, a)$, which was previously introduced in Sect. 10.2.1 and described in more detail in Sect. 10.3.1. The vertical density profile is assumed to

be Gaussian, so that the dust volume density is given by

$$\rho_{\rm d}(R,\phi,z) = \frac{\Sigma_{\rm d}(R)}{\sqrt{2\,\pi}\,H_{\rm d}(R)}\,\exp\left(-\frac{z^2}{2\,H_{\rm d}^2(R)}\right)\,, \tag{10.2}$$

where R and z refer to cylindrical coordinates and can be converted into spherical coordinates via $R = r\,\sin(\theta)$ and $z = r\,\cos(\theta)$, and θ describes the polar angle. The value of the dust scale height $H_{\rm d}(R)$ is grain size dependent, since the effect of dust settling is included. Large enough dust grains are decoupled from the gas and settle down to the midplane. Following Youdin & Lithwick (2007) and Birnstiel et al. (2010) the dust scale height can be estimated by (cf. derivation in Eq. 9.5)

$$H_{\rm d} = H \times \min\left(1, \sqrt{\frac{\alpha}{\min({\rm St}, 1/2)(1+{\rm St}^2)}}\right)\,, \tag{10.3}$$

where α is the viscous parameter, H is the gas scale height, and St corresponds to the Stokes number (Eq. 1.26). The latter is a dimensionless coupling constant that describes how well the dust particles couple to the gas. Our study focuses on the so-called Epstein regime, where the Stokes number is given by Eq. 1.27.

Opacity calculation

Mie theory is used for the opacity calculation, following the BHMIE code of Bohren & Huffman (1984), which assumes the dust grains to be spherically symmetric (cf. Sect. 2.4.3). The dust composition consists of a mixture between silicate (Draine, 2003), carbonaceous material (Zubko et al., 1996), and water ice (Warren & Brandt, 2008), which is consistent with Ricci et al. (2010b), who considered the bulk densities from Pollack et al. (1994). The fractional abundances are taken as 7%, 21%, and 42% so that the amount of vacuum is 30%. The opacity of the mixture is determined by means of the Bruggeman mixing theory. The absorption and scattering opacities, $\kappa_{\rm scat}$ and $\kappa_{\rm abs}$, as well as the scattering matrix elements Z_{ij} are calculated. Here, the notation Z_{ij} of the RADMC-3D code is used, which is related to the notation S_{ij} from Bohren & Huffman (1984) by $Z_{ij} = S_{ij}/(k^2 m_{\rm grain})$, where k is the wave number. Taking the angular integral of the Z_{11} matrix element gives the scattering opacity,

$$\kappa_{\rm scat}(a) = \oint Z_{11}(a,\theta)\,d\Omega \;= 2\pi \int_{-1}^{1} Z_{11}(\mu)\,d\mu\,, \tag{10.4}$$

where $\mu = cos(\theta)$.

As already mentioned in Sect. 10.2.1, 140 different grain sizes are considered. For the scattering phase function represented by Z_{11} as a function of scattering angle, Mie theory produces very strong oscillations if the wavelength of the incoming radiation is very small compared to the grain size. Therefore, a grain size distribution

between two neighboring grain size bins is applied with a MRN power-law index of -3.5 (Mathis et al., 1977). This averaging smears out the wiggles, giving more manageable opacity values. Furthermore, to avoid problems with the spatial resolution of our models, we define a cutoff value for Z_{11} setting an upper limit for the forward peaking of the phase function. This means that for very small scattering angles Z_{11} is set to a constant (typically to the value it has at 5 deg). This is reasonable since such low scattering angles are not relevant for our analysis.

The polarization by dust scattering is strongly dependent on the scattering angle, grain size, and wavelength. Therefore, to determine an effective polarization degree $(-Z_{12}(\theta)/Z_{11}(\theta))_{\rm eff}$, effective scattering matrix elements $Z_{11,\rm eff}(\theta)$ and $Z_{12,\rm eff}(\theta)$ have to be derived. In our case this is carried out by weighting the individual elements $Z_{11}(a,\theta)$ and $Z_{12}(a,\theta)$ by the corresponding dust density distribution $\Sigma_{\rm d}(a,r_0)$ at a specific radial position r_0. More precisely, we obtain

$$Z_{11(12),\rm eff}(\theta) = \frac{\int_{a_{\rm min}}^{a_{\rm max}} \sigma_{\rm d}(a,r_0)\, Z_{11(12)}(a,\theta)\, da}{\int_{a_{\rm min}}^{a_{\rm max}} \sigma_{\rm d}(a,r_0)\, da}\,, \tag{10.5}$$

so that the effective polarization degree is determined by

$$(-Z_{12}(\theta)/Z_{11}(\theta))_{\rm eff} = -\frac{\int_{a_{\rm min}}^{a_{\rm max}} \sigma_{\rm d}(a,r_0)\, Z_{12}(a,\theta)\, da}{\int_{a_{\rm min}}^{a_{\rm max}} \sigma_{\rm d}(a,r_0)\, Z_{11}(a,\theta)\, da}\,. \tag{10.6}$$

Temperature profile

Since we are only interested in the scattering, for simplicity we assume that the dust temperatures are the same for all grain species. Thus, for the dust temperature profile of the disk a power-law distribution is adopted,

$$T(r) = T_0 \left(\frac{r}{r_0}\right)^{2f-1}\,, \tag{10.7}$$

where T_0 is set to 65 K, r_0 is equal to 20 au and f corresponds to 0.25. The parameters are chosen such that they coincide with those of the hydrodynamical FARGO simulations and are in agreement with the disk geometry found in observations of T Tauri disks (e.g., D'Alessio et al., 2001).

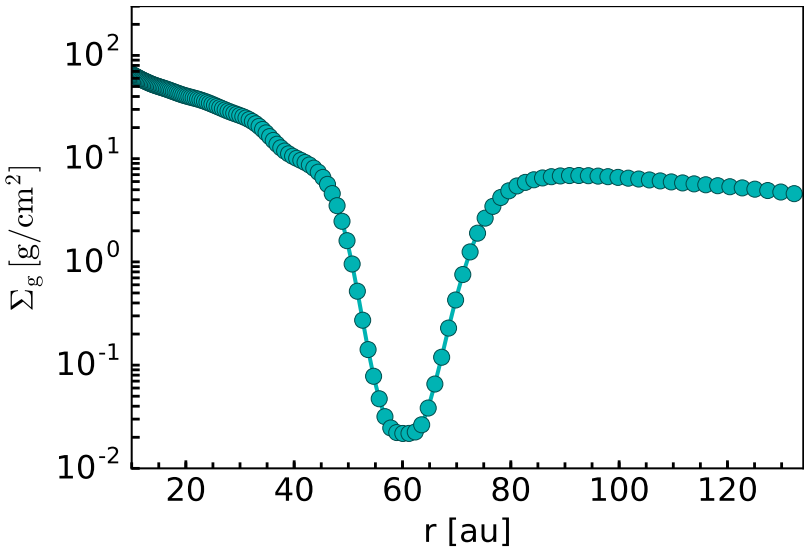

Figure 10.2: Azimuthally averaged radial gas surface density profile after 1000 orbits of evolution for a planet with a planet-to-star mass ratio of 10^{-3} located at 60 au in a turbulent, flared disk.

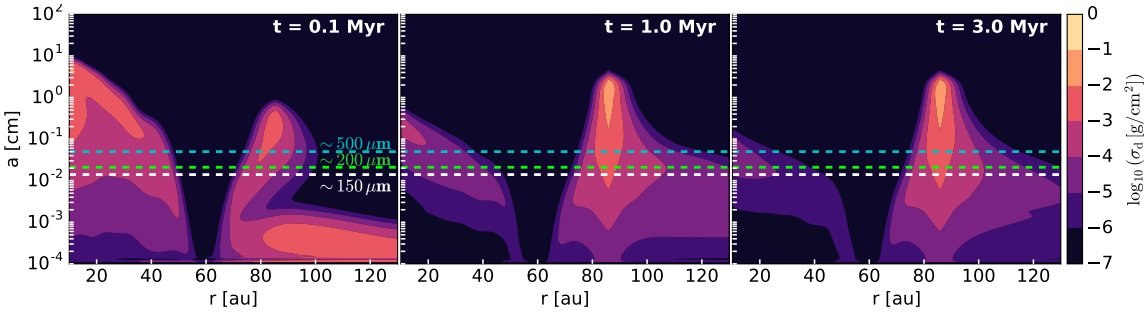

Figure 10.3: Snapshots of the vertically integrated dust density distribution for evolutionary times of 0.1, 1 and 3 Myr. The planet is located at 60 au and the planet-to-star mass ratio is 10^{-3}. The horizontal dashed lines represent the particle sizes corresponding to a size parameter of $x = 2\pi a/\lambda \sim 1$ considering $\lambda = 0.87$ mm, $\lambda = 1.3$ mm, and $\lambda = 3.1$ mm. If the dominant grain size at a certain disk location is less than $\sim \lambda/2\pi$, there is significant polarization in scattered light.

10.3 Results

10.3.1 Gas and dust density distributions

Figure 10.2 illustrates the azimuthally averaged gas surface density profile after 1000 orbits of evolution of the planet-disk interaction processes. The embedded planet with a planet-to-star mass ratio of 10^{-3} ($1\,M_{jup}$ for our case) is located on a fixed circular orbit at 60 au in a flared, viscous ($\alpha = 10^{-3}$) disk. A pronounced gap is opened by the planet, whereas its width is constrained by the planet mass. The presence of the planet generates a pressure bump in the otherwise monotonically

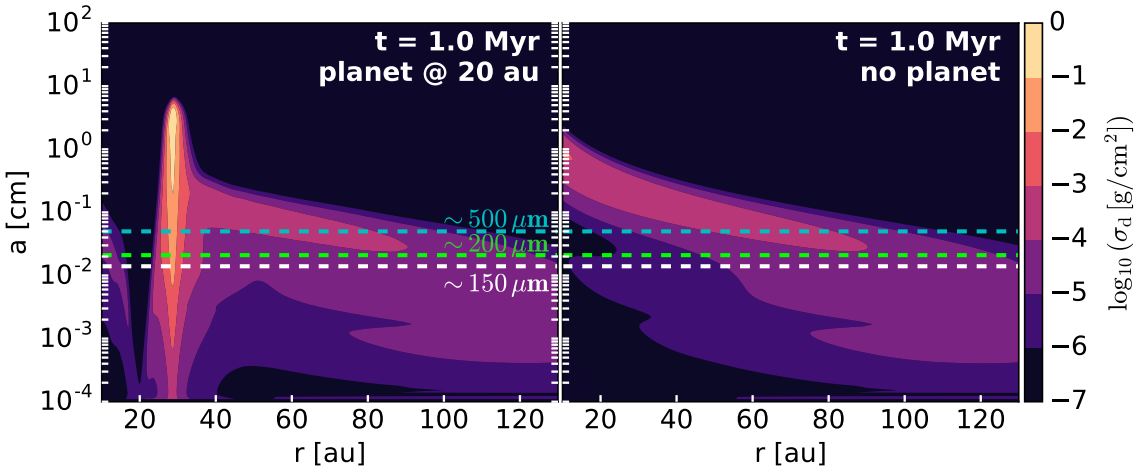

Figure 10.4: Vertically integrated dust density distribution after 1 Myr of dust evolution for the planet embedded at 20 au (left) and the comparison case without any planet (right).

decreasing pressure distribution (see Pinilla et al. 2012a for detailed discussion). The vertically integrated dust density distribution (cf. Eq. 10.1) for three different times of dust evolution (0.1, 1, and 3 Myr) is shown in Fig. 10.3. As we noticed for the gas density, the planet also clearly carves a gap in the dust thereby influencing the distribution of dust particle sizes in the inner and outer disk. Large dust grains that are mm in size are trapped at the pressure maximum, which is located at a larger radius than the gap edge in the gas density. Smaller, micron-sized particles can pass the pressure maximum and radially drift to the inner disk region. Dust particles in the outer regions of the disk grow until they reach a size of mm and remain there several million years. Additionally, the result of a comparison simulation without any planet after 1 Myr of dust evolution in the disk is shown in Fig. 10.4. In this case no pressure bump is created, instead the dust just grows, fragments, and drifts toward the star without building any accumulation of mm-sized grains in the outer disk regions.

10.3.2 Analysis of polarization maps

As shown in Kataoka et al. (2015) even without a specific central light source, the continuum emission is polarized as a result of self-scattering if the dust emission exhibits quadrupole anisotropy at certain positions in the disk. In this section we investigate the characteristic polarization pattern for a transition disk and discuss the detection possibility with current (sub-)mm observations. The basic polarization mechanism is explained by means of a reference face-on disk model. Moreover, the effects on the polarization of disk inclination, observing wavelength, dust size evolution, dust composition, and presence of the planet are studied.

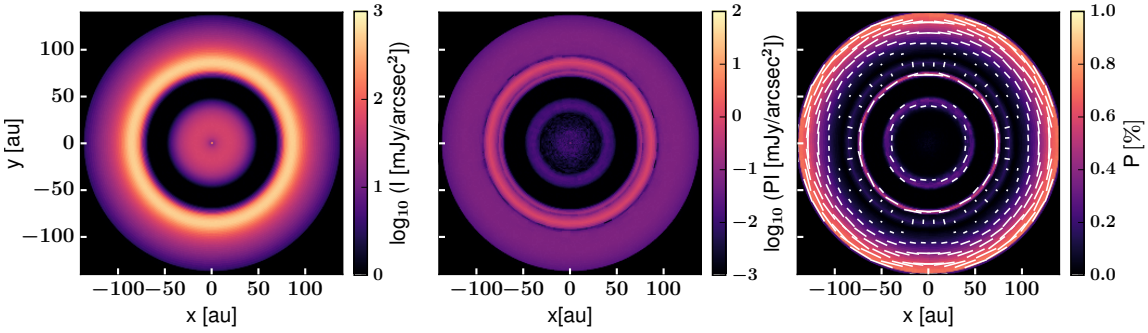

Figure 10.5: Intensity I, polarized intensity PI, and polarization degree P overlaid with polarization vectors for the reference model (planet-to-star mass ratio of 10^{-3}, planet located at 60 au, 1 Myr of dust evolution, dust opacity mixture, $\lambda = 0.87$ mm, face-on disk).

Reference simulation

As a reference simulation we define the case of a planet with planet-to-star mass ratio of 10^{-3} located at 60 au taking the dust evolution of the disk after 1 Myr and an opacity mixture as described in Sect. 10.2.2. By means of RADMC-3D the intensity and polarized intensity images are calculated at a reference wavelength of $\lambda = 0.87$ mm (ALMA Band 7) considering anisotropic scattering with polarization. Figure 10.5 displays the Stokes I intensity, polarized intensity PI $= \sqrt{Q^2 + U^2}$, and polarization degree $P = PI/I$ with overlaying polarization vectors for a face-on disk with respect to the line of sight. The intensity image reveals the structure of the transition disk, such that a gap is detected around the planet's position. As explained in the previous Sect. 10.3.1, mm grains are trapped in the pressure maximum at ~ 85 au and generate the bright emission ring at that location.

Polarization generally depends on the observing wavelength, grain size and scattering angle. For small, micrometer-sized particles the scattering opacity is much smaller than the absorption opacity in the mm. Scattering at mm wavelengths becomes efficient if the dust grains are as large as a few hundred micrometers. In addition, there is also an upper grain size limit for significant polarization due to scattering. As discussed in Kataoka et al. (2015), the maximum grain size that is responsible for producing polarization is determined by $a_{\max} \sim \lambda/2\pi$. This is illustrated by the horizontal dashed lines in Figs. 10.3 and 10.4. If grains larger than that size are present at a certain location in the disk, no polarization is expected. To distinguish between different scattering regimes, the size parameter $x = 2\pi a/\lambda$ is important (Bohren & Huffman, 1984). For the Rayleigh scattering regime with $x < 1$, i.e., for the grain size that is smaller than the wavelength, the polarization curve as a function of scattering angle $(-Z_{12}(\theta)/Z_{11}(\theta))_{\text{eff}}$ is symmetric and features a peak at $\theta = 90°$. This can be clearly seen in Fig. 10.6 for most disk locations for a wavelength of 0.87 mm. One also recognizes that for certain radii where mm/cm grains dominate, for example, at the pressure bump region around 90 au (yellow line) and in the very inner disk at 20 au (black line), there is a sign flip in the polarization,

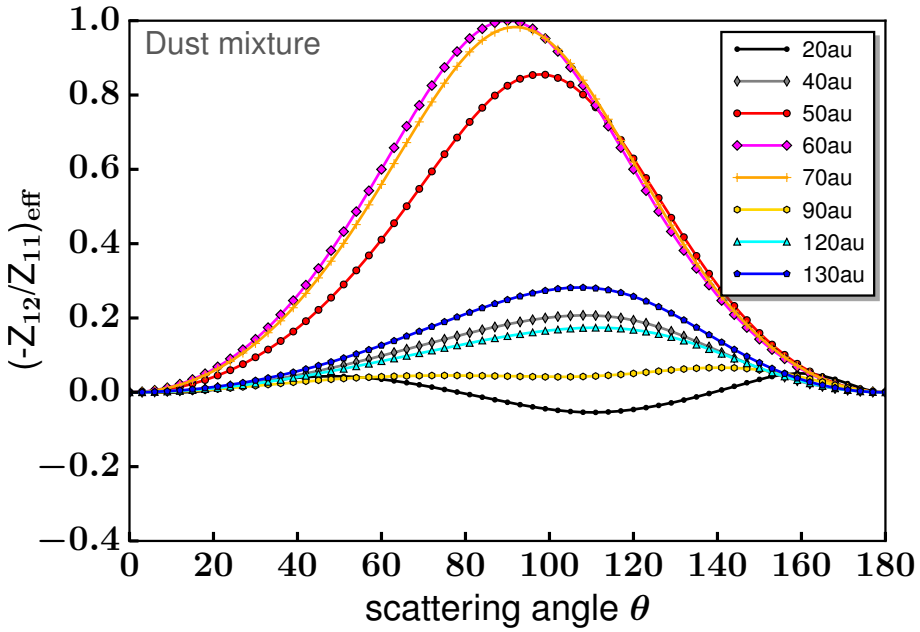

Figure 10.6: Effective degree of polarization $(-Z_{12}(\theta)/Z_{11}(\theta))_{\rm eff}$ of the dust grains dependent on the scattering angle θ. Several locations throughout the disk are chosen and indicated in different colors.

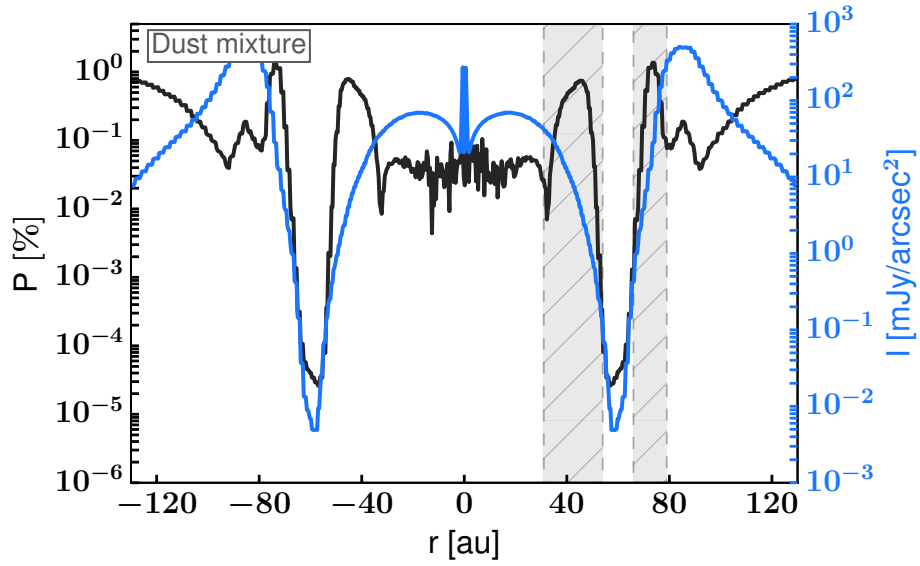

Figure 10.7: Radial cut of the intensity profile (blue) and polarization degree (black) along the major axis for the case in Fig. 10.5. The gray crosshatched areas visualize the two inner polarization peaks.

which is known as polarization reversal (Daniel, 1980; Fischer et al., 1994; Kirchschlager & Wolf, 2014). This generally influences the orientation of the polarization vectors. However, effects of negative polarization are not expected in our simulations

since the absolute polarization values are very small at those positions in the disk where negative polarization occurs.

The polarization map in the right panel of Fig. 10.5 shows a three-ring structure. These features are unique for the polarization owing to dust self-scattering in a transition disk hosting a gap and pressure bump caused by a giant planet. The positions of the rings coincide with those locations of the disk where the dust grains have a maximum size of $a_{\max} \approx 150\,\mu$m for $\lambda = 0.87\,$mm. This can be verified by looking at the dashed blue line in the center panel of Fig. 10.3 and counting the crossing points/regions for which this condition is fulfilled. This is the case just around the gap and in the outer disk beyond the pressure bump, also illustrated in Fig. 10.7. The third ring is wider in the radial dimension because the suitable maximum grain size is met for the whole outer part $\gtrsim 110\,$au. The high polarization degree is unaffected by the disk boundaries, proven by a model with an extended disk radius of 300 au instead of 140 au. At the location of the pressure bump big cm and mm grains ($\gg 150\,\mu$m), which do not produce polarization, are present as well. Although the polarized intensity is not zero, since there are particles with a suitable size for polarization, the amount of unpolarized intensity is high. Hence, the ratio of polarized to unpolarized radiation is tiny and no polarization is expected in that region. Another important prerequisite to have such a significant polarization degree is that the radiation field has a strong gradient field. Thus, the third ring has the highest polarization degree since it is located outside of the bright intensity ring. The dominant photon source for the outer disk is determined by the thermal emission from this intensity peak.

The two inner rings are inside of the bright emission ring. For the innermost ring, it is expected that the incident radiation originates primarily from the very inner disk acting as a point source. The polarization vectors in all rings are orientated in azimuthal direction for this face-on disk. Two effects play an important role here, the propagation direction of incident photons and the sign of the polarization. Most of the incident photons for the last scattering come from the inner disk or emission from the ring region and, therefore, propagate radially outward. Thus, assuming that we are in the Rayleigh scattering regime and hence there is no polarization reversal, the radiation is azimuthally polarized.

It should be emphasized that if the amount of polarized intensity is too low, no polarization can be detected, even if the polarization degree itself were high. Since the polarized intensity is highest around 85 au, the second and third polarization ring might be observationally most important. The width of the bright emission ring in PI is $\sim 30\,$au, which defines the minimum spatial resolution needed to resolve the ring structure.

Effect of disk inclination

Figure 10.8 shows polarization maps for different disk inclinations (20°, 40°, 60°, and 90°) with respect to the observer. All other simulation parameters are the same as in the reference model presented in Sect. 10.3.2 and shown in Fig. 10.5. The general polarization degree structure, i.e., the number and position of the rings, stays the same since the dust density distribution has not been changed. Nonetheless, the amount of polarization and orientation of the polarization vectors drastically changes. In Sect. 10.3.2 we showed that a high polarization degree for a face-on disk is linked to a strong flux gradient, which causes the polarization vectors to be azimuthally orientated. In the following this mechanism is referred to as gradient-induced polarization. For an inclined disk there is an interplay between this effect and inclination-induced quadrupole polarization, which, in the following, is called sideways polarization. Both polarization mechanisms are sketched in Fig. 10.9.

The light coming from a direction along the major axis is scattered by 90° in an inclined disk and, therefore, fully polarized along the minor axis in the Rayleigh limit. Contrarily, incident light from the minor axis is scattered by $90° \pm i$, which is then partially polarized along the major axis of the disk. Thus, the majority of the polarization vectors are orientated along the minor axis. Qualitatively, Yang et al. (2016) found a similar polarization vector behavior for the specific case of HL Tau using a semianalytic model. To better understand the sideways polarization, one should first take a look at the case of an edge-on disk (right most panel of Fig. 10.8). The basic mechanism is illustrated in Fig. 10.9. The polarization effect seen in this case is comparable to that for a tube-like density distribution (cf. Fig. 5 in Kataoka et al., 2015) in that bending the tube would form a ring. The radiation inside the tube is polarized radially and so it is detected for the edge-on disk because the net flux from the azimuthal direction is larger than that from the radial direction. Since the midplane is, however, optically thick, the polarization degree values themselves are quite low. The decrease of polarization degree at optically thick regions was also reported in Kataoka et al. (2015). Furthermore, the vector orientation changes for the location where the vertical optical depth reaches unity. Therefore, the vertical gradient of radiation dominates and the polarization vectors are azimuthally orientated. Intermediate inclined disks, such as $i = 20°$, 40° or 60°, indicate that for all rings there is a decrease of polarization along the minor axis and enhanced polarization along the major axis. In the outer ring the gradient-induced polarization and, therefore, the azimuthal vector orientation still dominates, since the major emission comes from the inside. As already mentioned, the bright intensity ring works as the thermal emission source here. In contrast, the inclination-induced sideways effect is strong for the central region inside of the intensity ring, where the gradient-induced polarization is already weak for the face-on disk. Hence, there is a polarization direction change by 90° along the minor axis in the inner disk. Indeed, the fraction of scattered radiation polarized due to disk inclination gets larger with increasing inclination angle.

The polarization detection generally depends on the spatial resolution. If the disk cannot be spatially resolved, i.e., it is seen as a point source, it depends on the disk inclination whether polarization can be actually detected. Considering this case, for a face-on disk, where exclusively gradient-induced polarization acts, the polarization components cancel out ending in no polarization at all. However, for an inclined disk, where the sideways polarization plays an important role, polarization can be detected even for a point source. In Fig. 10.10 the net polarization $\sqrt{(\sum Q)^2 + (\sum U)^2}/\sum I$ is plotted versus the disk inclination angle. It is shown that the net polarization is zero for the face-on disk, gradually increases with inclination, and peaks at 60°. Then, it slightly decreases again for the edge-on disk. This clearly indicates that sideways polarization is the dominant factor for the net polarization. Since we are interested in detecting the characteristic polarization features when dust tapping is triggered by a planet embedded in the disk, we do not consider edge-on disks in the following simulations. The disk inclination angle is set to an intermediate value of 40° to obtain polarization at a high level and still resolve the structures. Since the polarization degree is up to $\sim 2\%$ in this case, it is likely to be detected with ALMA observations. A spatial resolution as high as $0\farcs2$ is required to safely resolve the emission rings in PI, and hence the polarization structures. Because of the nondetection of polarization by previous observational studies, we strongly argue here that a high enough spatial resolution is the key for our science goals.

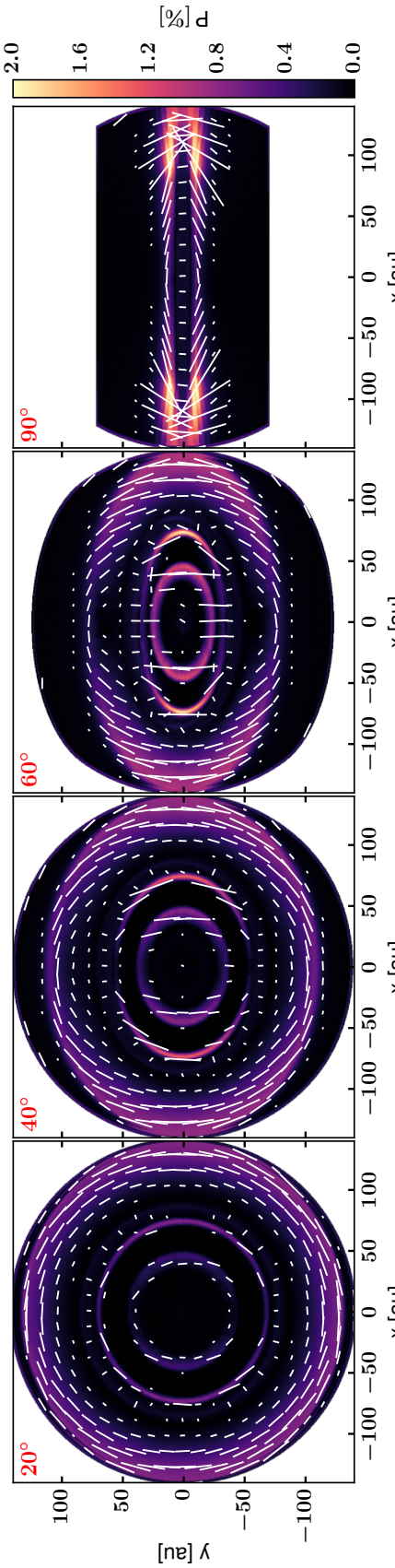

Figure 10.8: Polarization degree maps with overplotted polarization vectors for different disk inclination angles (20°, 40°, 60°, and 90° from left to right) after 1 Myr of dust evolution. The images are produced at 0.87 mm. The reference face-on model can be found in Fig. 10.5.

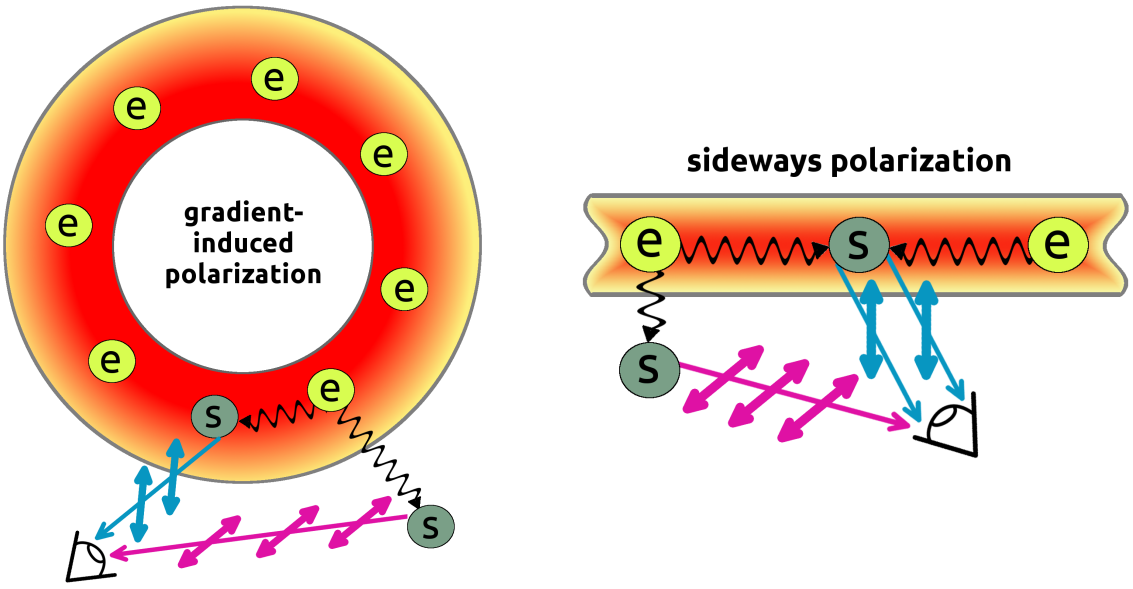

Figure 10.9: Sketch illustrating the difference between gradient-induced polarization (left) and sideways polarization (right). The left sketch considers a face-on disk, while the observer has an edge-on view for the right image. Circles with character 'e' stand for dust grains working as an emitter; those with 's' work as a scatterer.

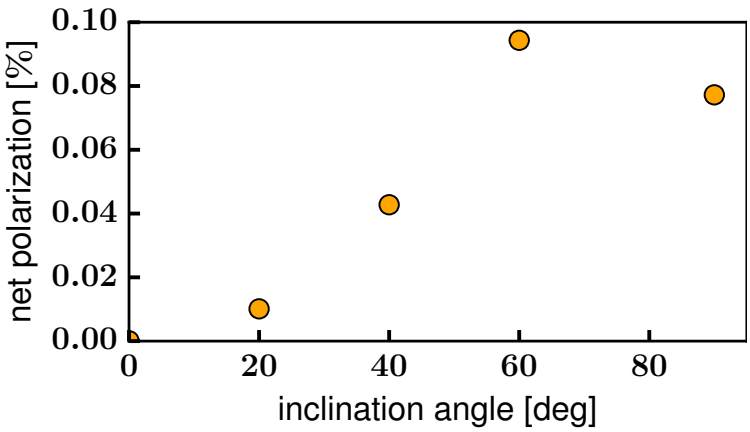

Figure 10.10: Net polarization dependent on the disk inclination angle for the cases shown in Fig. 10.8.

Wavelength dependence of polarization rings

Observations at different wavelengths are most sensitive to different particle sizes. Furthermore, as described in Sect. 10.3.2, the maximum grain size for producing polarization is proportional to the observing wavelength. Hence, although the basic polarization ring structure stays the same, the ring locations slightly change with the

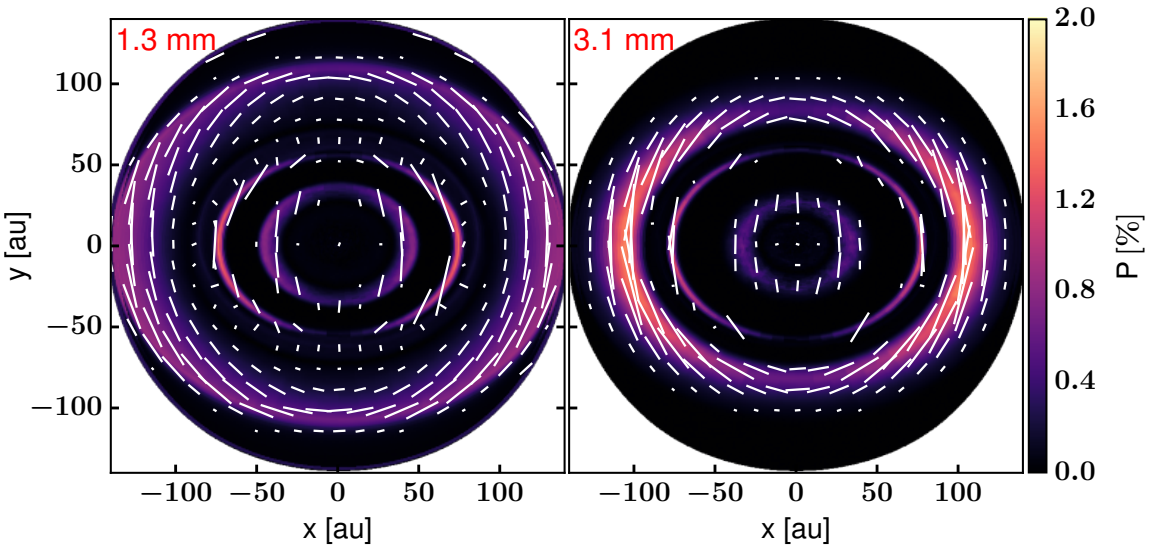

Figure 10.11: Polarization maps with overplotted polarization vectors at $\lambda = 1.3\,\mathrm{mm}$ (ALMA Band 6) and $\lambda = 3.1\,\mathrm{mm}$ (ALMA Band 3) after 1 Myr of dust evolution and for a disk inclination angle of 40°.

wavelength. More precisely, the innermost and outermost rings move inward, while the middle ring moves in the opposite direction for longer wavelengths as shown in Fig. 10.11. The moving distance of the polarization peak is $\sim 20\,\mathrm{au}$ for the third ring, which is large enough to be detectable with the two ALMA Bands 3 and 7. This is what we expect from the dust density distribution in Fig. 10.3, center panel. A spatial segregation of the grain size distribution is modeled with our dust transport for each grain size along with coagulation and fragmentation of grains. The crossing point of the most upper horizontal dashed line (representative for $\lambda = 3.1\,\mathrm{mm}$) with the maximum available grain size is further inside than for the two lower horizontal lines (representing the shorter observing wavelengths). The maximum polarization degree is approximately a factor of two higher for $\lambda = 3.1\,\mathrm{mm}$ compared to $\lambda = 0.87\,\mathrm{mm}$. The reason for this is that the albedo $\eta = \kappa_{\mathrm{scat}}/(\kappa_{\mathrm{abs}} + \kappa_{\mathrm{scat}})$ increases with grain size and the amount of polarized intensity with respect to the unpolarized intensity is higher for longer wavelengths.

Effect of dust size evolution

We study the polarization degree at different time snapshots to understand whether and how the polarization map changes with the dust evolution timescale. We show the results for 0.1, 1, and 3 Myr in Fig. 10.12. At a very early dust evolution time, only the two inner polarization rings are produced. The reason for the absence of the third ring is that grains have not grown to sizes larger than 10 microns in the outer disk at that stage of evolution. The absorption opacity dominates over the scattering opacity for the small grains so that their scattering at mm wavelengths is inefficient. At longer times of evolution, grains grow to larger sizes and drift to the region of high

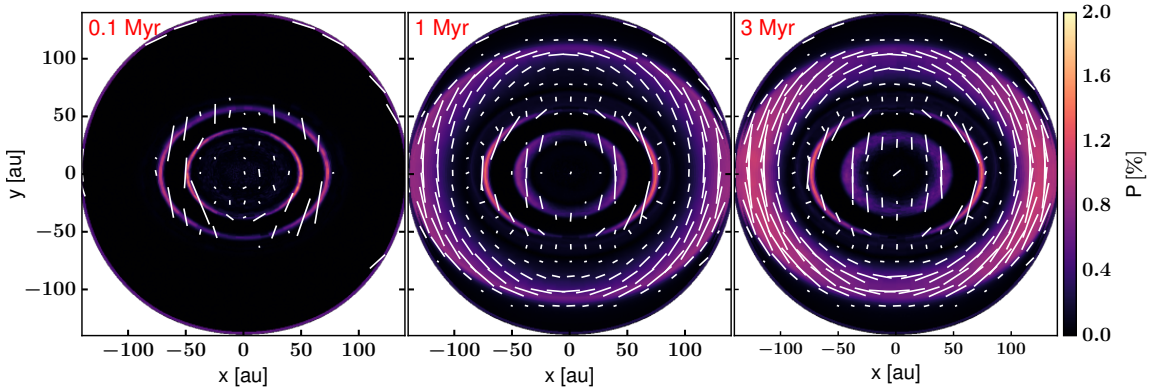

Figure 10.12: Polarization maps with overplotted polarization vectors after 0.1 Myr, 1 Myr, and 3 Myr of dust evolution and for a disk inclination angle of 40°. The images are produced at 0.87 mm.

Table 10.2: Dependence of the net polarization on the dust composition.

Dust species	Net polarization [%]
Mixture	0.042
Silicate	0.048
Carbon	0.25
Water ice	0.006

Notes. The fractional abundances for the mixture are taken as 7% silicate, 21% carbon and 42% water ice, so that the amount of vacuum is 30%.

pressure. The third polarization ring already appears after approximately 0.5 Myr because of this efficient grain growth mechanism. From 1 Myr of dust evolution on there is a quite stable situation for the overall polarization structure. At t = 3 Myr only the polarization degree in the innermost ring is slightly reduced owing to the ongoing drift of particles toward the star. Contrarily, the maximum polarization degree in the outermost ring becomes slightly higher.

Effect of dust composition

We study the effect of the dust composition on the polarization by considering three 'extreme' cases of pure silicate, pure carbon, and pure water ice apart from our usual mixture (7% silicate, 21% carbon, and 42% water ice). We find that the dust composition has no effect on the overall polarization ring structure. In all cases, three polarization rings are produced at the described locations. This is a large advantage of dust scattering as a method to constrain the grain sizes in protoplanetary disks. For a more quantitative study, the net polarization for the models at 40° inclination is listed in Table 10.2. At first sight it is remarkable that the values for the mixture and the pure silicate case are almost equal. This is not surprising, since the refrac-

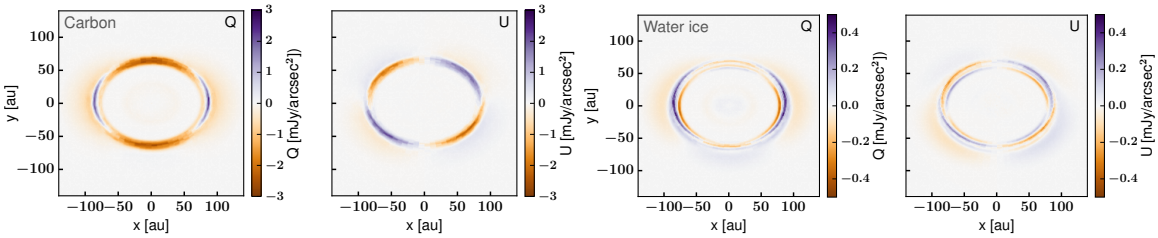

Figure 10.13: Stokes Q and Stokes U maps for the models considering pure carbon (left) and pure water ice (right) opacities, respectively. We note a difference in the color map scaling.

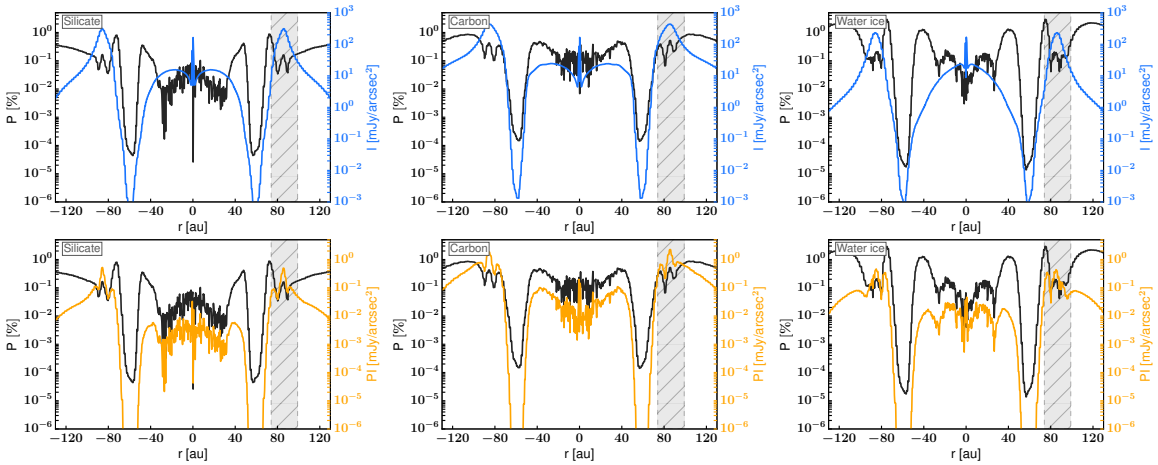

Figure 10.14: *Top row:* radial cuts of the intensity (blue) and polarization degree (black) along the major axis for different dust grain species. The gray crosshatched area visualizes the location of the highest intensity peak. *Bottom row:* radial cuts of the polarized intensity (orange) and polarization degree (black) along the major axis for different dust grain species. The gray shaded area again illustrates the highest polarized intensity peak.

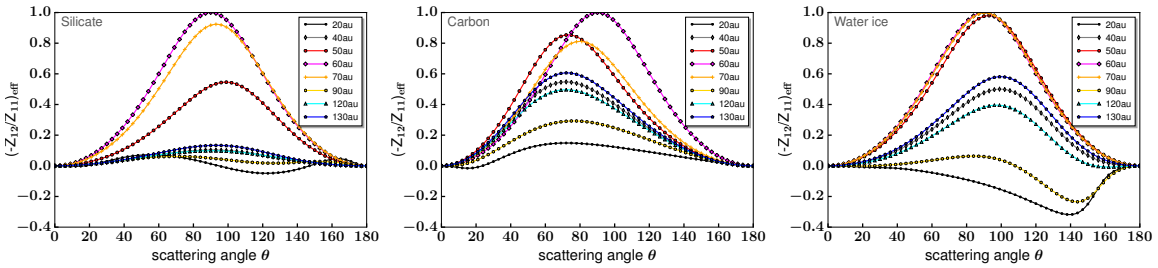

Figure 10.15: Effective degree of polarization $(-Z_{12}(\theta)/Z_{11}(\theta))_{\rm eff}$ of different dust grain species dependent on the scattering angle θ. Several locations throughout the disk are chosen and highlighted in different colors.

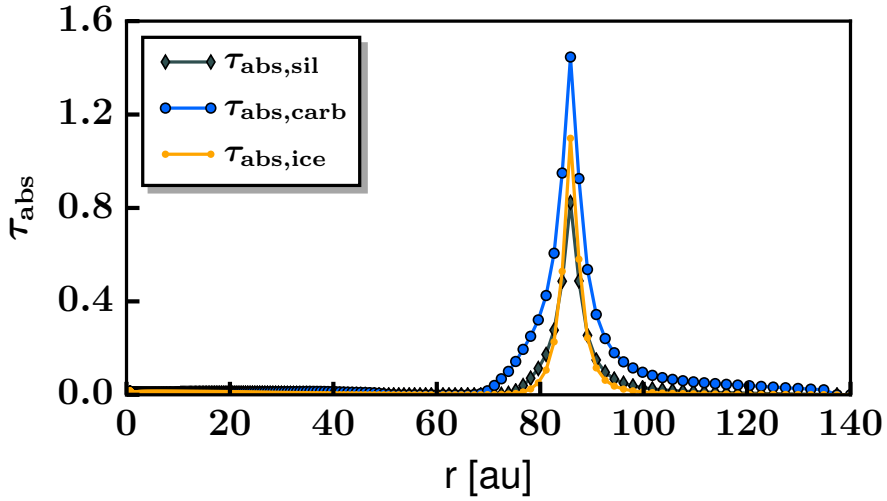

Figure 10.16: Optical depth τ_{abs} for $\lambda = 0.87\,\mathrm{mm}$ dependent on the radius for different dust species.

tive index of the mixture is dominated by silicates due to its high material density, even though its volume fraction is small. Hence, the polarization curves plotted in Fig. 10.15 for the silicate case and those for the dust mixture shown in Fig. 10.6 are comparable. As a consequence, for any mixture including silicates the polarization degree hardly depends on the dust composition. The situation changes for pure carbon with its high net polarization, and the opposite case of pure water ice, for which the lowest net polarization is found. This is explained by Fig. 10.13 illustrating the Stokes Q and U images. The negative Q values (brown color) clearly exceed the amount of positive Q (purple color) for carbon. Since the absolute value of $\sum Q$ is nearly two orders of magnitude higher than that for $\sum U$, the net polarization is determined by the Stokes Q component and is larger than zero in the end. For water ice the summed up Q value dominates the U component, however, it is still substantially lower than for carbon. These results are also supported by the polarized intensity profiles plotted in the bottom row of Fig. 10.14. The polarized intensity peaks are highest for carbon and lowest for water ice, silicate is situated in between. Furthermore, Fig. 10.15 illustrates the effective degree of polarization. For carbon the polarization curves show the highest polarization degrees for all radii considered and no polarization reversal is detected between the relevant scattering angles of 50° and 130°. Contrarily, the maxima for the polarization curves of pure water ice are lower and considerable negative polarization exists. Overall, these effects lead to the low net polarization of water ice compared to the mixture, the pure silicate, and pure carbon case.

Apart from the net polarization, there are also significant differences in the local polarization degree. We once again explain the two limiting cases of pure carbon and water ice. Interestingly, the behavior of the net polarization calculations has transformed. The polarization degree is plotted in Fig. 10.14 (black lines). It is

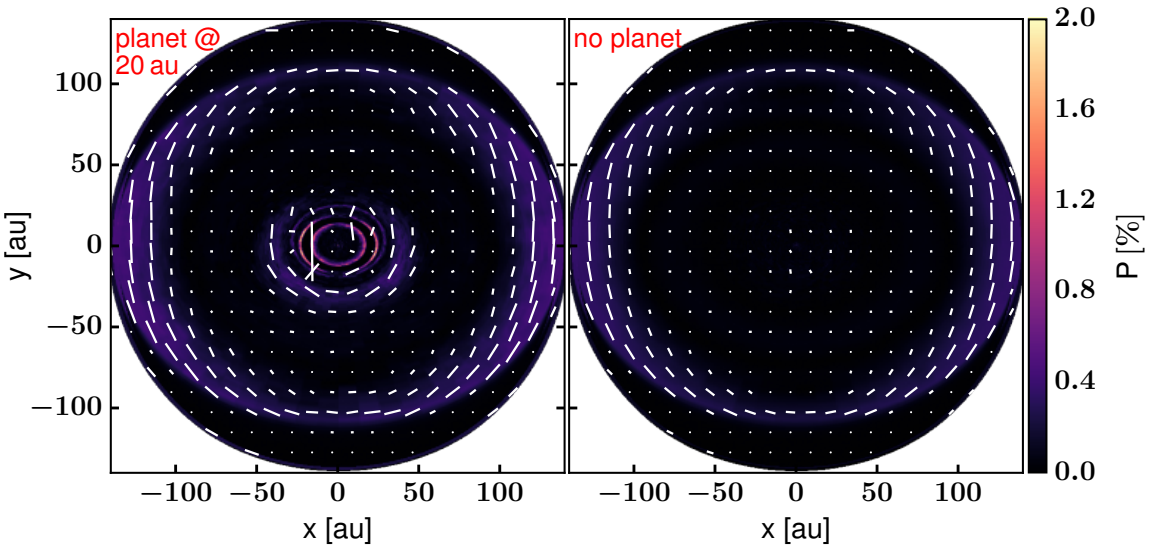

Figure 10.17: Polarization maps with overplotted polarization vectors for the disk model with the planet located at 20 au and for a comparison model without any embedded planet; both maps are at $\lambda = 0.87$ mm. The maps are shown after 1 Myr of dust evolution and for a disk inclination angle of 40°.

basically determined by the flux gradients shown in the radial intensity cuts in the top row of Fig. 10.5 and by the effective polarization curves in Fig. 10.15. From the former, one can understand the differences in the polarization degree of the innermost and outermost peak. The gradient of the intensity curve is much steeper for water ice leading to a higher polarization degree. Although the difference in the flux gradient is also slightly seen for the second polarization peak, it is noticeable that optical depth effects also come into play. In Fig. 10.16 an effective optical depth at a specific location is introduced that considers the vertically integrated dust density, $\tau_{\rm abs}(r') = \sum_{j=0}^{N_{\rm a}-1} \sigma_{\rm d}(r', a_j)\, \kappa_{\rm abs}(a_j)$, is plotted for $\lambda = 0.87$ mm. At the position of the second ring (~ 70 au), the optical depth of carbon is larger than for water ice. Considering that we investigate inclined disks, which even increases the optical depth along the line of sight, this means that the carbon model is marginally optically thick. Therefore, the corresponding radiation field is isotropic, so that we do not expect any polarization. Thus, the second peak in the polarization degree for water ice is also higher than the associated peak for the carbon case.

Effect of the planet and its position

As discussed in Sect. 10.3.1, the presence of a planet triggers the trapping mechanism for mm-sized dust grains in the pressure bump outside of the planet orbit. Depending on whether the planet is embedded at 20 au or 60 au, the gap width increases because of the radial density change and the pressure maximum is located at 30 au and 90 au, respectively. Figure 10.17 shows the polarization degree for the planet at 20 au and a comparison model without any planet, for both cases at $\lambda = 0.87$ mm. All other

disk parameters are exactly the same as in the reference model. As mentioned before the two inner polarization rings are located just at the intensity gap edges. Hence, for the 20 au case those rings are situated further inside with a narrower separation. Without any giant planet embedded in the disk only the outermost polarization ring remains. This is obvious since a gap and pressure bump in the dust distribution are missing as seen in Fig. 10.4. There is only one crossing point between the horizontal lines and the maximum grain size layer. Therefore, polarization detection due to dust self-scattering can distinguish between transition disks hosting a gap and pressure bump, on the one hand, and protoplanetary disks with a continuous surface density distribution, on the other hand. We note that if the dust at the inside of the gap is depleted, thereby converting the gap into a complete cavity, the inner ring cannot be detected. Thus, in this case only the outer two rings are visible.

10.4 Summary and conclusions

We present a new technique to investigate the dust trapping scenario in transition disks hosting a pressure bump by means of mm-wave polarization of scattered thermal emission. More precisely, the continuum emission is polarized owing to dust self-scattering of an anisotropic radiation field induced by disk inclination. For the mm-wave polarization to work, the scattering grains must have grown to a maximum size of a few hundred microns. Additionally, further populations of either very small micron-sized or mm-/cm-sized grains need to be present to account for the large portion of unpolarized continuum emission. Our model predictions at different ALMA Bands (Bands 3, 6, and 7) are based on self-consistent dust growth models and radiative transfer calculations, which allows us to estimate the polarization degree in disks hosting a massive planet. The planet is considered to be located at 20 au and 60 au, respectively. Compared to previous studies a dust size distribution in radial direction is included in our model. Measuring the dust polarization degree is a direct and an unambiguous method to probe the location of large particles (a few hundred micron to mm-sized particles, depending on the observing wavelength) when particle trapping occurs in the disk. We emphasize that the polarization technique presented can be applied to any disk with ring-like dust structures segregating the grain sizes, and is not limited to the gap opening scenario by planets. In this work, we focus on transition disks because they are excellent candidates where planet formation may be ongoing. The main findings of this work are the following:

1. The polarization pattern of a disk hosting a planetary gap after 1 Myr of dust evolution shows a characteristic three-ring structure, where the two inner, narrow rings are located just at the gap edges. Additionally, there is a third polarization ring in the outer disk beyond 100 au with a larger radial extension. Detecting such a distinctive ring structure with polarization observations may represent the radial size distribution of dust grains and hint at regions with a specific grain size corresponding to the wavelength.

2. For an inclined disk, there is an interplay between polarization originating from a flux gradient and from an inclination-induced anisotropy. The fraction of scattered radiation polarized due to disk inclination increases with the inclination angle. For intermediate inclined transition disks, the polarization degree at mm wavelengths is as high as 2 %, which is well above the detection limit of future ALMA polarization observations. A spatial resolution as high as 0.″2 is required to certainly resolve the ring structure in polarized intensity.

3. The local degree of polarization is very sensitive to the maximum grain size at a certain location in the disk. Large cm and mm grains do not contribute to the polarization, which leads to a significant local reduction of the polarization degree, for example, at the pressure bump region in our transition disk models. Hence, if the maximum grain size is larger than a few hundred microns, the polarization is not detectable, even if numerous small grains are present and contribute.

4. For face-on disks, the polarization vectors are in azimuthal direction within the highest polarized intensity regions. The majority of the polarization vectors in the two inner rings are orientated along the minor axis for inclined disks. In the outer ring the gradient-induced polarization and, therefore, the azimuthal vector orientation still dominates.

5. With increasing observing wavelengths the innermost and outermost polarization rings move inward by a detectable distance, while the middle ring moves slightly, radially outside. Hence, the positions of the two rings at the gap edges are shifted in opposite directions. For the outermost ring the moving distance is ~ 20 au, comparing the results at 0.87 mm and 3.1 mm. Furthermore, without any giant planet embedded in the disk, this third ring reflects the only polarized region, even though the polarization degree is quite low.

6. We find that the dust composition has no effect on the overall polarization ring structure. The presence of even a very small fraction of silicate in the dust mixture causes the local polarization degree and net polarization to be very similar to the case of pure silicate species. Silicate grains dominate the refractive index of the dust mixture, and the fractional abundances of carbonaceous material and water ice hardly affect the polarization pattern. A significant change of the local polarization degree with dust species can be led back to either optical depths effects or different flux gradients.

We showed that polarization due to dust self-scattering is a powerful tool to constrain the grain size in protoplanetary disks independent of the spectral index. Nevertheless, there are also other polarization mechanisms such as alignment of dust grains

along the magnetic field vectors and alignment due to a radiation anisotropy. A keystone to investigate in future work is how to distinguish between these mechanisms. Further multi-wave and spatially resolved polarization observations of protoplanetary disks are necessary. The wavelength and grain size dependence of polarization are also the key points from the modeling side. Owing to the self-scattering mechanism we expect the polarization degree to significantly change with the observing wavelength, while it is thought to be approximately constant because of magnetically aligned grains in a toroidal magnetic field (Cho & Lazarian, 2007).

10.5 Outlook: millimeter polarization in the transition disk HD 100546

The content of this section is based on a paper in preparation by Pohl et al., *in prep.*

In this section, ongoing observational work on mm polarization in the context of transition disks in presented. The planet-forming disk around HD 100546 was observed by ALMA in Band 7 in continuum polarization mode during Cycle 4 (2016.1.00497.S, PI: A. Pohl) for the first time in order to map its mm-wave polarization. Based on the polarized emission and polarization degree detection we aim to get new constraints on the dust grain size distribution of this transition disk. HD 100546 is the third protoplanetary disk (after HD 142527 and HL Tau) that is observed in ALMA's full continuum polarization mode. The high angular resolution and sensitivity of ALMA enable to trace the polarization down to 0.3%, previously unattainable.

10.5.1 The target: properties of HD 100546

HD 100546 is a well studied Herbig Ae/Be star with a spectral type of B9Vne (Levenhagen & Leister, 2006). The planet-forming disk around HD 100546 is a bright transition disk that is moderately inclined ($44° \pm 3°$ Walsh et al., 2014) with respect to the line of sight and located at a distance of (109 ± 4) pc (Gaia Collaboration et al., 2016). An inner hole stretching from a few au out to $10 - 15$ au was detected in previous ALMA Cycle 0 observations (Walsh et al., 2014), which could result from the presence of an infant planetary companion of $\sim$20 M_{jup} near the inner disk cavity wall (Acke & van den Ancker, 2006; Brittain et al., 2009, 2014; Currie et al., 2015). However, the lack of planet-like features at its presumed location in GPI H-band spectra hint at a connection to disk emission. Moreover, high contrast imaging gives evidence for a young, potentially still forming massive planet of at least $\sim$15 M_{jup} at $\sim$50 au (Quanz et al., 2013, 2015; Currie et al., 2014). Recently, Rameau et al. (2017) rather suggest a disk scattered light origin for the emission at the location of this putative protoplanet. The large gas disk ($r > 400$ au) has been spatially resolved in thermal CO emission (Pineda et al., 2014; Walsh et al., 2014), while most of the emission at mm wavelengths comes from a narrow ring concentrated at 26 au

and a second, potentially fainter ring located at 190 au. Such ring-like emission in transition disks can be explained by dust evolution, and/or hinting towards dynamical interactions of the disk with planets (Pinilla et al., 2015b). Since the system is already at a relatively advanced age (∼10 Myr), a large amount of dust growth is expected to have happened. Hence, a detailed modeling study suggests that significant spatial variations in the grains size distribution across the HD 100546 disk are expected.

10.5.2 ALMA polarization observations of HD 100546

HD 100546 was observed by ALMA on 2016 October 26, 2017 April 23, and 2017 May 06. The antenna configuration for the low angular resolution data (∼0.″7) was C40-2 with 44 antennas operating with a maximum baseline of 460 m. The antenna configuration for the high angular resolution data (∼0.″2) was C40-5 with 43/45 antennas operating with a maximum baseline of 1124 m. The correlator processed four spectral windows centered at 350.5, 348.5, 338.5, 336.5 GHz with a bandwidth of 2 GHz each. The bandpass, amplitude, and phase were calibrated by observations of J11074449, J11366827, J11456954, and J14274206, respectively. The raw data were reduced by the European ALMA Regional Centre. The synthetic beam sizes are 0.″77 × 0.″61 (∼83.9 au × 66.5 au) and 0.″20 × 0.″17 (∼21.8 au × 18.5 au), respectively.

10.5.3 First results

Figure 10.18 shows the total intensity, polarized intensity, and polarization degree for the low angular resolution ALMA data at 890 μm. The contour lines in the middle and right plots represent the continuum emission, and the turquoise stripes visualize the polarization direction. The vectors are not scaled with the polarization fraction and have the same length. The polarized emission is successfully detected with a central concentration. As smaller baselines were used for this data set, it is suitable to explain the overall disk structure and polarization mechanism at work. At the observing wavelength of 890 μm, the polarization vectors are oriented parallel to the disk minor axis forming a uniform pattern, and the maximum polarization degree is about 0.8%. Both of these facts can be interpreted by the self-scattering of thermal dust emission in a moderately inclined disk (cf. Fig. 10.8, and Kataoka et al., 2016a). Polarization contribution due to grain alignment with a magnetic field (vectors would be oriented in radial or azimuthal direction for a toroidal and poloidal configuration, respectively) or with a radiation field (vectors would be oriented in azimuthal direction) cannot be completely excluded, but due to the uniform polarization direction self-scattering seems to play the dominant role here (see Fig. 10.20).

The long baseline campaign of HD 100546 can be used to investigate the disk-substructures in total intensity and polarized intensity. The corresponding high resolution data is shown in Fig. 10.19. The continuum emission reveals a lopsided structure peaking in the northeast, which was undetected in previous ALMA observations due to lower spatial resolution. The difference in continuum contrast between

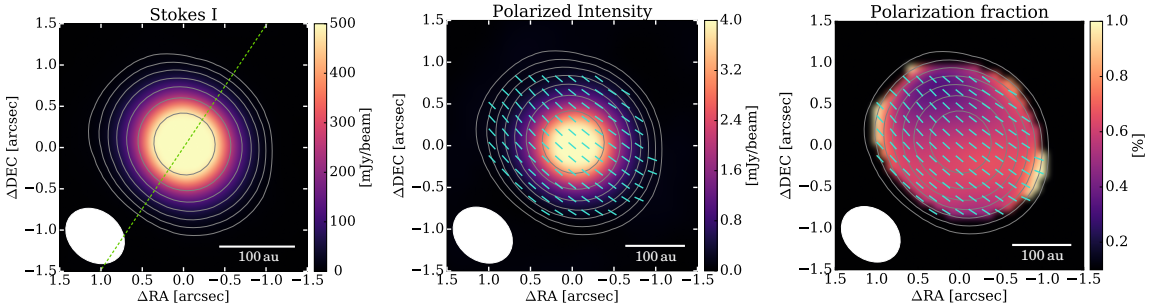

Figure 10.18: ALMA Band 7 (890 μm) low angular resolution observations of the transition disk around HD 100546. From left to right maps of the intensity, polarized intensity, and polarization degree are shown. The gray contours indicate the continuum emission (10, 20, 40, 80, 160, 320, 640)$\times\sigma_{\rm I}$ (= 0.8 mJy beam^{-1}). The disk's semi-major axis is indicated with the dashed diagonal line in the Stokes I image (PA of $\sim$146 deg). The turquoise vectors (same length for all) illustrate the polarization vectors and are drawn where the polarized intensity is larger than 5 $\sigma_{\rm PI}$. The synthetic beam size is 0.″77 $\times$ 0.″61, indicated with the white ellipse. North is up, east is left.

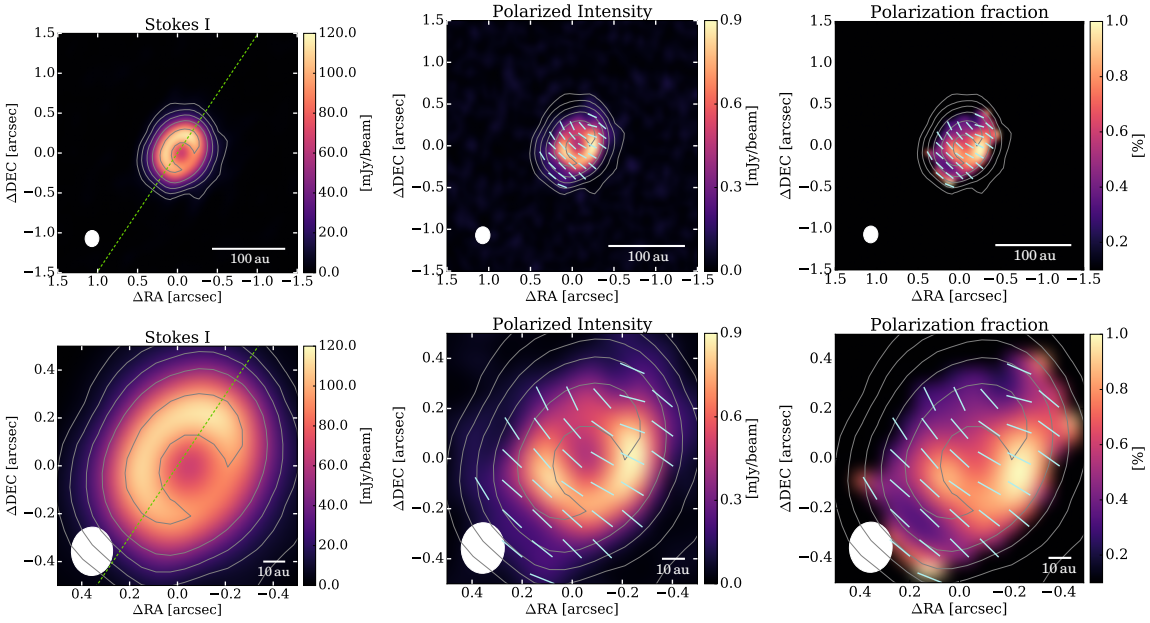

Figure 10.19: ALMA Band 7 (890 μm) high angular resolution observations of the transition disk around HD 100546. From left to right maps of the intensity, polarized intensity, and polarization degree are shown. The bottom row shows a zoom-in of the central part. The gray contours indicate the continuum emission (10, 20, 40, 80, 160)$\times\sigma_{\rm I}$ (= 0.6 mJy beam^{-1}). The disk's semi-major axis is indicated with the dashed diagonal line in the Stokes I image (PA of $\sim$146 deg). The turquoise vectors (same length for all) illustrate the polarization vectors and are drawn where the polarized intensity is larger than 5 $\sigma_{\rm PI}$. The synthetic beam size is 0.″20 $\times$ 0.″17, indicated with the white ellipse. North is up, east is left.

the northeast and southwest sides is a factor of ∼1.5. Because of this low contrast and the large extension with an azimuth coverage of ∼250 deg, the asymmetry is very different from other lopsided disks, for example IRS 48 and HD 142527. From a theoretical point of view, such a large scale vortex is in agreement with a long-term evolution modeling study of vortices being triggered by the Rossby wave instability (Regály et al., 2012). Remarkably, the polarized intensity also shows a lopsided structure with similar azimuth coverage as the continuum, but with a peak shifted towards the southwest. The polarized intensity has a peak of 1.034 mJy/beam, which corresponds to a $\sim 35\,\sigma_{\rm PI}$ detection with $\sigma_{\rm PI} = 0.029$ mJy. Overall, this leads to a high polarization degree of up to 1% in the southwest, while it is less than 0.3% in the northeast.

There is strong evidence that these results show the trapping of dust by a vortex. The peanut-shaped region around the peak of the dust continuum is where the polarized intensity is lowest. This suggests the presence of a vortex structure, where mm or bigger particles can be trapped to grow to larger sizes. The polarization due to scattering for such big grains is negligible at 890 μm. In other words, such large grains are not expected to be present at the azimuthal region surrounding the dust trap, where significant polarized emission is detected. This part of the disks is dominated by grains with a maximum size of around ∼150 μm (size parameter $x = 2\pi a/\lambda \simeq 1$). Figure 10.21 shows a sketch of the dust trap situation that is likely present in HD 100546. It is noted that the few hundred micron-sized grains are principally distributed all over the disk and produce polarization, but at the intensity peak the amount of unpolarized intensity dominates because the maximum grain size is on the order of mm or cm. How dust grain sizes are exactly distributed and trapped across the vortex remains to be investigated by a multi-wavelength analysis and dust evolution with vortex-formation modeling. It is reminded here that the focus is on the azimuthal dependence of the polarization fraction rather than on the radial structures as in Sects. 10.2 - 10.3, because radially the dust trap is unresolved at the requested resolution.

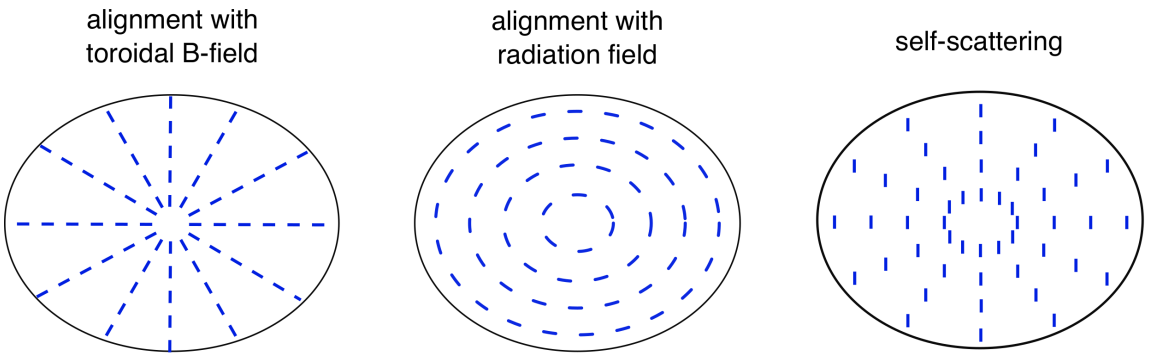

Figure 10.20: Schematic illustration of the polarization vectors arising from different polarization mechanisms (grains aligned with a toroidal magnetic field, grains aligned with a radiation anisotropy, and self-scattering of the thermal dust emission). The disk's major axis lies horizontally. The figure is adapted from Fig. 3 in Kataoka et al. (2017).

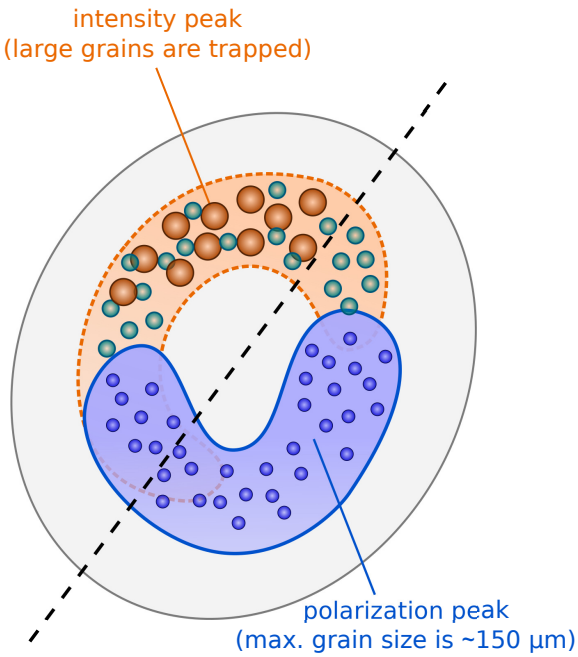

Figure 10.21: Cartoon of the proposed dust structure of HD 100546. The orange area represents the peanut-shaped region around the total intensity peak, while the blue area indicates the peak region of the polarized intensity. The large grains concentrate in the dust trap in the north. Small and intermediate-sized particles are distributed over the whole disk extent.

10.5.4 Comparison with previous observations

When comparing the ALMA HD 100546 and HL Tau (Kataoka et al., 2017; Stephens et al., 2017) polarization data, it turns out that the results at Band 7 on large scales (Fig. 10.18) are very similar for these two targets. The uniform morphology at wavelengths smaller than 1 mm matches the expectation of polarization due to self-scattering for inclined disks. It provides polarization vectors parallel to the minor axis since the self-scattering is more sensitive to inclination-induced quadrupole anisotropy (see Sect. 10.3.2). However, at an observing wavelength of 3 mm Kataoka et al. (2017) suggest radiative grain alignment as a likely mechanism for causing the dust polarization detected in HL Tau. Interestingly, Stephens et al. (2017) recently presented an ALMA multi-wavelength polarization analysis of HL Tau and found indeed evidence that at least two disk polarization mechanisms operate at mm wavelengths. At 1.3 mm, the polarization morphology appears to be a mix of the polarization morphologies at 870 μm and 3 mm. These findings are not consistent with polarized emission from grains aligned with a toroidal magnetic field. This supports the fact that the wavelength dependence of the polarization fraction is small in the case of the grain alignment. Contrarily, it is rather strong in the case of self-scattering because scattering-induced polarization is only efficient when the maximum grain size is around $\lambda/2\pi$ (see Sect. 10.3.2).

At first glance, on smaller scales, the HD 100546 data show similarities to polarization observations of the transition disk around HD 142527 (Kataoka et al., 2016b). The polarized intensity also displays a ring-like structure with a clear peak, of which the location is different from the peak of the continuum emission. However, the contrast for the peanut-shaped region compared to the surrounding ring is much higher for HD 142527. For both targets, the polarized intensity has a local minimum at the peak of the continuum. While for HD 100546 the azimuthal shift between these two peeks is almost 180 deg, it is rather 90 deg for HD 142527. Especially for the latter, it remains to be studied whether the asymmetry of the polarized intensity between the leading and the trailing sides of the peanut structure could be correlated with the difference of the trapping size ahead of the vortex. Moreover, changes in the temperature distribution could also reduce or enhance the polarization pattern by changing the radiation field. Another difference between the two targets concerns the polarization degree. HD 142527 shows a polarization fraction as high as 14%, which is unlikely to be explained by pure self-scattering. In the case of HD 100546, the polarization degree is in a lower range (maximum around 1%) as expected from scattering. These points strongly indicate that our new ALMA observations of HD 100546 offer the first look at a dust trap with polarized scattering in the mm regime.

11 | Summary and outlook

The material made of gas and dust in circumstellar disks around PMS stars is the cradle of planet formation. The accretion or dispersal of this material within approximately ten to twenty million years sets tight constraints on the formation timescale of asteroids, and planets, both terrestrial and gas-giant. Statistically, planet formation appears to be a highly efficient process with ∼3700 exoplanet detections in our cosmic neighborhood to date. The architectures of these explanetary systems are very diverse, but deviate from our own solar system. This raises the question about the habitability of exoplanets and whether the solar system benefited from a particular formation environment. The initial conditions and evolution of circumstellar disks must have a direct influence on the fundamental properties of their planetary systems. The availability of new-generation instruments, such as VLT/SPHERE with its extreme AO system and the mm array ALMA, is about to revolutionize this research field by providing us with a view of disks with unprecedented detail at the spatial scales where planet formation occurs. However, despite these advances, the direct detection of forming planets within their host disks remains challenging. Thus, one of the main objectives is the study of physical processes that influence the disk evolution including the search for indirect signatures of planet formation, such as the imprints that it leaves on the disk.

11.1 Summary

This thesis consists of a collection of different projects that all have in common that they investigate the properties that planet-forming disks reveal when observed in polarized scattered light at multiple wavelengths. The first focus is set on modeling scattered light images in the context of planet-disk interactions, with a parameter study on the influence of heating/cooling effects, disk self-gravity, viscosity, disk and planet masses (Chapter 3). The observational part focuses on polarimetric data from the VLT/SPHERE instrument, a dedicated imager for the direct detection of circumstellar disks and exoplanets, which started its operation a little more than three years ago, in line with the beginning of the work presented in this thesis. High contrast, high resolution scattered light observations at optical and NIR wavelengths are used to probe the distribution of small micron-sized grains in the disk surface layer. Thus, these images commonly reveal substructures including gaps, cavities,

spiral arms, shadows, and brightness asymmetries. This thesis investigates how these disk features relate to planet-disk interactions and dust evolution processes (Chapters 4, 5, 7, 8). Scattered light also contributes to the understanding of dust properties, which is shown by analyzing scattering angles and brightness contrasts for inclined disks (Chapters 6). Moreover, it is outlined that the disk scattering surface height can serve as an independent tracer for the bulk gas mass distribution (Chapter 9).

Furthermore, apart from the classical scattering picture of optical and NIR light, the second part of this thesis follows a new path to interpret polarized emission at (sub-)mm wavelengths as the self-scattering of thermal dust emission. It is shown that this is a newly established idea to investigate particle trapping in planet-forming disks and to impose constraints on the grain sizes (Chapter 10).

For all modeling effort, state-of-the-art 3D radiative transfer simulations are used to impose qualitative and quantitative constraints on the disk structure and dust properties. They include a full treatment of multiple scattering and polarization, and consider detailed density distributions and dust opacities. Nevertheless, it must be noted at this point that radiative transfer is a quite complicated exercise, and that, of course, there also exist limitations. Certain assumptions about the disk properties have to be made like, for instance, for the dust opacity. Therefore, one should keep in mind that uncertainties are inherent to every model and that, consequently, not all the encrypted observational information may be retrieved. In the following, the individual contributions that this thesis makes to the research field of planet-forming disks are summarized.

Chapter 1 provides an introduction to the research topics covered in this thesis, where an emphasis is placed on the theoretical and observational aspects of planet-forming disks. Chapter 2 focuses on the foundations of radiative transfer modeling, an essential tool used throughout this thesis to compute observational signatures of disks in order to compare simulation results with observations over a wide range of wavelengths.

Chapter 3 studies the appearance of the main observational features of transition disks in scattered light observations, distinct gaps and spiral arms. Different spiral arm excitation scenarios are explored that consider either a companion located inside a completely stable disk, a gravitationally unstable disk without a perturber, or a marginally gravitationally stable disk with an embedded giant planet. 2D non-isothermal hydrodynamic simulations including viscous heating and a cooling prescription are combined with 3D dust continuum radiative transfer models. It is found that the resulting contrast between planet-induced spirals and the surrounding disk in scattered light is higher for pressure scale height variations, i.e. thermal perturbations, than for pure surface density variations. Shock heating along a spiral increases the scale height of a disk locally. This causes bumps on the disk surface, which are irradiated by the star, and thus produce a significant brightness contrast. Self-gravity effects suppress any vortex modes and tend to produce spirals that are

more tightly wound near the planet's position. If the disk is only marginally gravitationally stable with a Toomre parameter around unity, a sufficiently massive planet can trigger gravitational instability in the outer disk. The density waves created by this instability can overlap with the planet-induced wakes resulting in large-scale, more open spiral arms in the outer disk. With our model setup, there is either one dominant primary spiral when the planet is working as a trigger for gravitational instability or higher mode spirals with similar contrasts are seen when the disk is already initially unstable. However, the explanation of the origin of symmetric, open double-armed spirals remains challenging.

In Chapter 4, the investigation of spiral arms in scattered light images is continued by means of an individual case study. VLT/SPHERE polarimetric images in the NIR are presented for the nearly edge-on transition disk around the T Tauri star RY Lup. This is the first scattered light image of this disk, whose shape is detected with high spatial resolution and sensitivity. Due to the high inclination with respect to the line of sight the disk appears as a double-arc at projected separations in the 100 au range. The observed disk features can be interpreted as spiral arms, as supported by in-depth numerical planet-disk interaction simulations. Taking recent progress in the research field into account, 3D hydrodynamical simulations that consider a companion external to the spirals are performed and paired with 3D radiative transfer simulations. The spiral arms could be launched by one low mass planet ($\sim$2 M_{jup}) located at $\sim$190 au orbiting outside of the scattered light disk. The mass of the planet is in agreement with the mass detection limits for planetary companions obtained from SPHERE contrast curves.

In Chapter 5, the transition disk around the Herbig Ae star HD 100453 is studied with VLT/SPHERE polarimetric differential imaging observations at optical wavelengths. A cavity edge in the form of a bright rim with azimuthal brightness variations, two localized shadow lanes, and a pair of symmetric spiral arms are detected. A radiative transfer model with a strongly misaligned inner disk matches both the location and width of the shadows. The azimuthal brightness variation along the rim can basically be explained by the polarization being maximized along the semi-major axis. However, a 1D semi-analytical model is developed that describes scale height modulations induced by the pressure difference between the shadows and the surrounding regions. It opens a discussion on whether this effect can enhance the azimuthal brightness asymmetry. Although the M dwarf companion is a likely explanation for the spiral arms, it is speculated that they could be also related to the shadows due to their close vicinity.

In Chapter 6 the focus is shifted from spirals to gap and ring structures. The VLT/SPHERE polarimetric and angular differential imaging observations of the transition disk around the T Tauri star T Cha are highlighted. Its outer disk is resolved in scattered light with unprecedented angular resolution and signal-to-noise. The images reveal a highly inclined disk ($\sim$69 deg) with a double wing and a no-

ticeable east-west brightness asymmetry. The significant amount of non-azimuthal polarization signal in the U_ϕ image is in accordance with theoretical predictions for multiple scattering in an inclined disk. A radiative transfer model is constructed, which finds that a ring-like disk emission with a gap of ∼30 au in size best matches the observations. The peak emission lies further out than estimated for the ring at mm wavelengths. Scattered light images of inclined disks are affected by the product of the phase function and the polarization phase curve. In order to self-consistently reproduce the intensity and polarimetric images, it turns out that the dust grains, responsible for the scattered light, need to be dominated by sizes of around ten microns. No companion candidate is found within the gap structure. A point source is detected at an angular distance of 3.5″ from the central star. It is, however, not a bound companion. Planets more massive than 8.5 M_{jup} are ruled out at a distance from 0.″1 to 0.″3 from the central star. At larger separations, the limit decreases to 2 M_{jup}.

Chapter 7 reports on $J-$band polarized intensity imaging of the nearly face-on transition disk around the Herbig Ae star HD 169142 with VLT/SPHERE. Moreover, the findings are compared to recent ALMA dust continuum data, making this study one of the pioneering multi-wavelength analyses at high angular resolution. NIR polarized scattered light is observed down to 0.″16 (∼19 au) hinting at an inner gap devoid of dusty scattering material that exceeds the coronagraph region. We confirm the previously detected double ring structure at 0.″18 (∼21 au) and 0.″56 (∼65 au), and marginally detect a faint third gap at 0.″70-0.″73 (∼81-85 au). Significant small-scale azimuthal brightness variations with clear dips are detected along both rings. The modeling effort follows the idea of active planet formation in HD 169142. A physical disk model is developed by combining dust evolution models in a disk perturbed by two giant planets, as well as disk models with a parameterized dust size distribution. The model based on dust evolution simulations with two massive embedded planets is able to reproduce the ring locations and gap width in polarized intensity, as well as the ring structures and gap depth in the ALMA dust continuum image at 1.3 mm. However, it fails to reproduce the contrast between the rings and the gap depths in scattered light. Models with a constant gas-to-dust ratio and a power law for the dust size distribution better reproduce the gap depth in scattered light, suggesting that dust filtration at the outer edges of the gaps is less effective than predicted in current dust evolution models. Such multi-wavelength analyses can provide feedback on the model assumptions, and can be used to calibrate our understanding of microphysical dust properties and processes, for example the constituents of aggregates and the fragmentation efficiency.

Chapter 8 investigates the effect that different ice lines (H_2O, CO, and NH_3) have on the dust evolution in circumstellar disks around Herbig stars, where radial changes of the fragmentation velocities are considered. Radiative transfer calculations are performed using the resulting dust density distributions in order to compare with current multi-wavelength observations. A clear emission gap is formed between

ice lines, which is surrounded by ring-like structures. The gaps are expected to be shallower and narrower at mm emission compared to the NIR, in contrast to model predictions of particle trapping with the presence of gas pressure bumps. It is also found that the structures in the radial intensity profiles at various wavelengths strongly depend on the disk viscosity.

In Chapter 9 a new independent method to constrain the distribution of the disk bulk mass is outlined in order to solve the enigma of low gas-to-dust ratios in disks recently observed in ALMA surveys. It is demonstrated in a theoretical disk model that the scattering surface height depends sensitively on the disk gas mass. In order to be applicable to real observations, the degeneracy of the dust mass and the turbulent velocity has to be broken. It is argued that this can be achieved with SED fitting constraints and ALMA spectroscopy measurements, respectively.

Chapter 10 proposes to establish a new independent method to investigate dust trapping and to constrain grain sizes in planet-forming disks. By means of detailed dust evolution models combined with radiative transfer calculations, the dust polarization at mm wavelengths is studied in the radial dust trapping scenario, when a giant planet opens a gap in the disk. The efficiency of self-scattering of thermal dust emission and thus the strength of the induced polarization signal depends on the anisotropy of the thermal dust emission and on the grain size. It is shown that self-scattering by large dust grains with a high enough albedo produces detectable polarized emission at sub-mm wavelengths. This leads to a polarization pattern of a transition disk that shows a distinctive ring structure with a polarization degree up to 1% after beam convolution. For a face-on disk, within the highest polarized intensity regions, the polarization vectors are oriented in the azimuthal direction. For an inclined disk, there is an interplay between polarization originating from a flux gradient and inclination-induced quadrupole polarization. Thus, since self-scattering is more sensitive to the latter, the polarization vectors are instead parallel to the minor axis of the disk.

In addition, polarization observations towards the inclined circumstellar disk around HD 100546 from ALMA at 890 μm are presented for the first time. The uniform polarization pattern suggests that self-scattering is the dominating mechanism, which produces polarization vectors parallel to the minor axis of the disk. The high resolution ($\sim$0.″2) data reveal an asymmetric intensity and polarized intensity peak, where the emission peaks are shifted by nearly 180 deg. This is a strong evidence for a vortex structure with azimuthal particle trapping, where the particles in the dust trap have grown to large sizes ($\gg 150\,\mu$m). Such grain sizes produce significant continuum emission, but a negligible polarized signal at sub-mm wavelengths.

11.2 Concise thematic conclusions

Drawing prevailing conclusions is challenging, since planet formation is a rapidly evolving field of research. This section summarizes the lessons learned from the results presented in this thesis and deals with them in a broader perspective. The three main topics of this thesis are considered: spiral arms, ring structures, and constraints from sub-mm polarization.

Spiral arms

So far, clearly symmetric double-arm spirals have been observed in polarized scattered light images of three transitional objects (HD 135344B/SAO 206462, MWC 758, HD 100453), which host older and thus less luminous stars. In contrast, only one disk with two symmetric spiral arms was detected in dust continuum sub-mm emission around a very young star, Elias 2-27. Unfortunately, none of the objects have yet been observed in optical/NIR light and at (sub-)mm wavelengths with similar high spatial resolution. For example, SAO 206462 observations reveal a different shape of disk substructures at different wavelengths. Instead of spiral arms, the sub-mm ALMA observations show a large-scale horseshoe in the dust continuum, although the low angular resolution of these images cannot exclude the presence of mm spirals either. The Elias 2-27 system is unfortunately too embedded to be observed in scattered light at short wavelengths. Nevertheless, further follow-up observations of the scattered light targets with $m = 2$ spirals at longer wavelengths should help towards deciding which scenario is at work in the systems. Three different hypotheses are discussed for the origin of spiral morphologies in circumstellar disks - a gravitationally unstable disk, a companion internal or external to the spirals, and shadow-induced spirals.

For Elias 2-27, its young age and the high disk mass $[0.04, 0.14]\,M_\odot$ suggests that the disk can be massive enough to be gravitationally unstable. Moreover, the disk could have already fragmented and formed a giant planet in the outer disk that is responsible for the large-scale, two-armed spiral structure. The shocks associated with spiral arms in self-gravitating disks can also have an effect on the chemistry of the disk material, which can be investigated with line emission observations, e.g. CO or HCO^+.

Among all possible origins for the spirals arms in SAO 206462, MWC 758, and HD 100453, the gravitational planet-disk interaction of a planetary or substellar companion orbiting exterior to the spirals provides the smallest contradiction with the observational evidences. A self-gravitating origin seems unlikely due to the relatively old system ages and the low disk-to-star mass ratios, although the latter could be underestimated by up to one order of magnitude. An undetected companion internal to the spirals could be involved in clearing the disk cavity, but only a single, tightly wound spiral arm eventually dominates the disk appearance in scattered light. Pressure gradients due to temperature differences between shadowed and illuminated regions induce spiral structures in the density field. Although these spirals emerge

independently of whether self-gravity is considered or not, it is not clear whether they can be maintained on longer timescales and whether their contrast with the background disk is comparable to the observational results. Dedicated hydrodynamical simulations are needed to further conclude on this scenario. Therefore, it is speculated that an undetected planetary companion - or in the case of HD 100453 the known M-dwarf companion - that is located in the outer disk or beyond may be responsible for exciting the observed spiral structures. The only caveat of this scenario is that no planetary companion has yet been detected in the outer part of these transition disks. A further caveat is that a massive enough planet will create a disk gap in both dust and gas, which should be visible in scattered light and also in the large grains observable in (sub-)mm. However, current observations lack sensitivity for the outer disk, which might explain why gaps around possible planetary orbits are not detected.

Complementary total intensity data sets can be used to determine a detection limit, that means an upper mass, for possible companions. A precise constraint for the planet mass and location based on observed spiral profiles is difficult as such inverse approaches suffer from the degeneracy between the disk geometry, disk mass, scale height profile, and viscosity. Nevertheless, the strong brightness contrast of the arms with respect to the background disk hints at Jupiter-mass perturbers, for which the induced spirals no longer follow the linear wave propagation theory. The perturber's location is further limited by the spirals' launching point, as spirals generate shocks and become visible more than a few scale heights away from the planet.

Ring & gap structures

Clear multiple gap- and ring-like structures have been observed in scattered light in about ten planet-forming disks, where some of the targets show such features even at longer wavelengths (e.g., TW Hya, HD163296, HD 169142). Chapters 7 and 8 discuss that, besides planet-disk interactions and magnetic field effects, there are various alternative interpretations for their origin including dust evolution processes near ice lines. A key point to distinguish between different dust accumulation scenarios is the total gas surface density. Both, massive planets or radial variations of the disk viscosity, for example at the outer edge of a dead zone, can cause strong variations in the gas surface density, such as gaps and bumps. For the ice line models presented in this thesis, a significant change of the gas surface density is not expected near the ice lines. As already pointed out for the spirals, another important approach is to compare observations at multiple wavelengths, preferably at similar high angular resolution. Models of dust trapping by a giant planet embedded in the disk or by changes of the disk viscosity predict a deeper and wider gap at mm emission compared to the NIR scattered light. The exact opposite is the case for gaps between ice lines, which are expected to be shallower and narrower at mm emission. For the planet hypothesis, the exploration of sophisticated dust models show that quantitatively extracting properties such as the mass of possible gap-opening planets from

observed gap properties is highly degenerate. Instead, the location of the outer edge of a dust gap in (sub-)mm is a better indicator to estimate the mass of a presumed planet. From contrast curves obtained by direct imaging observations only upper limits on planet masses have been derived so far.

Sub-millimeter polarization

Most recently, polarization of thermal dust emission at (sub-)mm wavelengths has been detected toward a handful of disks. Particularly interesting are the Class I/II disk of HL Tau, and the Herbig Ae/Be late-stage disks around HD 142527 and HD 100546. The polarization morphologies are not consistent with the commonly expected grain alignment with toroidal magnetic fields, but self-scattering and alignment due to a radiation anisotropy are probable mechanisms. For the case of HL Tau, polarization observations at 0.87 mm, 1.3 mm, and 3 mm suggest that the dominant polarization mechanism is strongly wavelength dependent. Thus, multi-wavelength observations are the key to distinguish between the different polarization scenarios. A first conclusion is that the sub-mm polarized emission is consistent with polarization due to self-scattering for two out of three disks. Therefore, from this we can assume to get new insights into the understanding of dust properties and growth processes.

Currently, the grain sizes inferred from polarization in disks outside of dust traps have a maximum of a few hundred microns, which is much smaller than the mm and larger particles derived from the opacity index from continuum emission at optically thin wavelengths. This finding has the potential to change the picture of substructure formation in disks. Given that grains have de facto only grown up to a few hundred microns in size, they are more coupled to the gas than mm- and cm-sized grains. Depending on whether a disk is found to be geometrically thin or thick, this might require weaker or stronger turbulence, which in turn determines the dust settling. A possible solution for the inconsistency between opacity index and polarization grain size estimates is to consider multiple grain populations. Roughly speaking, a first population is made up of smaller grains that produce significant polarized emission in the disk, while the second population of large grains emits significant continuum emission, but does not contribute to the polarization signal.

A limitation of current models is that they all assume compact, spherical grains for the absorption and scattering opacity calculations. A possible idea to solve the problem that spectral index measurements and polarization observations indicate different grain sizes might be to consider porous aggregates. However, a lack of accurate scattering opacity calculations at mm wavelengths does not yet allow for this to be simulated. Moreover, alternative parameters can also affect the total polarization fraction, especially optical depth effects and the vertical disk structure.

11.3 Outlook

In this section, follow-up projects that could emerge from the findings in this work are outlined. Because of stunning new images of planet-forming disks obtained by high contrast and high resolution instruments such as VLT/SPHERE, research has been mainly focusing on individual target analyses. However, with recent ALMA disk surveys serving as an example, and more and more PDI data sets available, a statistical approach of studying polarimetric images of disks is favorable. Questions about differences and similarities between protoplanetary disk features around T Tauri and Herbig stars have to be addressed. Furthermore, the taxonomy of disks is the key to obtain new insights into their evolutionary paths. Multi-wavelength analyses of disk systems will play a key role at similar spatial resolution, which are required to understand the physical origin of disk substructures. While planets have been directly detected in a significant number of debris disks, there is no unambiguous detection of a giant planet nor a circumplanetary disk in gas-rich protoplanetary disks. Pushing ALMA to its sensitivity limits the (kinematic) imprints of an accreting planet could be spotted within the surrounding circumstellar disk.

The potential of mm-wave polarization observations should also be highlighted. ALMA now regularly detects the polarized emission of evolved disks, but its physical origin remains debated. In particular, data at sub-mm wavelengths, where self-scattering seems to be the dominant mechanism, can be used for further testing of dust growth and trapping scenarios. Again, the research would benefit from a large survey of disks, for which grain size constraints are obtained at the disk midplane from both absorption and scattering opacities. The role of optically thick disks and grain properties, such as porous dust aggregates, remains one of the important tasks to be solved in the future.

From a technical point of view, the biggest ground-based telescopes that are currently in operation have primary mirror diameters of about eight to ten meters. Fortunately, in light of emerging observing facilities and techniques substantial progress in the field of planet-forming disks can be expected in the years to come. Within a decade, for example the James Webb Space Telescope (JWST), a new space facility with a 6.5 m mirror diameter, and ESO's European Extremely Large Telescope (E-ELT) with a primary mirror diameter of 39 m will guarantee exciting times for planet formation research and will extend the wavelength coverage towards the MIR.

Presently operating telescopes and promising new instrument innovations will allow for more sensitive individual target and sample observations than ever before. The gallery of planet forming disk images will be extended, which will provide a testing environment for calibrating and refining current state-of-the art disk evolution and planet formation models.

A | Appendix

A.1 Symbol conventions

Table A.1: List of variables

Symbol	Description
a	Grain size
A	Surface area
α	Shakura-Sunyaev $\alpha-$parameter
α_{IR}	Spectral index in the mid- to near-infrared
α_{mm}	Spectral index in the mm
$\alpha_{\nu}^{\mathrm{abs}}$	Absorption coefficient
$\alpha_{\nu}^{\mathrm{scat}}$	Scattering coefficient
$B_{\nu}(\mathrm{T})$	Planck function
β	Exponent of disk scale height profile; spectral index
β_{cool}	Cooling parameter
β_{s}	Exponent of sound speed profile
c_{s}	Sound speed
d	Distance
D	Diffusion coefficient
δ	Power law index for surface density profile
Δ	Impact parameter
e	Eccentricity
E	Energy

Table A.1: (continued)

Symbol	Description
ϵ_ν	Photon destruction probability
η	Pressure support parameter
η_ν	Albedo
f	Power law index for temperature profile
F	Flux
F_D	Gas drag force
F_λ	Monochromatic flux density per wavelength
F_ν	Monochromatic flux density per frequency
g	Surface gravity
g_ν	Scattering anisotropy factor
G	Gravitational constant
γ	Exponent of orbital velocity profile
h	Disk aspect ratio
h_p	Disk aspect ratio at the planet's position
H	Pressure scale height
H_p	Pressure scale height at the planet's position
H_s	Scattering surface height
i	Inclination angle
I	Stokes component (total intensity)
I_ν	Monochromatic intensity
j_ν	Emissivity
J_ν	Zeroth moment: mean intensity
k	Radial wave number
k_B	Boltzmann constant
κ_ν	Mass-weighted opacity
L	Luminosity
$L_\star$	Luminosity of the central star
λ	Wavelength
λ_mfp	Mean free path of gas molecule

Table A.1: (continued)

Symbol	Description
m	Mass;
	azimuthal wave number
M	Mass
$m_{\rm p}$	Proton mass
$M_{\rm d}$	Dust mass
$M_{\rm g}$	Gas mass
$M_{\rm p}$	Planet mass
$M_\star$	Mass of central star
$M_\odot$	Solar mass
$\dot{M}_{\rm accr}$	Mass accretion rate
μ	Molecular weight of the gas
N_γ, $\mathrm{N_{phot}}$	Number of photon packages
$N_{\rm r}$	Number of grid cells in $r-$direction
N_ϕ	Number of grid cells in $\phi-$direction
N_θ	Number of grid cells in $\theta-$direction
$\vec{n}$	Direction vector
ν	Frequency
$\nu_{\rm t}$	Viscosity
Ω	Orbital frequency
$\Omega_{\rm K}$	Keplerian angular velocity
p	Exponent for grain size distribution
P	Pressure;
	degree of polarization
PI	Linear polarization signal
$\varphi_{\rm inc}$	Grazing angle
ϕ	Azimuthal angle;
	scattering phase function
Φ	Potential
ψ	Spiral pitch angle

Table A.1: (continued)

Symbol	Description
q	Planet-to-star mass ratio; exponent of number density
Q	Stokes vector component
$Q_{\pm}$	Heating and cooling terms
$\mathcal{Q}$	Toomre parameter
r, R	Radius
r_{c}	Corotation radius
r_{p}	Orbital planet radius
r_{H}	Hill radius
$\mathcal{R}_{\mathrm{g}}$	Universal gas constant
$R_{\star}$	Radius of central star
$R_{\odot}$	Solar radius
Re	Reynolds number
ρ	Density
ρ_{d}	Dust density
ρ_{g}	Gas density
ρ_{s}	Solid density of particle
S_{ij}	Scattering matrix elements
S_{ν}	Source function
Sc	Schmidt number
St	Stokes number
Σ	Surface density
Σ_{d}	Dust surface density
Σ_{g}	Gas surface density
t	Time
t_{s}	Stopping time
T	Temperature
T_{eff}	Effective temperature
$T_{\star}$	Temperature of central star

Table A.1: (continued)

Symbol	Description
$T_{\rm g}$	Gravitational torque
$T_{\rm tid}$	Tidal torque
$T_{\rm visc}$	Intrinsic viscous angular momentum transfer rate
τ_ν	Optical depth
θ	Polar angle;
	scattering angle
U	Stokes vector component
v	Velocity
V	Stokes vector component
x	Cartesian coordinate;
	size parameter
ξ	Refinement factor
y	Cartesian coordinate
z	Vertical disk height;
	cartesian or cylindrical coordinate
$Z_{\rm ij}$	Scattering matrix elements

A.2 Abbreviations

Table A.2: List of abbreviations

2D	Two-dimensional
3D	Three-dimensional
ADI	Angular differential imaging
ALMA	Atacama Large Millimeter Array
AO	Adaptive optics
APEX	Atacama Pathfinder Experiment
cADI	Classical angular differential imaging
CARMA	Combined Array for Research in Millimeter-wave Astronomy
CC	Companion candidate
CMD	Color-magnitude diagram
CO	Carbon monoxide
CTTS	Classical T Tauri star
DEC	Declination
DPI	Dual-band Polarimetric Imaging
DRH	SPHERE data reduction and handling pipeline
ESA	European Space Agency
FOV	Field of view
FWHM	Full width at half maximum
G/D	Gas-to-dust ratio
GPI	Gemini Planet Imager
GTO	Guaranteed time observation
HiCIAO	High Contrast Instrument for the Subaru next generation Adaptive Optics
HST	Hubble Space Telescope
HD	Hydrogen deuteride
IFS	Integral Field Spectrograph
IRAS	InfraRed Astronomical Satellite
IRDIS	The Infra-Red Dual-beam Imager and Spectrograph

Table A.2: (continued)

IRS	Infrared Spectrograph
ISM	Interstellar medium
ISO	Infrared Space Observatory
IUE	International Ultraviolet Explorer
IWA	Inner working angle
JCMT	James Clerk Maxwell Telescope
JD	Julian date
JWST	James Webb Space Telescope
LTE	Local thermodynamic equilibrium
MHD	Magnetohydrodynamics
MRI	Magnetorotational instability
MRN	Mathis, Rumpl and Nordsieck
NACO	Nasmyth Adaptive Optics System (NAOS) Near-Infrared Imager and Spectrograph (CONICA)
NASA	National Aeronautics and Space Administration
NICMOS	Near Infrared Camera and Multi-Object Spectrometer
NIR	Near-infrared
NOEMA	NOrthern Extended Millimeter Array
PA	Position angle
PAH	Polyaromatic hydrocarbon
PCA	Principal component analysis
PDI	Polarimetric differential imaging
PMS	Pre-main sequence
PSF	Point spread function
RA	Right ascension
SED	Spectral energy distribution
SDI	Spectral differential imaging
SHINE	SpHere INfrared survey for Exoplanets
SMA	Submillimeter Array
SNR	Signal-to-noise ratio

Table A.2: (continued)

SPHERE	Spectro-Polarimetric High-contrast Exoplanet REsearch
TLOCI	Template Locally Optimized Combination of Images
VBB	Very broad band
VLA	Karl G. Jansky Very Large Array
VLT	Very Large Telescope
VLTI	Very Large Telescope Interferometer
WISE	Wide-Field Infrared Survey Explorer
WTTS	Weak-line T Tauri star
YSO	Young stellar object
ZIMPOL	Zurich IMaging POLarimeter

A.3 List of figures

A.4 List of tables

B | List of own publications

Bibliography of first-author papers used in this thesis:

- **Pohl, A.**, Pinilla, P., Benisty, M., Ataiee, S., Juhasz, A., Dullemond, C. P., van Boekel, R., Henning, Th.; *Scattered light images of spiral arms in marginally gravitationally unstable discs with an embedded planet*, MNRAS (2015), 453 (2): 1768–1778

- **Pohl, A.**, Kataoka, A., Pinilla, P., Dullemond, C. P., Henning, Th., Birnstiel, T.; *Investigating dust trapping in transition disks with millimeter-wave polarization*, A&A (2016), 593, A12

- **Pohl, A.**, Sissa, E., Langlois, M., Mueller, A., Ginski, C., van Holstein, R. G., Vigan, A., Mesa, D., Maire, A.-L., Henning, Th., Gratton, R., Olofsson, J., van Boekel, R., Benisty, M., Biller, B., Boccaletti, A., Chauvin, G., Daemgen, S., de Boer, J., Desidera, S., Dominik, C., Garufi, A., Janson, M., Kral, Q., Ménard, F., Pinte, C., Stolker, T., Szulágyi, J., Zurlo, A., Bonnefoy, M., Cheetham, A., Cudel, M., Feldt, M., Kasper, M., Lagrange, A.-M., Perrot, C., Wildi, F.; *New constraints on the disk characteristics and companion candidates around T Chamaeleontis with VLT/SPHERE*, A&A (2017), 605, A34

- **Pohl, A.**, Benisty, M., Pinilla, P., Ginski, C., de Boer, J., Avenhaus, H., Henning, Th., Zurlo, A., Boccaletti, A., Augereau, J.-C., Birnstiel, T., Dominik, C., Facchini, S., Fedele, D., Janson, M., Keppler, M., Kral, Q., Langlois, M., Ligi, R., Maire, A.-L., Ménard, F., Meyer, M., Pinte, C., Quanz, S. P., Sauvage, J.-F., Szestre, É, Stolker, T., Szulágyi, J., van Boekel, R., van der Plas, G., Villenave, M., Baruffolo, A., Baudoz, P., Le Mignant, D., Maurel, D., Ramos, J., Weber, L.; *The circumstellar disk HD 169142: gas, dust and planets acting in concert?*, ApJ (2017), 850, 1

Bibliography of co-author papers used in this thesis:

- Benisty, M., Stolker, T., **Pohl, A.**, de Boer, J., Lesur, G., Dominik, C., Dullemond, C. P., Langlois, M., Min, M., Wagner, K., Henning, Th., Juhasz, A., Pinilla, P., Facchini, S., Apai, D., van Boekel, R., Garufi, A., Ginski, C., Ménard, F., Pinte, C., Quanz, S. P., Zurlo, A., Boccaletti, A., Bonnefoy, M., Beuzit, J. L., Chauvin, G., Cudel, M., Desidera, S., Feldt, M., Fontanive, C., Gratton, R., Kasper, M., Lagrange, A.-M., LeCoroller, H., Mouillet, D., Mesa, D., Sissa, E., Vigan, A., Antichi, J., Buey, T., Fusco, T., Gisler, D., Llored, M., Magnard, Y., Moeller-Nilsson, O., Pragt, J., Roelfsema, R.; *Shadows and spirals in the protoplanetary disk HD 100453*, A&A (2017), 597, A42

- Kataoka, A., Tsukagoshi, T., **Pohl, A.**, Muto, T., Nagai, H., Stephens, I. W., Tomisaka, K., Momose, M.; *The evidence of radio polarization induced by the radiative grain alignment and self-scattering of dust grains in a protoplanetary disk*, ApJL (2017), 844, L5

- Langlois, M., **Pohl, A.**, Lagrange, A.-M., Maire, A.-L., Mesa, D., Boccaletti, A., Gratton, R., Denneulin, L., Klahr, H., Vigan, A., Benisty, M., Dominik, C., Bonnefoy, M., Ménard, F., Avenhaus, H., Cheetham, A., van Boekel, R., de Boer, J., Chauvin, G., Desidera, S., Feldt, M., Galicher, R., Ginski, C., Girard, J., Henning, Th., Janson, M., Kopytova, T., Kral, Q., Ligi, R., Messina, S., Peretti, S., Pinte, C., Sissa, E., Stolker, T., Zurlo, A.; *First scattered light detection of a nearly edge-on transition disk around the T Tauri star RY Lup*, submitted to A&A, under revision

- Pinilla, P., **Pohl, A.**, Stammler, S., Birnstiel, T.; *Dust density distribution and imaging analysis of different ice lines in protoplanetary disks*, ApJ (2017), 845, 68

Bibliography of co-author papers cited in this thesis:

- Benisty, M., Juhasz, A., Boccaletti, A., Avenhaus, A., Milli, J., Thalmann, C., Dominik, C., Pinilla, P., Buenzli, E., **Pohl, A.**, Beuzit, J.-L., Birnstiel, T., de Boer, J., Bonnefoy, M., Chauvin, G., Christiaens, V., Garufi, A., Grady, C., Henning, Th., Huelamo, N., Isella, A., Langlois, M., Ménard, F., Mouillet, D., Olofsson, J., Pantin, E., Pinte, C., Pueyo, L.; *Asymmetric features in the protoplanetary disk MWC 758*, A&A (2015), 578, L6

- Garufi, A., Meeus, G., Benisty, M., Quanz, S. P., Banzatti, A., Kama, M., Canovas, H., Eiroa, C., Schmid, H. M., Stolker, T., **Pohl, A.**, Rigliaco, E., Ménard, F., Meyer, M., van Boekel, R., Dominik, C.; *The evolution of protoplanetary disks from their taxonomy in scattered light: Group I vs Group II*, A&A (2017), 603, A21

- Garufi, A., Benisty, M., Stolker, T., Avenhaus, H., de Boer, J., **Pohl, A.**, Quanz, S. P., Dominik, C., Ginski, C., Thalmann, C., van Boekel, R., Boccaletti, A., Henning, Th., (+ SPHERE consortium); *Three years of SPHERE: the latest view of the morphology and evolution of protoplanetary discs*, ESO The Messenger (September 2017), 169, 32–37

- Janson, M., Thalmann, C., Boccaletti, A., Maire, A.-L., Zurlo, A., Marzari, F., Meyer, M. R., Carson, J. C., Augereau, J.-C., Garufi, A., Henning, Th., Desidera, S., Asensio-Torres, R., **Pohl, A.**; *Detection of sharp symmetric features in the circumbinary disk around AK Sco*, ApJL (2016), 816, L1

- Juhasz, A., Benisty, M., **Pohl, A.**, Dullemond, C. P., Dominik, C., Paardekooper, S.-J.; *Spiral arms in scattered light images of protoplanetary discs: are they the signposts of planets?*, MNRAS (2015), 451 (2), 1147–1157

- Kataoka, A., Tsukagoshi, T., Momose, M., Nagai, H., Muto, T., Dullemond, C. P., **Pohl, A.**, Fukagawa, M., Shibai, H., Hanawa, T., Murakawa, K.; *Submillimeter polarization observation of the protoplanetary disk around HD 142527*, ApJL (2016), 831, L12

- Ligi, R., Vigan, A., Gratton, R., de Boer, J., Benisty, M., Boccaletti, A., Quanz, S. P., Meyer, M., Ginski, C., Sissa, E., Henning, Th., Beuzit, J.-L., Biller, B., Bonnefoy, M., Chauvin, G., Cheetham, A. C., Cudel, M., Delorme, P., Desidera, S., Feldt, M., Galicher, R., Girard, J., Janson, M., Kasper, M., Kopytova, T., Lagrange, A.-M., Langlois, M., LeCoroller, H., Maire, A.-L., Ménard, F., Mesa, D., Peretti, S., Perrot, C., Pinilla, P., **Pohl, A.**, Rouan, D., Stolker, T., Samland, M., Wahhaj, Z., Wildi, F., Zurlo, A., Buey, T., Fantinel, D., Fusco, T., Jaquet, M., Moulin, T., Ramos, J., Suarez, M., Weber, L.; *Investigation of the inner structures around HD169142 with VLT/SPHERE*, MNRAS (2018), 473 (2), 1774–1783

- Maire, A.-L., Stolker, T., Messina, S., Mueller, A., Biller, B., Currie, T., Dominik, C., Boccaletti, A., Bonnefoy, M., Chauvin, G., Galicher, R., Millward, M., **Pohl, A.**, Brandner, W., Henning, Th., Lagrange, A.-M., Langlois, M., Meyer, M. R., Quanz, S. P., Vigan, A., Zurlo, A., van Boekel, R., Buenzli, E., Buey, T., Desidera, S., Feldt, M., Fusco, T., Ginski, C., Giro, E., Gratton, R., Hubin, N., Lannier, J., Le Mignant, D., Mesa, D., Peretti, S., Perrot, C., Ramos, J. R., Salter, G., Samland, M., Sissa, E., Stadler, E., Thalmann, C., Udry, S., Weber, L.; *Testing giant planet formation in the transitional disk of SAO 206462 using deep VLT/SPHERE imaging*, A&A (2017), 603, A21

- Szulágyi, J., van der Plas, G., Meyer, M. R., **Pohl, A.**, Quanz, S. P., Mayer, L., Daemgen, S., Tamburello, V.; *Observability of Forming Planets and their Circumplanetary Disks I. – Parameter Study for ALMA*, MNRAS (2018), 473 (3), 3573–3583

- van Boekel, R., Henning, Th., Menu, J., de Boer, J., Langlois, M., Mueller, A., Avenhaus, H., Boccaletti, A., Schmid, H. M., Thalmann, Ch., Benisty, M., Dominik, C., Ginski, Ch., Girard, J. H., Gisler, D., Lobo Gomes, A., Ménard, F., Min, M., Pavlov, A., **Pohl, A.**, Quanz, S. P., Rabou, P., Roelfsema, R., Sauvage, J.-F., Teague, R., Wildi, F., Zurlo, A.; *Three radial gaps in the disk of TW Hydrae imaged with SPHERE*, ApJ (2017), 837, 132

C | Bibliography

Absil, O., Milli, J., Mawet, D., et al. 2013, A&A, 559, L12 101

Acke, B., & van den Ancker, M. E. 2006, A&A, 449, 267 208

Adachi, I., Hayashi, C., & Nakazawa, K. 1976, Progress of Theoretical Physics, 56, 1756 15

Adams, F. C., Lada, C. J., & Shu, F. H. 1987, ApJ, 312, 788 5

Ageorges, N., Fischer, O., Stecklum, B., Eckart, A., & Henning, T. 1996, ApJL, 463, L101 104

Alcala, J. M., Covino, E., Franchini, M., et al. 1993, A&A, 272, 225 96

Alexander, R., Pascucci, I., Andrews, S., Armitage, P., & Cieza, L. 2014, Protostars and Planets VI, 475 10

Alexander, R. D., & Armitage, P. J. 2007, MNRAS, 375, 500 12

Alexander, R. D., Clarke, C. J., & Pringle, J. E. 2006a, MNRAS, 369, 216 12

Alexander, R. D., Clarke, C. J., & Pringle, J. E. 2006b, MNRAS, 369, 229 12

Allard, F., Guillot, T., Ludwig, H.-G., et al. 2003, in IAU Symposium, Vol. 211, Brown Dwarfs, ed. E. Martín, 325 118

ALMA Partnership, Brogan, C. L., Pérez, L. M., et al. 2015, ApJL, 808, L3 28, 29, 30, 125

Amara, A., & Quanz, S. P. 2012, MNRAS, 427, 948 101

Andersson, B.-G., Lazarian, A., & Vaillancourt, J. E. 2015, ARA&A, 53, 501 34

Andre, P., & Montmerle, T. 1994, ApJ, 420, 837 32

Andrews, S. M., & Williams, J. P. 2005, ApJ, 631, 1134 33, 56, 185

Andrews, S. M., & Williams, J. P. 2007, ApJ, 671, 1800 33

Andrews, S. M., Wilner, D. J., Espaillat, C., et al. 2011, ApJ, 732, 42 12, 57, 95

Andrews, S. M., Wilner, D. J., Hughes, A. M., Qi, C., & Dullemond, C. P. 2010, ApJ, 723, 1241 57

Andrews, S. M., Wilner, D. J., Zhu, Z., et al. 2016, ApJL, 820, L40 30, 125, 168

Ansdell, M., Williams, J. P., Manara, C. F., et al. 2017, AJ, 153, 240 33

Ansdell, M., Williams, J. P., van der Marel, N., et al. 2016, ApJ, 828, 46 12, 33, 56, 77, 80, 82, 85, 86, 175, 176

Apai, D., Pascucci, I., Brandner, W., et al. 2004, A&A, 415, 671 127

Armitage, P. J. 2013, Astrophysics of Planet Formation 6

Ataiee, S., Pinilla, P., Zsom, A., et al. 2013, A&A, 553, L3 64, 147

Audard, M., Ábrahám, P., Dunham, M. M., et al. 2014, Protostars and Planets VI, 387 11

Avenhaus, H., Quanz, S. P., Schmid, H. M., et al. 2014, ApJ, 781, 87 30, 32, 54, 95, 99, 128

Avenhaus, H., Quanz, S. P., Schmid, H. M., et al. 2017, AJ, 154, 33 31, 54

Baehr, H., & Klahr, H. 2015, ApJ, 814, 155 60

Bai, X.-N. 2013, ApJ, 772, 96 11

Bai, X.-N. 2016, ApJ, 821, 80 11, 166

Bai, X.-N., & Stone, J. M. 2013, ApJ, 769, 76 11

Balbus, S. A., & Hawley, J. F. 1991, ApJ, 376, 214 11, 166

Banzatti, A., Pinilla, P., Ricci, L., et al. 2015, ApJL, 815, L15 154, 157

Barenfeld, S. A., Carpenter, J. M., Ricci, L., & Isella, A. 2016, ApJ, 827, 142 33, 175

Barge, P., & Sommeria, J. 1995, A&A, 295, L1 18

Baruteau, C., & Masset, F. 2008a, ApJ, 672, 1054 57

Baruteau, C., & Masset, F. 2008b, ApJ, 678, 483 57

Baruteau, C., Crida, A., Paardekooper, S.-J., et al. 2014, Protostars and Planets VI, 667 19

Bastien, P., & Menard, F. 1990, ApJ, 364, 232 104

Beckwith, S., Sargent, A. I., Scoville, N. Z., et al. 1986, ApJ, 309, 755 28, 29

Beckwith, S. V. W., & Sargent, A. I. 1991, ApJ, 381, 250 33, 185

Beckwith, S. V. W., Sargent, A. I., Chini, R. S., & Guesten, R. 1990, AJ, 99, 924 32, 56

Benisty, M., Juhasz, A., Boccaletti, A., et al. 2015, A&A, 578, L6 30, 31, 54

Benisty, M., Stolker, T., Pohl, A., et al. 2017, A&A, 597, A42 30, 31, 54, 87, 88, 96, 107

Bergin, E. A., Cleeves, L. I., Gorti, U., et al. 2013, Nature, 493, 644 33, 55, 176

Bertrang, G. H.-M., & Wolf, S. 2017, MNRAS, 469, 2869 34

Béthune, W., Lesur, G., & Ferreira, J. 2016, A&A, 589, A87 125

Beuzit, J.-L., Feldt, M., Dohlen, K., et al. 2008, in Proc. SPIE, Vol. 7014, Ground-based and Airborne Instrumentation for Astronomy II, 701418 19

Biller, B., Lacour, S., Juhász, A., et al. 2012, ApJL, 753, L38 94

Biller, B. A., Males, J., Rodigas, T., et al. 2014, ApJL, 792, L22 127

Birnstiel, T., & Andrews, S. M. 2014, ApJ, 780, 153 141, 160

Birnstiel, T., Andrews, S. M., Pinilla, P., & Kama, M. 2015, ApJL, 813, L14 161, 162

Birnstiel, T., Dullemond, C. P., & Brauer, F. 2010, A&A, 513, A79 13, 14, 16, 56, 134, 135, 153, 154, 156, 177, 188, 190

Birnstiel, T., Klahr, H., & Ercolano, B. 2012, A&A, 539, A148 155

Birnstiel, T., Ormel, C. W., & Dullemond, C. P. 2011, A&A, 525, A11 155

Bjorkman, J. E., & Wood, K. 2001, ApJ, 554, 615 45, 46

Blondel, P. F. C., & Djie, H. R. E. T. A. 2006, A&A, 456, 1045 136

Blum, J., & Münch, M. 1993, Icarus, 106, 151 15

Blum, J., & Wurm, G. 2000, Icarus, 143, 138 153

Boccaletti, A., Abe, L., Baudrand, J., et al. 2008, in Proc. SPIE, Vol. 7015, Adaptive Optics Systems, 70151B 99, 127

Bohren, C. F., & Huffman, D. R. 1983, Absorption and scattering of light by small particles 39, 48, 108

Bohren, C. F., & Huffman, D. R. 1984, Nature, 307, 575 62, 190, 194

Bolton, S. J., Adriani, A., Adumitroaie, V., et al. 2017, Science, 356, 821 1

Boss, A. P. 1997, Science, 276, 1836 18

Brauer, F., Dullemond, C. P., & Henning, T. 2008, A&A, 480, 859 13

Brauer, F., Dullemond, C. P., Johansen, A., et al. 2007, A&A, 469, 1169 56

Brittain, S. D., Carr, J. S., Najita, J. R., Quanz, S. P., & Meyer, M. R. 2014, ApJ, 791, 136 208

Brittain, S. D., Najita, J. R., & Carr, J. S. 2009, ApJ, 702, 85 208

Brown, J. M., Blake, G. A., Dullemond, C. P., et al. 2007, ApJL, 664, L107 95, 96

Bryden, G., Chen, X., Lin, D. N. C., Nelson, R. P., & Papaloizou, J. C. B. 1999, ApJ, 514, 344 22

Canovas, H., Ménard, F., de Boer, J., et al. 2015, A&A, 582, L7 99, 104, 113, 128

Canovas, H., Rodenhuis, M., Jeffers, S. V., Min, M., & Keller, C. U. 2011, A&A, 531, A102 99, 100

Canovas, H., Hardy, A., Zurlo, A., et al. 2017, A&A, 598, A43 126

Carrasco-González, C., Henning, T., Chandler, C. J., et al. 2016, ApJL, 821, L16 30, 125

Casassus, S., Marino, S., Pérez, S., et al. 2015, ApJ, 811, 92 189

Cassan, A., Kubas, D., Beaulieu, J.-P., et al. 2012, Nature, 481, 167 3

Castelli, F., & Kurucz, R. L. 2004, ArXiv Astrophysics e-prints, astro-ph/0405087 47, 48, 85

Chauvin, G., Lagrange, A.-M., Bonavita, M., et al. 2010, A&A, 509, A52 116, 117

Cheetham, A., Huélamo, N., Lacour, S., de Gregorio-Monsalvo, I., & Tuthill, P. 2015, MNRAS, 450, L1 97

Chen, L., Kospal, A., Abraham, P., et al. 2017, ArXiv e-prints, arXiv:1709.06514 143

Chen, X. P., Henning, T., van Boekel, R., & Grady, C. A. 2006, A&A, 445, 331 87

Chiang, E. I., & Goldreich, P. 1997, ApJ, 490, 368 8

Cho, J., & Lazarian, A. 2007, ApJ, 669, 1085 34, 208

Christiaens, V., Casassus, S., Perez, S., van der Plas, G., & Ménard, F. 2014, ApJL, 785, L12 31, 54

Ciesla, F. J., & Cuzzi, J. N. 2006, Icarus, 181, 178 167

Cieza, L. A., Olofsson, J., Harvey, P. M., et al. 2011, ApJL, 741, L25 96

Clarke, C. 2011, The Dispersal of Disks around Young Stars, ed. P. J. V. Garcia, 355–418 11

Clarke, C. J., Gendrin, A., & Sotomayor, M. 2001, MNRAS, 328, 485 12

Claudi, R. U., Turatto, M., Gratton, R. G., et al. 2008, in Proc. SPIE, Vol. 7014, Ground-based and Airborne Instrumentation for Astronomy II, 70143E 99

Cleeves, L. I. 2016, ApJL, 816, L21 155

Cleeves, L. I., Bergin, E. A., Qi, C., Adams, F. C., & Öberg, K. I. 2015, ApJ, 799, 204 168

Close, L. M., Follette, K. B., Males, J. R., et al. 2014, ApJL, 781, L30 94

Collins, K. A., Grady, C. A., Hamaguchi, K., et al. 2009, ApJ, 697, 557 87, 88

Connerney, J. E. P., Adriani, A., Allegrini, F., et al. 2017, Science, 356, 826 1

Cossins, P., Lodato, G., & Clarke, C. J. 2009, MNRAS, 393, 1157 55

Crida, A., Morbidelli, A., & Masset, F. 2006, Icarus, 181, 587 22, 23, 66, 134, 143

Currie, T., Cloutier, R., Brittain, S., et al. 2015, ApJL, 814, L27 208

Currie, T., Muto, T., Kudo, T., et al. 2014, ApJL, 796, L30 208

Cuzzi, J. N., & Zahnle, K. J. 2004, ApJ, 614, 490 16

D'Alessio, P., Calvet, N., & Hartmann, L. 2001, ApJ, 553, 321 191

D'Alessio, P., Cantö, J., Calvet, N., & Lizano, S. 1998, ApJ, 500, 411 79

D'Angelo, G., Henning, T., & Kley, W. 2002, A&A, 385, 647 23

Daniel, J.-Y. 1980, A&A, 87, 204 195

Davis, Jr., L., & Greenstein, J. L. 1951, ApJ, 114, 206 34

de Boer, J., Salter, G., Benisty, M., et al. 2016, A&A, 595, A114 31, 125, 131, 183

de Gregorio-Monsalvo, I., Ménard, F., Dent, W., et al. 2013, A&A, 557, A133 56

de Juan Ovelar, M., Min, M., Dominik, C., et al. 2013, A&A, 560, A111 167, 186, 187

de Juan Ovelar, M., Pinilla, P., Min, M., Dominik, C., & Birnstiel, T. 2016, MNRAS, 459, L85 143, 188

Demyk, K., Meny, C., Leroux, H., et al. 2013, in Proceedings of The Life Cycle of Dust in the Universe: Observations, Theory, and Laboratory Experiments (LCDU2013). 18-22 November, 2013. Taipei, Taiwan, 44 56

Dent, W. R. F., Torrelles, J. M., Osorio, M., Calvet, N., & Anglada, G. 2006, MNRAS, 365, 1283 141, 142

Desch, S. J., & Turner, N. J. 2015, ApJ, 811, 156 166

Dipierro, G., & Laibe, G. 2017, MNRAS, 469, 1932 24, 25, 144, 145

Dipierro, G., Laibe, G., Price, D. J., & Lodato, G. 2016, MNRAS, 459, L1 24, 25, 144, 145, 151, 167

Dipierro, G., Price, D., Laibe, G., et al. 2015, MNRAS, 453, L73 126

Dittrich, K., Klahr, H., & Johansen, A. 2013, ApJ, 763, 117 151

Dodson-Robinson, S. E., & Salyk, C. 2011, ApJ, 738, 131 144

Dohlen, K., Langlois, M., Saisse, M., et al. 2008, in Proc. SPIE, Vol. 7014, Ground-based and Airborne Instrumentation for Astronomy II, 70143L 78

Dolginov, A. Z., & Mitrofanov, I. G. 1976, Ap&SS, 43, 291 34

Dolginov, A. Z., & Stepinski, T. F. 1994, ApJ, 427, 377 166

Dominik, C., & Tielens, A. G. G. M. 1997, ApJ, 480, 647 120

Dong, R., & Fung, J. 2017, ApJ, 835, 146 136, 145, 151

Dong, R., Fung, J., & Chiang, E. 2016a, ApJ, 826, 75 79, 83, 97, 126

Dong, R., Hall, C., Rice, K., & Chiang, E. 2015a, ApJL, 812, L32 55, 74

Dong, R., Rafikov, R. R., & Stone, J. M. 2011, ApJ, 741, 57 20

Dong, R., Zhu, Z., Fung, J., et al. 2016b, ApJL, 816, L12 75, 93

Dong, R., Zhu, Z., Rafikov, R. R., & Stone, J. M. 2015b, ApJL, 809, L5 54, 75, 79, 126

Dong, R., Zhu, Z., & Whitney, B. 2015c, ApJ, 809, 93 54, 81, 82, 96, 167

Dorschner, J., Begemann, B., Henning, T., Jaeger, C., & Mutschke, H. 1995, A&A, 300, 503 49, 50, 62, 179

Draine, B. T. 2003, ApJ, 598, 1026 49, 82, 108, 135, 190

Draine, B. T. 2006, ApJ, 636, 1114 33

Draine, B. T. 2011, Physics of the Interstellar and Intergalactic Medium 4

Draine, B. T., & Weingartner, J. C. 1996, ApJ, 470, 551 34

Draine, B. T., & Weingartner, J. C. 1997, ApJ, 480, 633 34

Drążkowska, J., & Dullemond, C. P. 2014, A&A, 572, A78 16

Drążkowska, J., Windmark, F., & Dullemond, C. P. 2013, A&A, 556, A37 16

Drążkowska, J., Windmark, F., & Dullemond, C. P. 2014, A&A, 567, A38 16

Duffell, P. C. 2015, ApJL, 807, L11 23, 24

Duffell, P. C., & MacFadyen, A. I. 2013, ApJ, 769, 41 23, 24

Dullemond, C. P. 2012, Lecture notes, University of Heidelberg, http://www.ita.uni-heidelberg.de/~dullemond/lectures/radtrans_2012/index.shtml 39

Dullemond, C. P., & Dominik, C. 2004a, A&A, 417, 159 58

Dullemond, C. P., & Dominik, C. 2004b, A&A, 421, 1075 9, 177

Dullemond, C. P., & Dominik, C. 2005, A&A, 434, 971 96

Dullemond, C. P., Dominik, C., & Natta, A. 2001, ApJ, 560, 957 176

Dullemond, C. P., Juhasz, A., Pohl, A., et al. 2012, RADMC-3D: A multi-purpose radiative transfer tool, Astrophysics Source Code Library, ascl:1202.015 39, 45, 61, 82, 107, 134, 187

Dunkin, S. K., Barlow, M. J., & Ryan, S. G. 1997, MNRAS, 286, 604 126, 136

Dutrey, A., Guilloteau, S., Duvert, G., et al. 1996, A&A, 309, 493 56

Dzyurkevich, N., Flock, M., Turner, N. J., Klahr, H., & Henning, T. 2010, A&A, 515, A70 18

Dzyurkevich, N., Turner, N. J., Henning, T., & Kley, W. 2013, ApJ, 765, 114 144

Epstein, P. S. 1924, Phys. Rev., 23, 710 14

Ercolano, B., Clarke, C. J., & Hall, A. C. 2011, MNRAS, 410, 671 10

Ercolano, B., & Pascucci, I. 2017, Royal Society Open Science, 4, 170114 10, 11, 12

Espaillat, C., Calvet, N., D'Alessio, P., et al. 2007, ApJL, 670, L135 27

Evans, II, N. J., Dunham, M. M., Jørgensen, J. K., et al. 2009, ApJS, 181, 321 25

Facchini, S., Birnstiel, T., Bruderer, S., & van Dishoeck, E. F. 2017, A&A, 605, A16 141

Fairlamb, J. R., Oudmaijer, R. D., Mendigutía, I., Ilee, J. D., & van den Ancker, M. E. 2015, MNRAS, 453, 976 88

Favre, C., Cleeves, L. I., Bergin, E. A., Qi, C., & Blake, G. A. 2013, ApJL, 776, L38 176

Fedele, D., Carney, M., Hogerheijde, M. R., et al. 2017, A&A, 600, A72 26, 126, 127, 132, 133, 135, 136, 141, 142

Ferreira, J., Dougados, C., & Cabrit, S. 2006, A&A, 453, 785 11

Fischer, O., Henning, T., & Yorke, H. W. 1994, A&A, 284, 187 195

Fischer, O., Henning, T., & Yorke, H. W. 1996, A&A, 308, 863 104

Flaherty, K. M., Hughes, A. M., Rosenfeld, K. A., et al. 2015, ApJ, 813, 99 166, 178

Flaherty, K. M., Hughes, A. M., Rose, S. C., et al. 2017, ApJ, 843, 150 166, 178

Flock, M., Henning, T., & Klahr, H. 2012, ApJ, 761, 95 166

Flock, M., Ruge, J. P., Dzyurkevich, N., et al. 2015, A&A, 574, A68 55, 96, 125, 151

Follette, K. B., Grady, C. A., Swearingen, J. R., et al. 2015, ApJ, 798, 132 95

Folsom, C. P., Bagnulo, S., Wade, G. A., et al. 2012, MNRAS, 422, 2072 136

Forgan, D., Rice, K., Cossins, P., & Lodato, G. 2011, MNRAS, 410, 994 55

Foucart, F., & Lai, D. 2013, ApJ, 764, 106 94

French, R. H., Winey, K. I., Yang, M. K., & Qiu, W. 2007, Australian Journal of Chemistry, 60, 251 152

Fromang, S., & Nelson, R. P. 2005, MNRAS, 364, L81 185

Fu, W., Li, H., Lubow, S., Li, S., & Liang, E. 2014, ApJL, 795, L39 64

Fung, J., Shi, J.-M., & Chiang, E. 2014, ApJ, 782, 88 23, 24, 134

Fusco, T., Rousset, G., Rabaud, D., et al. 2004, Journal of Optics A: Pure and Applied Optics, 6, 585 99

Fusco, T., Petit, C., Rousset, G., et al. 2006, in Proc. SPIE, Vol. 6272, Society of Photo-Optical Instrumentation Engineers (SPIE) Conference Series, 62720K 97

Fusco, T., Sauvage, J.-F., Petit, C., et al. 2014, in Proc. SPIE, Vol. 9148, Adaptive Optics Systems IV, 91481U 97

Gaia Collaboration, Brown, A. G. A., Vallenari, A., et al. 2016, A&A, 595, A2 30, 77, 80, 87, 96, 116, 126, 168, 208

Galicher, R., & Marois, C. 2011, in Second International Conference on Adaptive Optics for Extremely Large Telescopes. Online at <A href="http://ao4elt2.lesia.obspm.fr">http://ao4elt2.lesia.obspm.fr</A>, id.P25, P25 114

Galicher, R., Marois, C., Macintosh, B., et al. 2016, A&A, 594, A63 115

Gammie, C. F. 2001, ApJ, 553, 174 58, 59, 74

Garufi, A., Quanz, S. P., Avenhaus, H., et al. 2013, A&A, 560, A105 54

Garufi, A., Quanz, S. P., Schmid, H. M., et al. 2016, A&A, 588, A8 31, 106, 109, 125

Garufi, A., Meeus, G., Benisty, M., et al. 2017a, A&A, 603, A21 78, 126

Garufi, A., Benisty, M., Stolker, T., et al. 2017b, ArXiv e-prints, arXiv:1710.02795 31

Ginski, C., Stolker, T., Pinilla, P., et al. 2016, A&A, 595, A112 31, 99, 125, 131, 183

Girart, J. M., Beltrán, M. T., Zhang, Q., Rao, R., & Estalella, R. 2009, Science, 324, 1408 34

Girart, J. M., Rao, R., & Marrone, D. P. 2006, Science, 313, 812 34

Gold, T. 1952a, Nature, 169, 322 34

Gold, T. 1952b, MNRAS, 112, 215 34

Goldreich, P., & Nicholson, P. D. 1989, ApJ, 342, 1075 22

Goldreich, P., & Tremaine, S. 1979, ApJ, 233, 857 19

Goldreich, P., & Tremaine, S. 1980, ApJ, 241, 425 19, 21

Gonzalez, J.-F., Laibe, G., & Maddison, S. T. 2017, MNRAS, 467, 1984 13

Gonzalez, J.-F., Pinte, C., Maddison, S. T., Ménard, F., & Fouchet, L. 2012, A&A, 547, A58 151

Goodman, J., & Rafikov, R. R. 2001, ApJ, 552, 793 20, 24

Grady, C. A., Schneider, G., Hamaguchi, K., et al. 2007, ApJ, 665, 1391 126, 131

Grady, C. A., Muto, T., Hashimoto, J., et al. 2013, ApJ, 762, 48 30, 54

Guilloteau, S., Dutrey, A., Piétu, V., & Boehler, Y. 2011, A&A, 529, A105 33, 185

Gulkis, S., Allen, M., von Allmen, P., et al. 2015, Science, 347, aaa0709 1

Gundlach, B., & Blum, J. 2015, ApJ, 798, 34 153, 154

Güttler, C., Blum, J., Zsom, A., Ormel, C. W., & Dullemond, C. P. 2010, A&A, 513, A56 15

Haghighipour, N., & Boss, A. P. 2003, ApJ, 598, 1301 17

Hamaker, H. 1937, Physica, 4, 1058 152

Hartmann, L., Calvet, N., Gullbring, E., & D'Alessio, P. 1998, ApJ, 495, 385 10

Hashimoto, J., Dong, R., Kudo, T., et al. 2012, ApJL, 758, L19 95

Henning, T., & Stognienko, R. 1996, A&A, 311, 291 33, 56, 185

Herbig, G. H. 1960, ApJS, 4, 337 4

Hildebrand, R. H. 1988, Astrophysical Letters and Communications, 26, 263 34

Hoang, T., & Lazarian, A. 2009, ApJ, 697, 1316 34

Hollenbach, D. J., Yorke, H. W., & Johnstone, D. 2000, Protostars and Planets IV, 401 11

Huélamo, N., de Gregorio-Monsalvo, I., Macias, E., et al. 2015, A&A, 575, L5 96, 103, 107, 108, 109, 120, 121

Huélamo, N., Lacour, S., Tuthill, P., et al. 2011, A&A, 528, L7 97

Hughes, A. M., Hull, C. L. H., Wilner, D. J., & Plambeck, R. L. 2013, AJ, 145, 115 34

Hughes, A. M., Wilner, D. J., Cho, J., et al. 2009, ApJ, 704, 1204 34

Hull, C. L. H., Plambeck, R. L., Kwon, W., et al. 2014, ApJS, 213, 13 34

Husmann, T., Loesche, C., & Wurm, G. 2016, ApJ, 829, 111 151

Ida, S., & Makino, J. 1993, Icarus, 106, 210 18

Isella, A., Carpenter, J. M., & Sargent, A. I. 2010a, ApJ, 714, 1746 95

Isella, A., Natta, A., Wilner, D., Carpenter, J. M., & Testi, L. 2010b, ApJ, 725, 1735 95

Israelachvili, J. N. 1992, Academic Press 152, 154

Jaeger, C., Mutschke, H., Begemann, B., Dorschner, J., & Henning, T. 1994, A&A, 292, 641 49, 50, 62, 179

Janson, M., Thalmann, C., Boccaletti, A., et al. 2016, ApJL, 816, L1 78, 106, 121

Johansen, A., Klahr, H., & Henning, T. 2011, A&A, 529, A62 16

Johansen, A., Oishi, J. S., Mac Low, M.-M., et al. 2007, Nature, 448, 1022 16

Johansen, A., Youdin, A., & Klahr, H. 2009, ApJ, 697, 1269 18, 151, 185

Jones, R. V., & Spitzer, Jr., L. 1967, ApJ, 147, 943 34

Juhász, A., Benisty, M., Pohl, A., et al. 2015, MNRAS, 451, 1147 54, 58, 64, 73, 79, 80, 97, 189

Kama, M., Bruderer, S., Carney, M., et al. 2016, A&A, 588, A108 126

Kanagawa, K. D., Muto, T., Tanaka, H., et al. 2015, ApJL, 806, L15 145

Kataoka, A., Muto, T., Momose, M., Tsukagoshi, T., & Dullemond, C. P. 2016a, ApJ, 820, 54 35, 186, 209

Kataoka, A., Okuzumi, S., Tanaka, H., & Nomura, H. 2014, A&A, 568, A42 120, 185

Kataoka, A., Tanaka, H., Okuzumi, S., & Wada, K. 2013, A&A, 557, L4 16

Kataoka, A., Tsukagoshi, T., Pohl, A., et al. 2017, ApJL, 844, L5 34, 186, 211, 212

Kataoka, A., Muto, T., Momose, M., et al. 2015, ApJ, 809, 78 35, 36, 82, 186, 189, 193, 194, 197

Kataoka, A., Tsukagoshi, T., Momose, M., et al. 2016b, ApJL, 831, L12 34, 186, 213

Kenyon, S. J., & Hartmann, L. 1987, ApJ, 323, 714 8, 153

Kessler-Silacci, J., Augereau, J.-C., Dullemond, C. P., et al. 2006, ApJ, 639, 275 27

Kirchschlager, F., & Wolf, S. 2014, A&A, 568, A103 195

Klahr, H., & Bodenheimer, P. 2006, ApJ, 639, 432 18

Klahr, H., & Kley, W. 2006, A&A, 445, 747 79

Klahr, H. H., & Bodenheimer, P. 2003, ApJ, 582, 869 18

Klahr, H. H., & Henning, T. 1997, Icarus, 128, 213 17, 185

Klahr, H. H., Henning, T., & Kley, W. 1999, ApJ, 514, 325 79

Kley, W., & Nelson, R. P. 2012, ARA&A, 50, 211 19, 21, 22

Kohler, F. 1977, Berichte der Bunsengesellschaft für physikalische Chemie, 81, 775 152

Kokubo, E., & Ida, S. 1996, Icarus, 123, 180 18

Kokubo, E., & Ida, S. 1998, Icarus, 131, 171 18

Kouwenhoven, M. B. N., Brown, A. G. A., Zinnecker, H., Kaper, L., & Portegies Zwart, S. F. 2005, A&A, 430, 137 87

Kretke, K. A., & Lin, D. N. C. 2007, ApJL, 664, L55 18, 151

Krijt, S., Ciesla, F. J., & Bergin, E. A. 2016, ApJ, 833, 285 155, 176

Kuhn, J. R., Potter, D., & Parise, B. 2001, ApJL, 553, L189 127

Lacour, S., Biller, B., Cheetham, A., et al. 2016, A&A, 590, A90 94

Lada, C. J. 1987, in IAU Symposium, Vol. 115, Star Forming Regions, ed. M. Peimbert & J. Jugaku, 1–17 5

Lada, C. J. 2005, Progress of Theoretical Physics Supplement, 158, 1 4

Lada, C. J., & Wilking, B. A. 1984, ApJ, 287, 610 5

Lagage, P.-O., Doucet, C., Pantin, E., et al. 2006, Science, 314, 621 183

Lambrechts, M., & Johansen, A. 2012, A&A, 544, A32 18

Langlois, M., Dohlen, K., Augereau, J.-C., et al. 2010, in Proc. SPIE, Vol. 7735, Ground-based and Airborne Instrumentation for Astronomy III, 77352U 78

Langlois, M., Pohl, A., & The SPHERE consortium. 2017, Submitted to A&A 77, 80

Lazareff, B., Berger, J.-P., Kluska, J., et al. 2017, A&A, 599, A85 12, 88, 126, 136, 147

Lazarian, A. 2007, Journal of Quantitative Spectroscopy and Radiative Transfer, 106, 225 34, 186

Lesur, G., Kunz, M. W., & Fromang, S. 2014, A&A, 566, A56 11

Levenhagen, R. S., & Leister, N. V. 2006, MNRAS, 371, 252 208

Ligi, R., Vigan, A., Gratton, R., et al. 2018, Monthly Notices of the Royal Astronomical Society, 473, 1774 127, 147

Lin, D. N. C., & Papaloizou, J. 1979, MNRAS, 186, 799 19, 21

Lin, D. N. C., & Papaloizou, J. 1986, ApJ, 307, 395 21

Lin, D. N. C., & Papaloizou, J. C. B. 1993, in Protostars and Planets III, ed. E. H. Levy & J. I. Lunine, 749–835 22

Lin, M.-K. 2014, MNRAS, 437, 575 18

Lin, M.-K., & Papaloizou, J. C. B. 2010, MNRAS, 405, 1473 19

Lin, M.-K., & Papaloizou, J. C. B. 2011, MNRAS, 415, 1426 67

Lodato, G., & Rice, W. K. M. 2004, MNRAS, 351, 630 55, 93

Lodato, G., & Rice, W. K. M. 2005, MNRAS, 358, 1489 55

Long, F., Herczeg, G. J., Pascucci, I., et al. 2017a, ApJ, 844, 99 175

Long, Z. C., Fernandes, R. B., Sitko, M., et al. 2017b, ApJ, 838, 62 88

Lorén-Aguilar, P., & Bate, M. R. 2015, MNRAS, 453, L78 151

Lucy, L. B. 1999, A&A, 344, 282 45

Lynden-Bell, D., & Pringle, J. E. 1974, MNRAS, 168, 603 10, 22, 153, 178

Lyra, W., Turner, N. J., & McNally, C. P. 2015, A&A, 574, A10 55, 93

Macías, E., Anglada, G., Osorio, M., et al. 2017, ApJ, 838, 97 126, 127, 133, 147

Macintosh, B. A., Graham, J. R., Palmer, D. W., et al. 2008, in Proc. SPIE, Vol. 7015, Adaptive Optics Systems, 701518 19

Maire, A.-L., Langlois, M., Dohlen, K., et al. 2016, 9908, 990834 115, 116, 127, 128

Malik, M., Meru, F., Mayer, L., & Meyer, M. 2015, ApJ, 802, 56 23

Mamajek, E. E. 2009, in American Institute of Physics Conference Series, Vol. 1158, American Institute of Physics Conference Series, ed. T. Usuda, M. Tamura, & M. Ishii, 3–10 11

Manara, C. F., Fedele, D., Herczeg, G. J., & Teixeira, P. S. 2016, A&A, 585, A136 10

Manara, C. F., Robberto, M., Da Rio, N., et al. 2012, ApJ, 755, 154 10

Manara, C. F., Testi, L., Natta, A., et al. 2014, A&A, 568, A18 12

Mann, R. K., & Williams, J. P. 2010, ApJ, 725, 430 33

Manset, N., Bastien, P., Ménard, F., et al. 2009, A&A, 499, 137 77, 78, 80

Marino, S., Perez, S., & Casassus, S. 2015, ApJL, 798, L44 31, 88, 107, 126, 189

Marley, M. S., Fortney, J. J., Hubickyj, O., Bodenheimer, P., & Lissauer, J. J. 2007, ApJ, 655, 541 81

Marois, C., Lafrenière, D., Doyon, R., Macintosh, B., & Nadeau, D. 2006, ApJ, 641, 556 101

Marois, C., Zuckerman, B., Konopacky, Q. M., Macintosh, B., & Barman, T. 2010, Nature, 468, 1080 114

Martín-Doménech, R., Muñoz Caro, G. M., Bueno, J., & Goesmann, F. 2014, A&A, 564, A8 155

Masset, F. 2000, A&AS, 141, 165 57, 187

Mathis, J. S., Rumpl, W., & Nordsieck, K. H. 1977, ApJ, 217, 425 48, 191

Mayor, M., & Queloz, D. 1995, Nature, 378, 355 3

McClure, M. K., Bergin, E. A., Cleeves, L. I., et al. 2016, ApJ, 831, 167 33, 55, 176

Meeus, G., Waters, L. B. F. M., Bouwman, J., et al. 2001, A&A, 365, 476 88

Meeus, G., Pinte, C., Woitke, P., et al. 2010, A&A, 518, L124 126

Merín, B., Brown, J. M., Oliveira, I., et al. 2010, ApJ, 718, 1200 27, 95

Meru, F., & Bate, M. R. 2012, MNRAS, 427, 2022 60

Mesa, D., Gratton, R., Zurlo, A., et al. 2015, A&A, 576, A121 102

Mie, G. 1908, Annalen der Physik, 330, 377 43

Min, M., Canovas, H., Mulders, G. D., & Keller, C. U. 2012, A&A, 537, A75 121

Min, M., Dominik, C., Hovenier, J. W., de Koter, A., & Waters, L. B. F. M. 2006, A&A, 445, 1005 43

Min, M., Dullemond, C. P., Dominik, C., de Koter, A., & Hovenier, J. W. 2009, A&A, 497, 155 45

Min, M., Hovenier, J. W., & de Koter, A. 2005, A&A, 432, 909 43

Min, M., Rab, C., Woitke, P., Dominik, C., & Ménard, F. 2016, A&A, 585, A13 51

Min, M., Stolker, T., Dominik, C., & Benisty, M. 2017, A&A, 604, L10 88

Miotello, A., Bruderer, S., & van Dishoeck, E. F. 2014, A&A, 572, A96 56

Miotello, A., van Dishoeck, E. F., Kama, M., & Bruderer, S. 2016, A&A, 594, A85 56

Miotello, A., van Dishoeck, E. F., Williams, J. P., et al. 2017, A&A, 599, A113 176

Momose, M., Morita, A., Fukagawa, M., et al. 2015, PASJ, 67, 83 126, 128, 130, 132, 147

Monnier, J. D., Harries, T. J., Aarnio, A., et al. 2017, ApJ, 838, 20 126, 128, 130, 132, 133, 140, 142, 147

Montesinos, M., Perez, S., Casassus, S., et al. 2016, ApJL, 823, L8 31, 93

Mordasini, C., Alibert, Y., Benz, W., Klahr, H., & Henning, T. 2012, A&A, 541, A97 175

Mueller, H. 1948, J. Opt. Soc. Am., 38, 661 43

Mumma, M. J., & Charnley, S. B. 2011, ARA&A, 49, 471 155

Murphy, S. J., Lawson, W. A., & Bessell, M. S. 2013, MNRAS, 435, 1325 96

Musiolik, G., Teiser, J., Jankowski, T., & Wurm, G. 2016a, ApJ, 818, 16 153

Musiolik, G., Teiser, J., Jankowski, T., & Wurm, G. 2016b, ApJ, 827, 63 153

Muto, T., Grady, C. A., Hashimoto, J., et al. 2012, ApJL, 748, L22 20, 30, 54

Natta, A., Testi, L., Calvet, N., et al. 2007, Protostars and Planets V, 767 27

Ogilvie, G. I., & Lubow, S. H. 2002, MNRAS, 330, 950 20, 65, 93

Ohta, Y., Fukagawa, M., Sitko, M. L., et al. 2016, PASJ, 68, 53 95

Okuzumi, S. 2009, ApJ, 698, 1122 15

Okuzumi, S., Momose, M., Sirono, S.-i., Kobayashi, H., & Tanaka, H. 2016, ApJ, 821, 82 125, 146, 151, 155

Okuzumi, S., Tanaka, H., Kobayashi, H., & Wada, K. 2012, ApJ, 752, 106 16

Okuzumi, S., Tanaka, H., Takeuchi, T., & Sakagami, M.-a. 2011a, ApJ, 731, 95 15

Okuzumi, S., Tanaka, H., Takeuchi, T., & Sakagami, M.-a. 2011b, ApJ, 731, 96 15

Olofsson, J., Benisty, M., Augereau, J.-C., et al. 2011, A&A, 528, L6 96, 107

Olofsson, J., Benisty, M., Le Bouquin, J.-B., et al. 2013, A&A, 552, A4 96, 97, 107, 108, 109, 120

Ormel, C. W., Dullemond, C. P., & Spaans, M. 2010, Icarus, 210, 507 18

Ormel, C. W., & Klahr, H. H. 2010, A&A, 520, A43 18

Osorio, M., Anglada, G., Carrasco-González, C., et al. 2014, ApJL, 791, L36 126, 127, 133, 134

Ossenkopf, V. 1993, A&A, 280, 617 14, 120

Owen, J. E., Clarke, C. J., & Ercolano, B. 2012, MNRAS, 422, 1880 12

Owen, J. E., Ercolano, B., & Clarke, C. J. 2011, MNRAS, 412, 13 12

Paardekooper, S.-J. 2012, MNRAS, 421, 3286 60

Paardekooper, S.-J., & Mellema, G. 2004, A&A, 425, L9 144, 167

Paardekooper, S.-J., & Mellema, G. 2006, A&A, 453, 1129 18, 24, 144, 167

Panić, O., Hogerheijde, M. R., Wilner, D., & Qi, C. 2008, A&A, 491, 219 126, 131, 134

Panić, O., & Min, M. 2017, MNRAS, 467, 1175 155

Papaloizou, J., & Lin, D. N. C. 1984, ApJ, 285, 818 21, 22, 66

Papaloizou, J. C. B., & Terquem, C. 1995, MNRAS, 274, 987 94

Pascucci, I., Testi, L., Herczeg, G. J., et al. 2016, ApJ, 831, 125 12, 33, 175

Paszun, D., & Dominik, C. 2009, A&A, 507, 1023 153

Pavlov, A., Möller-Nilsson, O., Feldt, M., et al. 2008, in Proc. SPIE, Vol. 7019, Advanced Software and Control for Astronomy II, 701939 101

Pérez, L. M., Carpenter, J. M., Chandler, C. J., et al. 2012, ApJL, 760, L17 33

Pérez, L. M., Chandler, C. J., Isella, A., et al. 2015, ApJ, 813, 41 33

Pérez, L. M., Carpenter, J. M., Andrews, S. M., et al. 2016, Science, 353, 1519 30, 54

Picogna, G., & Kley, W. 2015, A&A, 584, A110 144

Pierens, A., & Huré, J.-M. 2005, A&A, 433, L37 65

Pineda, J. E., Quanz, S. P., Meru, F., et al. 2014, ApJL, 788, L34 208

Pinilla, P., Benisty, M., & Birnstiel, T. 2012a, A&A, 545, A81 18, 151, 167, 186, 187, 193

Pinilla, P., Birnstiel, T., Ricci, L., et al. 2012b, A&A, 538, A114 17, 120, 137, 140, 161, 167, 185

Pinilla, P., Birnstiel, T., & Walsh, C. 2015a, A&A, 580, A105 134, 137

Pinilla, P., de Juan Ovelar, M., Ataiee, S., et al. 2015b, A&A, 573, A9 96, 126, 137, 146, 209

Pinilla, P., Flock, M., Ovelar, M. d. J., & Birnstiel, T. 2016, A&A, 596, A81 18, 123, 125, 151, 161

Pinilla, P., Pohl, A., Stammler, S. M., & Birnstiel, T. 2017, ApJ, 845, 68 125, 151

Pinte, C., Harries, T. J., Min, M., et al. 2009, A&A, 498, 967 82, 189

Pinte, C., Ménard, F., Duchêne, G., & Bastien, P. 2006, A&A, 459, 797 45

Piso, A.-M. A., Öberg, K. I., Birnstiel, T., & Murray-Clay, R. A. 2015, ApJ, 815, 109 155

Pohl, A., Kataoka, A., Pinilla, P., et al. 2016, A&A, 593, A12 35, 36, 135, 156, 185

Pohl, A., Pinilla, P., Benisty, M., et al. 2015, MNRAS, 453, 1768 20, 53, 79, 80, 82, 97

Pohl, A., Benisty, M., Pinilla, P., et al. 2017, The Astrophysical Journal, 850, 52 26, 125

Pohl, A., Sissa, E., Langlois, M., et al. 2017, A&A, 605, A34 31, 78, 95, 128

Pollack, J. B., Hollenbach, D., Beckwith, S., et al. 1994, ApJ, 421, 615 33, 56, 190

Pollack, J. B., Hubickyj, O., Bodenheimer, P., et al. 1996, Icarus, 124, 62 10, 18

Poppe, T., Blum, J., & Henning, T. 2000, ApJ, 533, 472 153

Powell, D., Murray-Clay, R., & Schlichting, H. E. 2017, ApJ, 840, 93 155

Preibisch, T., Ossenkopf, V., Yorke, H. W., & Henning, T. 1993, A&A, 279, 577 49, 179

Purcell, E. M. 1979, ApJ, 231, 404 34

Qi, C., Öberg, K. I., Wilner, D. J., et al. 2013, Science, 341, 630 168

Quanz, S. P., Amara, A., Meyer, M. R., et al. 2015, ApJ, 807, 64 208

Quanz, S. P., Avenhaus, H., Buenzli, E., et al. 2013, ApJL, 766, L2 126, 208

Racine, R., Walker, G. A. H., Nadeau, D., Doyon, R., & Marois, C. 1999, PASP, 111, 587 102

Rafikov, R. R. 2002, ApJ, 572, 566 20, 22, 24, 66

Raman, A., Lisanti, M., Wilner, D. J., Qi, C., & Hogerheijde, M. 2006, AJ, 131, 2290 126

Rameau, J., Follette, K. B., Pueyo, L., et al. 2017, AJ, 153, 244 208

Rao, R., Girart, J. M., Lai, S.-P., & Marrone, D. P. 2014, ApJL, 780, L6 34, 186

Rao, R., Girart, J. M., Marrone, D. P., Lai, S.-P., & Schnee, S. 2009, ApJ, 707, 921 34

Rapson, V. A., Kastner, J. H., Millar-Blanchaer, M. A., & Dong, R. 2015, ApJL, 815, L26 125

Regály, Z., Juhász, A., Sándor, Z., & Dullemond, C. P. 2012, MNRAS, 419, 1701 151, 211

Reggiani, M., Quanz, S. P., Meyer, M. R., et al. 2014, ApJL, 792, L23 127

Ribas, Á., Merín, B., Bouy, H., & Maud, L. T. 2014, A&A, 561, A54 11

Ricci, L., Mann, R. K., Testi, L., et al. 2011, A&A, 525, A81 185

Ricci, L., Testi, L., Natta, A., & Brooks, K. J. 2010a, A&A, 521, A66 17, 33, 185

Ricci, L., Testi, L., Natta, A., et al. 2010b, A&A, 512, A15 33, 108, 135, 157, 185, 190

Ricci, L., Trotta, F., Testi, L., et al. 2012, A&A, 540, A6 185

Rice, W. K. M., Armitage, P. J., Bate, M. R., & Bonnell, I. A. 2003a, MNRAS, 339, 1025 60

Rice, W. K. M., Lodato, G., Pringle, J. E., Armitage, P. J., & Bonnell, I. A. 2004, MNRAS, 355, 543 55

Rice, W. K. M., Lodato, G., Pringle, J. E., Armitage, P. J., & Bonnell, I. A. 2006, MNRAS, 372, L9 151, 167

Rice, W. K. M., Wood, K., Armitage, P. J., Whitney, B. A., & Bjorkman, J. E. 2003b, MNRAS, 342, 79 96

Riviere-Marichalar, P., Merín, B., Kamp, I., Eiroa, C., & Montesinos, B. 2016, A&A, 594, A59 126

Robitaille, T. P. 2010, A&A, 520, A70 45

Rodmann, J., Henning, T., Chandler, C. J., Mundy, L. G., & Wilner, D. J. 2006, A&A, 446, 211 185

Ros, K., & Johansen, A. 2013, A&A, 552, A137 16, 151

Rosotti, G. P., Juhasz, A., Booth, R. A., & Clarke, C. J. 2016, MNRAS, 459, 2790 24, 25, 126, 144, 145, 151, 167

Rotundi, A., Sierks, H., Della Corte, V., et al. 2015, Science, 347, aaa3905 1

Ruge, J. P., Flock, M., Wolf, S., et al. 2016, A&A, 590, A17 18, 125

Rybicki, G. B., & Lightman, A. P. 1979, Radiative processes in astrophysics 39

Safronov, V. S. 1972, Evolution of the protoplanetary cloud and formation of the earth and planets. 17

Saito, E., & Sirono, S.-i. 2011, ApJ, 728, 20 151

Sallum, S., Eisner, J. A., Close, L. M., et al. 2015, ApJ, 801, 85 97

Schmid, H. M., Joos, F., & Tschan, D. 2006, A&A, 452, 657 32, 127, 128

Schmid, H.-M., Downing, M., Roelfsema, R., et al. 2012, in Proc. SPIE, Vol. 8446, Ground-based and Airborne Instrumentation for Astronomy IV, 84468Y 88, 100

Schoonenberg, D., & Ormel, C. W. 2017, A&A, 602, A21 167

Schräpler, R., Blum, J., Seizinger, A., & Kley, W. 2012, ApJ, 758, 35 15

Schräpler, R., & Henning, T. 2004, ApJ, 614, 960 14, 177

Schwarz, K. R., Bergin, E. A., Cleeves, L. I., et al. 2016, ApJ, 823, 91 176

Segura-Cox, D. M., Looney, L. W., Stephens, I. W., et al. 2015, ApJL, 798, L2 34, 186

Semenov, D., Henning, T., Helling, C., Ilgner, M., & Sedlmayr, E. 2003a, A&A, 410, 611 56

Semenov, D., Henning, T., Ilgner, M., Helling, C., & Sedlmayr, E. 2003b, in Astronomical Society of the Pacific Conference Series, Vol. 288, Stellar Atmosphere Modeling, ed. I. Hubeny, D. Mihalas, & K. Werner, 361 49

Seok, J. Y., & Li, A. 2017, ApJ, 835, 291 126

Shakura, N. I., & Sunyaev, R. A. 1973, A&A, 24, 337 10, 120

Simon, J. B., & Armitage, P. J. 2014, ApJ, 784, 15 18, 125, 151

Simon, J. B., Bai, X.-N., Armitage, P. J., Stone, J. M., & Beckwith, K. 2013a, ApJ, 775, 73 11

Simon, J. B., Bai, X.-N., Stone, J. M., Armitage, P. J., & Beckwith, K. 2013b, ApJ, 764, 66 11

Simon, J. B., Hughes, A. M., Flaherty, K. M., Bai, X.-N., & Armitage, P. J. 2015, ApJ, 808, 180 166

Soummer, R. 2005, ApJL, 618, L161 99

Soummer, R., Pueyo, L., & Larkin, J. 2012, ApJL, 755, L28 101, 102

Spiegel, D. S., & Burrows, A. 2012, ApJ, 745, 174 81

Stammler, S. M., Birnstiel, T., Panić, O., Dullemond, C. P., & Dominik, C. 2017, A&A, 600, A140 125, 151, 155, 167

Stephens, I. W., Looney, L. W., Kwon, W., et al. 2014, Nature, 514, 597 34, 186

Stephens, I. W., Yang, H., Li, Z.-Y., et al. 2017, ArXiv e-prints, arXiv:1710.04670 34, 186, 212

Stolker, T., Dominik, C., Avenhaus, H., et al. 2016, A&A, 595, A113 30, 31, 54, 88, 95, 126

Strom, K. M., Strom, S. E., Edwards, S., Cabrit, S., & Skrutskie, M. F. 1989, AJ, 97, 1451 12, 27

Suzuki, T. K., & Inutsuka, S.-i. 2009, ApJL, 691, L49 166

Szulágyi, J., Mayer, L., & Quinn, T. 2017, MNRAS, 464, 3158 18

Szulágyi, J., Morbidelli, A., Crida, A., & Masset, F. 2014, ApJ, 782, 65 18

Takahashi, S. Z., & Inutsuka, S.-i. 2014, ApJ, 794, 55 126, 151

Takami, M., Karr, J. L., Hashimoto, J., et al. 2013, ApJ, 772, 145 121

Takeuchi, T., & Ida, S. 2012, ApJ, 749, 89 16

Takeuchi, T., & Lin, D. N. C. 2002, ApJ, 581, 1344 15

Tamura, M., Hough, J. H., & Hayashi, S. S. 1995, ApJ, 448, 346 186

Tang, Y.-W., Guilloteau, S., Dutrey, A., et al. 2017, ApJ, 840, 32 31, 54

Tazaki, R., Lazarian, A., & Nomura, H. 2017, ApJ, 839, 56 34

Tazaki, R., Tanaka, H., Okuzumi, S., Kataoka, A., & Nomura, H. 2016, ApJ, 823, 70 51, 120

Tazzari, M., Testi, L., Ercolano, B., et al. 2016, A&A, 588, A53 33

Teague, R., Guilloteau, S., Semenov, D., et al. 2016, A&A, 592, A49 30, 166, 168, 178

Teiser, J., & Wurm, G. 2009, MNRAS, 393, 1584 15

Testi, L., Natta, A., Shepherd, D. S., & Wilner, D. J. 2001, ApJ, 554, 1087 33, 185

Testi, L., Birnstiel, T., Ricci, L., et al. 2014, Protostars and Planets VI, 339 29, 33

Thalmann, C., Schmid, H. M., Boccaletti, A., et al. 2008, in Proc. SPIE, Vol. 7014, Ground-based and Airborne Instrumentation for Astronomy II, 70143F 88, 100

Thalmann, C., Grady, C. A., Goto, M., et al. 2010, ApJL, 718, L87 95

Thalmann, C., Mulders, G. D., Janson, M., et al. 2015, ApJL, 808, L41 95

Thalmann, C., Janson, M., Garufi, A., et al. 2016, ApJL, 828, L17 31

Thamm, E., Steinacker, J., & Henning, T. 1994, A&A, 287, 493 141

Thomas, N., Sierks, H., Barbieri, C., et al. 2015, Science, 347, aaa0440 1

Tobin, J. J., Kratter, K. M., Persson, M. V., et al. 2016, Nature, 538, 483 54

Toomre, A. 1964, ApJ, 139, 1217 19, 55

Torres, C. A. O., Quast, G. R., Melo, C. H. F., & Sterzik, M. F. 2008, Young Nearby Loose Associations, ed. B. Reipurth, 757 96, 118

Trotta, F., Testi, L., Natta, A., Isella, A., & Ricci, L. 2013, A&A, 558, A64 33

Tsukagoshi, T., Nomura, H., Muto, T., et al. 2016, ApJL, 829, L35 125

Uribe, A. L., Klahr, H., Flock, M., & Henning, T. 2011, ApJ, 736, 85 151

van Boekel, R., Henning, T., Menu, J., et al. 2017, ApJ, 837, 132 30, 31, 125, 168, 176

van der Marel, N., van Dishoeck, E. F., Bruderer, S., Pérez, L., & Isella, A. 2015, A&A, 579, A106 95, 120

van der Marel, N., Verhaar, B. W., van Terwisga, S., et al. 2016, A&A, 592, A126 27, 95

van der Plas, G., Wright, C. M., Ménard, F., et al. 2017, A&A, 597, A32 125

van't Hoff, M. L. R., Walsh, C., Kama, M., Facchini, S., & van Dishoeck, E. F. 2017, A&A, 599, A101 168

Varnière, P., Quillen, A. C., & Frank, A. 2004, ApJ, 612, 1152 23

Varnière, P., & Tagger, M. 2006, A&A, 446, L13 18

Vigan, A., Moutou, C., Langlois, M., et al. 2010, MNRAS, 407, 71 99

Vigan, A., Bonnefoy, M., Ginski, C., et al. 2016, A&A, 587, A55 115

Wada, K., Tanaka, H., Suyama, T., Kimura, H., & Yamamoto, T. 2009, ApJ, 702, 1490 154

Wada, K., Tanaka, H., Suyama, T., Kimura, H., & Yamamoto, T. 2011, ApJ, 737, 36 154

Wagner, K., Apai, D., Kasper, M., & Robberto, M. 2015a, ApJL, 813, L2 54, 88

Wagner, K. R., Sitko, M. L., Grady, C. A., et al. 2015b, ApJ, 798, 94 126, 131, 142, 147

Walsh, C., Juhász, A., Pinilla, P., et al. 2014, ApJL, 791, L6 56, 125, 208

Ward, W. R. 1997, Icarus, 126, 261 22

Warren, S. G., & Brandt, R. E. 2008, Journal of Geophysical Research (Atmospheres), 113, D14220 49, 50, 82, 108, 135, 190

Weidenschilling, S. J. 1977, MNRAS, 180, 57 14, 15

Weidenschilling, S. J. 1980, Icarus, 44, 172 15

Weidling, R., Güttler, C., Blum, J., & Brauer, F. 2009, ApJ, 696, 2036 15

Weingartner, J. C., & Draine, B. T. 2003, ApJ, 589, 289 34

Whipple, F. L. 1972, in From Plasma to Planet, ed. A. Elvius, 211 14, 15, 17, 185

Whitney, B. A., Robitaille, T. P., Bjorkman, J. E., et al. 2013, ApJS, 207, 30 44

Williams, J. P., & Best, W. M. J. 2014, ApJ, 788, 59 56

Wilner, D. J., D'Alessio, P., Calvet, N., Claussen, M. J., & Hartmann, L. 2005, ApJL, 626, L109 185

Windmark, F., Birnstiel, T., Güttler, C., et al. 2012a, A&A, 540, A73 16, 153

Windmark, F., Birnstiel, T., Ormel, C. W., & Dullemond, C. P. 2012b, A&A, 544, L16 16

Woitke, P., Min, M., Pinte, C., et al. 2016, A&A, 586, A103 85, 142

Wolf, S., Henning, T., & Stecklum, B. 1999, A&A, 349, 839 44

Wurm, G., & Blum, J. 1998, Icarus, 132, 125 14

Wurm, G., Paraskov, G., & Krauss, O. 2005, Icarus, 178, 253 15

Yang, H., Li, Z.-Y., Looney, L., & Stephens, I. 2016, MNRAS, 456, 2794 35, 186, 197

Youdin, A. N. 2011, ApJ, 731, 99 16, 126, 151

Youdin, A. N., & Goodman, J. 2005, ApJ, 620, 459 16

Youdin, A. N., & Lithwick, Y. 2007, Icarus, 192, 588 156, 177, 190

Zhang, K., Bergin, E. A., Blake, G. A., Cleeves, L. I., & Schwarz, K. R. 2017, Nature Astronomy, 1, 0130 168

Zhang, K., Blake, G. A., & Bergin, E. A. 2015, ApJL, 806, L7 125, 146, 154, 155

Zhu, Z., Dong, R., Stone, J. M., & Rafikov, R. R. 2015, ApJ, 813, 88 19, 20, 93

Zhu, Z., Nelson, R. P., Dong, R., Espaillat, C., & Hartmann, L. 2012, ApJ, 755, 6 17, 18, 126, 185

Zhu, Z., Nelson, R. P., Hartmann, L., Espaillat, C., & Calvet, N. 2011, ApJ, 729, 47 126, 151, 167

Zhu, Z., & Stone, J. M. 2014, ApJ, 795, 53 64, 69

Zhu, Z., Stone, J. M., & Rafikov, R. R. 2013, ApJ, 768, 143 23

Zsom, A., Ormel, C. W., Güttler, C., Blum, J., & Dullemond, C. P. 2010, A&A, 513, A57 15

Zubko, V. G., Mennella, V., Colangeli, L., & Bussoletti, E. 1996, MNRAS, 282, 1321 49, 50, 82, 108, 135, 190

Zurlo, A., Vigan, A., Mesa, D., et al. 2014, A&A, 572, A85 102

D | Acknowledgments

First and foremost, I would like to thank my advisors, Thomas Henning and Kees Dullemond, who guided me through the years of this thesis. I am very grateful that I was given the chance to join Heidelberg's two research groups on planet-forming disks. For me, this opened the great opportunity to learn about both, the observational and theroretical aspects of planet formation. Despite their own heavy workload, I would like to very much thank both of them for taking time to discuss projects, for supporting my ideas, and for their helpful comments on paper and proposal drafts. Thomas, thank you also for all the unique chances to present my work at so many international conferences during the last three years, and for your fantastic support all along. Kees, thank you for the tutoring that already started in the beginning of my Master's studies, and for teaching me the art of numerical hydrodynamics and radiative transfer modeling. I also want to express my gratitude to Leonardo Testi for agreeing to be the secondary referee of this thesis.

I would like to especially thank for the great support that I have received from three people, with whom collaborations turned out to be very fruitful and from whom I have learned a lot: Myriam Benisty, Akimasa Kataoka, and Paola Pinilla. Akimasa, thank you for teaching me about polarization, dust growth, and fluffy aggregates. I would like to thank you for the many spontaneous discussions during your time in Heidelberg, for astro-ph analysis sessions, and for always being patient in answering my questions. Apart from research, I also enjoyed our several trips to watch soccer, handball, and ice hockey in the stadiums. Myriam and Paola, your unbounded enthusiasm for astronomical research and your knowledge was very motivating, and your constant encouragement was essential for the completion of this work. I want to thank you for the numerous Skype conversations and all the discussions in person during your Heidelberg visits. Thank you for guiding me through the world of astronomy, for convincing me to be more optimistic, but at the same time teaching me how to maintain an appropriate level of skepticism.

I want to thank Roy van Boekel for being part of my IMPRS thesis committee, and for valuable comments on this thesis. I would also like to thank Hubert Klahr for our collaborations and for explaining me insightful details on planet-disk interaction processes. I am grateful to Jos de Boer, Carsten Dominik, Antonio Garufi, Christian Ginski, Rob van Holstein, Maud Langlois, Anne-Lise Maire, André Müller, Tomas Stolker and the rest of my collaborators from the SPHERE consortium for sharing

their insights on observational, technical, and theoretical topics of planets and disks. Furthermore, I learned a lot from discussions with Sareh Ataiee, Til Birnstiel, Attila Juhasz, Miriam Keppler, Takayuki Muto, Nicole Pawellek, Matthias Samland, Sebastian Stammler, Rich Teague, Philipp Weber, and many more people...

Many thanks go to the Elsässer crew at office E114 (Andreas, Christian, Paul) - it has been a great time with you guys! Furthermore, I also want to thank my office mates at ITA (Akimasa, Daniel, María Jesús, Sacha), who have contributed to an enjoyable working atmosphere.

I would like to thank all the members of the MPIA PSF theory group for creating an encouraging scientific environment. Particular thanks to Paul and Hans for taking care of the Theory Lunch orders on Tuesdays. Thanks, Andreas, for bothering me a long time until I eventually watched the Star Wars movies for the first time in my life - I would have definitely missed something without taking part in the weekly nerd discussions! Special thanks go to Hans for joining me in the HGSFP winterschool and for exploring together the fresh powder on snowing days, which was a lot of fun. Furthermore, many thanks go to André M. and Nicole for funny lunch times at MPIA, and the chats about the meaning of life and science.

Flying, skiing, and tennis are probably the best ways in the world to 'waste time'. Many thanks to the welcome distractions from science go to my friends from the flying club SFC Schwetzingen e.V. for stunning flights in powered aircrafts and gliders, relaxing summer evenings at the airfield and awesome skiing trips, and to my HTV tennis teammates for the training sessions and exciting tournaments. Moreover, there are several people that sometimes managed to convince me to take work less serious. Thank you, Esther & Tim, for having us over for dinner at your place numerous times, for skiing/snowboarding trips to the Black Forest and the Alpes, and for the North Sea tour. I would like to thank my beloved friends from Saarland (Anna, Benedikt, Corinna, Frauke, Michael, Rebecca, Sabrina, Sandra) for our long-lasting great friendship since our good old MPG days, thrilling exit room games, and supportive words from afar.

Last but not least, I want to thank my family for supporting me throughout these years. I am deeply indebted to my parents for their unfailing help with so many things, for their interest in what I am doing, and for food & care packages at the right time. I am thankful to the best brother one can think of, Matthias, for always being there for your little sister whenever I needed advice. Many thanks to you, Sara, and my two little nephews Aaron & Noah for your warm welcomes whenever I came home. I want to thank my grandparents, who were consistently interested in the status of my thesis. Lastly, and most importantly, I owe my deepest gratitude to André J. for his indispensable support, patience, and vital inspiration. It is truly great to have someone by my side who has the same passions for science, aviation, politics, traveling, mountains, skiing, hiking, music,... - thank you so much for sharing your views of the world with me!

The sky is not the limit

- it's where the fun begins!

Declaration

I hereby declare that this thesis is my own work and that I have used no other than the stated sources and aids.

Erklärung

Ich versichere, dass ich diese Arbeit selbstständig verfasst habe und keine anderen als die angegebenen Quellen und Hilfsmittel benutzt habe.

Heidelberg, 13.11.2017

.....
Adriana Pohl